Mechanism of spin-orbit torques in platinum oxide systems

Jayshankar Nath

Communauté
UNIVERSITÉ Grenoble Alpes

THÈSE

Pour obtenir le grade de

DOCTEUR DE LA COMMUNAUTÉ

UNIVERSITÉ GRENOBLE ALPES

Spécialité : **Physique de la Matière Condensée et du Rayonnement**

Arrêté ministériel : 25 mai 2016

Présentée par

Jayshankar NATH

Thèse dirigée par **Gilles GAUDIN**
et codirigée par **Ioan Mihai MIRON**

préparée au sein du **Laboratoire Spintronique et Technologie des Composants (SPINTEC)**
dans **l'École Doctorale Physique**

Mécanisme des Couples Spin-Orbite dans les Systèmes à l'Oxyde de Platine

Mechanism of Spin-Orbit Torques in Platinum Oxide Systems

Thèse soutenue publiquement le **5 Décembre 2019**,
devant le jury composé de :

M. Mairbek CHSHIEV
Professeur, SPINTEC/Université Grenoble Alpes, Président
M. Felix CASANOVA
Directeur de Recherche, CIC nanoGUNE, Rapporteur
M. Michel VIRET
Cadre Scientifique des EPIC, SPEC/CEA, Rapporteur
M. Mihai GABOR
Maître de Conférence, Université Technique de Cluj-Napoca, Examinateur

Résumé de la Thèse

Mécanisme des Couples Spin-Orbite

dans les Systèmes à l'Oxyde de Platine

par

Jayshankar NATH

Doctorat en Physique

Université Grenoble Alpes, 2019

Dr. Gilles GAUDIN, Directeur de Thèse

Dr. Mihai MIRON, Co-Directeur de Thèse

L'avènement du Big Data, Machine Learning (ML) et 5G a l'importance de certains paramètres clé des technologies mémoire tels que la consommation d'énergie, la non-volatilité, la vitesse, la taille et l'endurance. Les mémoires magnétiques à accès aléatoire (MRAM) telles que les MRAM à couple de transfert de spin (STT-MRAM) et les MRAM à couple de spin orbite (SOT-MRAM) sont devenues des concurrents incontournables de ce marché, dans l'objectif d'remplacer les RAM statiques (SRAM) et les RAM dynamiques (DRAM) actuelles basées sur la technologie CMOS (Complementary Metal-Oxide-Semiconductor). La commutation d'un bit mémoire dans les SOT-MRAMs s'appuie sur les spins générés via le couplage spin orbite (SOC) par l'application d'un courant de charge à travers un métal lourds (HM). Ces HM étant résistifs, des pertes ohmiques existent pendant le processus d'écriture. Un vaste corpus de travaux, tant universitaires qu'industriels, a été consacré à la recherche de moyens pour minimiser ces pertes et ainsi améliorer l'efficacité énergétique. De plus, le courant injecté dans la mémoire lors du processus d'écriture est contrôlé par un transistor de commutation CMOS. La taille de ce transistor augmente avec le courant de commutation. Par conséquent, une réduction de ce courant conduit également à un gain de densité de la mémoire.

Diverses approches visant à améliorer la génération de spins par unité de courant appliqué ont été adoptées pour atteindre cet objectif. Les premières ont consist à utiliser des métaux de transition présentant un SOC élevé, des alliages métalliques et/ou une phase structurelle résistive du métal. Des travaux plus récents se sont concentrés sur l'ingénierie de l'interface : insertion de couches ultrafines et utilisation de couches de capping formant des puits de spin. L'une des approches actuelles concerne l'utilisation de l'oxydation comme moyen d'augmenter les SOT. Différents groupes ont étudié l'effet de l'oxydation du HM, du Ferro-Magnétique (FM) ainsi que de la couche de capping constituée de métaux plus légers comme le cuivre. Bien que la majorité de ces travaux fass état d'une augmentation des SOT, les résultats et les conclusions ne sont pas cohérents. Des tendances divergentes d'augmentation des SOT, qui ont, à leur tour, été attribuées à des phénomènes physiques variés. Dans

ce travail, nous étudions les SOTs générés par l'oxydation de la couche de platine dans une pile multicouche Ta/Cu/Co/Pt.

Dans ce système, nous quantifions les SOTs en mesurant les couples par une technique de seconde harmonique. Nous observons en effet une augmentation des couples. Ceci est vérifié par des mesures de spin pumping qui montrent une augmentation de l'amortissement. Afin de déterminer l'origine de cette augmentation, nous avons construit un modèle décrivant l'oxydation du système basé sur des caractérisations électriques, magnétiques et matérielles ansi que des calculs ab-initio de la théorie fonctionnelle de la densité (DFT). Ceci nous a conduit à la conclusion que contrairement aux travaux précédents, qui expliquaient les résultats en se basant exclusivement sur un modèle où seul le HM était oxydé, dans la pratique l'oxygène près de l'interface FM/HM est pompé dans la couche FM. Ce phénomènz ne conduit pas seulement à une oxydation FM, mais laisse aussi le HM métallique à proximité de l'interface. En outre, ce modèle a été étayé par des mesures et des calculs des échanges symétrique et anti-symétrique. En tenant compte de ces observations et une fois les SOT quantifiés corrigés, nous ne constatons aucune augmentation observable des couples. Ceci nous amène à conclure que bien qu'au niveau du système il y ait une augmentation des SOTs avec l'oxydation du platine, il n'y a pas de contribution intrinsèque de l'oxyde de platine à l'augmentation des couples. Cette découverte a de vastes conséquences sur la conception de SOT-MRAM, affectant l'endurance, la consommation d'énergie et la magnéto-résistance tunnel (TMR).

Mots-clé: Couples de spin orbite (SOT), Mémoire magnétique à accès aléatoire (MRAM), Platine, Oxyde de platine, Couple de type amortissement, Couple de type champ, Mesures harmoniques de couples

Abstract of the Thesis

Mechanism of Spin-Orbit Torques

in Platinum Oxide Systems

by

Jayshankar NATH

Doctor of Philosophy in Physics

Université Grenoble Alpes, 2019

Dr. Gilles GAUDIN, Thesis Director

Dr. Mihai MIRON, Thesis Co-Director

The advent of Big Data, Machine Learning (ML) and 5G has placed a greater emphasis on certain key metrics of memory technology such as power consumption, non-volatility, speed, size, and endurance. Magnetic Random-Access Memories (MRAM) such as Spin Transfer Torque MRAM (STT-MRAM) and Spin-Orbit Torque MRAM (SOT-MRAM) have emerged as key contenders in this market, targeted towards replacing the current Complementary Metal-Oxide-Semiconductor (CMOS) based Static RAMs (SRAM) and Dynamic RAMs (DRAM). SOT-MRAMs rely on spins generated by applying a charge current through a metal with a high Spin-Orbit Coupling (SOC) to switch the magnetic memory bit. These Heavy Metals (HM) being resistive, lead to Ohmic losses during the write process. A vast body of work, both academic and industrial, has been dedicated to finding ways to minimize these losses and thereby enhance the energy efficiency. Moreover, the current that is injected into the device during the write process is controlled by a CMOS switching transistor. The size of this transistor increases with the switching current. Hence, a reduction in this current can also lead to a gain in the bit density of the memory.

Various approaches have been adopted to achieve this target by means of enhancing the generation of spins per unit applied current. The earliest approaches involved using transition metals with high SOC, metallic alloys and resistive structural phase of the metal. More recent works have focused on interfacial engineering via ultra-thin insertion layers and spin-sink capping materials. One of the current focus is on using oxidation as a means of enhancing the SOTs. Different groups have studied the effect of oxidation of the HM, the Ferro-Magnet (FM) as well as the capping layer consisting of lighter metals such as copper. Although majority of these works report an increase of SOTs in general, the results and conclusions are not consistent. Differing trends of SOT increase have been reported which in turn have been attributed to varied physical phenomenon. In this work, we study the SOTs generated by oxidizing the platinum layer in a Ta/Cu/Co/Pt multilayer stack.

We quantify the SOTs in this system using second harmonic torque measurements and do indeed observe an increase in torques. This is verified with spin-pumping measurements, observing an increase in the damping. In order to determine the origin of this increase, we built an oxidation model of the system based on electrical, magnetic and material characterizations and ab-initio Density Functional Theory (DFT) calculations. This led us to the conclusion that unlike previous works, which exclusively explained the findings based on a completely oxidized HM model, in practice the oxygen near the FM/HM interface gets pumped into the FM layer. This not only oxidizes the FM, but it also leaves the HM metallic near the interface. This model was further supported by measurements and calculations of the symmetric and anti-symmetric exchange, which were found to have a linear relationship. Accounting for these observations, once the quantified SOTs are corrected, we see no observable increase in torques. This leads us to conclude that although on a system level there is an increase of SOTs with platinum oxidation, there is no intrinsic contribution of platinum-oxide on the enhancement of torques. This finding has broad consequences in the design of SOT-MRAM, affecting endurance, power consumption and Tunneling Magneto-Resistance (TMR).

Keywords: Spin-Orbit Torques (SOT), Magnetic Random-Access Memory (MRAM), Platinum, Platinum Oxide, Damping-Like Torque, Field-Like Torque, Second Harmonic Torque Measurements

Parents, educators, colleagues, friends, and family.

There are people you count on in every walk of your life.

This work is dedicated to you all.

To my mentors

Table of Contents

List of Figures

Acknowledgements

The work presented here has been possible due to the encouragement, guidance, help, and support of many.

First and foremost, I would like to thank my thesis supervisors, Gilles Gaudin and Mihai Miron. Not only did they advise me on scientific matters, but they have become good friends during this work. The characteristics that have had a lasting impression on me are Mihai's intellectual curiosity and ability to break down complex scientific phenomena into simple, bite-sized pieces; And Gilles' humility and soft spoken-ness, diligence and his vast repertoire of knowledge. I can only aim to inculcate these standards that they have set for me, in my professional and personal life. Thank you both for standing by me during the good times and bad.

As probably is the case for many theses, I experienced difficulties, setbacks and hidden pitfalls during my thesis. From dicing induced sample damage to indium contamination from the sputtering target; and platinum oxidation from the residue of standard nitrile gloves. However, contrary to what I think of others, these pitfalls did not disappear on the day of the defense, which took place on the first day of French strikes, Dec. 5th, 2019. I would like to thank all the thesis committee members who managed to make it regardless of the travel difficulties. Mairbek Chshiev, Felix Casanova, Michel Viret and Mihai Gabor. Their valuable insights and their critical review of my work are greatly appreciated.

I would also like to thank my collaborators around the world. Ali Hallal and Mairbek Chshiev for the ab-initio calculations; Mihai Gabor for the FMR measurements; Sebastien Labau, Aymen Mahjoub and Bernard Pelissier for the AR-XPS measurements; Avinash Kumar Chaurasiya, Amrit Kumar Mondal and Anjan Barman for the BLS measurements; Eric Gautier for the TEM measurements; Peter Mills and Thomas Saerbeck for the neutron reflectometry measurements.

My special thanks to the people from SPINTEC who made significant contributions to this work. Alexandru Trifu, with whom I started this work on platinum oxidation; Stéphane Auffret for the countless sample depositions and Isabelle Joumard for the technical support.

I have further obtained help and guidance from the members of the SOT group at SPINTEC. Thomas Brächer for his help with fabrication and guidance; Mohamed Ali Nsibi, with whom I started this Ph.D. program and built a couple of MOKE microscopes with; Haozhe Yang from whom I learned the importance of putting together a quick setup to test something quickly; Alexandre Mouillon and Marc Drouard for help with the measurement setup and data analysis; Eva Schmoranzerova for being a sounding board for SOT measurements; Pyunghwa Jang, Edmond Chan, and Ugwumsinachi Oji for help with measurements; Mathieu Fabre for introducing me to Python; Soong-Geun Je for helping with the electrical setups.

I would also like to thank the members of the PTA for their valuable help in the fabrication of my devices, namely, Thierry Chevolleau, Jean-Luc Thomassin, Frédéric Gustavo, Marlène Terrier, Christophe Lemonias, Thomas Charvolin, Nicolas Chaix, Irène Peck, Guillaume Lavaitte, Jude Guelfucci, and Nathalie Marini.

My sincere gratitude to all the members of SPINTEC, past, and present. I have gained valuable guidance, insight and technical advice from many of you. Bernard Dieny, Ursula Ebels, Lucian Prejbeanu, Mairbek Chshiev, Vincent Baltz, Laurent Vila, Olivier Boulle, Claire Baraduc, and Olivier Klein; Lucian Prejbeanu and Olivier Fruchart for maintaining the welcoming atmosphere at SPINTEC for

PhDs and post-docs; Catherine Broisin, Rachel Mauduit, Sabrina Megias, Léa Althana and Céline Conche for help with all the administrative work; Daniel Solis Lerma for taking time to answer all my theoretical questions; Paulo Coelho and Jyotirmoy Chatterjee for help with the VSM; Léa Cuchet and Clarisse Ducruet (affiliated with Crocus Technology) for the same; Eric Billiet for the technical support; Roméo Juge, Titiksha Srivastava and Marco Mansueto for helping set up the *pot de thèse*; My officemates Cécile Naud and Caroline Thibault. In addition, I would like to thank all the members of SPINTEC for the numerous discussions over coffee or otherwise and helping make these years memorable.

My gratitude to the Université Grenoble Alps, SPINTEC, IRIG, CEA and CNRS for accepting me as a doctoral student. And to the European Union for funding my doctoral program under the Horizon 2020 program (Project 638656 Smart Design). I would also like to thank the École Doctorale de Physique for accepting the extension of my thesis, allowing me to wrap up my work completely.

There are people whose advice and guidance I have sought over the years and which has been highly valuable in this journey. A special thanks to all my mentors for taking time out of your busy lives to guide me.

I would finally like to thank my friends and family. There's more to life than the work presented here. From climbing mountains to having a nice *soirée* to just keeping me grounded. You all add color to my life. Thank you!

Chapter 1 Introduction

A diversified demand stemming primarily from consumer products and Internet of Things (IoT) devices has led to a spurt in the growth of the memory industry in the past decade. This has also led to faster adoption of Non-Volatile Memory (NVM) technologies such as Magnetic Random-Access Memories (MRAM). MRAMs are high-speed, low-power and non-volatile spintronic memories. It uses the Tunneling Magneto-Resistance (TMR) mechanism for the readout of the memory bit and can use either the Spin-Transfer Torque (STT) or the Spin-Orbit Torque (SOT) mechanism for the write operation. The schematics of STT-MRAM and SOT-MRAM are as shown in Figure 1.1.

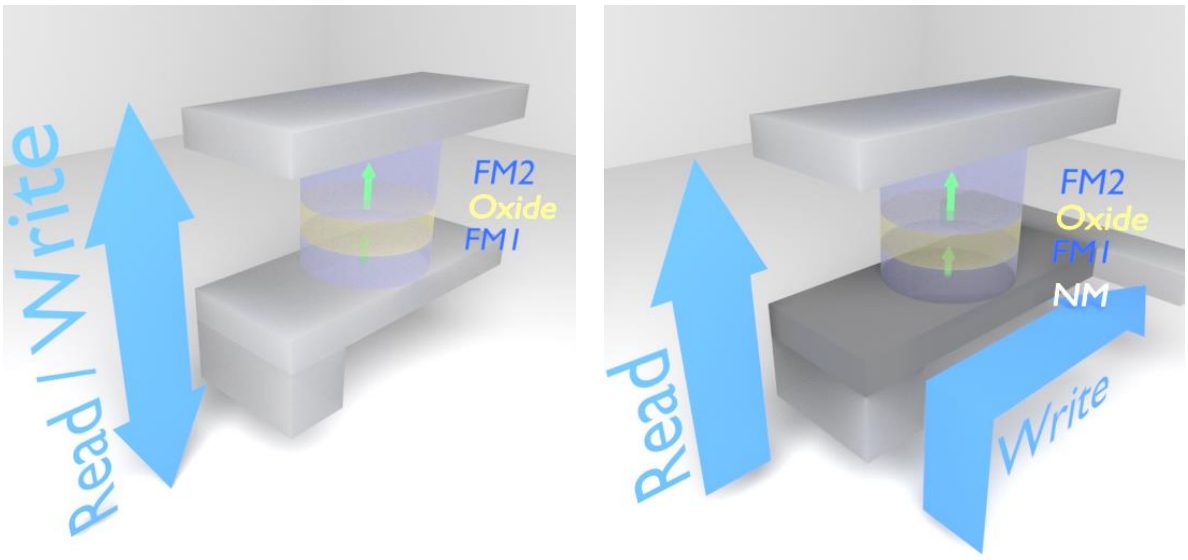

Figure 1.1: Schematics of (a) STT-MRAM and (b) SOT-MRAM

In SOT-MRAM, the write current is injected in the plane of the magnetic bit, decoupling the read and write paths. This leads to a lower current flowing through the oxide tunnel barrier, slowing the oxide aging and enhancing the overall endurance of the bit. Furthermore, this also enables the use of a tunnel barrier with a higher Resistance-Area (RA) product, leading to a lower read disturb and hence increased reliability. SOT-MRAMs typically use a tri-layer structure with inversion asymmetry. A current injected into the heavy metal (HM) layer with high Spin-Orbit Coupling (SOC) gives rise to various torques, namely the Field-Like (FL) torque and the Damping-Like (DL) torque. These torques act on the magnetization of the adjacent Ferro-Magnetic (FM) layer in order to switch it during the write

operation[1,2]. They originate primarily from two distinct mechanisms – the Spin Hall Effect (SHE), which is a bulk effect and the Inverse Spin Galvanic Effect (ISGE), which is an interfacial effect. The efficiency of these torques determines the write energy. It also determines the size of the switching transistor and correspondingly the overall memory density. Hence, it is vital to determine the mechanism underlying the SOTs in order to be able to engineer it for industrial applications.

Chapter 2 delves into the physics underlying these mechanisms. Starting from a short introduction to the geometric Berry phase, the reader is introduced to concepts such as the Spin-Orbit Interaction (SOI), the various Hall effects, the Rashba effect, and the spin-orbit torques. A clear understanding of these concepts is needed to appreciate the core of this work.

Chapter 3 details the tools utilized to complete this study. Importantly, it details the 2nd harmonic torque measurements, which is a powerful technique to not just to quantify the torques, but also gain insight into the magnetic system itself. This chapter also describes the successful construction and test of a Magneto-Optical Kerr Effect (MOKE) microscope capable of imaging ultra-thin magnetic structures which are magnetized in the plane of the film. It closes detailing the sample deposition, characterization and fabrication processes. This chapter is not exhaustive in its coverage of the numerous experimental techniques used in this study. However, these are described as and when encountered in the narrative of this work.

A large emphasis is placed on the energy efficiency of these MRAMs to be better positioned alongside their CMOS counterparts. Various approaches have been studied ranging from clever device designs to even cleverer utilization of the underlying physics to one's advantage. One such method that has witnessed significant research interest recently is the oxidation of the system. Oxidation has been the subject of intense scrutiny in both the academia and the industry since its utility in manufacturing Magnetic Tunnel Junctions (MTJ) with a perpendicular orientation of the magnetization was established. Hence, it is only natural that this knowledgebase is extended to SOTs. Different groups have studied the effect of oxidation of the Ferro-Magnetic (FM) layer and more recently the heavy metal layer on SOTs. HM oxidation has been described to generate SOTs comparable in strengths to that of Topological-Insulators (TI). Such an enhancement of torques could lead to a lower write current, and thereby higher energy efficiency and bit density of SOT-MRAMs. This increase in DL torques should also correspond to an increase in PMA, which determines the thermal stability of pMTJs. Hence, the oxidation of the HM appears to be a vital tool in the development of SOT-MRAMs for longer retention times and a net reduction in write energy.

Chapter 4 studies the mechanism of SOTs in platinum oxide systems. Beginning from a description of our devices on a 4" wafer, which enables us to make comparisons on a uniquely deposited sample, the premier section details extensive material characterizations which help gain knowledge into the material system and the oxidation process. This is followed up by experimental techniques which enable us to quantify the SOTs in these systems. We then rely on experimental and modeling techniques to build a model of the oxidized system, which is then pursued to understand the mechanism behind the observations.

Such detailed studies are a pre-requisite for any new technique to mature out of the laboratories. Extensive experimental and modeling works along with sound arguments are presented to the reader in support of the conclusions of this work.

Chapter 2 Background

In order to engineer our SOT devices, it is necessary to understand the relevant mechanisms that are present in such systems. This chapter discusses the phenomena underlying SOTs. We start out by describing the geometrical phase which can give rise to various transverse transport phenomena. We then consider this Hall type transport/ spin accumulation in the context of our system and the torques it can generate. A clear understanding of these mechanisms is needed to engineer SOT devices towards certain metrics such as energy efficiency, longer data retention time, etc. This chapter provides a brief introduction to these mechanisms.

2.1 Geometric Phase in Solids: Pancharatnam-Berry Phase

A quantum mechanical system, transported adiabatically around a closed loop in the external parameter space (magnetic field, electric field, etc.) acquires a dynamical phase, which depends on the energy of the system and the time it takes for the system to complete the loop, and a geometric phase which depends only on the geometry or the topology of the loop[3–5]. This geometric phase is known as the Pancharatnam-Berry phase or the Berry phase, which was discovered by S. Pancharatnam during his work on the interference of polarized light in 1956[6] and generalized by M. Berry in 1984[3].

Consider a vector that is always tangential to the surface. In the case of a flat surface, shown in Figure 2.1a, any translation of the vector in a closed loop (A'-P'-B'-Q'-A') without rotating the vector around the surface normal, returns the vector to its original state. In the case of a curved surface, shown inFigure 2.1b, this is no longer the outcome. A translation around a closed loop will result in an accumulated angle which is solely dependent on the geometry of the path. This accumulated angle, θ, is known as the anholonomy angle or the Hannay angle in mechanics.

In the case of a quantum mechanical system described by a Hamiltonian $H(\mathbf{R})$ that depends on a set of external parameters $\mathbf{R}(t) = (R_1, R_2\ldots)$, the Schrödinger's equation can be written as [4,5]:

$$H(\mathbf{R})|\mathrm{n}\rangle = E_n(\boldsymbol{R})|\mathrm{n}(\mathbf{R})\rangle \tag{2.1}$$

with eigenvalues $E_n(\boldsymbol{R})$ and eigenvectors $|\mathrm{n}(\mathbf{R})\rangle$. By performing an adiabatic closed-circuit C in the parameter space, the system acquires a phase given by

$$|\psi(T)\rangle = \exp[i(\delta_n + \gamma_n(C))]|\psi(0)\rangle \tag{2.2}$$

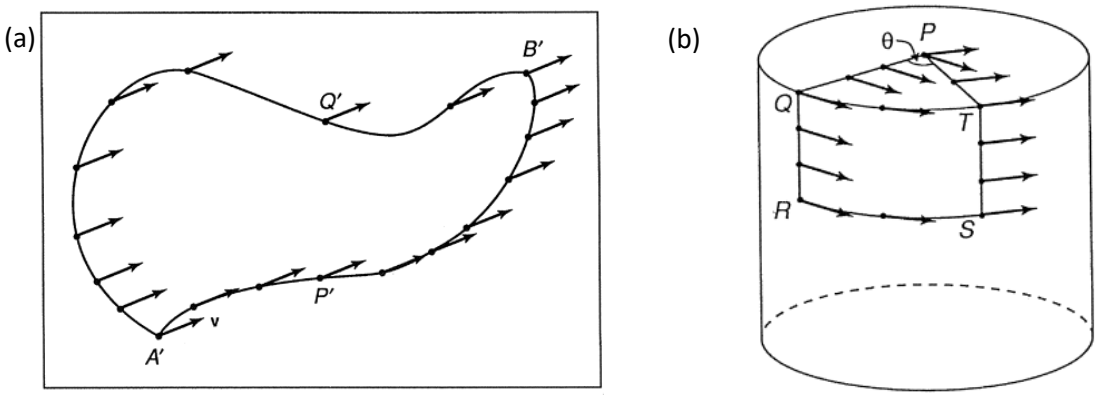

Figure 2.1: Parallel transport (a) on a Euclidean plane and (b) on a cylinder. Θ denotes the anholonomy angle. Figure adapted from ref. [7].

Here $|\psi(T)\rangle$ and $|\psi(0)\rangle$ are the final and initial states, δ_n is the dynamical phase and $\gamma_n(C)$ is the geometric Berry phase. The berry phase can be re-expressed in terms of the Berry vector potential or the Berry connection as [4,5]:

$$\gamma_n(C) = \oint_C \boldsymbol{A}^n(\mathbf{R}).d\boldsymbol{R} \tag{2.3}$$

Here $\boldsymbol{A}^n(\mathbf{R})$ is gauge dependent whereas the berry phase $\gamma_n(C)$ is a gauge-invariant, i.e. it is a physical quantity that can only be changed by an integer multiple of 2π under gauge transformation. Further, the Berry phase depends only on the geometrical aspect of the closed path and not on the time variation of the external parameters.

Following Stokes theorem, the Berry phase can also be re-written in terms of Berry curvature $\Omega_n(\mathbf{R})$ as

$$\gamma_n(C) = \iint_S \Omega_n(\mathbf{R})dR_1dR_2 \tag{2.4}$$

The Berry curvature describes the local geometric properties of the parameter space. In the case of a two-level system, it can be shown that the Berry curvature acts as the magnetic field generated by a monopole at the origin and the Berry phase acquired along a circuit is the flux of the monopole through the surface subtended by the circuit, C. The vector potential of this magnetic field is the Berry connection, $\boldsymbol{A}^n(\mathbf{R})$.

2.2 Spin-Orbit Interaction

A crystalline solid can be considered as a periodic lattice of ions, each generating its own local electric field **E**. Following the Lorentz transformation, an itinerant electron moving through such a crystal lattice will observe this local electric field as a magnetic field **B** ~ (**v** x **E**) in its frame of reference. Here **v** is the velocity of the electron. Because of this local effective magnetic field, the spin of the electron will try to align antiparallel to the effective field in order to minimize the energy. This, in turn, locks the spin of the electron to its momentum and is known as spin-momentum locking. The spin-orbit (SO) Hamiltonian is given by

$$H_{SO} = \frac{g_s\mu_B}{2mc^2}(\boldsymbol{E} \times \boldsymbol{K}).\boldsymbol{S} \tag{2.5}$$

denoting the locking of the electron's spin **S** and its momentum **K**. This Spin-Orbit Interaction (SOI) gives rise to various physical phenomena in magnetic materials, namely the magnetocrystalline anisotropy, magnetization damping, Anomalous Hall Effect (AHE), Anisotropic Magneto-Resistance (AMR), etc.

2.3 Berry phase in Hall Effects

As an electron moves through a crystalline solid, if the rate of change of the effective magnetic field is lower than that of the electron's Larmor frequency, the electron spin can follow the field adiabatically, accumulating a Berry phase. In order to make the Berry phase a gauge invariant, physically observable quantity, it is necessary to have the path C be closed. This can be achieved by applying an external magnetic field, inducing a cyclotron motion along a closed path in the momentum space, leading to magneto-oscillatory effects. The closed path can also be achieved by applying an electric field to vary the momentum across the entire Brillouin zone. In this case, the electron can acquire an anomalous velocity proportional to the Berry curvature. This anomalous velocity is transverse to the applied electric field, giving rise to the Hall effect. The Hall effect is the appearance of a voltage transverse to the applied current. This anomalous velocity manifests itself as a correction to the ordinary velocity which is given by the slope of the Bloch band, given by[5]:

$$\boldsymbol{v}_n(\boldsymbol{k}) = \frac{\partial \varepsilon_n(\boldsymbol{k})}{\hbar \partial \boldsymbol{k}} - \frac{e}{\hbar}\boldsymbol{E} \times \Omega_n(\boldsymbol{k}) \tag{2.6}$$

where the first term on the right accounts for the longitudinal velocity and the second term accounts for the transverse Hall velocity. Here, $\Omega_n(\boldsymbol{k})$ is the Berry curvature of the nth band. The Berry curvature is an intrinsic property of the band structure, is gauge invariant in itself and doesn't require a closed-loop to be defined like the Berry phase. It is then necessary to determine under which conditions the Berry curvature plays a non-negligible role in the determination of the anomalous velocity. This can be done based on symmetry arguments. While $\boldsymbol{v}$, $\boldsymbol{k}$ and $\boldsymbol{E}$ are antisymmetric with spatial inversion, only $\boldsymbol{v}$ and $\boldsymbol{k}$ change signs with time reversal. This results in the Berry curvature being odd with respect to time reversal and even with respect to spatial inversion symmetry. Hence, in crystals where both the time-reversal and the spatial inversion symmetry are broken, the effect of Berry curvature is negligible. However, in systems where only either one of the two is broken, the Berry curvature and in turn the transverse Hall velocity can be non-negligible.

The Hall effect is antisymmetric with respect to time reversal in the linear regime. Hence, a time reversal symmetry breaking term in the Hamiltonian is required to obtain a measurable Hall voltage. Although, there are 2D systems with time reversal symmetry, which exhibit non-linear Hall effect, these are beyond the scope of this work. Hence, centrosymmetric crystals with time-reversal symmetry,

$$E\left(\boldsymbol{k}, s^{\uparrow}\right) = E\left(\boldsymbol{k}, s^{\downarrow}\right) \tag{2.7}$$

as plotted in Figure 2.2a, displays no Hall effect. It is necessary to have broken time-reversal symmetry, by the use of an external magnetic field or an exchange field. In case of latter, it is also necessary to have spin-orbit coupling in order to break the symmetry under a global rotation of π of the spins. There can also be systems with non-trivial texture of magnetization, which can give rise to Topological Hall Effect (THE) even in the absence of SOC. However, these too are beyond the scope of this work.

The appearance of Hall voltage as a consequence of Berry curvature lies at the heart of various Hall effect type phenomena, namely the Anomalous Hall Effect and the Spin Hall Effect which are described

in the following sections. The contribution of the Berry curvature to these effects is considered an intrinsic part of the system.

2.4 Anomalous Hall Effect

The Anomalous Hall Effect (AHE) is the appearance of a voltage transverse to an applied current in Ferromagnetic (FM) metals. This can be attributed to intrinsic and extrinsic effects.

The intrinsic effect is related to the band structure of the metal and is as explained in the previous section. This contribution to the anomalous velocity was originally proposed by Karplus and Luttinger in 1954[8], who connected this phenomenon to the intrinsic SOI of the FM. However, it's only recently that this has been connected to the topological Berry curvature of the Bloch bands. Consider the case of a system with SOI and an exchange field[9]. The Hamiltonian and the energy spectrum can be written as:

$$\widehat{H}_0 = \frac{\hbar^2 k^2}{2m} + \lambda(\boldsymbol{k} \times \widehat{\boldsymbol{\sigma}}) \cdot \boldsymbol{e}_z - \Delta\widehat{\boldsymbol{\sigma}}_z \tag{2.8}$$

$$E_{\pm}(p) = \frac{\hbar^2 k^2}{2m} \pm \sqrt{\lambda^2 p^2 + \Delta^2} \tag{2.9}$$

Here the first term of the Hamiltonian corresponds to the kinetic energy. This is shown in Figure 2.2a, which shows the energy spectrum in the absence of SOI and exchange fields The second term corresponds to the Spin-Orbit Coupling (SOC). This leads to a linear dispersion of the band structure giving rise to two energy bands with spin chirality (mixed spins). This is shown in Figure 2.2b, in the absence of a exchange field. Here the colors indicate the different energy levels $E_+(p)$ and $E_-(p)$ and not the spin states. This Hamiltonian describes the Rashba effect, which is detailed in a later section. Here λ corresponds to the Rashba/SOC strength. The third term corresponds to the exchange field along the z-axis. In the absence of SOI, it leads to a splitting of the energy band as shown in Figure 2.2b. In the presence of SOI, this leads to a split gap in the energy spectrum given by 2Δ as shown in Figure 2.2d, also referred to as anti-crossing points in some cases. These figures were plotted with the parameters: m=1, λ=4, Δ=2.

Here the exchange field breaks the time-reversal symmetry and the SOI connects the spin of the electron to its orbital trajectory. The SOI, along with the broken time-reversal symmetry induces a Berry curvature in the band structure. This Berry curvature can be written as[5]:

$$\Omega_{\pm} = \mp \frac{\lambda^2 \Delta}{2(\lambda^2 k^2 + \Delta^2)^{3/2}} \tag{2.10}$$

The Berry curvature of the two bands are concentrated in the energy gap at k = 0 and have opposite signs, as shown in Figure 2.3. This constitutes the intrinsic contribution to the AHE and its strength varies depending on the position of the Fermi level with respect to the energy gap. Figure 2.3 was plotted with the parameters: m=1, λ=4, Δ=4.

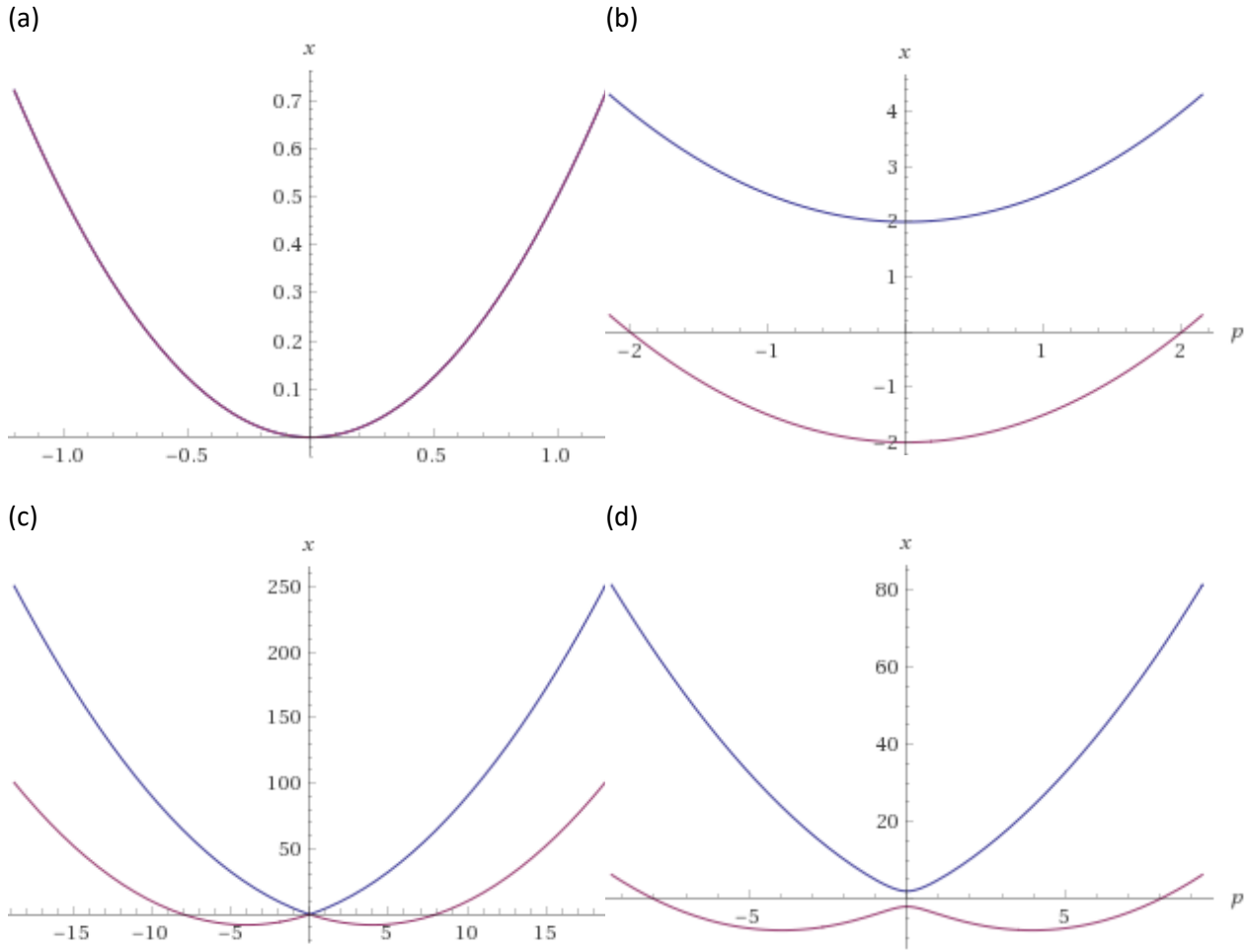

Figure 2.2: Energy dispersion curves in the presence of (a) no SOI or exchange field (b) only exchange Field (c) only SOI (d) SOI and exchange fields. The vertical axis denotes the energy and the horizontal axis denotes the momentum. The colors indicate different energy bands.

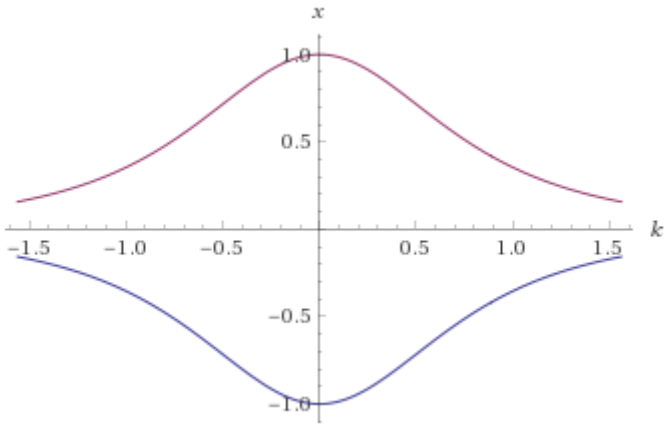

Figure 2.3: The Berry curvature of the two energy bands. It is opposite in signs and has a maximum at the energy gap. Here the vertical axis denotes the Berry curvature and the horizontal axis the wavenumber. The colors represent different energy bands.

The AHE can also have extrinsic contributions from scattering events, namely, skew scattering and side jump[10]. Skew scattering refers to the asymmetric scattering of the electron due to impurities, depending on SOI. This can be visualized in terms of the scattering cross-section, which depends on the spin state of the electron. The scattering angle of the electron depends on the relative orientation of its spin with respect to the effective magnetic field of the impurity that it experiences. This results in the asymmetric scattering of the electron depending on its spin state, leading to a transversal spin current. Skew scattering dominates in the low temperature, clean sample limit. However, at room temperature, in dirty samples, it is expected to play a smaller role. This can be worked out by adding an impurity related term to the Hamiltonian given in eq. 2.8[9].

Side jump is a purely quantum mechanical effect that refers to the spin-dependent displacement of the electron at impurity sites. Consider an itinerant electron traveling with a wavevector **k**. Scattering with an impurity with SOI will lead to a displacement transverse to **k**. However, the initial and final direction of motion remains the same. Upon comparison with the intrinsic mechanism, the intrinsic band structure related effect is expected to be the dominant one in transition metal ferromagnets[11] and should be so in our case as well.

2.5 Rashba Effect

In crystals with broken inversion symmetry, an internal electric field can be present which can give rise to SOI. This is true in the case of non-centrosymmetric zinc-blende structures as shown by Dresselhaus[12] and in systems with broken structural inversion symmetry as shown by Vas'ko[13] and Bychkov and Rashba[14]. The SO Hamiltonian in this case can be written in terms of the electron momentum as[15]

$$H_{SO}(\boldsymbol{p}) = -\mu_B(\nabla V \times \boldsymbol{p}).\boldsymbol{\sigma}/mc^2 \tag{2.11}$$

In this case, the SO Hamiltonian must be odd in momentum to preserve the time-reversal symmetry ($H_{SO}(-\boldsymbol{p}) = -H_{SO}(\boldsymbol{p})$). This is valid only in systems with broken spatial inversion symmetry. In systems studied in the work, the inversion symmetry is broken in the vertical z-direction giving rise to an interfacial electric field of the form $\boldsymbol{E} = E_Z\boldsymbol{e}_z$. This results in a SO Hamiltonian of the form

$$\hat{H}_R = \alpha_R(\boldsymbol{k} \times \hat{\boldsymbol{\sigma}}) \cdot \boldsymbol{e}_z \tag{2.12}$$

Here is the α_R Rashba parameter which denotes the strength of this coupling and is the $\hat{\boldsymbol{\sigma}}$ Pauli spin matrices. This has the same form of the Hamiltonian shown in eq. 2.8. This leads to spin-momentum locking and spin-split sub-bands as mentioned in the earlier section. Hence, when electrons pass through such a system, they experience the effect of the internal electric field in the form of an effective magnetic field, the Rashba field B_R. This causes the spins to precess around the direction of the Rashba field. This is shown in Figure 2.4. In case of paramagnetic materials, this leads to the polarization of the electrons along the direction of the field and is known as the inverse spin galvanic effect (ISGE) or the Edelstein effect from his seminal work on this topic[16].

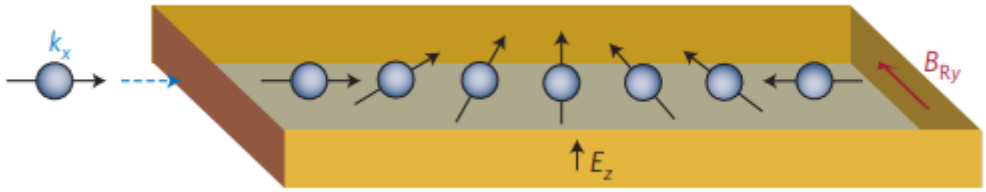

Figure 2.4: An electron moving in a Rashba system experiences a transverse Rashba magnetic field which causes the spin to precess around this field. Figure adapted from Manchon et. al.[15]

When a thin magnetic film is deposited on top of such a system, this polarization or accumulation of electron spin can exert a torque on the magnetization as was first demonstrated by Miron et al.[17]. This mechanism is detailed in a later section. It is to be noted that due to the screening effect in metals, this Rashba field is present only at the interface, on the order of a few Å. Further, it can also be described in terms of Berry curvature given by[15]

$$\boldsymbol{\Omega}(\boldsymbol{p}) \propto \alpha_R \nabla_p \times (\hat{\boldsymbol{\sigma}} \times \boldsymbol{p}) \tag{2.13}$$

This can be considered as the curl of the spins orthogonal to the momentum. Hence, it can also give rise to a current in the transverse direction when the time-reversal symmetry is broken.

2.6 Spin Hall Effect

The Spin Hall Effect (SHE) is the phenomena analogous to AHE, seen in normal metals (NM). Upon injecting a current into an NM with a large SOC, a transverse pure spin current is produced with a polarization perpendicular to the plane of the charge and spin current. Unlike the AHE, where the FM leads to a difference in majority and minority carries giving rise to a detectable transverse voltage, in SHE such detectable signals are lacking. Hence the early experiments used optical detection techniques[18,19]. Soon this technique was used to switch adjacent magnetic layer via Spin Transfer Torque (STT)[1,2].

The source of SHE is almost exactly the same as that of AHE and can be divided into intrinsic band structure based contributions and extrinsic impurity based ones. In case of the intrinsic contribution, the mechanism can be described by including a term describing the SOC. The initial theoretical works used either a Luttinger Hamiltonian which describes interacting electrons in semiconducting systems[20] or a Rashba model as described in the previous sections[21]. However, care must be taken to avoid over-simplification of the band structure, which could lead to the cancellation of the calculated intrinsic contribution by the extrinsic contributions[22]. This Hamiltonian can also be obtained from ab-initio calculations and then using a Kubo formalism, which describes the linear response of a quantity due to a time-dependent perturbation, we can obtain the longitudinal and transverse spin and charge conductivities[23]. The Berry curvature can also be obtained this way[23,24]. These theoretical studies reveal that as in the case of AHE, the band structure of the material plays an important role in SHE.

The left panel of Figure 2.5a shows the band structure of platinum calculated this way[23]. Comparing it with the spin Hall conductivity (SHC), it is evident that the conductivity peaks when the SOC splits the doubly degenerate d bands at the L and X high symmetry points. The SHC can be varied depending on the position of the Fermi level. This is consistent with the calculated Berry curvature which has similar peaks at L and X points, as shown in Figure 2.5b.

The SHC of transition metals has been widely studied. It can either be positive or negative depending on the filling of the d shell. Metals with d shells more than half-filled such as Pt, Pd, Au have a positive SHC whereas the ones with less than half-filled d shells such as Ta, Nb, W, Mo have negative values[24], indicating a dominant band structure-dependent intrinsic contribution to SHE.

The SHE can also have extrinsic contributions due to impurities, namely skew-scattering and side-jump mechanisms. Just as in AHE, the skew-scattering contribution is proportional to its transport lifetime τ. It arises from the asymmetric contribution to the disorder scattering in metals with SOC. The side-jump mechanism, on the other hand, is independent of the transport lifetime and arises from the transverse displacement of the electron upon scattering with an impurity. These mechanisms are analogous to the ones detailed for AHE.

The SHE leads to the generation of a transverse pure spin current upon the injection of a charge current. This is quantified in terms of the Spin Hall Angle (SHA) θ_{SHE} which is given as the ratio between the SHC, σ_{SHE}, and the longitudinal conductivity, σ_{xx} :

$$\theta_{SHE} = \frac{\sigma_{SHE}}{\sigma_{xx}} \tag{2.14}$$

This defines the efficiency of the material to generate spin currents upon the injection of a charge current. Another parameter of interest here is the spin diffusion length λ_{NM} which denotes the average distance the spins travel before they flip. Non-magnetic transition metals can have a spin diffusion length of the order of a few nm.

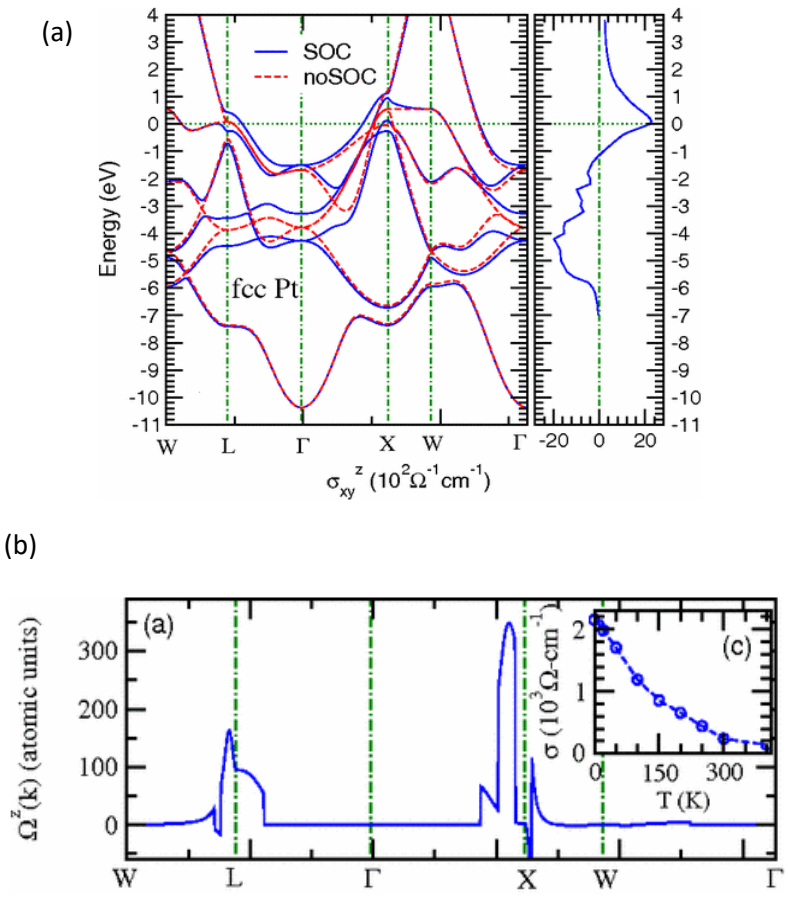

Figure 2.5: (a) Left panel: band structure, and right panel: spin Hall conductivity (SHC) of platinum fcc structure. (b) The corresponding Berry curvature at zero temperature. Plots adapted from Guo et. al.[23].

2.7 Spin-Orbit Torques

The SOT device element that we are concerned with consists of FM/NM bilayer system. Injection of an in-plane current, through the SOC mechanism (SHE and Rashba), generates torques that act on the magnetization of the FM layer, which is the magnetic memory element. This causes it to switch its orientation of magnetization. This is the basis of SOT-MRAM. The need for such a bi-layer system to generate torques are twofold: the SHE in the HM results in a pure spin current which can flow into the FM layer causing it to switch and the broken spatial inversion symmetry results in Rashba effect at the interface causing spin accumulation at the interface which can then act on the FM layer. Figure 2.6a shows the effect of SHE in a bi-layer system. Here the SOC leads to a spin current perpendicular to the device plane. These spins, initially polarized along an axis dictated by the SHE, precesses around the magnetization axis and dephases. In doing so, it transfers its angular momentum to the magnetic moment of the FM layer according to the conservation of angular momentum. This is the Spin Transfer Torque (STT) mechanism. Figure 2.6b shows the Rashba effect which is present in metals with a large SOC and broken inversion symmetry. In this case, there is a spin accumulation/reorientation along the FM/NM interface. These spins can act on the magnetization of the FM layer via the exchange mechanism.

As in the case of STTs, the SOT acting on the magnetic element can be split into two orthogonal torques, namely the Anti-Damping Torques (ADT), also known as the Damping - Like Torques (DLT), and the Field-Like Torques (FLT) as shown in Figure 2.6 and Figure 2.7. They are named so because they are analogous to the torques acting on a magnetic moment in a magnetic field (for a particular direction of magnetization). The direction of the AD field depends on the orientation of the magnetization, similar to the Gilbert damping, whereas the direction of the FL field is fixed by the polarization of the spin accumulation and in turn orients the magnetization along that direction, equivalent to the effect of a Zeeman field. These torques can be modeled as two additional terms in the Landau- Lifshitz equation (LLG) given by

$$\frac{d\boldsymbol{M}}{dt} = -\gamma\mu_0 \boldsymbol{M} \times \boldsymbol{H_{eff}} + \frac{\alpha}{M_s}\left(\boldsymbol{M} \times \frac{d\boldsymbol{M}}{dt}\right) + T_{DL} + T_{FL} \tag{2.15}$$

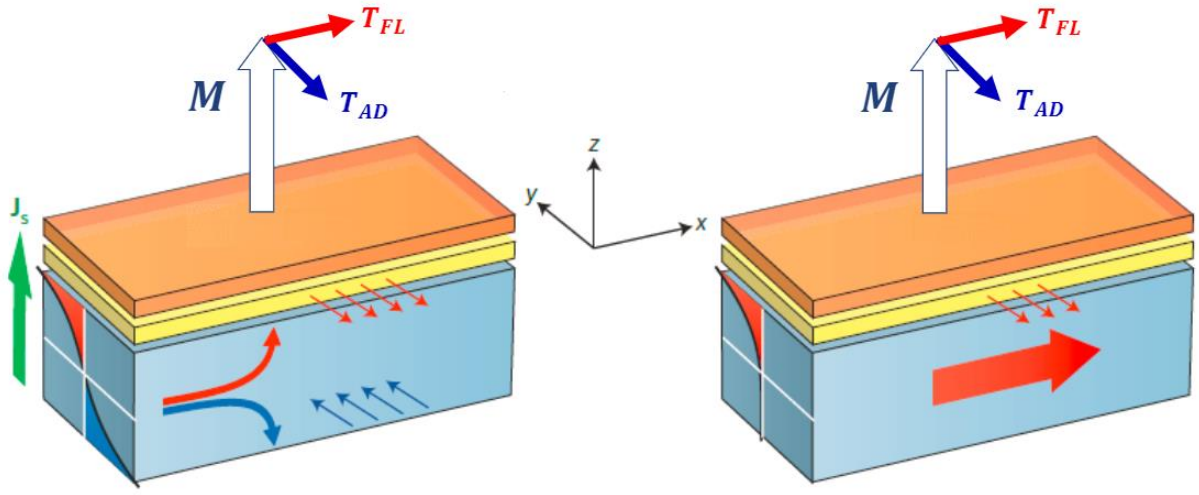

(a) (b)

Figure 2.6: SOT acting on the magnetization M of the FM as a result of (a) SHE (b) Rashba effect. Figure adapted from references [25,26].

Where,

$$\boldsymbol{T_{DL}} = T_{DL}\big(\boldsymbol{M} \times (\boldsymbol{M} \times (\boldsymbol{J_e} \times \hat{n}))\big) \tag{2.16}$$

$$\boldsymbol{T_{FL}} = T_{FL}((\boldsymbol{J_e} \times \hat{n}) \times \boldsymbol{M}) \tag{2.17}$$

Here T_{DL} and T_{FL} correspond to the strength of the damping-like and field-like torques respectively. These torques lead to effective fields that act on the magnetization, given by

$$\boldsymbol{B_{DL}} = B_{DL}((\boldsymbol{J_e} \times \hat{n}) \times \boldsymbol{M}) \tag{2.18}$$

$$\boldsymbol{B_{FL}} = B_{FL}\big(\boldsymbol{M} \times ((\boldsymbol{J_e} \times \hat{n}) \times \boldsymbol{M})\big) \tag{2.19}$$

Where B_{DL} and B_{FL} corresponds to the strength of the damping like and field like fields respectively. It is to be noted that higher-order terms can also have a significant contribution to the torques as described in ref. [27]. Also, the sign convention used here is based on that of a standard right-handed precession of a magnetic moment in the presence of an external magnetic field.

Interfacial scattering plays a significant role in such systems. Recent works considering a full 3D transport with electrons that can cross and scatter across the FM/NM interface with the applied field, show a significant interfacial contribution to DLT and FLT[28,29]. Recently there has also been works showing SOTs can be generated by the AHE in FM/NM/FM multilayers[30] and by Planar Hall Effect (PHE) in NM/FM/NM multilayers[31]. It has also been predicted[32] and experimentally demonstrated[33] that a transverse spin current with a polarization misaligned with the magnetization can be generated in an FM, upon injecting a current. These works show that although more effort is needed to have a comprehensive picture of the SOT phenomena, it can lead to more novel and efficient spintronic devices.

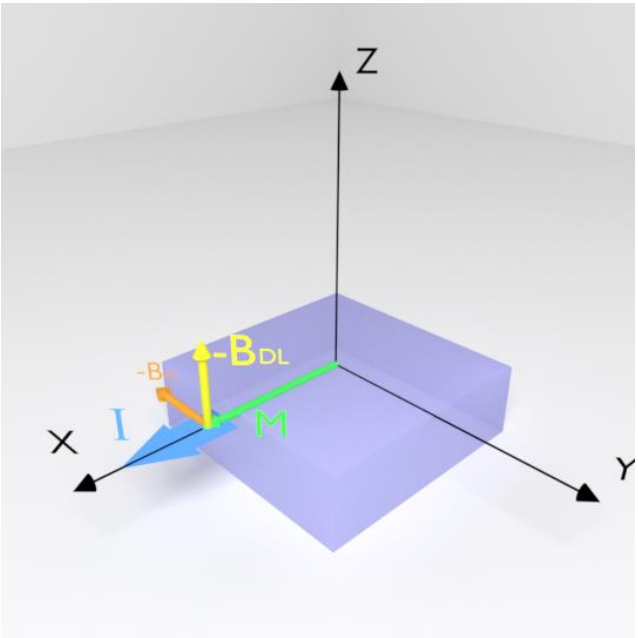

Figure 2.7: The SOTs acting on the FM layer can be decomposed into two orthogonal torques which effectively act on the magnetization in the form of two effective fields, the Damping-Like (DL) and the Field-Like (FL).

Chapter 3 Experimental Methods

This chapter details the experimental methods used in this work. It primarily consists of second harmonic torque measurements, in-plane Magneto-Optical Kerr Microscopy (MOKE) and sample deposition and metrology. Other techniques such as Reactive Ion Etching (RIE), Angle-Resolved X-ray Photoelectron Spectroscopy (AR-XPS), Ferro-Magnetic Resonance (FMR), etc. are detailed in later chapters when needed. This chapter also describes the sample fabrication techniques used for this work.

3.1 Second Harmonic Torque Measurement Technique

The second harmonic torque measurement is a powerful technique to extract the SOTs of different material systems. The FM can have in-plane or out-of-plane anisotropies including higher-order terms. This harmonic technique is also versatile, being useful to determine system properties when coupled to polarized light, thermal gradient, etc. or other specific applications such as to determine the dry friction of a magnetic layer, which can be helpful for Magnetic Tunnel Junction (MTJ) based memristive applications[34].

We quantify the SOTs of our samples using this measurement technique. This method consists of a standard Hall measurement setup wherein our samples are patterned into a Hall cross, as shown in. A small alternating current of 10 Hz is applied along one of the arms while the transverse voltage is measured along the other. Further, the magnetization can be rotated using an external field. This is a quasistatic measurement technique wherein the magnetization of the magnetic material is made to fluctuate in the small-angle regime using an AC current with a small frequency, 10Hz in our case. Its frequency is not high enough so as to activate the magnetization dynamics in the Gigahertz range. The working principle is as depicted in Figure 3.1. When a DC current is applied in our sample the magnetization of the sample is at a certain equilibrium position denoted by M in Figure 3.2 (a) dictated by the balance of the current-induced SOTs, the anisotropy including the demagnetizing field. This equilibrium position of the magnetization can also be attained using an external field B, as shown in Figure 3.2 (b). When a small change is induced in the applied current (using e.g. a small AC current as in our measurements), denoted by ΔI, the magnetization will fluctuate in the small-angle limit, denoted by $\Delta\Theta$. This will result in a new position of the magnetization denoted by M'. We can achieve this same position of magnetization by changing the externally applied field as well, denoted by B'. Hence by

keeping the change ΔΘ constant in both the cases, we have a direct comparison between the effective fields of the SOTs from the applied current and the external field. In other words, we can now quantify the SOTs in terms of the effective field that they generate, which is essential to be able to compare SOTs between different devices, mechanisms, etc.

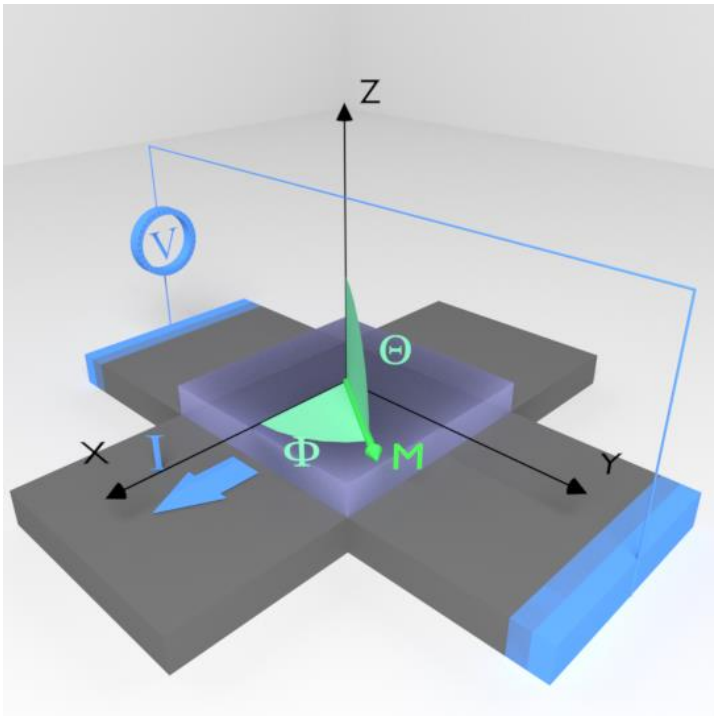

Figure 3.1: Hall measurement setup for 2nd harmonic torque measurements. A small AC current is applied along one of the arms of the Hall cross while the transverse voltage is measured along the other arm. An external field is used to rotate the magnetization of the sample.

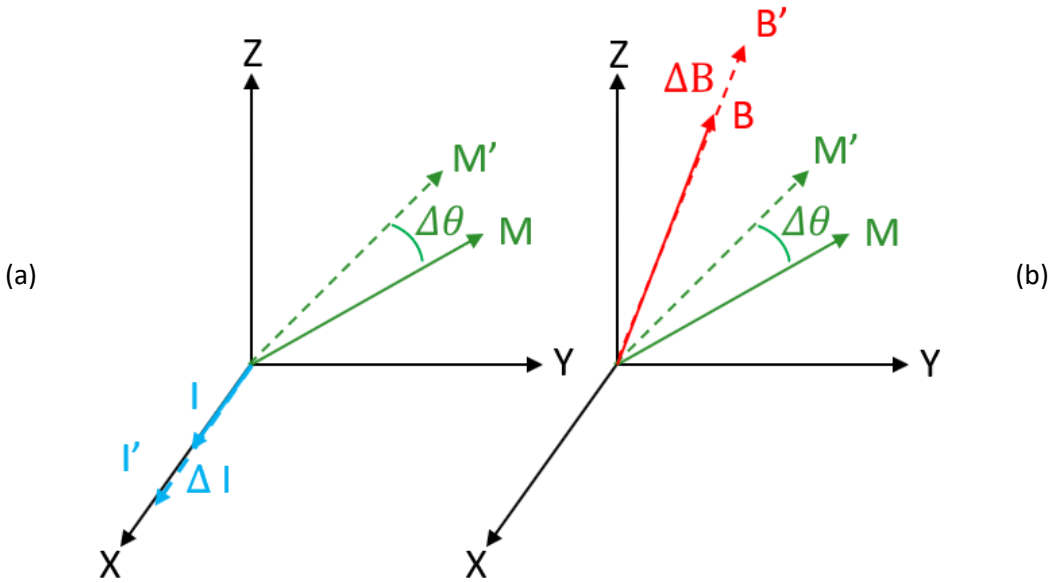

Figure 3.2: Working principle of the 2nd harmonic torque measurements. The variation of magnetization due to a small AC current (a) is compared to that caused by an externally applied field (b).

3.1.1 Expression of the Spin-Orbit Torques based on harmonic measurements

Following the works of Garello et. al.[27], Avci et. al.[35] and Hayashi et. al.[36], the transverse Hall voltage can be written as the product of the transverse Hall resistance, R_H, and the applied current, I_0,

$$V_H(t) = R_H(t) I_0 \cos \omega t \tag{3.1}$$

Here the current is written in terms of cosine so as to correspond with our measurement setup, which crops the sinusoidal function at the maximum. The hall resistance can be further expressed in terms of the static and dynamic parameters, namely, $\boldsymbol{B}_0$, the sum of external, anisotropy and demagnetizing fields and $\boldsymbol{B}_I = \boldsymbol{B}_{DL} + \boldsymbol{B}_{FL} - \boldsymbol{B}_{Oe}$, the sum of current-induced fields.

$$R_H(t) = R_H(\boldsymbol{B}_0 + \boldsymbol{B}_I(t)) \tag{3.2}$$

This, however, is without including any thermal effects. In practice, when the sinusoidal current is applied, the sample heats up, shifting the equilibrium position of magnetization. The oscillations caused by the dynamical parameters then occur around this new equilibrium position, rather than the original one set by the static parameters. This thermally induced shift can be expressed as the addition of a Joule heating term to the eq. 3.2, given by $R_T \cos^2 \omega t$. Following a Taylor series expansion around this new equilibrium position we obtain,

$$R_H(t) \approx R_H(\boldsymbol{B}_0) + \frac{dR_H}{d\boldsymbol{B}_I} \boldsymbol{B}_I \cos \omega t + R_T \cos^2 \omega t \tag{3.3}$$

Hence the Hall voltage can be written as

$$V_H(t) = \left(R_H(\boldsymbol{B}_0) + \frac{dR_H}{d\boldsymbol{B}_I} \boldsymbol{B}_I \cos \omega t + \frac{R_T}{2} (\cos 2\omega t + 1) \right) I_0 \cos \omega t \tag{3.4}$$

$$V_H(t) = \left(R_H(\boldsymbol{B}_0) + \frac{R_T}{2} \right) I_0 \cos \omega t + I_0 \frac{dR_H}{d\boldsymbol{B}_I} \boldsymbol{B}_I \cos^2 \omega t + I_0 \frac{R_T}{2} \cos \omega t \cos 2\omega t \tag{3.5}$$

Expanding the cosine terms further,

$$V_H(t) = \left(R_H(\boldsymbol{B}_0) + \frac{R_T}{2} \right) I_0 \cos \omega t + \frac{I_0}{2} \frac{dR_H}{d\boldsymbol{B}_I} \boldsymbol{B}_I (\cos 2\omega t + 1) + \frac{I_0}{4} R_T (\cos \omega t + \cos 3\omega t) \tag{3.6}$$

$$V_H(t) = I_0 \left(\frac{1}{2} \frac{dR_H}{d\boldsymbol{B}_I} \boldsymbol{B}_I + \left(R_H(\boldsymbol{B}_0) + \frac{R_T}{2} + \frac{R_T}{4} \right) \cos \omega t + \frac{1}{2} \frac{dR_H}{d\boldsymbol{B}_I} \boldsymbol{B}_I \cos 2\omega t + \frac{R_T}{4} \cos 3\omega t \right) \tag{3.7}$$

$$V_H(t) = I_0 \left(R_H^0 + \left(R_H^f + R_H^{3f} \right) \cos \omega t + R_H^{2f} \cos 2\omega t + R_H^{3f} \cos 3\omega t \right) \tag{3.8}$$

Where R_H^0, R_H^f, R_H^{2f} and R_H^{3f} represent the zeroth, first, second and third harmonic components of the Hall resistance. Here, $R_H^f = R_H(\boldsymbol{B}_0) + \frac{R_T}{2}$. This corresponds to the Hall resistance at equilibrium along with a component corresponding to the thermally induced shift of this equilibrium position of the magnetization. This thermally induced shift manifests as a rectification voltage and can be ignored. Further, it can be observed that the third harmonic signal related to the thermal contribution is present in the first harmonic as well. This contribution is subtracted from the first harmonic signal in our analysis. The Hall voltage can thus be written as

$$V_H(t) = I_0 \left(R_H^0 + R_H^f \cos \omega t + R_H^{2f} \cos 2\omega t \right) \tag{3.9}$$

The Hall resistance, in the first harmonic, represents the equilibrium position of the magnetization, **M**, and is given by

$$R_H^f = -\frac{1}{ne} + R_{AHE} \cos \theta_M + R_{PHE} \sin^2 \theta_M \sin 2\varphi_M \tag{3.10}$$

In case of metallic systems, the number of electrons, n, is large and hence the first term, the ordinary Hall resistance can be ignored. The first harmonic hall resistance can thus be written as

$$R_H^f = R_{AHE}\cos\theta_M + R_{PHE}\sin^2\theta_M \sin 2\varphi_M \tag{3.11}$$

The second harmonic component represents the current induced changes of the magnetization and can be expanded in the spherical coordinate system as

$$R_H^{2f} = \frac{1}{2}\frac{dR_H}{d\boldsymbol{B}_I}\boldsymbol{B}_I \tag{3.12}$$

$$R_H^{2f} = \frac{1}{2}\left(\frac{dR_H}{d\theta}\frac{d\theta}{d\boldsymbol{B}_I}\boldsymbol{B}_I + \frac{dR_H}{d\varphi}\frac{d\varphi}{d\boldsymbol{B}_I}\boldsymbol{B}_I\right) \tag{3.13}$$

$$R_H^{2f} = \frac{1}{2}\left[\frac{d\left(R_{AHE}\cos\theta + R_{PHE}\sin^2\theta\sin 2\varphi\right)}{d\theta}\frac{d\theta}{d\boldsymbol{B}_I}\boldsymbol{B}_I + \frac{d\left(R_{AHE}\cos\theta + R_{PHE}\sin^2\theta\sin 2\varphi\right)}{d\varphi}\frac{d\varphi}{d\boldsymbol{B}_I}\boldsymbol{B}_I\right] \tag{3.14}$$

$$R_H^{2f} = \frac{1}{2}\left[\left(R_{AHE}\frac{d\cos\theta}{d\theta} - 2R_{PHE}\sin 2\varphi\cos\theta\frac{d\cos\theta}{d\theta}\right)\frac{d\theta}{d\boldsymbol{B}_I}\boldsymbol{B}_I + R_{PHE}\sin^2\theta\frac{d\sin 2\varphi}{d\varphi}\frac{d\varphi}{d\boldsymbol{B}_I}\boldsymbol{B}_I\right] \tag{3.15}$$

$$R_H^{2f} = \frac{1}{2}\left[\left(R_{AHE} - 2R_{PHE}\cos\theta_M\sin 2\varphi_M\right)\frac{d\cos\theta_M}{d\boldsymbol{B}_I}\boldsymbol{B}_I + R_{PHE}\sin^2\theta_M\frac{d\sin 2\varphi_M}{d\boldsymbol{B}_I}\boldsymbol{B}_I\right] \tag{3.16}$$

Assuming uniaxial anisotropy contribution is negligible, the effect of current-induced fields on the magnetization can be separated into polar and azimuthal contributions,

$$\frac{d\cos\theta}{d\boldsymbol{B}_I}\boldsymbol{B}_I = \frac{d\cos\theta}{dB_I^\theta}B_I^\theta \tag{3.17}$$

$$\frac{d\sin 2\varphi}{d\boldsymbol{B}_I}\boldsymbol{B}_I = \frac{d\sin 2\varphi}{dB_I^\varphi}B_I^\varphi = 2\cos 2\varphi\frac{d\varphi}{dB_I^\varphi}B_I^\varphi \tag{3.18}$$

These contributions can now be compared to that of an external field, B_{ext}, which has the same effect on magnetization. Consider a differential element in a spherical coordinate system given by

$$d\boldsymbol{l} = dR\,\hat{r} + Rd\theta\,\hat{\theta} + R\,sin\theta\,d\varphi\hat{\varphi} \tag{3.19}$$

A differential field applied externally can be written in the same manner,

$$d\boldsymbol{B}_{\boldsymbol{ext}}^{\boldsymbol{total}} = dB_{ext}\,\hat{r} + B_{ext}d\theta_B\,\hat{\theta} + B_{ext}sin\theta_B d\varphi_B\,\hat{\varphi} \tag{3.20}$$

This is the field that acts on the magnetization when we vary the applied current or the external field slightly. Following the same method as the current induced field, we can separate out the differential field into its polar and azimuthal contributions and consider their effects on the magnetization individually. Further, in this work, we utilize angular scans for our torque measurement wherein we keep the external field constant while rotating it on the coordinate planes. This implies that we need to express the differential field in terms of its angular components, θ_B and φ_B. The angular scans that we perform are restricted to the x-y plane and the y-z plane. Hence, we can neglect the effect of the component of the external differential field along φ_B and θ_B on the magnetization along θ_B and φ_B respectively. This is shown in Figure 3.3.

During the angle scan, we keep the external field constant leading to $dB_{ext} = 0$ along the radial direction. We also neglect any change in the magnetization along the radial axis arising from SOTs. The differential field along the θ axis is

$$dB_{ext}^\theta = B_{ext}d\theta_B\,\hat{\theta} \tag{3.21}$$

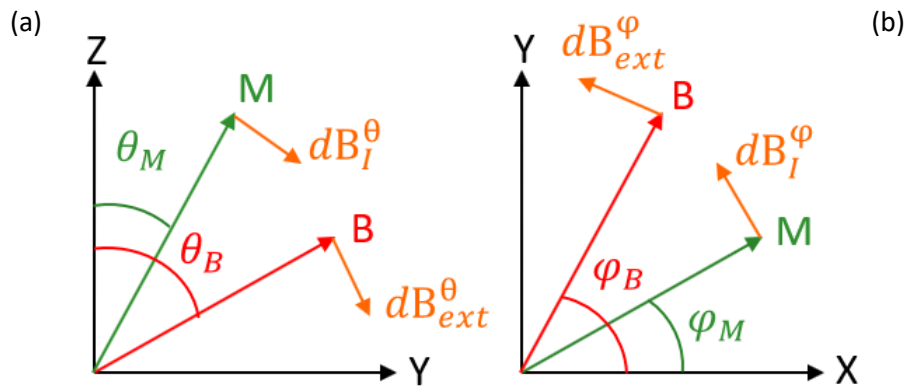

Figure 3.3: Projection of the differential external field on M along (a) θ and (b) φ directions.

And its projection on the magnetization, as shown in Figure 3.3, is given by

$$dB_I^\theta = dB_{ext}^\theta \cos(90 - \theta_M - (90 - \theta_B)) \tag{3.22}$$

$$dB_I^\theta = B_{ext} d\theta_B \cos(\theta_B - \theta_M) \tag{3.23}$$

Similarly, the differential field along the φ axis is given by

$$dB_{ext}^\varphi = B_{ext} sin\theta_B d\varphi_B \, \hat{\varphi} \tag{3.24}$$

And its projection on the magnetization

$$dB_I^\varphi = dB_{ext}^\varphi \cos(\varphi_B - \varphi_M) \tag{3.25}$$

$$dB_I^\varphi = B_{ext} sin\theta_B d\varphi_B \cos(\varphi_B - \varphi_M) \tag{3.26}$$

Substituting the differential fields back into the equation of 2nd harmonic resistance (3.16), we obtain

$$R_H^{2f} = \frac{1}{2}\Big[(R_{AHE} - 2R_{PHE}\cos\theta_M \sin 2\varphi_M)\frac{d\cos\theta_M}{B_{ext} d\theta_B \cos(\theta_B - \theta_M)} B_I^{\theta_M} + R_{PHE}\sin^2\theta_M \frac{d\sin 2\varphi_M}{B_{ext} sin\theta_B d\varphi_B \cos(\varphi_B - \varphi_M)} B_I^{\varphi_M}\Big] + R_{\Delta T}^{2f} \tag{3.27}$$

The same procedure can be applied in the case of field scans, wherein the external field is swept along a fixed axis in order to determine the torques. However as we do not use field scans to measure the torque in this work, the reader is referred to ref [27]. In equation (3.27), the $R_{\Delta T}^{2f}$ term refers to the second harmonic resistance due to the thermal gradient that is induced upon injection of a current into the sample. As our samples are deposited on a silicon/silicon dioxide substrate whereas the top is exposed to the atmosphere, there is a vertical thermal gradient in our samples giving rise to Anomalous Nernst Effect (ANE)[37–39]. We minimize lateral thermal gradients by utilizing a Hall cross rather than a Hall bar. However, any slight misalignment from the lithography process can induce a small lateral gradient as well. These thermo-electric signals add on to the zeroth and the second harmonic resistances that we measure experimentally since

$$\Delta T \propto I^2 R \propto I_0^2 \cos^2\omega t R_0 \propto \frac{1}{2} I_0^2 (\cos 2\omega t + 1) R_0 \tag{3.28}$$

In the case of metallic films, as in the case of our study, the dominant contribution to this thermo-electric signal is from the Anomalous Nernst Effect (ANE) and can be written as $E_{ANE} = -\alpha_{ANE}\Delta T \times \boldsymbol{m}$, where α_{ANE} denotes the ANE coefficient. Including this effect into eq. 3.27, we obtain

$$R_H^{2f} = \frac{1}{2}\Big[(R_{AHE} - 2R_{PHE}\cos\theta_M \sin 2\varphi_M)\frac{d\cos\theta_M}{B_{ext}d\theta_B\cos(\theta_B-\theta_M)}B_I^{\theta_M} + R_{PHE}\sin^2\theta_M \frac{d\sin 2\varphi_M}{B_{ext}sin\theta_B d\varphi_B\cos(\varphi_B-\varphi_M)}B_I^{\varphi_M}\Big] + I_0\alpha_{ANE}\Delta T\sin\theta_M\cos\varphi_M \quad (3.29)$$

As this work mostly deals with samples which have an easy plane anisotropy in the plane of the film, we mostly utilize in-plane angle scans, wherein we apply a constant rotating field in the plane of the film as shown in Figure 3.4(a). This method can also be utilized for samples with perpendicular anisotropy, with an anisotropy field much lower than that of the maximum applicable external field. As the field is only rotated in the plane of the film, $\theta_B = \frac{\pi}{2}$. Further, as we work with samples with easy plane anisotropy and very weak uniaxial in-plane anisotropy, we can expect the magnetization to closely follow the externally applied field. Hence, we have $\theta_B \sim \theta_M = \frac{\pi}{2}, \varphi_B \sim \varphi_M$. Including these constraints into the previous equation we obtain

$$R_H^{2f} = \frac{1}{2}\left[R_{AHE}\frac{d\cos\theta_M}{d\theta_B}\frac{B_I^{\theta_M}}{B_{ext}} + R_{PHE}\frac{d\sin 2\varphi_M}{d\varphi_B}\frac{B_I^{\varphi_M}}{B_{ext}}\right] + I_0\alpha_{ANE}\Delta T\cos\varphi_M \quad (3.30)$$

Taking the derivatives considering $\theta_B \sim \theta_M = \frac{\pi}{2}$ and $\varphi_B \sim \varphi_M$, we rewrite the equation as

$$R_H^{2f} = \frac{1}{2}\left[-R_{AHE}\sin\theta_M\frac{B_I^{\theta_M}}{B_{ext}} + 2R_{PHE}\cos 2\varphi_M\frac{B_I^{\varphi_M}}{B_{ext}}\right] + I_0\alpha_{ANE}\Delta T\cos\varphi_M \quad (3.31)$$

$$R_H^{2f} = \frac{1}{2}\left[-R_{AHE}\frac{B_I^{\theta_M}}{B_{ext}} + 2R_{PHE}\cos 2\varphi_M\frac{B_I^{\varphi_M}}{B_{ext}}\right] + I_0\alpha_{ANE}\Delta T\cos\varphi_M \quad (3.32)$$

As the anomalous Hall and planar Hall coefficients depend on the first harmonic response of the system, we need to consider the effect of a change in external field angle on the first harmonic resistance. This can be computed, by once again considering $\theta_B \sim \theta_M = \frac{\pi}{2}$, as follows

$$R_H^f = R_{AHE}\cos\theta_M + R_{PHE}\sin^2\theta_M\sin 2\varphi_M \quad (3.33)$$

$$\frac{dR_H^f}{d\theta_B} = R_{AHE}\frac{\mathrm{d}\cos\theta_M}{d\theta_B} + R_{PHE}\frac{\mathrm{d}\sin^2\theta_M}{d\theta_B}\sin 2\varphi_M \quad (3.34)$$

$$\frac{dR_H^f}{d\theta_B} = -R_{AHE}\sin\theta_M + R_{PHE}\sin 2\theta_M\sin 2\varphi_M \quad (3.35)$$

At $\theta_M = \frac{\pi}{2}$,

$$\frac{dR_H^f}{d\theta_B} = -R_{AHE} \quad (3.36)$$

In a similar manner, we can consider the effect of a small change in φ_B on R_H^f as

$$\frac{dR_H^f}{d\varphi_B} = R_{PHE}\sin^2\theta_M\frac{d\sin 2\varphi_M}{d\varphi_B} \quad (3.37)$$

$$\frac{dR_H^f}{d\varphi_B} = 2R_{PHE}\sin^2\theta_M\cos 2\varphi_M \quad (3.38)$$

$$\frac{dR_H^f}{d\varphi_B} = 2R_{PHE}\cos 2\varphi_M \quad (3.39)$$

Substituting these in eq. 3.32 we rewrite the equation for the second harmonic resistance as

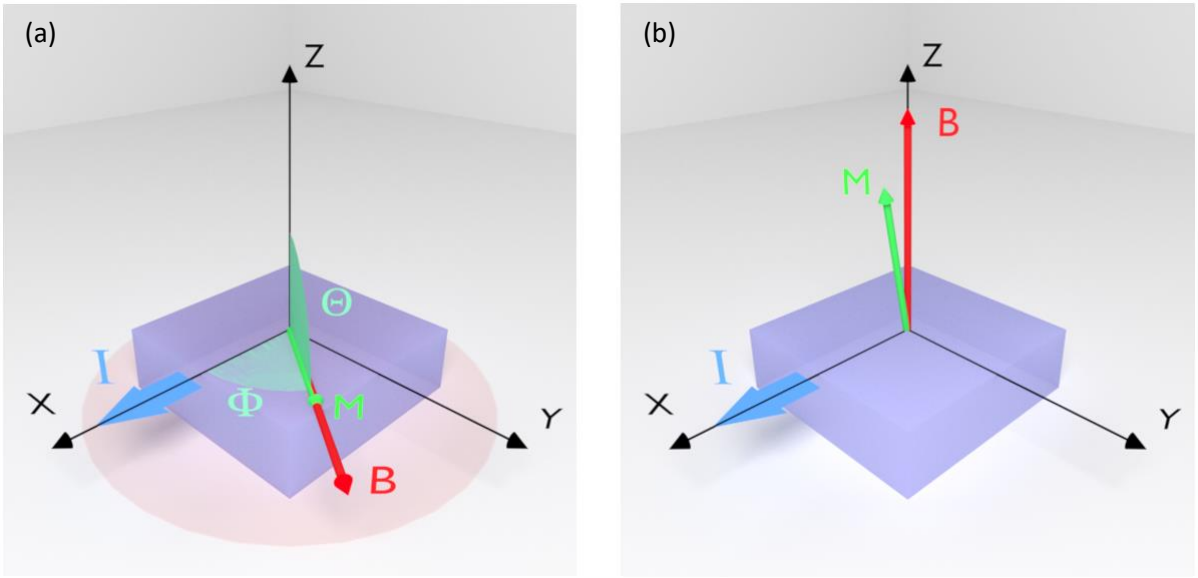

Figure 3.4: (a) In-plane angle scan. A constant external field is rotated in the plane of the sample. (b) Perpendicular field scan. An external field is swept perpendicular to the sample.

$$R_H^{2f} = \frac{1}{2}\left[\frac{dR_H^f}{d\theta_B}\frac{B_l^{\theta_M}}{B_{ext}} + \frac{dR_H^f}{d\varphi_B}\frac{B_l^{\varphi_M}}{B_{ext}}\right] + I_0\alpha_{ANE}\Delta T\cos\varphi_M \tag{3.40}$$

In practice, the planar Hall coefficient is extracted from the in-plane angle scan whereas the anomalous Hall coefficient is extracted from a perpendicular field scan, where the external field is swept in a direction perpendicular to the plane of the sample, as shown in Figure 3.4(b).

In order to proceed further, we need to consider the symmetries of the torques generated by the applied current. Using a standard Pt/Co/AlOx system as a reference, we can fix the signs of the orthogonal torques, DLT and FLT, as detailed in section 2.7 of the previous chapter and as shown in Figure 3.5. The DL field can be written in spherical coordinates by considering the following

$$\boldsymbol{B_{DL}} = B_{DL}(\boldsymbol{J_e}\times\hat{n})\times\boldsymbol{M}) \tag{3.41}$$

$$\boldsymbol{B_{DL}} = B_{DL}(\hat{y}\times\boldsymbol{M}) \tag{3.42}$$

$$\boldsymbol{B_{DL}} = B_{DL}\left[\|\hat{y}\|\|\hat{m}\sin\theta_M\|\sin\left(\frac{\pi}{2}-\varphi\right)(-\hat{z}) + \|\hat{y}\|\|\hat{m}\cos\theta_M\|\sin\left(\frac{\pi}{2}\right)(-\hat{x})\right] \tag{3.43}$$

As $\theta_M = \frac{\pi}{2}$,

$$\boldsymbol{B_{DL}} = B_{DL}\cos\varphi_M\,(-\hat{z}) \tag{3.44}$$

$$\boldsymbol{B_{DL}} = B_{DL}\cos\varphi_M\,\widehat{e_\theta} \tag{3.45}$$

In a similar fashion, the FL field can be decomposed into spherical coordinates as well.

$$\boldsymbol{B_{FL}} = B_{FL}\big(\boldsymbol{M}\times((\boldsymbol{J_e}\times\hat{n})\times\boldsymbol{M})\big) \tag{3.46}$$

$$\boldsymbol{B_{FL}} = B_{FL}\big(\boldsymbol{M}\times(\hat{y}\times\boldsymbol{M})\big) \tag{3.47}$$

$$\boldsymbol{B_{FL}} = B_{FL}\big[\|\hat{m}\sin\theta_M\|\cos\varphi_M\,\widehat{e_\varphi}\big] \tag{3.48}$$

$$\boldsymbol{B_{FL}} = B_{FL}\cos\varphi_M\,\widehat{e_\varphi} \tag{3.49}$$

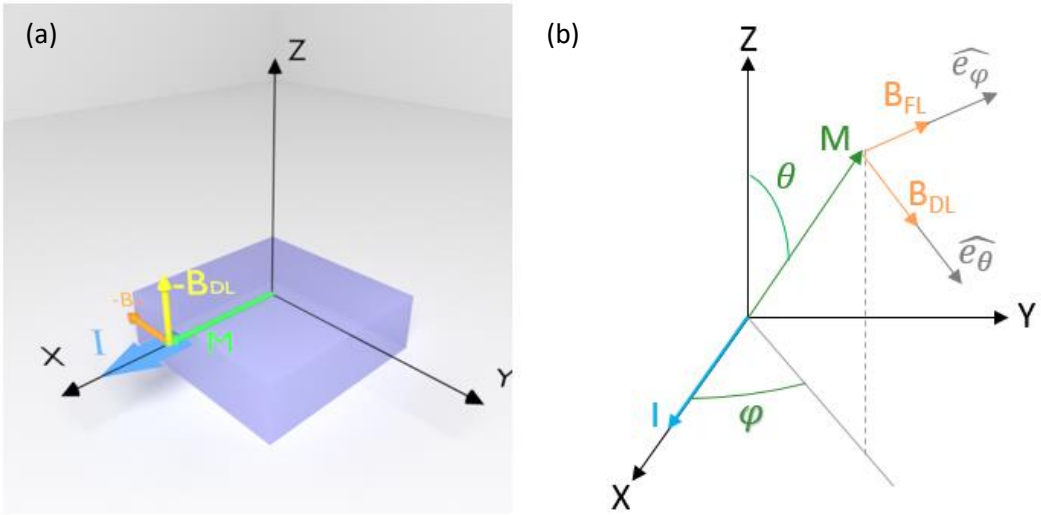

Figure 3.5: (a) The Damping-Like (DL) and the Field-Like (FL) fields acting on the magnetization. (b) These fields can be decomposed into its components along the Θ and φ axes.

These equations show that when a current is applied to the system, the DL field acts on the magnetization along the Θ axis whereas the FL field acts on the magnetization along the φ axis. Hence we can write

$$B_I^{\theta_M} = \boldsymbol{B_{DL}} = B_{DL}\cos\varphi_M \tag{3.50}$$

and

$$B_I^{\varphi_M} = \boldsymbol{B_{FL}} = (B_{FL} - B_{Oe})\cos\varphi_M \tag{3.51}$$

Here we have considered the effect of the Oersted field from the current flowing in the NM layers. According to our sign convention based on Pt/Co/AlOx, the FL and Oersted fields act anti-parallel on the FM layer. Hence the effective subtraction of the terms in the above equation. Substituting these terms in eq. 3.32 we obtain

$$R_H^{2f} = \frac{1}{2}\left[-R_{AHE}\frac{B_{DL}\cos\varphi_M}{B_{ext}} + 2R_{PHE}\cos 2\varphi_M\frac{(B_{FL}-B_{Oe})\cos\varphi_M}{B_{ext}}\right] + I_0\alpha_{ANE}\Delta T\cos\varphi_M \tag{3.52}$$

$$R_H^{2f} = \frac{1}{2}\left[-R_{AHE}\frac{B_{DL}}{B_{ext}}\cos\varphi_M + 2I_0\alpha_{ANE}\Delta T\cos\varphi_M + 2R_{PHE}\cos\varphi_M\cos 2\varphi_M\frac{(B_{FL}-B_{Oe})}{B_{ext}}\right] \tag{3.53}$$

$$R_H^{2f} = \frac{1}{2}\left[\left(-R_{AHE}\frac{B_{DL}}{B_{ext}} + 2I_0\alpha_{ANE}\Delta T\right)\cos\varphi_M + 2R_{PHE}(2\cos^3\varphi_M - \cos\varphi_M)\frac{(B_{FL}-B_{Oe})}{B_{ext}}\right] \tag{3.54}$$

Our experimental setup accounts for the factor of half and we obtain twice the second harmonic signal as the output. We can thus rewrite the above as

$$2R_H^{2f} = \left(-R_{AHE}\frac{B_{DL}}{B_{ext}} + 2I_0\alpha_{ANE}\Delta T\right)\cos\varphi_M + 2R_{PHE}(2\cos^3\varphi_M - \cos\varphi_M)\frac{(B_{FL}-B_{Oe})}{B_{ext}} \tag{3.55}$$

This second harmonic resistance contains the response from the DLT, FLT, and torques due to thermo-electric effects. We can hence define the second harmonic resistance based on its constituents as

$$2R_H^{2f} = R_{DL}^{2f} + R_{FL}^{2f} + R_{\Delta T}^{2f} = \left(-R_{AHE}\frac{B_{DL}}{B_{ext}} + 2I_0\alpha_{ANE}\Delta T\right)\cos\varphi_M + 2R_{PHE}(2\cos^3\varphi_M - \cos\varphi_M)\frac{(B_{FL}-B_{Oe})}{B_{ext}} \tag{3.56}$$

We can thus determine the constituents of the second harmonic resistance based on the corresponding angular symmetries. In order to separate them out from the thermal effects, we need to consider their dependence on the external field. The thermal effects do not depend on the strength of the external field, instead only depends on the orientation of the magnetization. This is evident in eq. (3.56) where the thermal term has no dependency on the external field whereas the DL and FL fields do. Further, in deriving eq. (3.56), we have ignored the effect of the static fields acting on the magnetization, namely the anisotropy and the demagnetization field, in eqs. (3.23, 3.26, 3.27). These need to be considered for an accurate determination of the DL and FL fields. The DL SOTs lead to the motion of the magnetization out of the plane of the sample, given by $\frac{dR_H^f}{d\theta_B}$. This motion is counteracted by the in-plane external field, which is already accounted for in eq. (3.56). In addition, the anisotropy and the demagnetization fields also pull the magnetization in the plane of the sample, counteracting the out-of-plane motion of the DL field. This needs to be accounted for in eq. (3.56). The same is true for the FL field, which tends to push the magnetization in the plane of the sample. This is counteracted by the in-plane external field and the in-plane uniaxial anisotropy. However, as our samples have negligible in-plane uniaxial anisotropy, this term can be ignored. Re-writing eq. (3.56) accounting for these static fields, we obtain

$$2R_H^{2f} = R_{DL}^{2f} + R_{FL}^{2f} + R_{\Delta T}^{2f} = -R_{AHE}\frac{B_{DL}}{(B_{ext}+B_{dem}+B_K)}\cos\varphi_M + 2R_{PHE}(2\cos^3\varphi_M - \cos\varphi_M)\frac{(B_{FL}-B_{Oe})}{B_{ext}} + 2I_0\alpha_{ANE}\Delta T\cos\varphi_M \quad (3.57)$$

Summarizing these results, we obtain

$$B_{DL} = \frac{\left(\frac{R_{DL}^{2f}}{-R_{AHE}}\right)}{\left(\frac{1}{B_{ext}+B_{dem}+B_K}\right)} \times \frac{1}{\cos\varphi_M} \quad (3.58)$$

$$B_{FL} - B_{Oe} = \frac{\left(\frac{R_{FL}^{2f}}{2R_{PHE}}\right)}{\left(\frac{1}{B_{ext}}\right)} \times \frac{1}{(2\cos^3\varphi_M - \cos\varphi_M)} \quad (3.59)$$

$$\alpha_{ANE} = \frac{R_{\Delta T}^{2f}}{2I_0\Delta T} \times \frac{1}{\cos\varphi_M} \quad (3.60)$$

3.1.2 Extraction of torques for an in-plane magnetized sample: Ta(3)/Cu(1)/Co(2)/Pt(3)

Let us now consider how we can use this technique in practice to extract SOTs for an in-plane magnetized sample. Here we consider a reference Ta(3)/Cu(1)/Co(2)/Pt(3) sample, which is used in the study of the mechanism of SOTs in oxidized platinum systems, detailed in the next chapter. The numbers in the parenthesis denote the thickness in nm. As this is an in-plane sample, we perform in-plane angular scan as shown in Figure 3.4 (a), where we rotate the external field in the plane of the sample while injecting a small ac current. We keep the frequency of this current constant at 10Hz and its amplitude a few mA so as to stay in the linear regime. We measure the transverse voltage output and decompose it into its different harmonics using Fast Fourier Transform (FFT). The first and second harmonic signals at different external field amplitudes are shown in Figure 3.6.

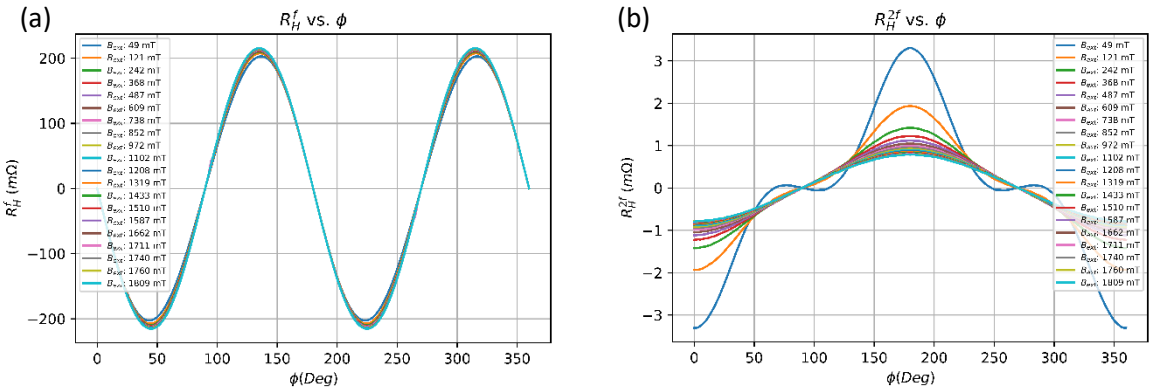

Figure 3.6: (a) First and (b) second harmonic Hall voltages from an in-plane angle scan of Ta(3)/Cu(1)/Co(2)/Pt(3).

The first harmonic resistance contains information regarding the equilibrium position of magnetization, and we can hence extract the PHE coefficient and the in-plane anisotropy[40,41] from this waveform. This first harmonic resistance can be expressed in terms of the φ_M angular dependence, by setting $\theta_M = \frac{\pi}{2}$ in eq. 3.11.

$$R_H^f = R_{PHE} \sin 2\varphi_M \tag{3.61}$$

Here, any variation in the φ angle from sample misalignment, etc. need to be corrected to avoid errors in the subsequent analysis. Though the R_{PHE} is expected to be constant due to the easy plane anisotropy of the sample, we notice that there is a very weak dependence on the external field, of a few mΩ as shown in Figure 3.7. This likely indicates the presence of small domains or magnetic clusters which gets saturated at a higher field. The negative sign corresponds to the $\frac{\pi}{2}$ phase offset of our first harmonic sinusoidal. The measured samples have a weak in-plane uniaxial anisotropy of around 1mT. This would have negligible effect on the extraction of SOTs.

The second harmonic resistance contains contributions from the DL, FL and thermal signals.

$$2R_H^{2f} = R_{DL}^{2f} + R_{FL}^{2f} + R_{\Delta T}^{2f} \tag{3.62}$$

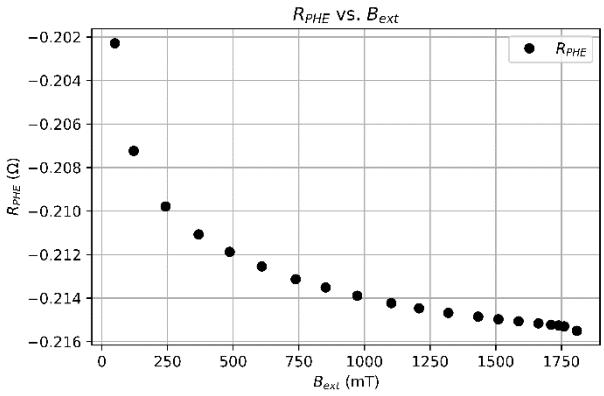

Figure 3.7: The PHE coefficient, at different external field amplitudes, extracted from the first harmonic Hall resistance.

These can be separated out into their constituents by considering their respective angular symmetries as shown in eq. 3.56. The DL and the thermal components have similar angular dependence while the FL has a different one as re-written in the following equations

$$R_{DL}^{2f} + R_{\Delta T}^{2f} \sim \cos\varphi_M \tag{3.63}$$

$$R_{FL}^{2f} \sim (2\cos^3\varphi_M - \cos\varphi_M) \tag{3.64}$$

In practice, the separation of components can be done either by curve fitting or by considering the difference in the zero-crossing between the different contributions. This way, any fitting can be avoided as well. The extracted curves of the contributions are plotted in fig. 3.8.

In order to extract the DL and FL fields from these resistance contributions, we need to obtain the AHE coefficient as well as the anisotropy field B_K. In this case of an in-plane sample, we can obtain the anisotropy field from the perpendicular field scan shown in Figure 3.4 (b), where the external field is swept in the direction perpendicular to the plane of the sample. The resultant first harmonic resistance shows a typical hard axis loop and the effective sum of the demagnetizing and the anisotropy field can be obtained from the field at which the resistance saturates, as shown in Figure 3.9 (a). It is to be noted that in order to accurately set the θ_B angle to zero, or in other words to apply the field exactly perpendicular the sample, we perform this measurement over a range of θ_M values close to zero and use the measurement with the highest first harmonic resistance value in saturation.

As the first harmonic resistance denotes the position of the magnetization, we can obtain the θ_M dependence of the first harmonic resistance assuming a simple cosine relationship, as shown in Figure 3.9 (b). The slope of this curve around $\theta_M = \frac{\pi}{2}$ denotes the change in resistance as the magnetization is pushed slightly out of the plane, $\frac{dR_H^f}{d\theta_M}$. The AHE coefficient is the negative of this value, given by eq. 3.36.

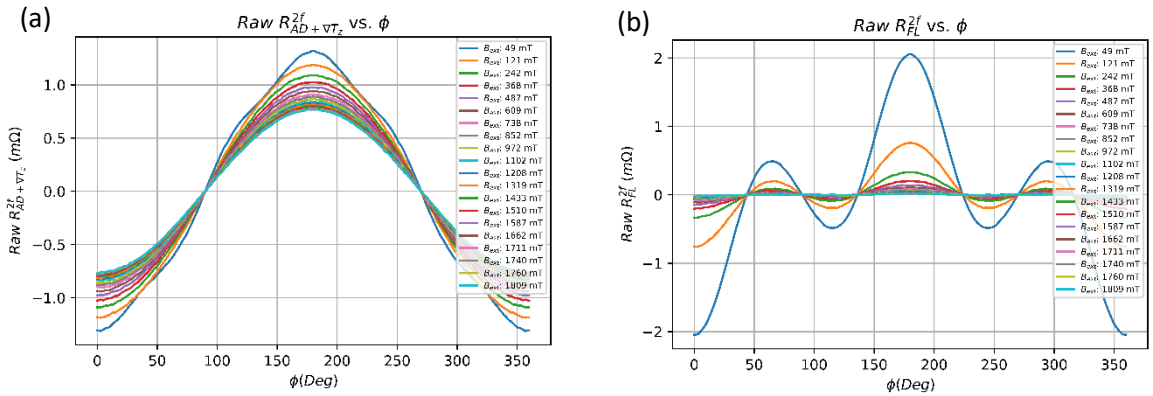

Figure 3.8: (a) The DL and thermal component and (b) the FL component extracted from the second harmonic Hall resistance.

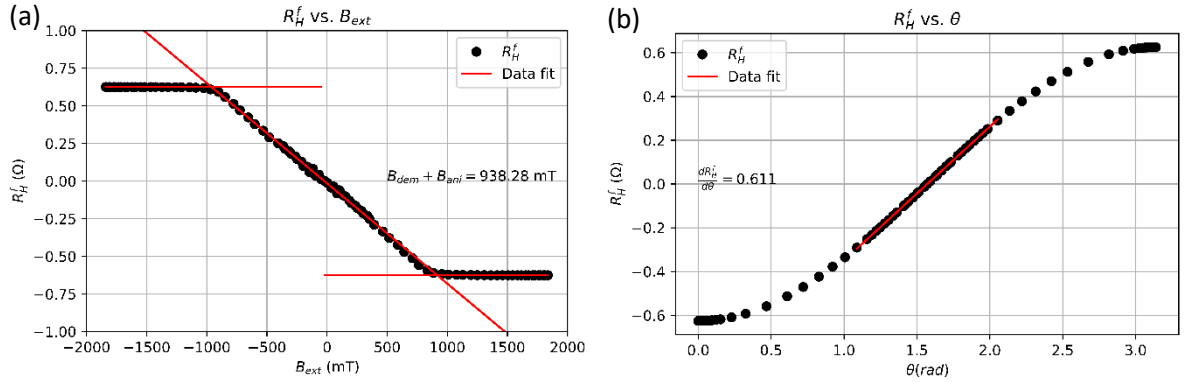

Figure 3.9: (a) Extraction of the demagnetizing (B_{dem}) and anisotropy field (B_{ani}) from the perpendicular field scan. (b) Extraction of the AHE coefficient from the same.

We can now use these values of the anisotropy field and the AHE coefficient in order to extract the SOT fields from their second harmonic resistance contributions. As expressed in eqs. 3.58-3.60, we can obtain these SOT fields by considering their field dependences. The DL field which acts perpendicular to the sample is aided by the perpendicular component of the external field whereas is opposed by the in-plane external field and the demagnetizing and anisotropy fields. Hence by plotting the second harmonic of the resistance, which has a cosine dependence on the φ angle as denoted in the first term on the right of eq. 3.56, against the field dependence, i.e. $\frac{1}{B_{ext}+B_{dem}+B_K}$, we can obtain the DL field and the thermal contribution. This is plotted in Figure 3.10 (a). The DL field is then given as the slope of this curve over the negative AHE coefficient.

$$B_{DL} = -\frac{slope}{R_{AHE}} \tag{3.65}$$

Unlike the DL or the FL torques, the thermal contribution has no dependence on the external field amplitude. And instead, at very high fields when the DL and FL fields are too weak to affect the magnetization, the only contribution to the second harmonic resistance is that of the thermal alone. Hence the thermal contribution to the second harmonic resistance can be obtained by considering the y-intercept of Figure 3.10 (a).

$$R_{\nabla T}^{2f} = y - intercept \tag{3.66}$$

The FL field acts on the magnetization in the plane of the sample. It is opposed only by the external field as these samples have negligible in-plane anisotropy, which can be obtained from the in-plane angle scans. Hence by plotting the FL contribution to the second harmonic resistance, which has a $\cos\varphi_M \cos 2\varphi_M$ angular dependence as denoted by the second term on the right of eq. 3.56, against $\frac{1}{B_{ext}}$, we can obtain the FL field. This is given by the slope of the curve shown in Figure 3.10 (b), over twice the PHE resistance coefficient.

$$B_{FL} - B_{Oe} = \frac{slope}{2R_{PHE}} \tag{3.67}$$

As the FL and the Oersted fields are opposed in this sample, the effective FL field contribution to the second harmonic resistance is quite weak and noisy. This is visible in Figure 3.8 where the amplitude of the second harmonic contribution of the FL is much weaker than those of the DL at higher fields, and in Figure 3.10 where the FL contribution curve is noisier as compared to that of the DL.

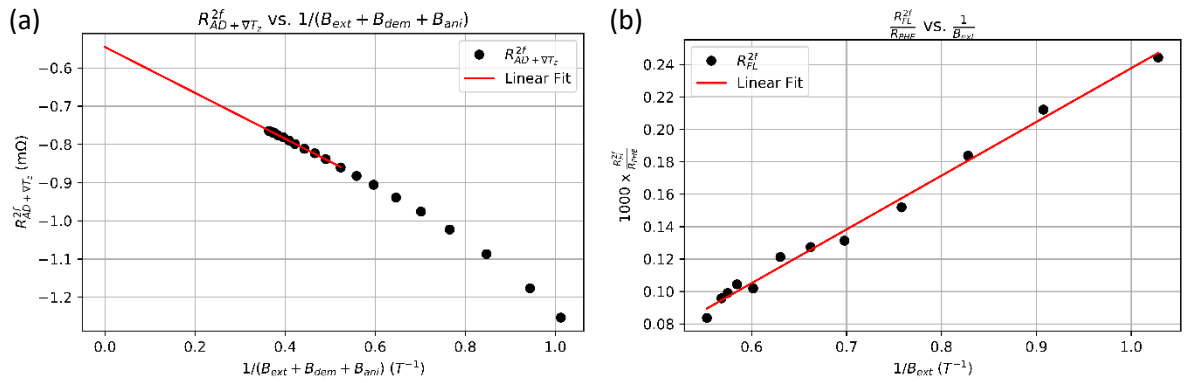

Figure 3.10: Extraction of (a) the DL field and the thermal component and (b) the FL field from the corresponding 2F resistance contributions by considering their field dependences.

Another point to be noted here is that the model used for the extraction of torques assumes a macro-spin model. Hence it is necessary that the magnetization is completely saturated. When not, it generally, manifests as a curvature of the DL and FL curves shown in Figure 3.10. This is visible in the DL curve at lower external fields (towards the right). To avoid an error in the calculation of the SOT fields from this curvature, we extract the slope of the curve only from the linear part, which corresponds to the fields above the complete PHE saturation shown in Figure 3.7.

Another point to be noted is that although the DL curve in Figure 3.10 is expected to have a non-zero y-intercept corresponding to the thermal component, the FL is inversely proportional to the external field and expected to be zero at very large fields. This should lead to a zero y-intercept of the curve. This, however, is not always the case as shown in Figure 3.11. In samples with a very low thickness of platinum or in samples exhibiting 2nd order anisotropy etc., we obtain a non-zero intercept. Figure 3.11 (a) plots the FL component of the second harmonic resistance of a plasma oxidized Ta3/Cu1/Co2/Pt1.5. More details regarding the thickness and oxidation are provided in the following chapter. The dashed line represents the linear fit of the curve leading to an FL field of -0.01 mT and a non-zero y-intercept of -0.2. However, considering the fact that the y-intercept should be ideally zero, we can fit the curve using a polynomial as denoted by the red curve. The slope that we need to consider in this case then is the tangent to this polynomial fit at zero. This leads to an FL field of -0.38 mT. It is evident that the FL field strength can vary vastly between the two methods.

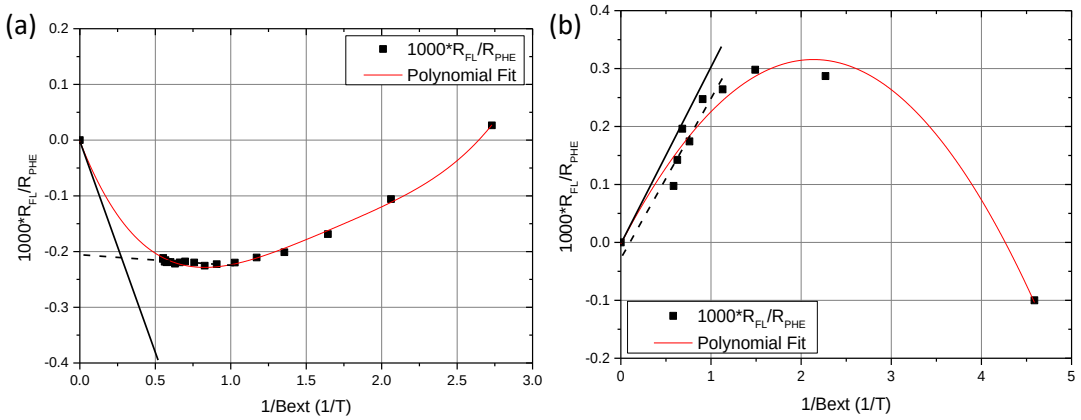

Figure 3.11: Correct extraction of FL field from the non-linear curvature for samples (a) Ta3/Cu1/Co2/Pt1.5 (OX) (b) Ta3/Co2/W3.

In some samples, these two methods can lead to FL fields of different signs even. Figure 3.11 (b) plots the FL component of Ta3/Co2/W3 samples.Though in this case, the difference in FL field strengths extracted by the two methods is not as significant, the non-linear curvature of the plot is more significant and visible. In our analyses, we have considered both these methods of extracting the FL field and are mentioned accordingly.

3.1.3 Extraction of torques for an out-of-plane sample: Ta(3)/Pt(3)/Co(0.9)/MgO(0.9)/Ta(2)

SOTs of samples with perpendicular anisotropy or having non-negligible second order anisotropy can be measured using the same in-plane angular scan technique as long as the anisotropy field amplitude is well below the maximum field that can be applied in the setup, ~2T in our case. Here we consider the case of Ta(3)/Pt(3)/Co(0.9)/MgO(0.9)/Ta(2) sample (annealed at 250 °C for 10 minutes), which was part of a study on skyrmion dynamics[42]. The first and second harmonic resistances and the DL and FL components extracted from the 2f resistance of the in-plane angular scans are shown in Figure 3.12 (a) - (d) respectively. The FL component is noisier at lower field amplitudes as the field might not be sufficient to saturate the magnetization completely in-plane. The second harmonic and the DL plots are inverted compared to the in-plane sample discussed previously. This reflects the fact that the platinum layer is on the opposite side of cobalt, resulting in an inverted DL torque.

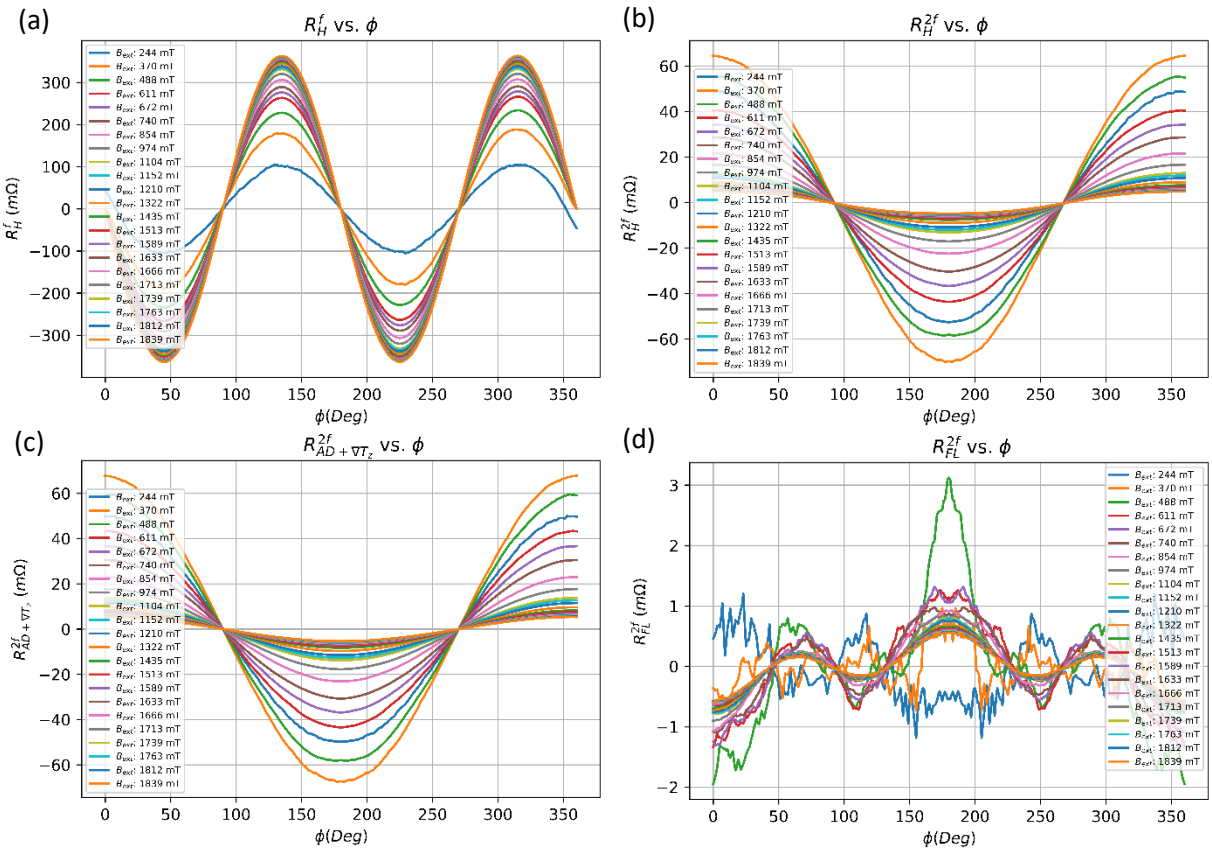

Figure 3.12: (a) First and (b) second harmonic Hall resistance of Ta(3)/Pt(3)/Co(0.9)/MgO(0.9)/Ta(2). (c) The DL and thermal, and (c) the FL component extracted from the 2f resistance for different external field amplitudes.

The AHE coefficient can be obtained from the perpendicular field scan like the previous case. Here the external field is swept in the direction perpendicular to the plane of the sample and the saturation value of the first harmonic resistance corresponds to the AHE coefficient. This is shown in Figure 3.13.

Though the in-plane angular scans are quite similar to the previous case of in-plane samples, we cannot utilize the same perpendicular field scan to determine the anisotropy field. Instead, we need to perform out-of-plane angular scans, where a constant field is rotated in a plane perpendicular to the sample. A schematic of this technique is shown in Figure 3.14.

The energy of the system that we consider, in the presence of an external field is given by

$$E = -B_{ext}M_s\cos(\theta_M - \theta_B) + \frac{B_{K1}M_s}{2}\sin^2\theta_M + \frac{B_{K2}M_s}{4}\sin^4\theta_M \quad (3.68)$$

Here B_{K1} and B_{K2} refer to the first and second-order uniaxial out-of-plane anisotropies. Minimizing the energy of the system with respect to θ_M we obtain

$$\frac{dE}{d\theta_M} = -B_{ext}M_s\sin(\theta_M - \theta_B) + B_{K1}M_s\sin\theta_M\cos\theta_M + B_{K2}M_s\sin^3\theta_M\cos\theta_M = 0 \quad (3.69)$$

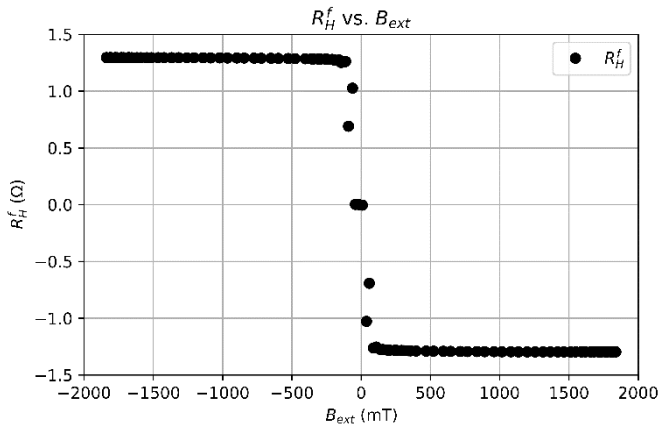

Figure 3.13: Perpendicular field scan of the sample. The external field is swept perpendicular to the plane of the sample.

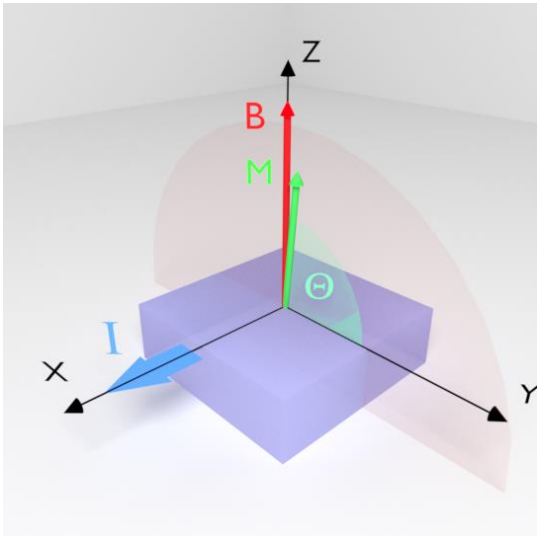

Figure 3.14: Out-of-plane angular scan. A constant field is rotated in a plane (shaded in light red) perpendicular to the sample plane.

Considering only the first-order anisotropy,

$$B_{K1} = \frac{B_{ext}\sin(\theta_M - \theta_B)}{\sin\theta_M \cos\theta_M} \tag{3.70}$$

We can use eq. 3.70 to determine the perpendicular anisotropy of the sample from the out-of-plane angle scans. The dependence of the first harmonic Hall resistance on the external field angle is plotted in Figure 3.15 (a). Similar to the previous case, assuming a cosine dependence of the magnetization on the θ_B angle, we can determine the θ_M from this plot. Then we can use eq. 3.70 to determine the angular dependence of the anisotropy field, as plotted in Figure 3.15 (b). This figure plots the dependence of the anisotropy field on the magnetization angle, expressed in terms of $\sin^2\theta_M$. By fitting and extending this curve to $\sin^2\theta_M = 0, 1$ to avoid the discontinuities, we can extract the corresponding anisotropy values B_{K0} and B_{K90}. Figure 3.15 (c) plots these values. B_{K90} corresponds to the case where the magnetization is forced in the plane of the sample, relevant to the in-plane angle scan measurements. Thus, we can thus fit the B_{K90} values corresponding to the external field as shown in Figure 3.15 (d) and use them in the analysis of our in-plane angle scans.

One point to note here is the external field dependence of the anisotropy field. Though generally when we talk of anisotropy fields, we consider a single number, this is not the case here. Here, the anisotropy field increases with the external field up to a saturation value of ~920 mT. This tells us that in-plane angular measurements performed above this field should adhere to the macro-spin model assumed in the analysis. We, however, notice that even above this external field amplitude, we have a field

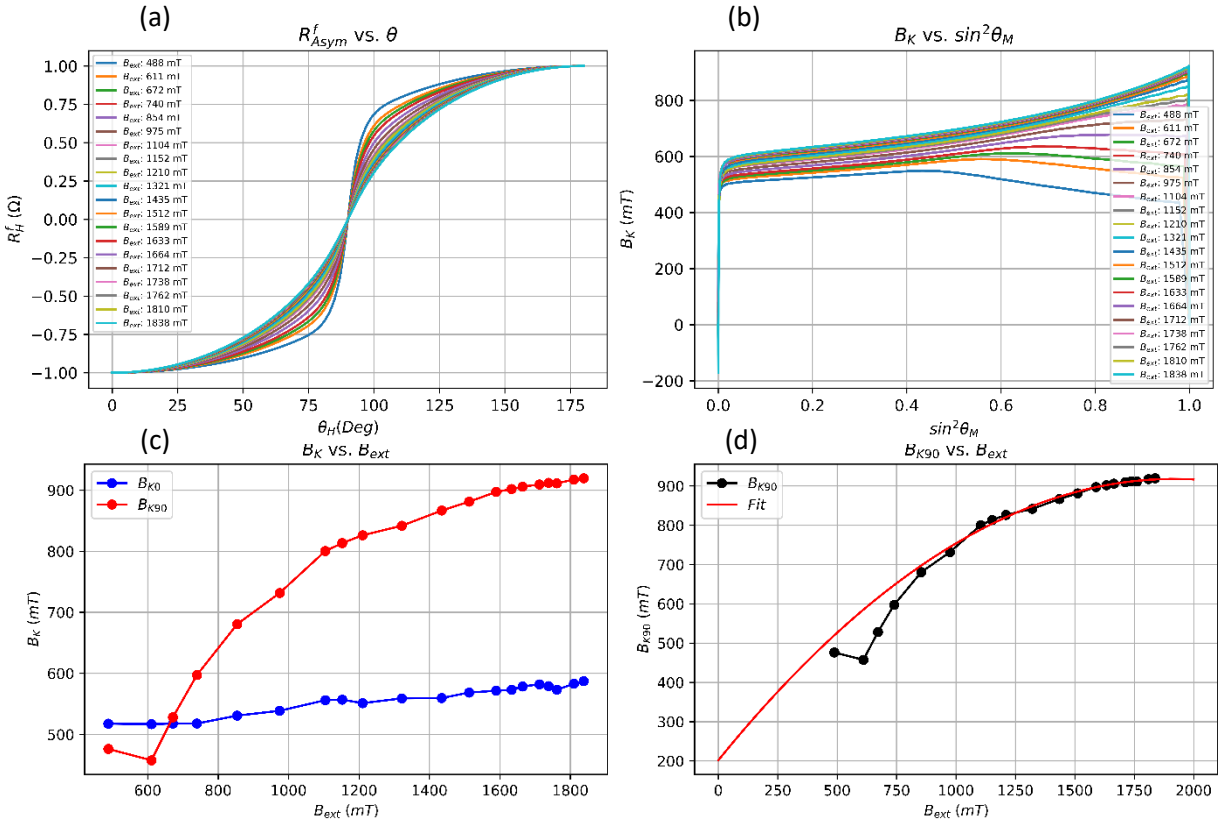

Figure 3.15: Extraction of the perpendicular anisotropy field from the out of plane angle scan. (a) Dependence of the first harmonic resistance on the external field angle. (b) Anisotropy field as a function of the magnetization angle. (c) Anisotropy field as a function of the external field angle. B_{K0} and B_{K90} corresponds to the anisotropy when the magnetization is pointing perpendicular and in the plane of the sample. (d) Fit of the B_{K90} to be used to extract the SOTs.

dependence of the anisotropy field. We attribute this to the fact that even at high fields, when the net magnetic moment may point in the direction of the external field, we could still have small clusters or magnetic domains with a small tilt in magnetization out-of-the-plane of the sample, pointing in up or down directions. This is depicted in Figure 3.16 by M_L. These domains progressively align their staggered magnetization along the external field as the magnetic field amplitude is further increased. This is depicted by M_H. We can thus use the effective anisotropy corresponding to each applied external fields of the in-plane angular scans to plot the SOT components of the second harmonic resistance.

Figure 3.17 (a) plots the DL and the thermal component of the second harmonic Hall resistance and Figure 3.17 (b) plots the FL component of the second harmonic resistance. The extraction of the FL field from this plot is straight forward as in the previous case since the perpendicular anisotropy does not affect the motion of the magnetization in the plane of the sample. The DL field extraction, however, is different since the anisotropy field now favors the motion of the magnetization out of the plane of the sample. This gives us the following relation for the DL field as

$$B_{DL} = \frac{\left(\frac{R_{DL}^{2f}}{-R_{AHE}}\right)}{\left(\frac{1}{B_{ext}+B_{dem}-B_K}\right)} \times \frac{1}{\cos\varphi_M} \tag{3.71}$$

This leads to a DL field of 1.116 mT/mA and an FL field of 0.422 mT/mA, which is consistent with literature values.

In order to verify the effect of varying the anisotropy field with the external field instead of using a constant value in the determination of the DL torque, we plot both the cases in Figure 3.18. It is evident that by utilizing the effective anisotropy at each field of the in-plane angle scan we obtain a more linear curve. This is consistent with the macro-spin model, re-affirming our hypothesis. Further, this technique can be used to determine the SOTs in samples with higher-order anisotropies by following the same procedure.

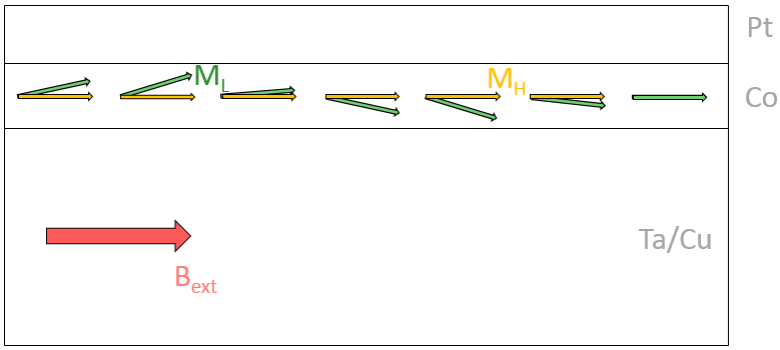

Figure 3.16: Schematic depicting the progressive alignment of the perpendicular magnetization with the strength of the in-plane external field B_{ext}. At lower fields, the magnetization can be staggered with a tilt along the perpendicular direction, corresponding to perpendicular magnetic domains, depicted by M_L. At higher fields, M_H, it is completely aligned with the external field.

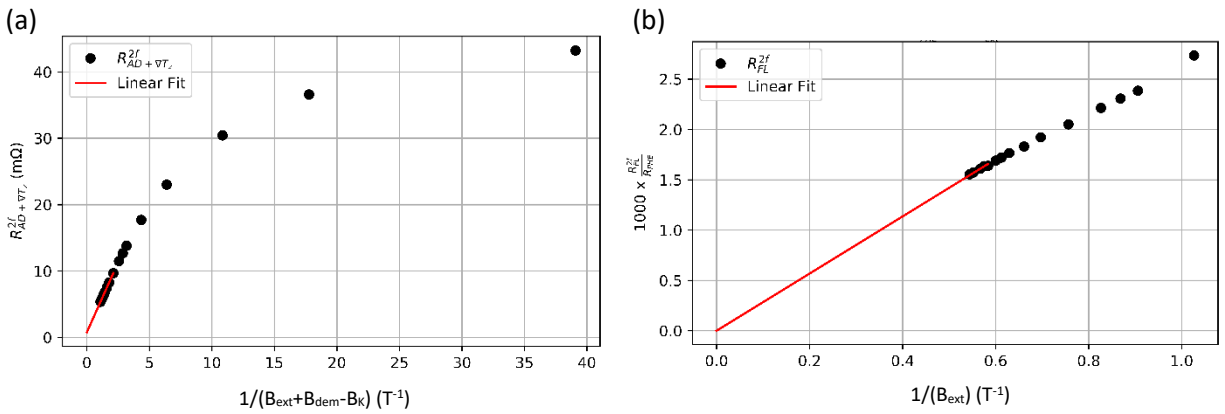

Figure 3.17: Extraction of (a) the DL field and the thermal component and (b) the FL field from the corresponding 2F resistance, for an out-of-plane sample.

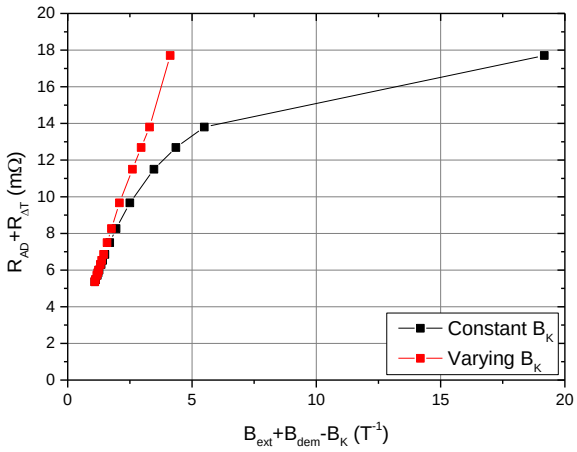

Figure 3.18: Comparison between keeping a constant B_K and using the effective B_K at each field.

3.1.4 Other angular symmetries of the second harmonic Hall resistance

We separated the second harmonic Hall resistance into its $\cos\varphi_M$ and $\cos\varphi_M \cos 2\varphi_M$ components in order to extract the torques as these relate directly to the DL and thermal components and the FL components respectively based on eqs. 3.63-3.64. However, in some samples especially at lower platinum thicknesses, there can be signals with angular symmetries other than these cosines, with amplitudes comparable to FL torques. Figure 3.19 plots the different components of the second harmonic Hall resistance that was extracted from an in-plane angle scan of Ta(3)/Cu(1)/Co(2)/Pt(1.5) at an external field amplitude of 1690 mT.

The DL component is two orders of magnitude greater than the FL component. However, the rest of the components are of the order of magnitude of the FL component and needs to be duly considered. If these signals are not real and are instead artifacts, it could indicate an error in the determination of the phase offset value of the angular scans. Hence, we re-performed these analyses by varying the phase offset to make a determination. It was confirmed that, even though by artificially varying the phase offset we can change the signal amplitudes, these components shown in Figure 3.19 are real and our phase offset calculation is valid. Hence, we need to determine the origin of these signals.

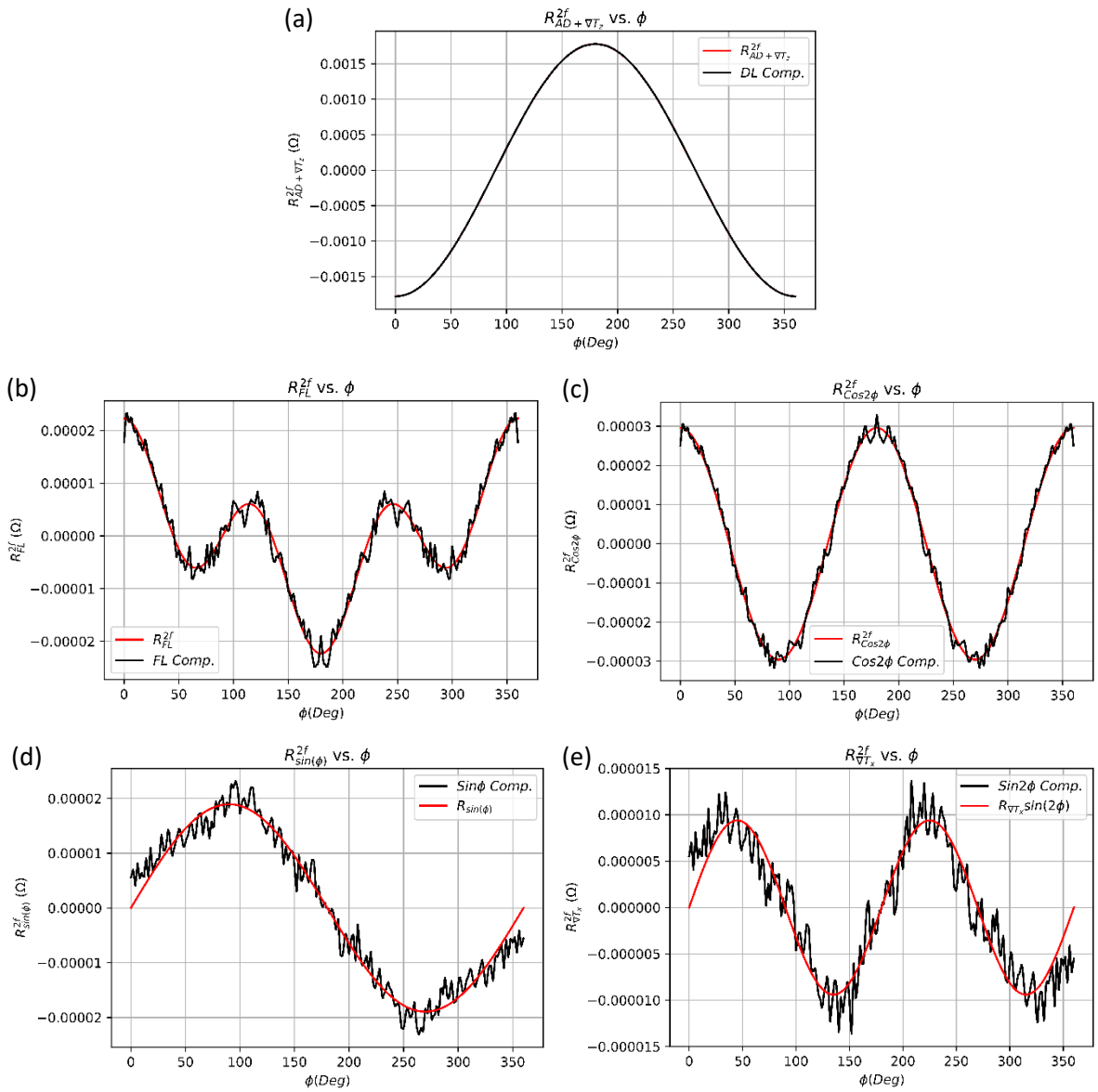

Figure 3.19: Components of the second harmonic Hall resistance considering all the angular symmetries. (a) DL and thermal (b) FL (c) cos2φ (d) sinφ (e) sin2φ components. The black lines are the signals extracted from the measured second harmonic resistance and the red lines are the fits.

It is highly likely that these signals have a thermal origin[38,39]. The sin2φ component could be due to Planar Nernst Effect (PNE) from an in-plane thermal gradient, which has the same signal symmetry. While the sinφ component could originate from the ANE component picked up by a lateral asymmetry in our voltage leads, i.e. longitudinal ANE component. In such a case, these signals shouldn't have any dependence on the external field. Figure 3.20 shows the field dependence of these signals. $\frac{1}{B_{ext}+B_K}$ corresponds to an out-of-plane effect on the magnetization and $\frac{1}{B_{ext}}$ corresponds to an in-plane effect. It is evident that the sinφ and the sin2φ components are indeed constant with field and hence thermally induced components of the second harmonic resistance.

The cos2φ signal is also likely thermally related as it has the same symmetry as that of the longitudinal PNE from an in-plane thermal gradient. It, however, might have a very weak dependence on the

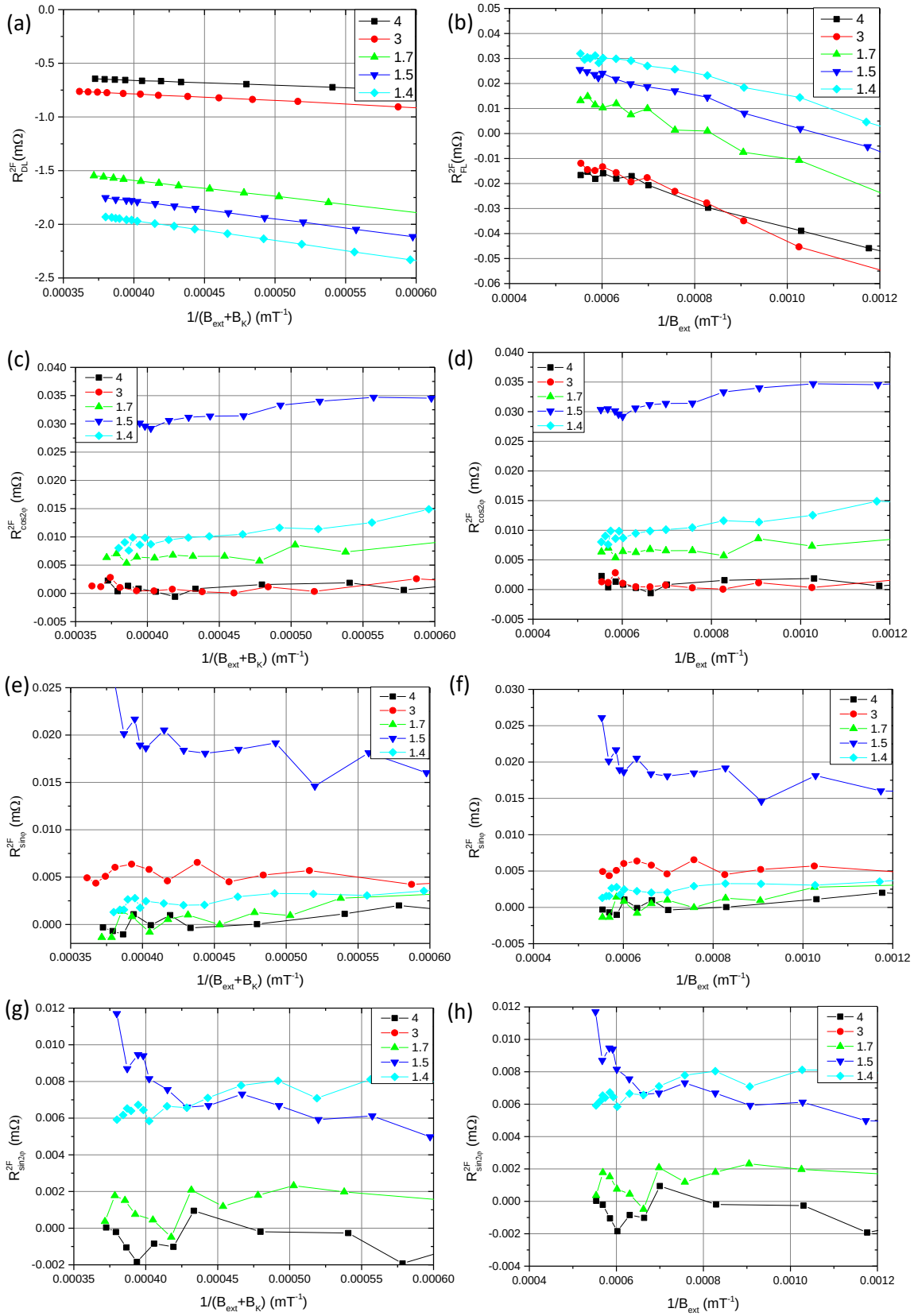

Figure 3.20: Amplitude of the 2F components against the external field. Dependence of (a) DL (c) cos2φ (e) sinφ (g) sin2φ components on $\frac{1}{B_{ext}+B_K}$. Dependence of (b) FL (d) cos2φ (f) sinφ (h) sin2φ components on $\frac{1}{B_{ext}}$. These denote the out-of-plane and in-plane effect of these 2f components on the magnetization. The numbers indicate the platinum thickness of the respective samples in nanometers of Ta(3)/Cu(1)/Co(2)/Pt.

external field as shown in Figure 3.20 (c, d). Any such dependence could be due to our transverse voltage being modulated by the Anisotropic Magneto Resistance (AMR). That is, since we use a voltage source instead of a current source, AMR can modulate the current that flows in our device. This modulated current can in turn give rise to a modulated transverse voltage, which has the same cos2φ symmetry.

By accounting for all of these effects in our data analysis, we can accurately determine the SOTs of the samples used for the studies presented here.

3.2 In-plane Magneto-Optical Kerr Effect (MOKE) Microscopy

MOKE is a widely used and versatile technique for quick determination of magnetic properties as well as detailed studies of magnetic textures such as domains[43–45], domain wall dynamics[44,45], skyrmionic bubbles[46], etc. This is especially critical in determining the magnetic reversal process in heterostructures used for SOT switching[1] where other phenomena such as Dzyalonshinskii-Moriya Interaction (DMI)[47,48] and chiral damping[49] can come into play. It has also been shown that the physics of domain wall dynamics and switching determined from such MOKE studies is valid down to nanometer scale devices[50] and can also be used to engineer new switching devices based on geometry alone[51].

3.2.1 Magneto-optical Kerr effect

Kerr effect is a magneto-optical effect that causes a rotation of the polarization angle upon reflection from a magnetic surface[52]. In case of transparent samples, where the polarization is rotated upon transmission through the sample, it is known as the Faraday effect[53]. Both are linear magneto-optical effects and caused by magnetic circular birefringence, where the refractive index of left and right circularly polarized light are different, and by magnetic circular dichroism, where the absorption coefficient of left and right circularly polarized light are different. These effects lead to a change in ellipticity and the polarization of light. The magneto-optical effect can be quadratic in nature as well such as the Voigt effect, otherwise known as the magnetic-linear birefringence. This effect was recently used to determine the Néel vector[54] as well as to image the domains of an antiferromagnet[55].

When an illuminating light hits a sample, it induces a local electric dipole due to the separation of charges. Kerr effect can thus be described using the dielectric law, which relates the electric displacement vector $\boldsymbol{D}$ to the electric vector of the illuminating light $\boldsymbol{E}$ as

$$\boldsymbol{D} = \epsilon \boldsymbol{E} + \boldsymbol{P} \tag{3.72}$$

Here ϵ denotes the electric permittivity of the material and $\boldsymbol{P}$ the polarization density, which includes both the permanent and the induced dipole moments in the material. In the case of a magnetic material, the polarization density can be re-written in terms of the magneto-optical constant Q, which is proportional to the saturation magnetization, and the magnetic moment $\boldsymbol{m}$ as[44]

$$\boldsymbol{D} = \epsilon \boldsymbol{E} + (iQ\boldsymbol{m} \times \boldsymbol{E}) \tag{3.73}$$

Hence the Kerr effect can be considered as a cross-product of the magnetic moment of the sample and the electric vector of the illuminating light. This forms the orthogonal component of the polarization of the reflected light, denoted by $\boldsymbol{K}$. This Kerr amplitude can be considered as due to the Lorentz

motion of the electrons due to the effect of the electric field of the incident light. The reflected light also contains a parallel component of polarization due to the regularly reflected light, denoted by $\boldsymbol{N}$. These two components recombine to form the electric vector of the reflected light. This results in a rotation of the polarization vector expressed as

$$\phi = \frac{\boldsymbol{K}}{\boldsymbol{N}} \tag{3.74}$$

As the Kerr rotation depends on the magnetization of the sample and the polarization of the incoming light, we have three configurations of the MOKE, namely the polar, longitudinal and the transverse MOKEs. These are depicted in Figure 3.21.

The polar MOKE is the most widely used and is utilized in studies of perpendicularly magnetized materials. In this case, the incident and reflected beams of light and the magnetic moment are perpendicular to the sample plane. This configuration gives rise to a Kerr amplitude perpendicular to

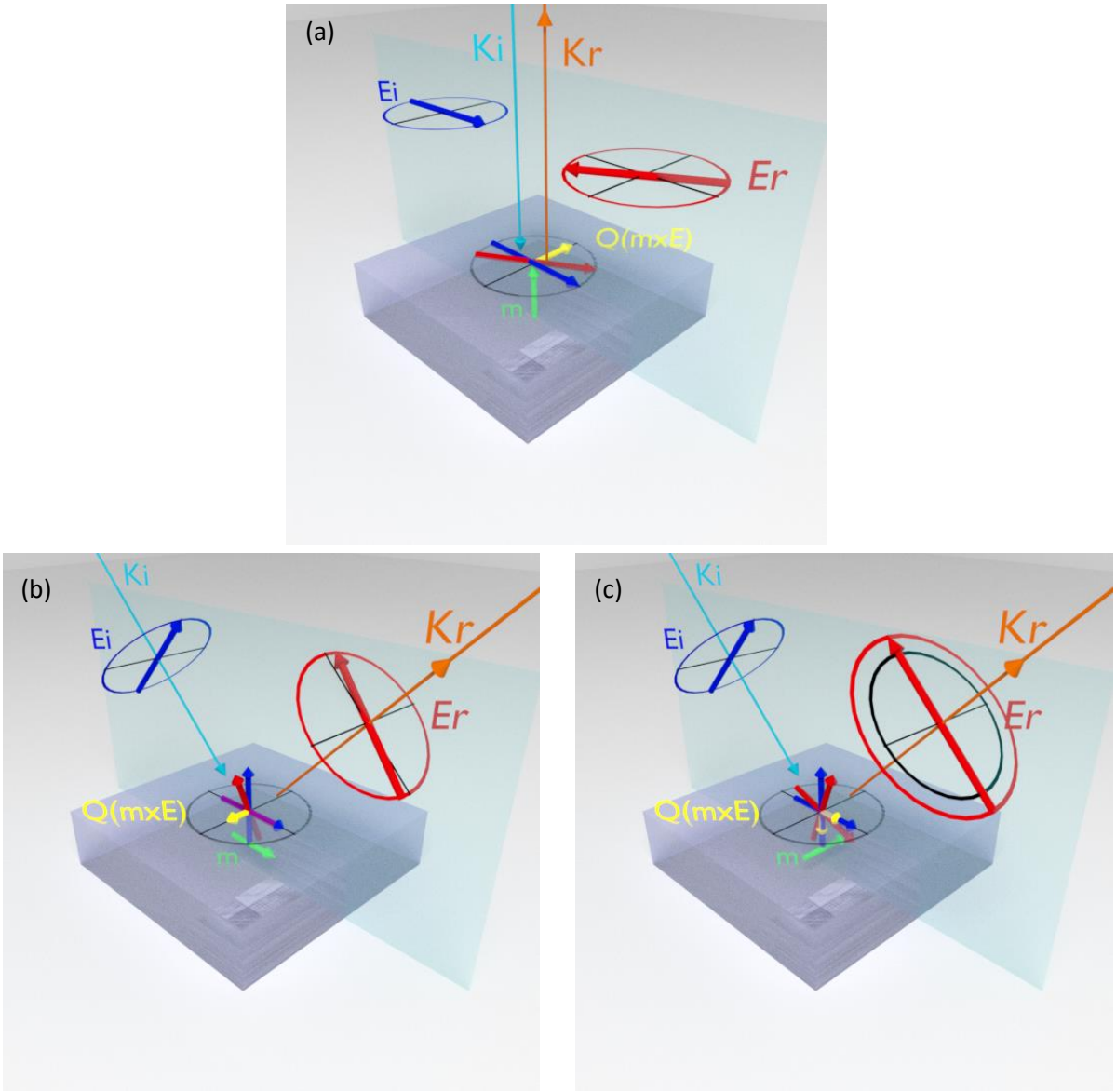

Figure 3.21: Configurations of MOKE. (a) Polar (b) Longitudinal (c) Transverse. Ki and Kr denotes the incident and the reflected beams of light. While Ei and Er their polarizations. M denotes the magnetization, depicted by the green arrow, and the cross product of m and E is depicted by the yellow arrow. The light blue plane denotes the plane of incidence.

the incident polarization, resulting in a rotated polarization of the reflected light. It is this slight rotation of polarization that is detected experimentally.

In case of in-plane magnetized samples, like those used in this work, we can no longer use a perpendicular incidence of light to the sample as it would only lead to an optical intensity effect and not a magneto-optical rotational effect. Hence, in this case, the light is incident at an angle to the sample. The incident polarization is parallel to the plane of incidence (p-polarization). Here, the plane of incidence is described as the plane containing the incident and the reflected beams of light, depicted by the blue plane in Figure 3.21. When the magnetization of the sample lies in the plane of incidence, as shown in Figure 3.21 (b), it is known as the longitudinal MOKE. This once again results in a rotation of the polarization out of the plane of incidence, which can be detected optically. The longitudinal MOKE is of an order of magnitude weaker than the polar MOKE[45]. This is due to the high refractive index of metallic magnetic films. Hence even a small out of plane component can conceal the longitudinal effects. This makes it an extremely difficult technique to implement and measure thin films with in-plane magnetization as the resulting signal could be very weak for imaging purposes.

When the magnetization lies transverse to the plane of incidence, it is known as transverse MOKE and illustrated in Figure 3.21 (c). In this case, the Kerr effect leads to a change in intensity of the reflected light. This, however, can be converted to a rotational effect by having the incident light polarization at an angle of $\frac{\pi}{4}$ to the plane of incidence (between s- and p- polarization) and compensating for the phase shift[44]. Though this can lead to an out-of-plane magnetization sensitivity as well. Transverse MOKE is used mostly for MOKE magnetometry rather than imaging.

3.2.2 Setup of the in-plane MOKE microscope

The optical components of an in-plane MOKE microscope are shown in Figure 3.22. It consists of an optical source which can uniformly illuminate the sample. This beam is passed through a cross slit aperture diaphragm to force the beam off the axis of the microscope, in effect selecting the off-axis beam. This is vital to obtain an oblique incidence on the sample and thereby a Kerr rotation. The light then passes through a polarizer which linearly polarizes the light at an angle determined by the MOKE configuration. This linearly polarized light then passes through the high Numerical Aperture (NA) objective, the curvature of the lens of which determines the angle of incidence on the sample. Once the sample is reflected off the surface of the sample, the light is elliptically polarized, which can be converted back to linear light using a compensator. It finally passes through an analyzer which is crossed with the polarizer in order to allow only the component orthogonal to the initial polarization of light, which corresponds to the Kerr rotation of the sample. It is hence necessary to adjust the optics for a good illumination and extinction ratio.

Though there have been numerous works on MOKE imaging of thick in-plane magnetized films, using MOKE microscopy on ultra-thin in-plane magnetized films is not that widespread due to the fundamental limitations mentioned before as well as technical ones to be detailed later. This is not the case with MOKE magnetometry using a laser, where the Signal to Noise Ratio (SNR) is much higher. Since we deal with in-plane magnetized samples with film thickness less than 2nm, it was necessary to build a sensitive in-plane MOKE microscope. This was complicated by the fact that we wanted to study micro and nanoscale patterned films where the magnetic volume available is much smaller, placing more stringent requirements on the setup.

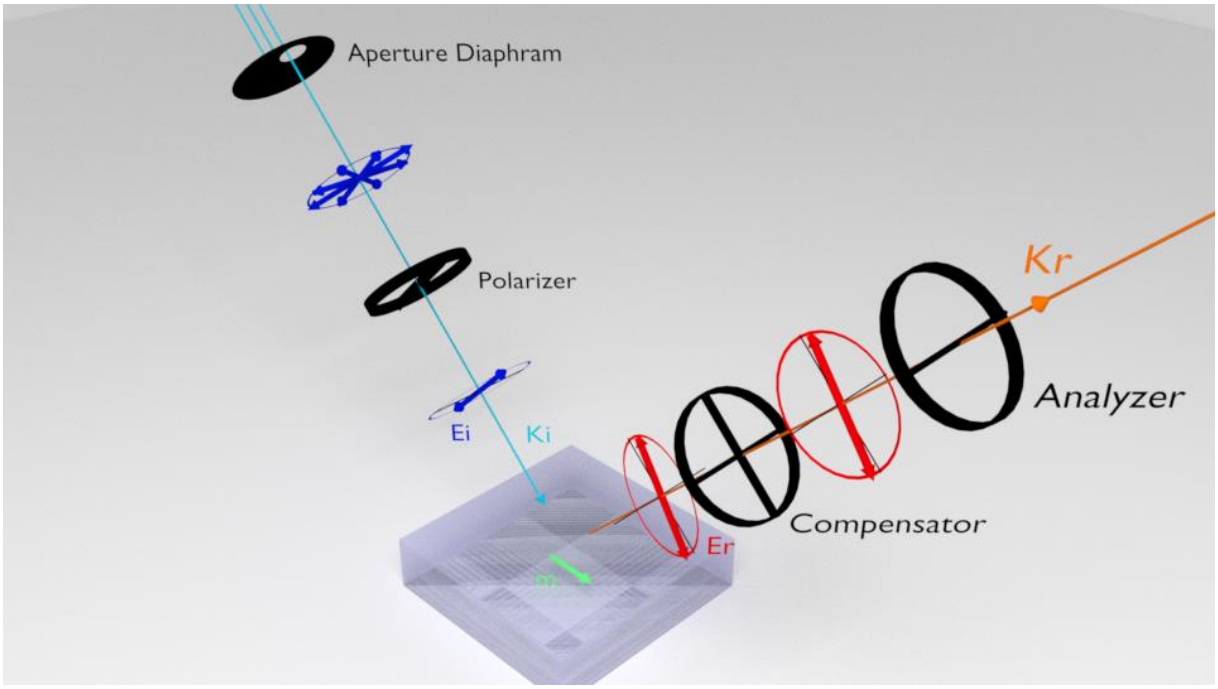

Figure 3.22: Optical components of an in-plane MOKE.

There are several factors that affect the sensitivity of the Kerr signal namely,

1. The thickness of the magnetic layer: limited by our system of interest
2. Magneto-optical constant: material dependent
3. The wavelength of light: material absorption and minimum feature size dependent
4. The angle of incident: higher the better for in-plane materials and can be changed with the numerical aperture of the objective lens
5. Refractive index of media: can lower the losses using oil immersion optics
6. Mechanical stability of the setup: sample drift, mechanical noise, etc.

Some of the parameters such as the thickness of the FM and the magneto-optical constant of the material are fixed and determined by the system under study whereas the other parameters can be tailored to our needs. Figure 3.23 shows the wavelength dependence of Co/Pt and Co/Pd superlattices. Although these curves vary depending on the number of layers and thickness of each layer, they all show a clear wavelength dependence. Further, the smallest resolvable feature size depends on the wavelength of the light used. We hence opted for a 455nm LED source for our setup. These LEDs were packaged into a cross shape in order to steer the light beam towards one side of the microscope column. A cross slit aperture further aids in this task. This not only allows us to obtain a non-perpendicular angular incidence but also allows us to utilize incident-angle differential-imaging to enhance the Kerr signal contrast. The LED system, cross slit aperture, in-plane electromagnet, and the imaging software were obtained from EVICO magnetics[56]. We opted for a Zeiss AX10 microscope on account of its large base which enabled us to set up the electro-magnetic components unhindered as well as add on other optical components for laser illumination etc. This microscope was coupled with a Hamamatsu high-speed digital CMOS camera as well high magnification and numerical aperture air and oil immersion optics. We designed solenoidal and Helmholtz coils for uniform perpendicular field and had them custom build. We also designed and build a low mechanical noise sample stage and a

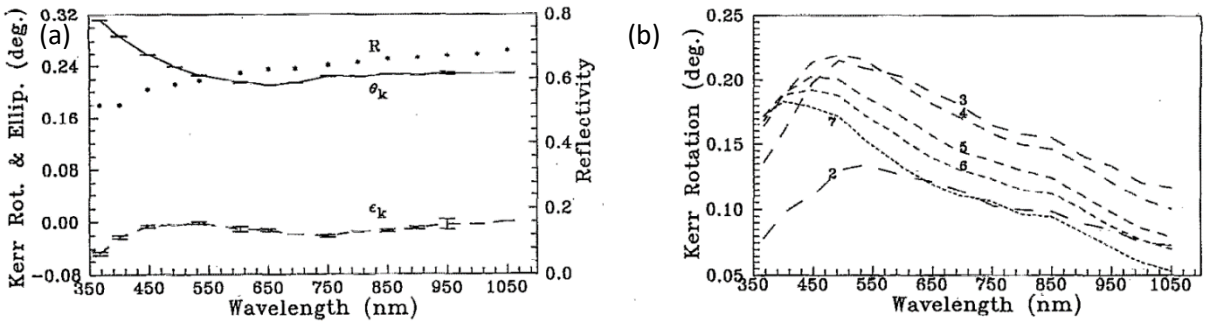

Figure 3.23: Wavelength dependence of Kerr rotation θ_K of (a) Co/Pt and (b) Co/Pd superlattices. Figures adapted from ref [176]

sample holder for high-frequency measurements. The sample stage was designed to allow rotation as well as motorized movements.

In order to use this optical setup for performing current-induced domain wall dynamics and switching experiments, we need to be able to inject electrical pulses. As shown in Figure 3.24, we use a delay generator to trigger a high-frequency pulse generator, which in turn injects a train of sub-nanosecond pulses into the sample with a 50Ω resistor in parallel for impedance matching. This electrical set up for the high-frequency pulse measurements allows us to apply up to 70V pulses with < 1ns pulse width and a maximum repetition rate of 1MHz. The electromagnets are powered directly via KEPCO power supplies and controlled using National Instruments (NI) DAQ PCIe card. The electromagnets and electrical components can be user run/controlled using a custom built Labview software. The completed setup is shown in Figure 3.25.

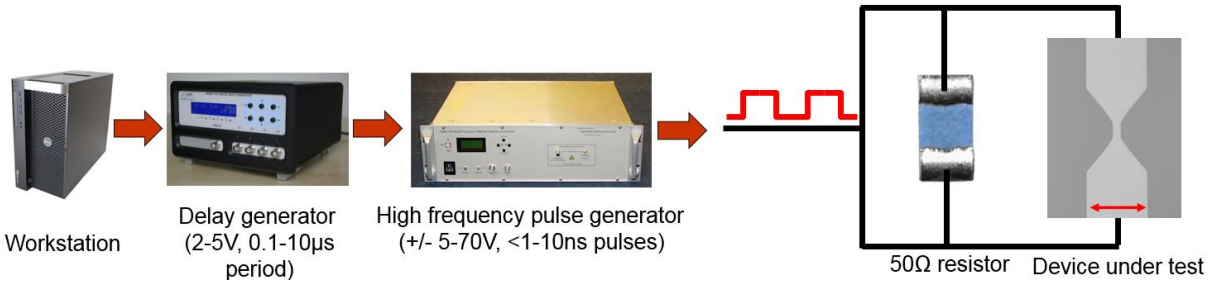

Figure 3.24: Electrical setup used to inject sub-nanosecond current pulses into the sample.

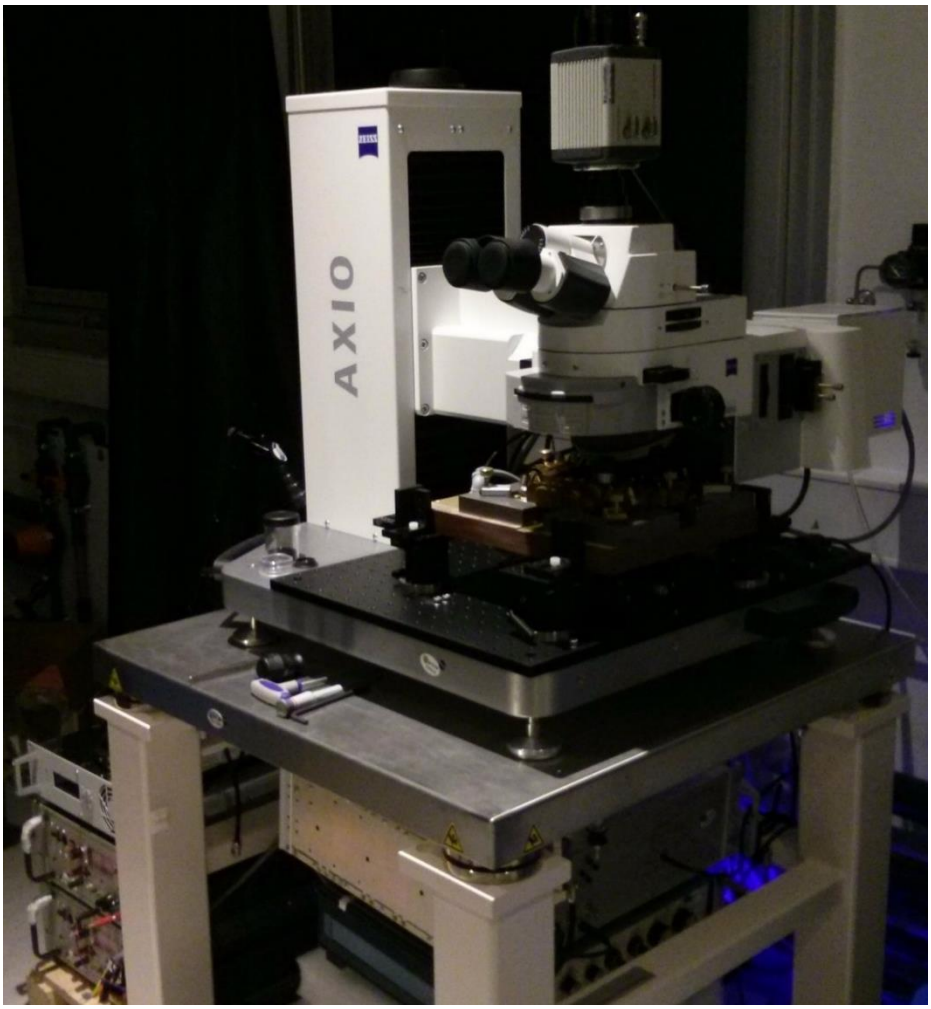

Figure 3.25: Photograph of the in-plane MOKE set up along with the electrical components.

3.2.3 Experimental studies using the in-plane MOKE microscope

In order to test the performance of our microscope, we performed quick measurements on in-plane samples. We worked on two samples primarily, Ta(3)/Cu(1)/$Co_{60}Fe_{20}B_{20}$(2)/Pt(2) and Ta(3)/Cu(1)/Co(2)/Pt(2) hereby referred to as sample 1 and 2 respectively. The light intensity captured by the CMOS camera can be averaged to perform in-plane hysteresis of the samples, similar to MOKE magnetometry. Figure 3.26 (a) shows the in-plane hysteresis of sample 1 with a switching field around 1.3 mT. This is seen in the MOKE imaging of Figure 3.26 (b), which shows the field switching of sample 1. These are differential images, which consists of the difference between before and after (applying the current/field pulse) images. The white and black contrast denotes the switching between the magnetization along the up and down directions respectively, along the applied external field. We can also switch the magnetization using current pulses. This is shown in Figure 3.26 (c). Here, 5000 pulses of 35V amplitude and 20ns width were applied to Hall cross devices patterned from sample 2. The magnetization switches depending on the direction of current denoted by the blue arrow. We can also use current pulses to move a domain wall as shown in Figure 3.26 (d). Here a domain wall is stabilized in the bridge section using field pulses. The yellow arrows denote the magnetization of the respective domains on left and right. By applying a current pulse, we can displace this domain wall in the direction denoted by x. Being differential images, these show only the contrast corresponding to the

displacement of the domain wall. Hence in the image on the left, the up domain moves to the right resulting in white contrast and in the image on the left, the down domain moves to the right resulting in black contrast. The direction of the domain wall motion is determined by the direction of the applied current pulses. Here, 10 pulses of 50V amplitude and 10nm duration were applied. With a sample resistance of 1.1KΩ, this corresponds to 45mA pulses. Multiple pulses were applied instead of one continuous one in order to reduce the effect of heating. Although the switching and the domain wall motion are consistent with the SOT model, we have not decoupled the contributions from the Oersted field and thermal effects.

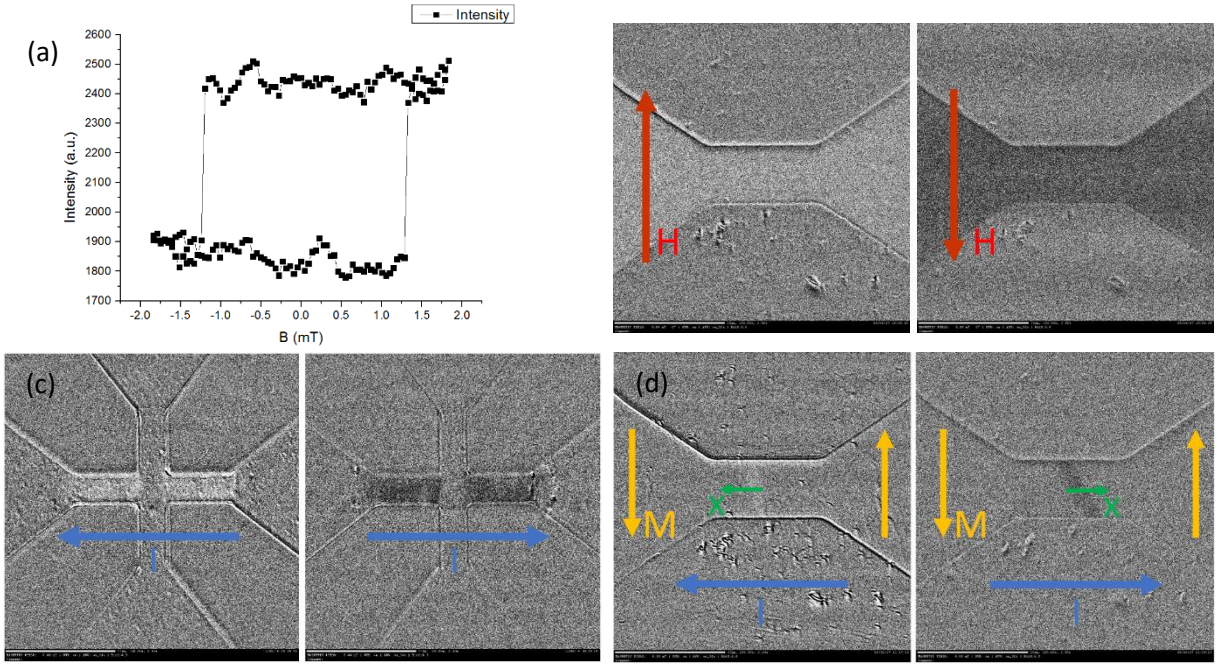

Figure 3.26: Examples of MOKE studies on in-plane magnetized samples. (a) Hysteresis loop (b) field switching (d) current induced domain wall motion in Ta (3)/Cu(1)/$Co_{60}Fe_{20}B_{20}$(2)/Pt(2). (c) Current induced switching of Ta (3)/Cu(1)/Co(2)/Pt(2).

3.3 Sample Deposition, Characterization, and Lithography

This section details the magnetron sputtering of our samples, the subsequent material characterizations, as well as the nano and microlithography techniques that we employed to fabricate our samples.

3.3.1 Magnetron sputtering

The samples used in this work were deposited at SPINTEC using a magnetron sputtering system from Actemium (now VINCI technologies) unless otherwise specified. This multi-chamber deposition system has 12 targets and is compatible with wafers up to 100mm in diameter. Magnetron sputtering is a type of Physical Vapor Deposition (PVD) method of depositing thin films. Here argon ions are bombarded onto a target causing the material to be sputtered off and condense onto the substrate. The magnetic field is used to increase the density of the plasma near the surface of the target. Although this setup

is capable of both Direct Current (DC) and Radio Frequency (RF) sputtering, our depositions are primarily performed using a DC current to generate the plasma as we work mostly with metallic thin films. In the case of MgO deposition, we deposit metallic Mg layer followed by an oxidation step. The oxidation is performed in an adjacent oxidation chamber so as to not contaminate the deposition chamber with oxygen. The setup has a base pressure of 8e-6 Pa which we reach using a cryogenic pump and we maintain an argon pressure of 0.2 Pa. The argon gas pressure along with the applied current determines the ion density. We run the system in constant current mode so as to keep the Ar ion density and thereby the deposition rate constant. Our setup doesn't use a quartz system to monitor the deposition thickness as our 12 targets do not converge to single location. Instead, depending on the target, the substrate holder is moved to the relevant position. Thus, the thickness of the film is determined by the time of deposition which is calibrated using calibration samples with thickness determined using X-ray reflectivity technique. The quality of the film depends on the working and base pressure, quality of target, deposition rate, wetting of the substrate, etc.

As our substrate holder can be moved, we can achieve two types of deposition, namely "on-axis" and "off-axis" deposition, illustrated in Figure 3.27 (a) and (b) respectively. In the case of on-axis deposition, the target and the substrate axes are aligned resulting in a uniform film deposition. The substrate is rotated during this deposition at 100 rpm to increase the film uniformity. The setup is also capable of heating the sample as well as applying a small magnetic field of around 2mT in the plane of the sample. However, we do not utilize these features during our depositions.

We can also obtain a wedge deposition by displacing the substrate. In practice, the substrate is displaced by 100 mm. This is known as "off-axis" deposition and allows us to have a film thickness gradient across the wafer. In this case, the sample is not rotated around its axis.

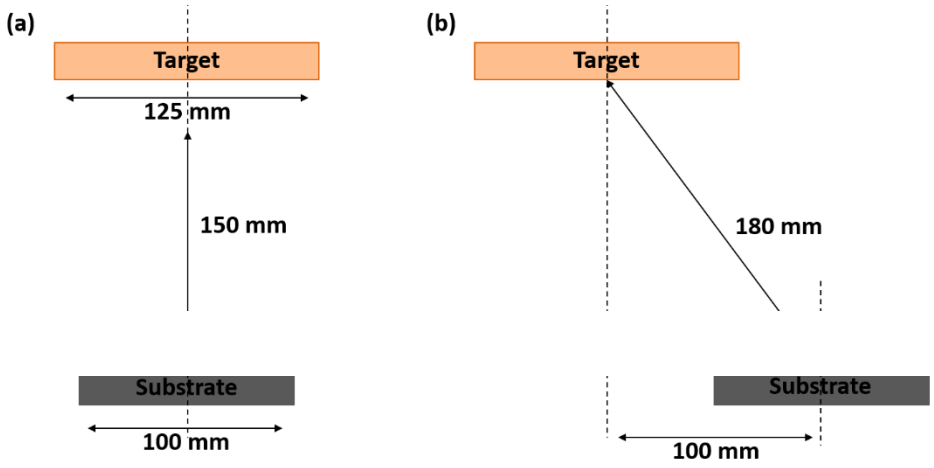

Figure 3.27: (a) On-axis deposition and (b) Off-axis deposition.

3.3.2 Determination of film thickness

It is necessary to accurately determine the film thickness in order to understand the mechanism of oxidation and SOTs detailed in the next chapter. Although in the case of on-axis deposition, the thickness is pre-calibrated, it is not so for off-axis depositions. It is hence necessary to calibrate the thickness of the sample with respect to the position of the wafer. Figure 3.28 (a) and (b) shows respectively the wafer level resistance maps of an on-axis and an off-axis Pt wafer of 4.5 nm nominal thickness. The nominal thickness refers to the on-axis thickness value. These resistance maps were measured using an automatic resistance mapper from CAPRES (now part of KLA), which utilizes 4-point

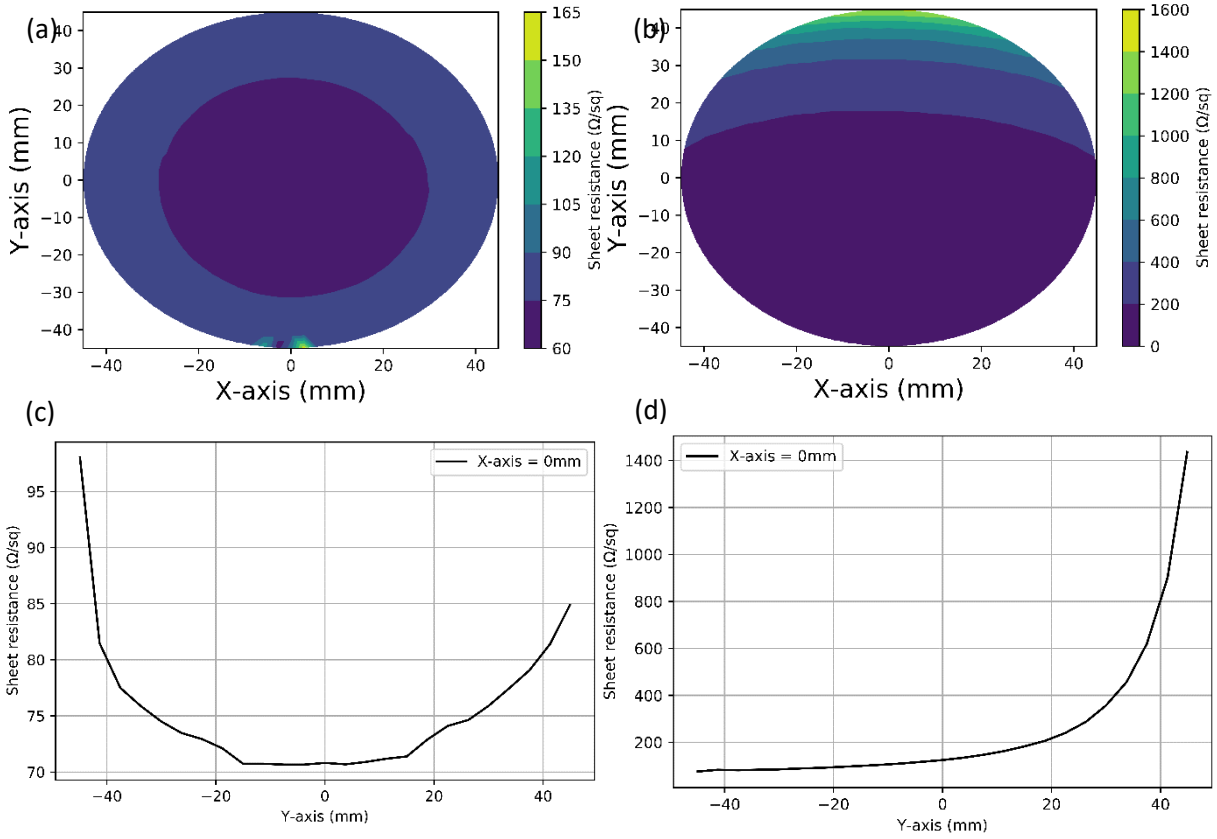

Figure 3.28: Wafer level resistance maps of (a) on-axis and (b) off-axis deposited Pt 4.5 nm wafers. (c) and (d) resistance plots along the x=0 line of these maps.

resistance measurement technique. The colors correspond to the sheet resistance. The main wafer flat is located at the bottom of the image. Figure 3.28 (c) and (d) plots the sheet resistance along the x=0 line on these wafers, which is parallel to the lateral displacement axis and is also perpendicular to the main flat of the wafer. As it can be seen, in both cases, there is a parabolic curvature of the deposited film thickness, originating purely from the geometry of deposition. Moreover, in case of the off-axis sample, a gradient is present in the resistance values and hence in the film thickness along this axis.

We traditionally determined the film thickness using on-axis calibration samples which were grown on silicon strips in order to determine the dependence of thickness on film conductance, as plotted in Figure 3.29. In this method, we can determine the film thickness from the deposition rate, which is already calibrated. By measuring the sample resistance using 4-point resistance method, we can obtain the dependence of the film conductance on the film thickness. We can then use this dependence to determine the film thickness of our measurement samples.

However, the samples we use for our experiments are sputter deposited on a 100 mm wafer. We noticed that the platinum growth on a silicon strip compared to that of a 100 mm wafer is slightly different, resulting in different conductance values. Hence comparing our experimental samples with our original calibration samples would be inaccurate. To overcome this, we decided to deposit and calibrate platinum thickness using 100 mm wafers. We did this by depositing three samples on-axis, which gives us access to the conductance of the nominal on-axis thickness of platinum. And three samples off-axis, which provides us with three wedges of different thicknesses. Normally, in the case of on-axis depositions, the wafer stage is rotated to obtain a uniform growth. However, in this case, the wafer stage is kept stationary so as to correlate with our off-axis samples, which are grown without rotation. The conductance as a function of the deposition position of these samples is shown in Figure

3.30 (a). Here, the three colors correspond to the three different on-axis thicknesses of samples. The conductance was measured using the automatic resistance mapper. The flat edge of the off-axis wafer is considered the origin of the x-axis, such that the deposition axis is at -50.75 mm. Hence, the three curves towards the left side of the Figure 3.30 (a) correspond to the three on-axis samples and the three curves to the right correspond to the three off-axis samples. The sharp tails to the left of these curves are due to the wafer name being etched along the flat of the wafer, changing the conductance.

Each value of the conductance in this plot corresponds to a unique platinum thickness. Hence, the determination of the platinum thickness corresponding to the sample translation during deposition now turns into an optimization problem. We need to find a function, which will cause the three off-axis curves on the right hand side of the plot in Figure 3.30 (a) to overlap as each conductance value corresponds to a unique thickness of platinum. The resulting fitting function is then used to plot the dependence of the conductance on the platinum thickness, as shown in Figure 3.30 (b).

As shown, all three curves overlap, indicating that each conductance value corresponds to a unique platinum thickness. By determining the fitting function for platinum thickness using this method, we can avoid potential errors arising from the variation of resistivity with thickness, the variation of off-axis growth at different thicknesses, etc.

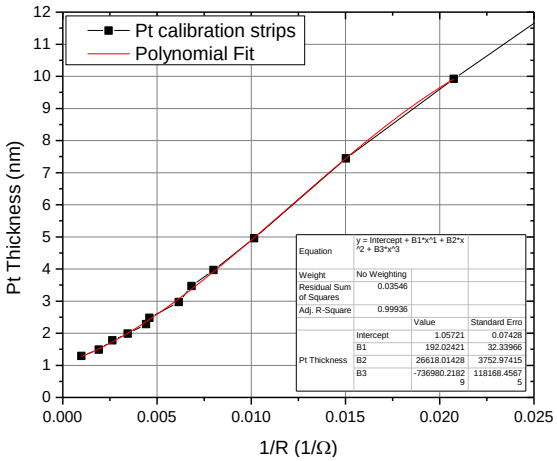

Figure 3.29: Dependence of Pt thickness on conductance, based on calibration strips.

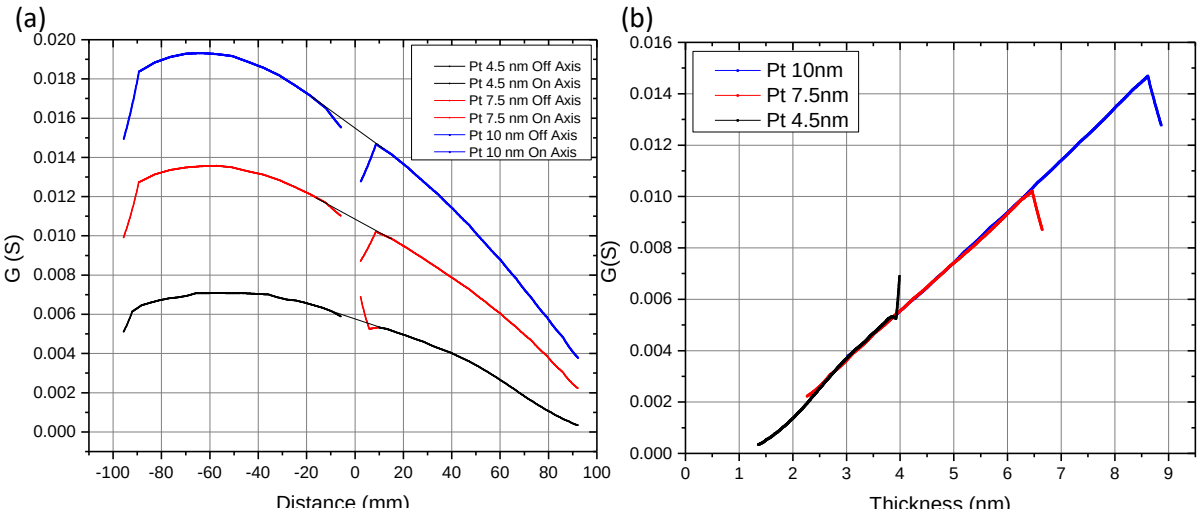

Figure 3.30: (a) Conductance of Pt calibration samples with respect to position on wafer. (b) Dependence of conductance on the thickness of platinum determined via optimization method.

Moreover, it is vital that the sample thickness is calibrated on a regular basis since the deposition rate decreases with time as the distance between the substrate and the target increases.

3.3.3 Magnetic film characterization

The magnetic properties of the ferromagnetic film will determine the response of it to the SOTs generated by the applied current. Energetically, it is easy to understand that keeping the number of spins acting on the FM constant, the torques generated and measured will depend inversely on the magnetic moment per unit area. Hence it is vital to determine the magnetic properties of the thin films deposited by our sputtering system. We do so using a Vibrating Sample Magnetometer (VSM) from Microsense (now part of KLA). A VSM consists of electromagnets which uniformly magnetize the sample and a piezoelectric material which vibrates the sample. It then utilizes pick up coils to measure the induced voltage, which is proportional to the magnetic moment.

VSMs are calibrated using calibration samples provided by the supplier. These are circular in shape. And the square samples generally used can be approximated to have a similar dipolar field as these calibration samples. Our samples, on the other hand, are rectangular in shape with a ratio of length to width equal to 4.33. Hence the dipolar fields of our samples could distort the measured magnetic moment values. To overcome this issue, we fabricated our own rectangular calibration sample of Co(65.8)/Al(2). The film thickness was measured using X-ray reflectivity measurements. All the VSM measurements in this work are calibrated to this sample.

We consider two sets of samples in this sub-section, Co(x)/Al(2) and Ta(3)/Cu(2)/Co(x)/Pt(3). Here x refers to the varying thickness of the cobalt layer in nanometers. The saturation magnetization of these samples is plotted in Figure 3.31 (a) and (b) respectively. It is quite clear from these plots that the intermixing and roughness of the FM layer is smaller in the case of Ta(3)/Cu(2)/Co(x)/Pt(3). This is because tantalum is a good seed layer and allows better growth of films with smaller roughness above it. This prevents the sharper drop in the Ms values at lower cobalt thickness, as seen in Co(x)/Al(2). We can determine the dead layer thickness and the average Ms by plotting Ms*t as a function of film thickness. This is plotted in Figure 3.31 (c) and (d) for the two sets of samples respectively. The dead layer, which is due to intermixing between FM and the layers above and below, is larger in the case of Co(x)/Al(2). The average Ms, given by the slope of these curves, is fairly even between the two sets of samples. By considering the difference in area between the hard axis and the easy axis MH loops, we can determine the effective anisotropy of the sample. From the thickness dependence plot of this anisotropy, we can separate out the interfacial and volume anisotropies as shown in Figure 3.31 (e) and (f). As expected, the second sample set has a higher interfacial anisotropy due to the capping with platinum. Hence, the magnetic properties of our FM films are qualitatively and quantitatively consistent to ones reported in literature.

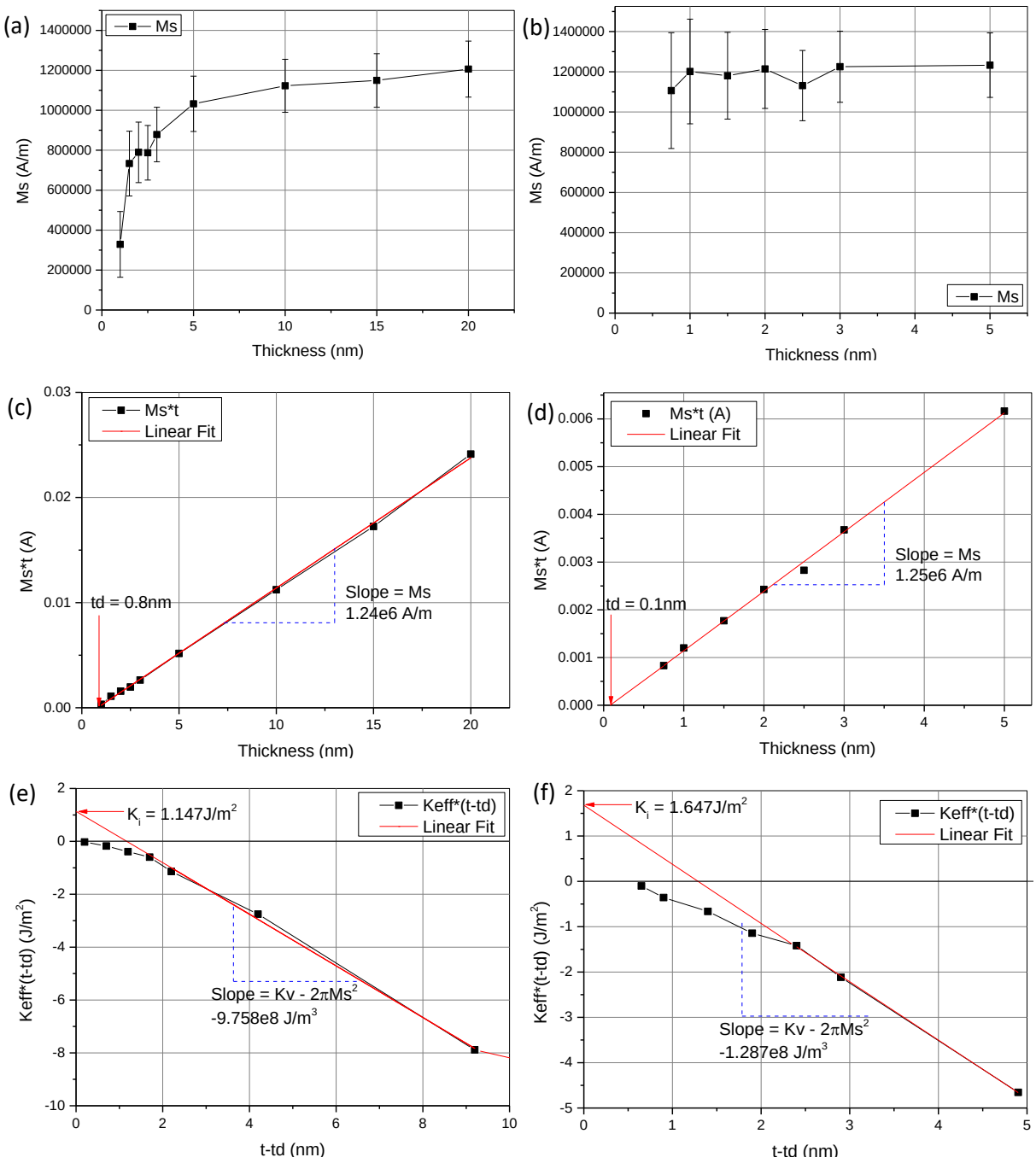

Figure 3.31: (a),(b) Saturation magnetization, (c), (d) extraction of dead layer thickness and average Ms and (e), (f) extraction of interfacial and volume anisotropies of Co(x)/Al(2) and Ta(3)/Cu(2)/Co(x)/Pt(3) respectively.

3.3.4 Device fabrication

In order to perform electrical measurements, it is necessary to pattern thin films into micro and nanoscale devices. Traditionally we used to use e-beam lithography to fabricate our devices, which was time-consuming and expensive. In order to be able to process more wafers, we decided to pattern the devices for 2nd harmonic torque measurements and studying domain wall dynamics using photolithography.

For this purpose, we designed Ultra-Violet (UV) lithography masks and had them fabricated by Compugraphics. These masks were patterned on sapphire substrates so as to be compatible with Deep UV lithography. Moreover, they were MPT coated to reduce the adhesion of photoresist or residue on the masks. Our mask set for 100 mm wafers consists of 3 levels. The first is for markers for alignment with subsequent photolithography or E-Beam Lithography (EBL) steps. It also includes the numbering for the devices. The second layer consists of Hall cross devices and two terminal domain wall devices. The third layer consists of contact pads, which are used to deposit a gold layer on the contacts to make the wire bonding easier as well as to reduce the device resistance if needed. There are close to 24000 devices on this mask set and are closely packed and covers a significant portion of the total surface area. This allows us greater flexibility in measuring devices at any point on the wafer surface. The complete gds design, as well as the chip design, are shown in Figure 3.32.

In order to be able to fabricate the devices, it is necessary to develop the process recipe. The first recipe we developed is fairly straightforward using a single UV photoresist, AZ 1512HS. UV lithography uses UV light to expose the photoresist. The process flow of this recipe is illustrated in Figure 3.33 and the recipe is as follows:

- Spin coat AZ 1512HS, which is a positive thin resist from MicroChemicals GmbH, on to the wafer at 4000 rpm, 2000 rpm/s for 60 seconds. We generally use thermalized silicon [100] wafers. Use of [100] wafers allows easier cleavage while the 0.5/1 µm thick SiO_2 layer prevents electrical shorts. The wafer is then soft-baked at 100 °C for 90s to obtain a resist thickness of around 1.2 µm. Ensure the wafer is sufficiently cooled for around 10 minutes.
- The resist is exposed for 25s after a 10s hard contact with the mask. We use an MJB4 mask aligner from SUSS MicroTec. The resist is then developed for 30s using a 1:1 solution of AZ Developer from MicroChemicals and DI water. The developer is then removed by rinsing in DI water for 5 min. AZ 1512HS being a positive resist, the exposed areas get washed away by the developer whereas the unexposed regions over the devices remain.
- Perform Ion Beam Etching (IBE) to etch the exposed areas down to the substrate. IBE is a dry plasma etch method which utilizes inert Argon ions to bombard the etch region. This is a purely physical etch process. Although we use a standard etch recipe for our micron-scale devices, for nano-pillars, etc., the etch profile can be tuned by the etch angle and power. Additionally, we need to be careful about re-deposition of etched material onto the nano/micro-structures.

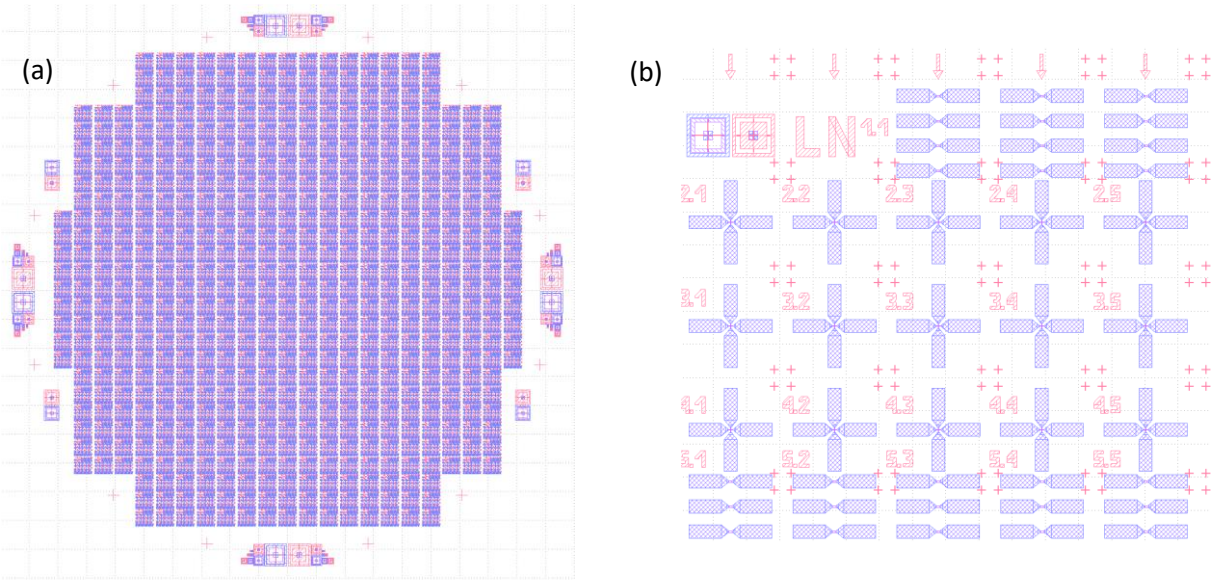

Figure 3.32: (a) Wafer level gds design. (b) Chip level gds design.

We use either an MU400 from Plassys or an SCIA Mill 150 from SCIA Systems to perform the IBE. We also have access to a Secondary Ion Mass Spectrometer (SIMS) to determine the etch stop. However, this is not critical as longer etch times will just lead to etching into the Si/SiO_2 substrate.

- The IBE etch can burn the top resist layer, making it harder to strip. It can be somewhat overcome by etching the top resist layer in an oxygen plasma for 3 minutes. For this purpose, we utilize the Inductively Coupled Plasma - Reactive Ion Etching (ICP-RIE) technique with oxygen-argon plasma. The argon is used to reduce the etch rate. It also adds to the physical etching process. We use flow rates of 5 sccm for oxygen and 20 sccm for argon. It is to be noted that for electrical measurements where we wire bond the sample, the residual resist is not an issue and this step can be considered optional.
- Strip resist with acetone. Generally, the sample is kept overnight in acetone and then rinsed with Iso-Propyl Alcohol (IPA). The stripping can be accelerated using an ultrasonicator.

Although this recipe works well for devices used for electrical measurements, as mentioned earlier, the devices can have residual material left on them once the resist gets burned during the IBE step as shown in Figure 3.34. It is even worse in case of samples with a capping layer of alumina, where we have noticed that the resist tends to adhere to the top layer and is extremely difficult to remove. Such a residual cover makes this recipe unsuitable for optical studies.

In order to have a clean top surface on the devices, it is necessary to shield the top surface from the AZ series of resists. To do this we developed a new recipe consisting of dual resists. The process flow is illustrated in Figure 3.35 and the recipe is as follows:

- Spin coat Poly(Methyl MethaAcrylate) (PMMA) 2% on the wafer at 5000 rpm, 2000 rpm/s for 60 seconds. It is then soft-baked at 130°C for 5 minutes. The temperature is set much lower

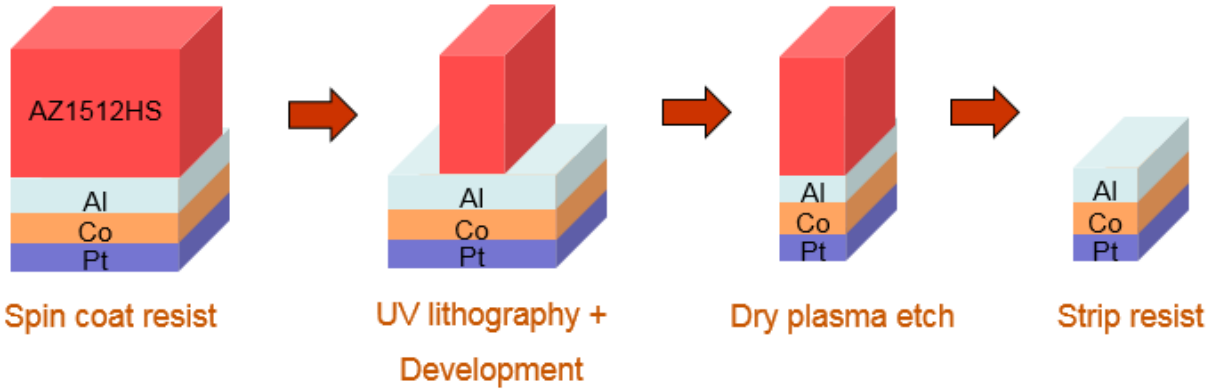

Figure 3.33: Single resist microlithography process flow.

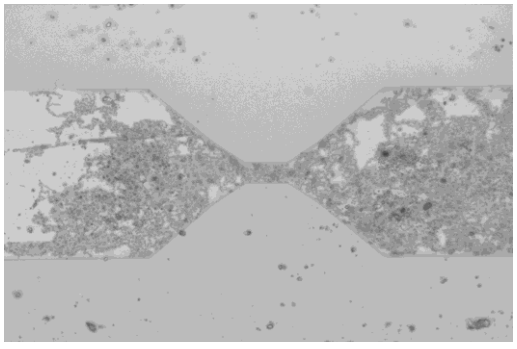

Figure 3.34: Residual resist on a device with a capping layer of alumina.

than the recommended value so as to not cause any thermal diffusion in our material stacks during the soft bake. We typically have a resist thickness of around 90 nm.

- Once the wafer is sufficiently cool after about 10 minutes, the UV resist AZ 1512 HS is spun coat at 4000 rpm, 2000 rpm/s for 60 seconds. It is then soft-baked at 100 °C for 90s to obtain a resist thickness of 1.2 µm as before. It is vital to cool down the wafer before this step to not intermix both the resists. Also, one needs to be careful when spin coating non-circular samples to avoid non-uniformity in resist thickness, especially around the edges. Such non-uniformity can lead to a bad contact with the UV mask resulting in bad exposure.
- The wafer is then exposed for 25s after a 10s hard contact with the mask. It is then developed for 30s using a 1:1 solution of AZ Developer and DI water. The developer is then removed by rinsing in DI water for 5 min to obtain a UV resist coverage on top of the areas intended for devices. The PMMA still has complete coverage across the sample.
- In order to remove the PMMA layer, we perform a soft oxygen plasma etch using the RIE for 3 minutes. We use a mixture of oxygen (5 sccm) and argon (20 sccm) gases to reduce the etch rate. We can determine the etch stop using laser reflectometry. Even though this RIE step can slightly oxidize the material stack, it would be limited to the areas outside the device and shouldn't affect our measurements.
- Now that the areas to be etched are not covered with PMMA, we can perform dry etch using the IBE. We needn't concern regarding the top burnt layer of resist since the PMMA layer ensures that the AZ 1512 HS resist will be easily removed.
- Strip both the resists using acetone. This step can be performed by placing the sample upside-down on a watch glass in the beaker containing the acetone. This will ensure that any residue will fall down onto the watch glass instead of settling back onto the sample. After a few hours, the sample is removed from the actone while simultaneously being rinsed with acetone to wash away any residue picked up from the top surface of the liquid. It is then transferred into another beaker with fresh acetone. Use ultrasonication if needed. It is then transferred to a beaker containing IPA, rinsed and ultrasonicated. The sample is ready after drying it with nitrogen gas.

This recipe can be used to fabricate clean micron-scale samples as shown in Figure 3.36. Figure 3.36 (a) and (b) shows the optical micrograph of the Hall cross and the domain wall bus respectively while Figure 3.36 (c) shows the Scanning Electron Microscopy (SEM) image of the Hall cross. It can be noticed that there is small shadowing and/or re-deposition from the IBE step. The use of PMMA not only leads to clean samples but also allows us flexibility in terms of various process parameters such as UV exposure time etc.

In case we need alignment markers or device numbering, we perform additional steps prior to the sample fabrication detailed previously. These additional steps are:

- Spin coat PMMA 2% and soft bake as before.
- After cooling, spin coat AZ 5214 at 4000 rpm, 2000 rpm/s for 60 seconds. It is then soft-baked at 100 °C for 120s to obtain a resist thickness of 1.4 µm. AZ 5214 is an image reversal resist, i.e. it can act as a positive or negative resist depending on exposure.
- Perform a normal exposure of 5.5s using the UV mask for the marker level and then perform a post bake at 120°C for 120s.

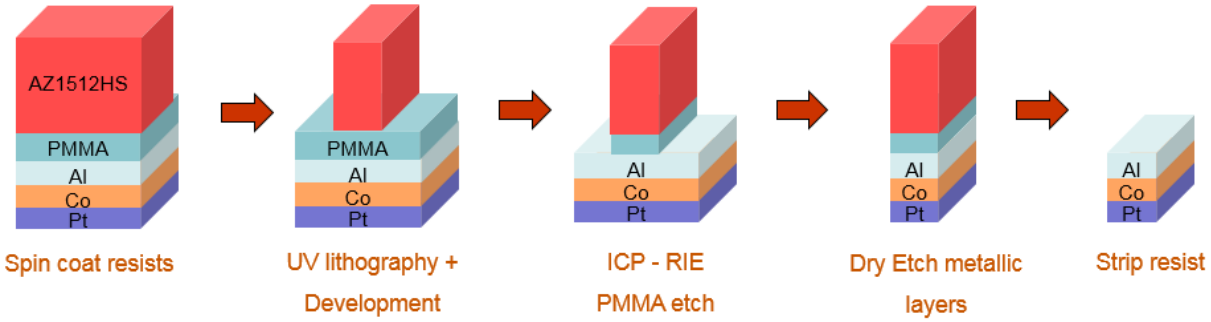

Figure 3.35: Dual resist microlithography process flow.

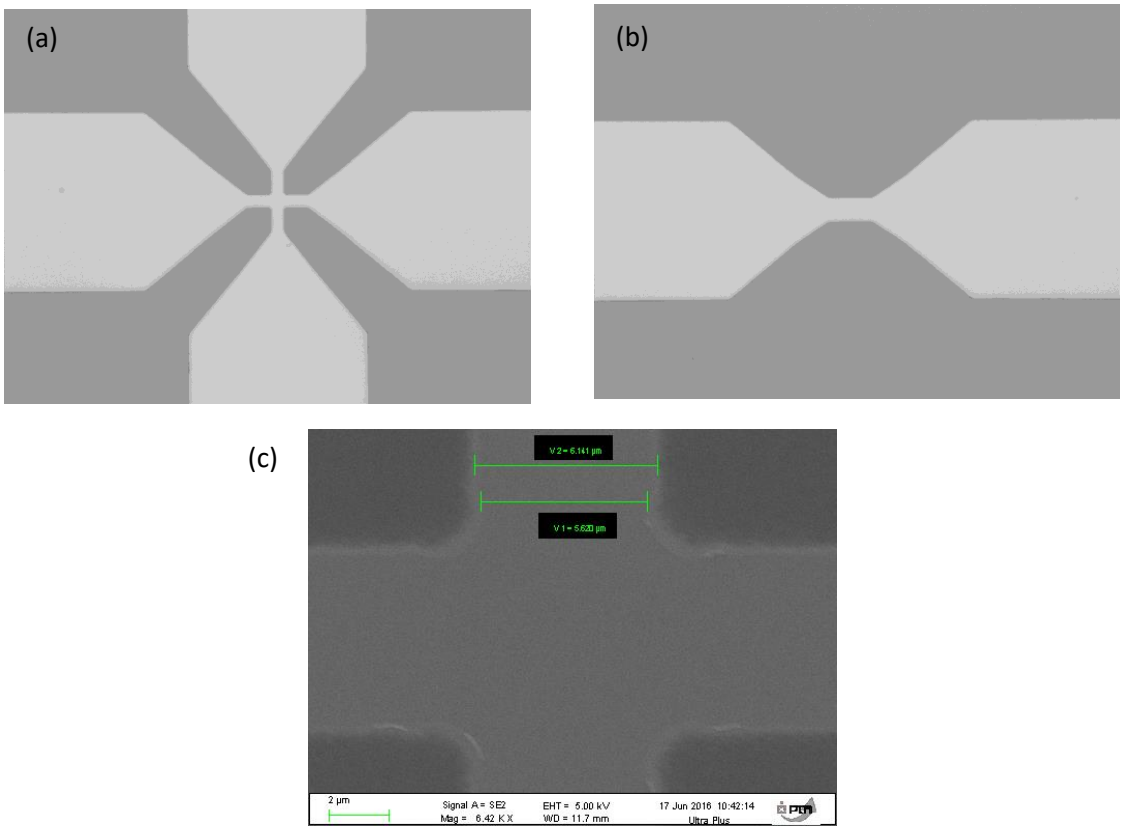

Figure 3.36: Optical micrographs of (a) Hall cross device and (b) domain wall bus. (c) SEM image of Hall cross.

- In order to obtain the effect of a negative resist, we need to further perform a flood exposure, which is a UV exposure without a mask, for 33s. It is then developed for 40s using a 1:1 solution of AZ Developer and DI water. The developer is then removed by rinsing in DI water for 5 min. After development, the unexposed areas corresponding to the markers and numbers will be washed away, exposing the PMMA underneath.
- Perform a soft oxygen RIE for 3 minutes to etch away the PMMA layer protecting the sample in the areas of the markers and number.

- We can now deposit materials for the markers and numbers. We use e-beam evaporator for this performing this step. An e-beam evaporator is a type of PVD which uses an electron beam to evaporate the target material which then condenses on to the sample surface. In order to have good adhesion, we first deposit a thin layer of titanium of 10 nm. This is followed by a thin layer of gold of 60 nm which should be sufficient for obtaining a good contrast optically or in the e-beam lithography system. We further deposit a 20nm of Ti if there is a subsequent IBE step to protect the Au layer.
- The sample is then left in acetone overnight for the lift-off process. It is then ultrasonicated and cleaned to obtain the completed wafer.

Once the markers are deposited, it can be used to perform e-beam lithography (EBL) alignment. EBL uses an electron beam to expose the resist instead of UV light. This allows for nanoscale feature size, however, is slower as the exposure is done via a raster scan method. We use this method in case we need devices with a non-standard design or if we need to pattern nano-shapes on the FM layer of the already fabricated micron-scale devices. We generally prefer using a hard mask for patterning nanostructures on the FM layer of the stack[51]. In this case, we can use a positive resist such as PMMA or ZEP 520A. Here we detail the process using the latter:

- Spin coat ZEP 520A resist at 4000 rpm, 2000 rpm/s for 60 seconds. It is then soft-baked at 180 °C for 5min. We generally obtain a uniform 360 nm thick resist coverage. Depending on the substrate it may be necessary to use an adhesion promoter. In this case, we spin coat HDMS or Dupont VM652 at 4000 rpm, 2000 rpm/s for 60 seconds prior to the EBL resist.
- Perform EBL (a dose of 480$\mu C.cm^2$ for 100KV accelerating voltage). Develop for 60s using [1:1] Methyl IsoButyl Ketone (MIBK): IPA solution and then a further 20s using [89:1] MIBK:IPA solution.
- Use e-beam evaporation to deposit 25 nm of Ti. This Ti layer forms the hard mask for our samples. We also deposit a test sample with 4 nm Cr and 20 nm Ti. This determines our etch stop. The actual thickness of the Ti layer depends on the stack and the layers that need to be etched in the subsequent step.
- Perform lift-off by leaving the sample in acetone for a certain duration after which it is ultrasonicated and rinsed with IPA before drying with nitrogen.
- The exposed areas on the sample are then etched using the IBE. We use the Cr etch stop marker to make sure that the pattern is protected by a thin layer of Ti.
- In case of nano-patterning the FM layer of samples such as Pt/Co/AlOx, once the nano-pattern is protected by Ti, we can wet etch the AlOx layer down to the Co layer. For this purpose, we use the AZ 326 MIF developer which contains TetraMethyl Ammonium Hydroxide (TMAH), which is an Al etchant. The sample is etched for 30s using this etchant.
- Once the AlOx capping is removed, the FM is in direct contact with air oxidizing it. If needed, we can perform a soft oxygen plasma etch to make sure the FM is completely oxidized outside the nanostructure. This ensures that we have an HM under-layer which is electrically conductive whereas the FM layer is conductive and magnetic only underneath the nano-patterned structure at room temperature.

We also have the capability to perform laser lithography. In this case, we can use standard UV photoresists and recipes. However, the dose rate and the development time needs to be calculated depending on the reflectivity of the sample. These techniques mentioned in this subsection ensures that we are fully capable of fabricating samples for the studies mentioned in this work.

This chapter detailed the sample deposition and fabrication as well as the experimental techniques utilized in this work. The UV lithography enables us to quickly fabricate devices whereas the e-beam allows us nanometer resolution. The laser allows us flexibility in terms of device design. The 2nd harmonic torque measurement technique detailed here is a powerful technique to extract torques acting on a FM. It can be adapted to various other scenarios where the driving force is not SOTs, but polarized light, strain, etc. The MOKE microscope is a powerful and versatile tool for quick sample verification as well as detailed switching and domain wall studies. This too can be adapted to various other scenarios such as studying magneto-optics, magneto-plasmonics, etc. The studies detailed in this work are not limited to the techniques mentioned here. Instead, various other experimental techniques were needed in this work and are detailed as and when needed.

Chapter 4 Mechanism of SOTs in Platinum Oxide Systems

In SOT-MRAM, a current injected into a HM layer generates SOTs which act on the FM layer in order to switch its magnetization. In case of both the STT-MRAM and SOT-MRAM, the current injection into the device is controlled by a Complementary Metal-Oxide-Semiconductor (CMOS) switching transistor as shown in Figure 4.1 (a) and (b) respectively. A TEM cross-sectional micrograph of an integrated MTJ-CMOS stack is shown in Figure 4.1 (c). The MTJ, being compatible with the CMOS Back End of Line (BEOL), is patterned at the metallization layer, M5 in this case. A cartoon of this image is illustrated in Figure 4.1 (d). The size of the MTJ is generally much smaller than that of the CMOS switching transistor, which is underneath the M1 level, fabricated in the silicon wafer. The size of this transistor is defined by the switching current needed by the MTJ. Hence, the smaller the current, smaller the size of the switching transistor and the more densely packed the memory can be. The switching current also determines the write energy needed to write the information in a single memory cell. Hence, it is vital to reduce the current needed to switch the MTJ magnetization.

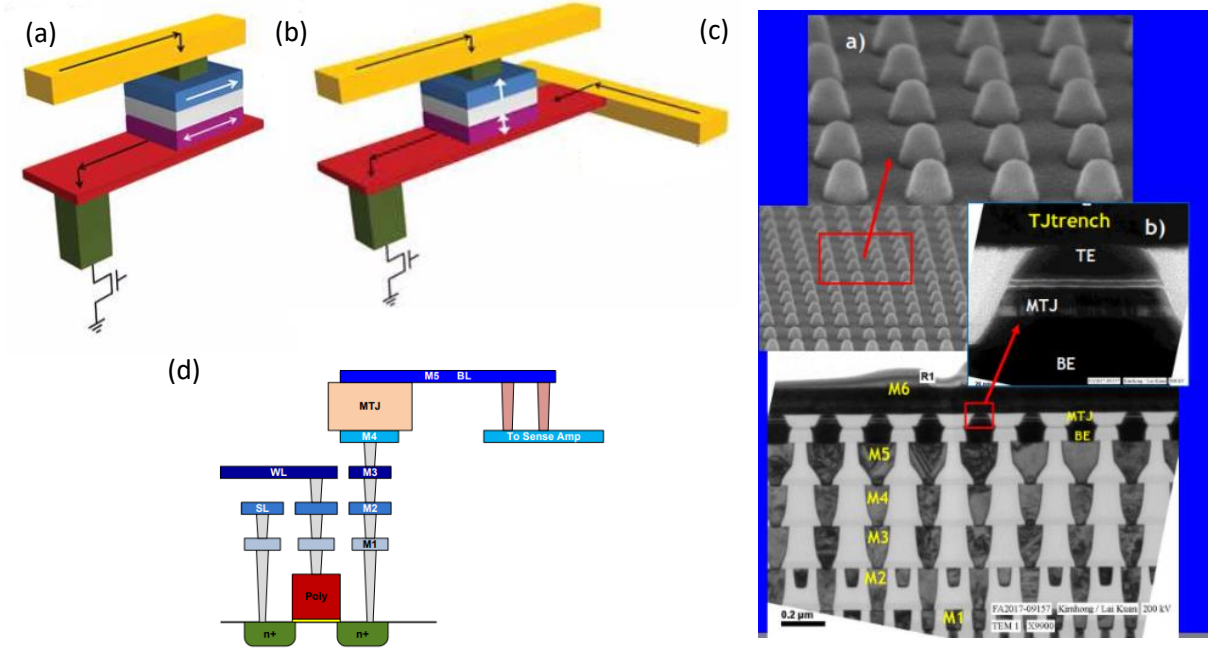

Figure 4.1: Schematics of (a) STT-MRAM and (B) SOT-MRAM indicating the switching CMOS transistor. Images obtained from SPINTEC. (c) TEM cross section of an MTJ integrated in a CMOS chip showing the different metallization levels. Image adapted from[177]. (d) Schematics of a CMOS integrated MTJ, adpated from ref.[178].

The switching current can be reduced by enhancing the strength of SOTs generated by per unit current. In a metallic, ferromagnetic system, there are different means to achieve this based on engineering the materials chosen for the different layers and the structure of the stack of the MTJ. One is by using transition metals[24] in the NM layer such as Pt[1,27,57], Pd[58,59], Ta[2,60,61], W[62–64], Hf[65,66], etc. or rare earth materials such as Gd[67], etc., where the strong SOC leads to a strong Berry curvature and hence the increase in torques. One can also increase the strength of SOTs by increasing the resistivity of the NM layer. This can be achieved either by using a more resistive phase of the metal such as the beta- phase of Ta[2], W[62] or by engineering the resistivity of the NM during growth[68,69]. This increase in SOTs has been attributed to interfacial effects[70] as well as enhanced scattering. The large SOC and resistivity also play a role in metallic alloys and doped NM layers, achieving the same result[71–73]. As the interface plays a large role in these devices, the interface can be modified by ultra-thin insertion layers to increase the SOTs[64,74–76]. The interfacial transparency and the electric profile across the interfaces also plays a role in the selection of the FM[77] and the oxide capping layer[66]. One can further employ structures where the FM is sandwiched between NMs with opposite SHA[78–80] or where the HM/FM is capped with a spin sink such as Ru[81] or Ir[80] to effectively increase the SOTs by reducing the spin reflection at that interface. Another route to enhance the SOTs is via oxidation.

4.1 Oxidation and Spin-Orbit Torques

Oxygen present at the interface between a transition metal and an oxide can result in interfacial Perpendicular Magnetic Anisotropy (PMA)[82]. This has been widely studied in Pt/CoFeB/MOx[83,84] and Pt/Co/MOx[85–87] systems at SPINTEC, where MOx stands for various metallic oxides. As detailed in Yang et. al.[88] and Manchon et. al.[86], in these systems, the 3*d* bands of the ferromagnet are responsible for both the magnetization and the anisotropy. As shown in Figure 4.2, for an Fe/MgO system, the broken symmetry at the interface leads to the crystal-field splitting of the 3*d* bands of the ferromagnet with the bands perpendicular to the plane (d_{xz}, d_{yz}, d_{z^2}) being different in energy than the bands in the plane of the film (d_{xy}, d_{x^2}-d_{y^2}). The energy difference between the bands and the band filling impacts the magnetic anisotropy of the ferromagnet. In the presence of oxygen at the interface, these 3d_{z^2} bands of the ferromagnet hybridize with the 2p_z bands of the oxygen resulting in a Bloch state with the majority Δ_1 symmetry around the Fermi energy level.

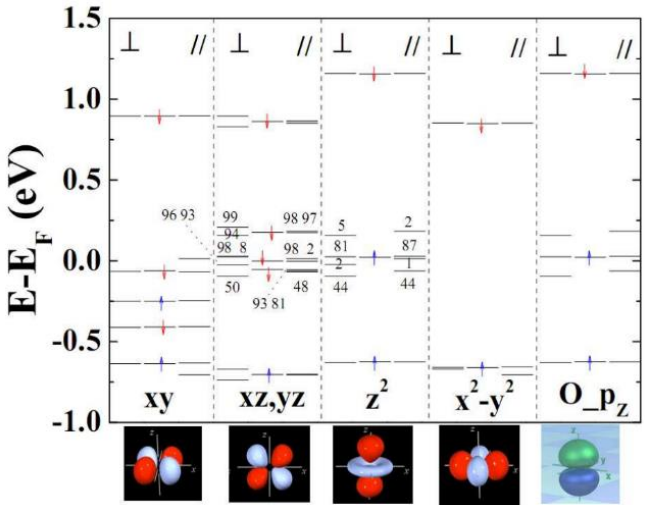

Figure 4.2: Wave function character at the Γ point of optimally oxidized Fe/MgO interface. The different columns correspond to the Fe 3*d* and the O 2*p* orbitals. The three sub-columns correspond to the perpendicular (left) and in-plane (right) orientation of magnetization and the case with no SOI (center). Adapted from Yang et. al.[88].

In the presence of SOI, these bands are further split around the Fermi level. This band splitting is asymmetric, with the out of the plane d_{xz} and d_{yz} being split stronger and lower in energy than their in-plane counterparts, which leads to an anisotropy that favors the perpendicular orientation. The PMA is further strengthened by the mixing of the $d_{xz,yz}$with the d_{z^2} and p_z bands, i.e majority Δ_1 and minority Δ_5 symmetries. The strength of this mixing and hence the PMA depends on the level of oxidation.

As the Bloch states are modulated by the oxidation conditions, the Tunneling Magneto- Resistance (TMR) and the PMA are correlated[84] and has been successfully employed in the realization of perpendicular MTJs for STT-MRAMs[89] since. It has also been successfully utilized to develop Voltage Controlled Magnetic Anisotropy (VCMA) based MRAMs, such as the Magneto-electric Random Access Memory (MeRAM)[90]. Here, by voltage gating, the occupancy of the orbitals at the interface can be modified allowing the control of the interfacial magnetic anisotropy[90–92]. The interfacial voltage difference between an FM and a MOx also lies at the heart of the Rashba effect. The interfacial Rashba effect can give rise to SOTs[17,93], which can be used for magnetization switching. Oxidation can also be used to break the lateral inversion symmetry of these SOT structures, enabling switching without the application of an external magnetic field[94]. As the degree of oxidation plays a role in the strength of the Rashba effect and the PMA, it could also play a role in the strength of the SOTs.

One of the first works on the effect of oxidation on SOTs is of Emori et. al.[95] who studied the effect of FM oxidation on SOTs in Pt/Co/GdOx multilayers. They oxidized the Co layer using voltage-controlled oxygen migration from the GdOx layer and observed a large increase in DL torques whereas the FL torques remained constant. They attributed this effect to the change in electronic potential at the Co/GdOx interface. Another work along the same line is by Qui et. al.[96] who studied the effect of FM oxidation on SOTs in Pt/CoFeB/MgO/SiO_2 multilayers. By varying the thickness of the SiO_2 capping layer, they could vary the degree of oxidation of the CoFeB layer. They observed a change in sign of the DL torques with oxidation. They claimed this effect was either due to an enhancement of the Rashba effect with oxidation[97] or an enhancement of Rashba-type interfacial SOC due to orbital angular momentum, in materials with strong atomic SOC [98]. They followed up on this work with voltage-controlled SOT switching in Pt/Co/GdOx devices[99]. Here, the application of voltage pulses leads to oxygen pumping from GdOx into Co, which in turn modulates the SOT. They observed a change in sign in both the FL and DL torques with oxidation. They correlated the sign change of FLT with that of the Rashba coefficient when oxygen is present between Co and Pt, using ab-initio calculations. Other works on FM oxidation include the work of Hibino et. al.[100] where the Co is naturally oxidized post FM deposition in a Ta/Pt/Co/HfO_2 stack. They observe an increase in both the DL and FL torques, which they attribute to a Rashba component. This is similar to the result of Emori et. al.[95] and they do not observe the sign change observed by Qui et. al.[96] or Mishra et. al.[99]. They continued this work using a CoOx insertion layer between Co and Pt in a multilayer stack of Ta/Pd/Co/CoOx/Pt[101] and yet again observed an increase in both DL and FL torques. They attributed this increase to an enhanced spin mixing conductance due to the antiferromagnetic nature of CoOx, which might be visible even above the Néel temperature[102].

Another line of research into the effect of oxidation on SOTs is by utilizing a light metal with a low SOC such as copper. An et. al.[103] naturally oxidized the top surface of Cu in NiFe/Cu bi-layer stack and observed an increase in spin-torque efficiency ξ_{FMR}, along with the presence of DL torque, which they attribute to spin-dependent scattering in the bulk of the Cu/Cu_2O. They followed up on this work to report on the presence of the DL torque and an increase in FL torque with sign reversal in plasma oxidized CuOx/NiFe bi-layers[104]. They attribute this to Rashba effect and spin-dependent disorder scattering respectively. Another work in the same direction is by Enoki et. al.[105], who investigated the

weak antilocalization effect in copper oxides. They determined Elliot-Yafet spin relaxation mechanism[106,107] to be dominant in plasma oxidized copper oxide whereas D'yakonov-Perel mechanism to be dominant in the naturally oxidized copper oxide at higher elastic scattering rates. They further observe an increase in SOI which is attributed to the spatial gradation of the CuOx of the naturally oxidized sample.

4.1.1 Studies on the effect of HM oxidation on SOTs

One of the first works on the effect of oxidizing the HM on SOTs is of Demasius et. al.[108]. They oxidized tungsten during the growth of their stack, SiOx(25)/WOx(6)/$Co_{40}Fe_{40}B_{20}$(6)/TaN(2), by introducing oxygen in the sputtering chamber. By varying the oxygen gas flow in the chamber between 0-3%, they could vary the atomic oxygen concentration in their films between 0-44%. By studying the Spin Torque - Ferromagnetic Resonance (ST-FMR) of their system, they observed an increase in the SHA associated with the DL torques up to an oxygen concentration of 12.1%. Beyond that, it saturates as plotted in Figure 4.3 (a). They attribute this effect to an interfacial effect as the torques do not scale with the oxygen concentration, resistivity or the microstructure of W. An et. al. published a couple of works in this direction studying the effect of oxidized platinum on SOTs[109,110] using ST-FMR. In their first work they study PtOx/$Ni_{81}Fe_{19}$(6)/SiO_2(4) stacks where the PtOx is oxidized during deposition with an oxygen flow rate of Q=0-35%. By varying Q between 0 and 10%, they observe an increase in DL efficiency from 0.044 to 0.059 and FL efficiency from -0.0042 to -0.017. They consider this Q range as the moderately oxidized range, as the current is expected to flow in PtOx layer. Above this Q limit, they consider the PtOx to be completely insulating and determine the torques assuming a 0.5nm thin interfacial layer. By varying Q between 15 and 35% they observe an increase in DL efficiency from ~0.3 to ~0.6 and FL efficiency from ~-0.01 to -0.115. They attribute this increase to an interfacial effect arising either from interfacial spin-dependent scattering or from interfacial Rashba effect. They also show current-induced switching in CoPt layers and voltage control of torques in this work. Their second work considered the effect of higher oxygen flow during deposition, Q = 50% to 100%. They observe an increase in DL efficiency from 0.44 to 0.92 and FL efficiency from -0.039 to -0.19, as shown in Figure 4.3 (b). They attribute this effect to interfacial SOC induced Berry curvature. Their group continued this work and published their most recent results in Asami et. al.[111]. By performing spin pumping using FMR, they observe an enhanced spin-mixing conductance of $g_{eff}^{\uparrow\downarrow}$ = 1.38 x $10^{19}$$m^{-2}$ in PtOx/$Ni_{81}Fe_{19}$/SiO_2/Au. They also observe a quenching of this conductance by inserting an ultrathin insertion layer of Cu between the permalloy and platinum oxide layers. Hence, they attribute this enhancement to spin-to-charge conversion at the Rashba interface between the FM/oxide. Hajzadeh et. al.[112] have tried to explain these increases based on electron scattering at the surface oxide charges. The increase in torques in their model depends on the surface oxidation condition, the current flow path, and the electronic interface condition. They attribute the increase seen in Demasius et. al.[108] to interfacial Rashba effect and the increase in An et. al.[109,110] to a combination of Rashba and surface oxide charges.

To summarize, to study the effect of oxidation on SOTs, three routes have been explored: FM oxidation, light metal (LM) oxidation and HM oxidation. Comparing works on FM oxidation, there is a lack of consensus on the sign and enhancement of SOTs. Works by Qiu et. al.[96] and Mishra et. al.[99] observe an increase and a change in sign of SOTs. This was however not the case of an earlier work of Emori et. al.[95] who observed an increase of just the DL SOT or that of Hibino et. al.[100] and Hasegawa et. al.[101] who observed an increase of both DL and FL SOTs. These works did not observe a change in sign of SOTs. Moreover, there is a lack of consensus on the cause of the observed changes in SOTs. The proposed mechanisms include the change in the electronic potential at the FM interface, the Rashba

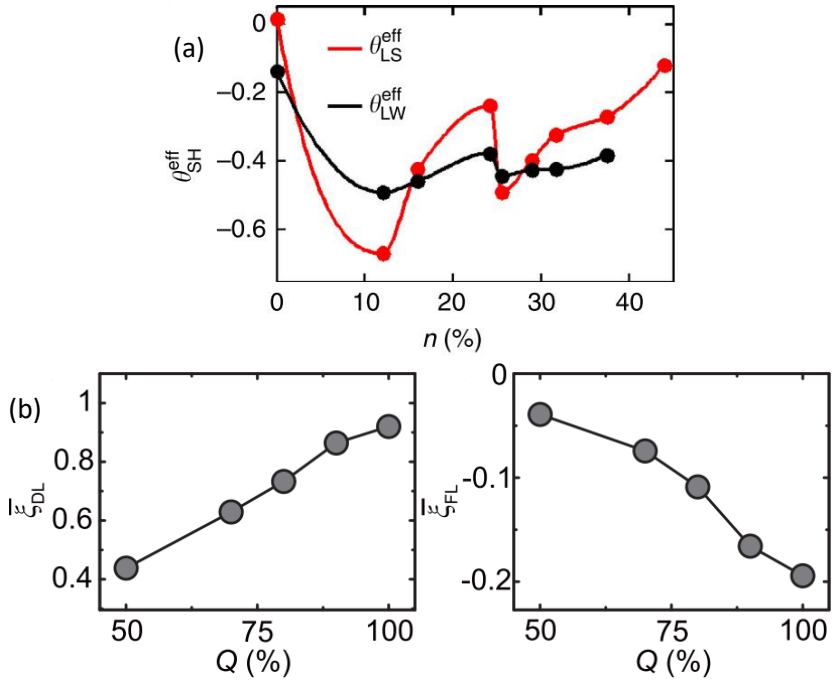

Figure 4.3: (a) Spin Hall angle versus atomic concentration of oxygen in WOx in a stack of SiOx(25)/WOx(6)/CoFeB(6)/TaN(2). Plot adapted from reference [108]. (b) Efficiencies of DL and FL torques versus the oxygen flow in the chamber during deposition of PtOx in a stack of PtOx/NiFe/SiO_2. Plot adapted from reference [109].

effect, the contribution of orbital angular momentum and the enhanced spin-mixing conductance near the Néel temperature. The works on light metal oxidation are quite the same with a lack of consensus regarding the cause and effects. An et. al.[103] observed an increase in spin-torque efficiency while Gao et. al.[104] observed an increase in FL SOTs with sign reversal. These effects have been attributed to spin-dependent scattering and Rashba effects. Enoki et. al.[105] observed an increase in SOI attributed to spatial gradation of oxidation. The picture is the same considering the works on HM oxidation. Demasius et. al.[108] observed an increase in SHA with oxidation up to a certain extent beyond which it saturated. This was hence attributed to an interfacial effect. However, the other works in this field see a non-saturating increase in SOTs with oxidation. An et. al.[109,110] attributed this increase to interfacial Rashba effect. Asami et. al.[111] observed an increase in spin-mixing conductance that they attributed to enhanced interfacial spin-absorption due to interfacial SOC. Once again, there is no coherent picture explaining these results. Moreover, all these works are generally performed assuming a single model of either FM, HM or LM oxidation, and a combination of these effects are explicitly ruled out.

4.2 Experimental Design

From the discussions above, numerous works have studied the role of oxygen on SOTs. However, there still are inconsistencies between some of the experiments as well as questions regarding the validity of some of the assumptions made in the data treatment. Moreover, although most of these studies attribute the enhancement of SOTs to some interfacial effect, the exact physical mechanism contributing to this enhancement is not completely clear. In this work, we aim to study the mechanisms of SOTs in platinum oxide-based heterostructures. The questions we aim to tackle are threefold:

1. Is the generation of SOTs in such systems primarily an interfacial or a bulk effect? And in any case, what is the exact mechanism behind it?

2. Oxidation increases the resistance of the device. Can we keep the switching voltage constant and perform switching, such that the switching current is reduced?
3. This reduced current switching inherently assumes an enhancement of SOTs produced per unit current. Is that valid?

To tackle these questions, we use the model shown in Figure 4.4. It consists of a bi-layer of platinum and cobalt. If we are able to oxidize platinum such that there is a gradation of oxygen in the platinum layer, we can study the thickness dependence of SOTs in such structures. The current progressively flows closer to the interface with the oxidation of platinum (as we move from left to right). This should enable us to differentiate between interfacial and bulk effects in such structures.

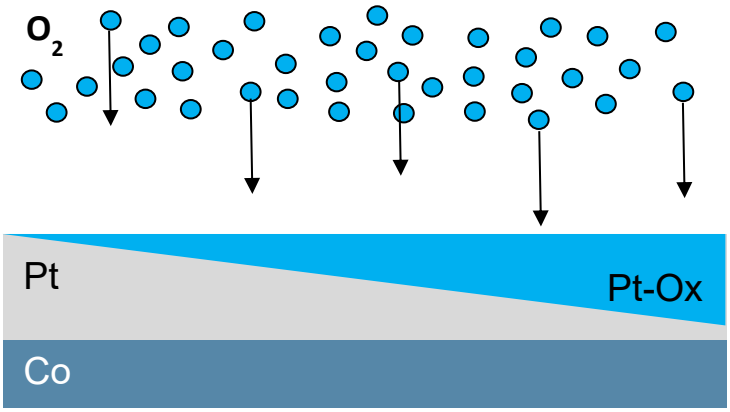

Figure 4.4: Experimental design. By varying the depth of oxidation in platinum layer, we can study and differentiate the interfacial and bulk mechanisms of SOT generation.

4.3 Sample Deposition and Material Characterization

4.3.1 Magnetron sputtering and wafer die planning

To realize the experimental model shown above, in practice we work with Ta(3)/Cu(1)/Co(2)/Pt(4-1) stacks grown on 100 mm silicon wafers with 1 µm thick thermalized SiO_2 layer. Here Pt(4-1) refers to a wedge of Pt ranging from 4nm ti 1nm. The Cu/Co/Pt forms the asymmetric structure for the generation of SOTs. Ta provides a good seed layer to grow this heterostructure as Ta/Cu is immiscible and so is Cu/Co. Moreover, the Ta seed does generate SOTs in the Co layer, though this can be corrected for. The 2 nm Co film ensures a uniform in-plane ferromagnetic film. Pt is the HM layer, although there should be some intermixing with Co. The Ta seed does generate SOTs as well. Though this can be corrected for. These depositions were performed by Stéphane Auffret at SPINTEC using magnetron sputtering discussed in the previous chapter. The uniform layers are grown “on-axis” while the platinum wedge is grown “off-axis.” The bottom Ta is likely amorphous while the rest of the layers should be polycrystalline having a [111] texture. The wafer is immediately coated with a 5-10 µm thick resist, AZ 4562 to prevent any unwanted oxidation. This resist is stripped before performing any wafer processing such as oxidation or micro-lithography. When this stack undergoes uniform oxidation as shown in Figure 4.6, it results in a uniform platinum oxide layer which follows the top profile of the wedge of platinum. The result is a gradation of Pt/PtOx, as designed in our experimental model. The oxidation process is detailed further on.

By performing the entire study on a single wafer, we can ensure that the material properties of all the devices are kept constant and the changes that we measure are purely related to oxidation effects.

This is not possible in case of samples grown during different depositions, where even consecutive

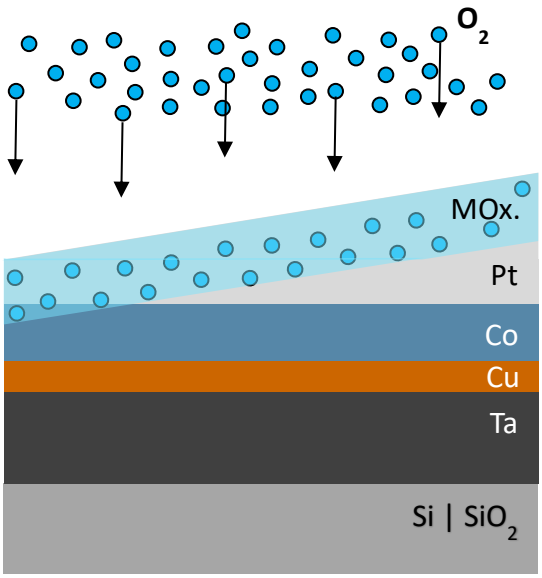

Figure 4.6: The device stack used in this experiment: Ta(3)/Cu(1)/Co(2)/Pt(4-1). The light blue shading indicates the oxidized region, denoted as MOx.

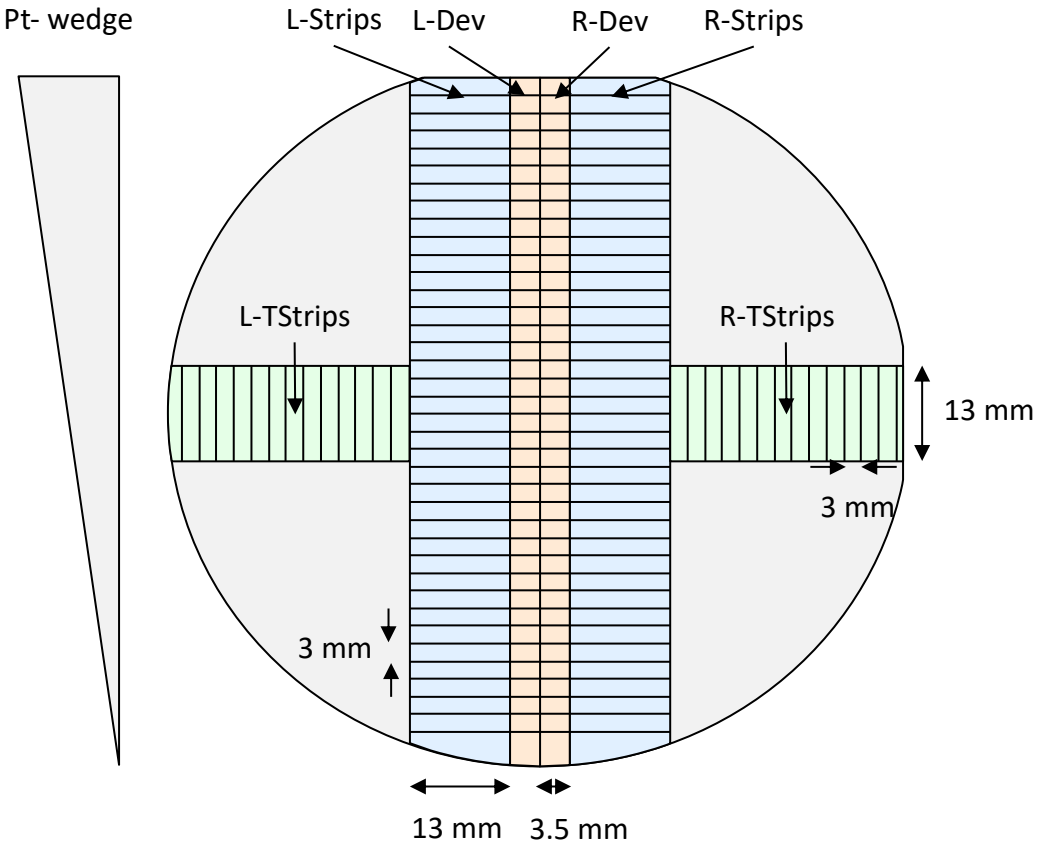

Figure 4.5: Dicing schematic of the wafer. The design is laterally symmetric. The platinum wedge is shown on the left. The color codes correspond to their respective functions in the experiments. Resistance and magnetic measurements are performed on the blue and green strips. The devices are fabricated on the orange colored strips.

deposition runs with the same conditions lead to slight differences in material properties.

The deposited wafer is diced into strips, as shown in Figure 4.5, using a DAD-321 dicing saw from DISCO Corporation. The blue strips are diced along the platinum wedge whereas the green strips are diced transverse to the platinum wedge. The device slices denoted in the image as “L-Dev” and “R-Dev” are initially diced as long elongated strips and only after microlithography, diced into smaller pieces shown in the schematic. This is to aid in the lithography process. The dicing is laterally symmetric. This is to account for any lateral asymmetry occurring from the magnetron sputtering process. Any such asymmetry could impact the oxidation process and our subsequent analysis.

4.3.2 Material characterization: Tunneling Electron Microscopy (TEM) and Energy Dispersive X-ray Spectroscopy (X-EDS)

In order to determine the quality of the deposited films, we decided to perform TEM analysis on our samples. These analyses were performed by SERMA Technologies at Grenoble. In TEM imaging, a beam of electrons is passed through a thin lamella of the sample. These electrons interact with the electrons of the sample before reaching the detector. High-resolution images can be captured due to the small electron wavelength. In practice, the samples need to be fine lamellas through which the electron beam is passed. We performed these analyses on a sample with a thicker copper and platinum layer. The sample surface is protected by carbon and tungsten capping and a thin lamella is sliced using an FEI Strata DB400 Focused Ion Beam (FIB). The high-resolution TEM imaging was performed on an FEI Tecnai OSIRIS equipped with an X-EDS detector with ChemiSTEM technology. The TEM image is shown in Figure 4.7 (a). The analyses show that the layers have roughness, which when averaged over the thickness of the sample leads to a blurring of the interfaces. Hence, these images are to be taken qualitatively. Further, electron diffraction on similar set of samples showed that the Cu, Co, and Pt layers are indeed polycrystalline.

We also performed X-EDS analyses to determine the chemical composition of the sample. In these analyses, the incident electron beam excites electrons from the inner shell of the atom. When the hole created in that way is filled by an electron from a higher energy shell, X-rays are emitted whose properties are characteristic of the atomic structure of the emitting element. Hence the EDS spectra can provide information regarding the chemical composition of the sample. These analyses were performed using a Scanning TEM in the High-Angle Annular Dark-Field (STEM-HAADF) mode. The resulting images are shown in the three panels of Figure 4.7 (b). They color correspond to Pt, Co, Cu, and Ta layers. We also wanted to study the oxidized samples using this technique. It, however, doesn’t have the spatial resolution to study the oxygen diffusion in our samples in the nanometer length scales.

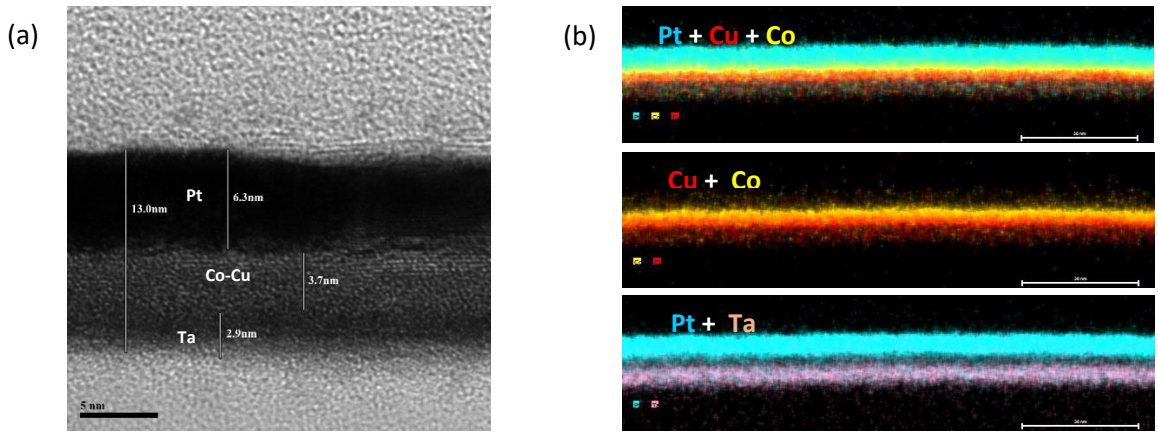

Figure 4.7: (a) TEM image of Ta/Cu/Co/Pt and the corresponding (b) chemical analysis with X-EDS.

4.3.3 Sample characterization: conductance and saturation magnetization

In order to characterize the conductance of our samples, we performed 4-point resistance measurements on the entire set of strips. In our setup, the voltage probes were spaced 6 mm apart and the current probes 10 mm apart. This ensures that the current flow is uniform between the voltage probes. The resulting conductance plot for the strips along the platinum wedge is shown in Figure 4.8 (a). Here L and R correspond to the side of the wafer and UO1 refers to the samples being un-oxidized. The blue and gray triangles line up perfectly, indicating negligible lateral asymmetry in the samples.

Next, the magnetic moment of the strips was measured using VSM technique described in the previous chapter. This is plotted in Figure 4.8 (b). Once again, there is negligible lateral asymmetry. However, there is a curvature in the plot indicative of the slight variation in the thickness of the deposited Co layer around the vertical symmetry axis. This is common in “on-axis” depositions where the wafer is rotated during deposition. It is also visible in the wafer-level resistance map shown in Figure 3.28 of the previous chapter. We now need to determine the effect plasma oxidation has on the conductance and the magnetization of the sample.

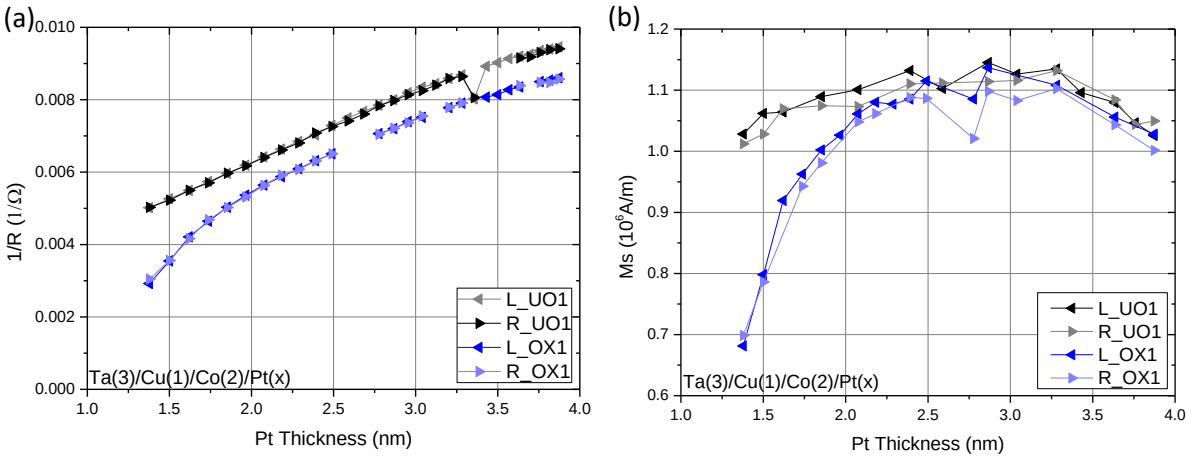

Figure 4.8: Effect of oxidation on (a) conductance and (b) saturation magnetization. UO1 and OX1 refer to Un-Oxidized and Oxidized samples. L and R refer to the lateral side on the wafer.

4.3.4 Plasma oxidation

The plasma oxidation of platinum is performed on all the "L-Dev" slices except for a select few which are needed for other material characterizations. The "R-Dev" slices form our reference un-oxidized devices.

As platinum cannot be oxidized in ambient conditions, we perform the oxidation in an argon-oxygen plasma in an Inductively Coupled Plasma - Reactive Ion Etching (ICP-RIE) chamber. A schematic of an ICP-RIE is shown in Figure 4.9. Here, a strong Radio Frequency (RF) electromagnetic field is used to generate a plasma in the chamber. The RF coil power is set to 100 Watts (antenna power supply) and oscillates at 13.56 MHz This ionizes the Ar and O_2 gas, creating a plasma. The wafer platter is DC isolated, allowing the electrons stripped from the gases to accumulate on the surface. This negative charge build-up causes the positive ions in the plasma to drift on to the wafer, where it chemically reacts with the material. We use a mixture of gases to control the oxidation conditions. The Ar and O_2 flow rates are set to 20 and 5 sccm respectively. This ensures that the oxidation is soft since the non-oxidizing agent Ar dilutes the oxidizing agent O_2. The soft oxidation allows us to control the depth and stoichiometry of the oxidation of the thin platinum film. Further, we keep the patter voltage to zero (bias power supply). This ensures that the ions are not accelerated towards the wafer surface where it could kinetically etch the material. These conditions result in an ionic energy of approximately 10-20 eV and an ionic density of 10^{11}-10^{12} ions/cm^3.

The effects of plasma treatment of bare platinum are quite well studied[113–116]. Such a plasma treatment is expected to result in a platinum oxide layer of uniform thickness consisting mostly of PtO_2 with PtO defects. This is visible in the conductance plots of the oxidized samples shown in blue in Figure 4.8 (a). Here OX1 refers to the samples being oxidized. Above a platinum thickness of 1.8 nm, we observe a uniform reduction in conductance compared to the un-oxidized samples denoted by the black curves. However, below this thickness, we notice a sharper drop in conductance. This could either be attributed to through oxidation into cobalt or to an increased resistivity of platinum at such small thicknessess. This can be verified from the magnetization curves shown in Figure 4.8 (b). This plot shows that above 1.8 nm, there is only superficial oxidation of cobalt from the plasma oxidation process. However, below this thickness, there is indeed through oxidation into cobalt, sharply reducing its magnetization. We verified these measurements with the second set of samples denoted by UO2 and OX2 in Figure 4.10. The plots indicate that with slightly different oxidation conditions, there isn't as significant penetration of oxygen into the cobalt layer as compared to the initial set of samples.

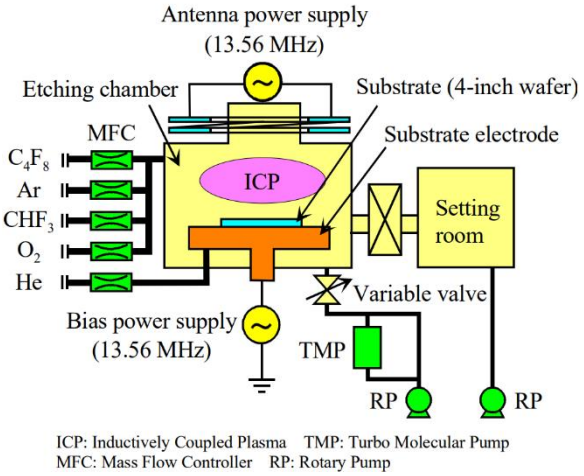

Figure 4.9: Schematic of an ICP-RIE used for oxidation of our samples. Figure adapted from reference[179].

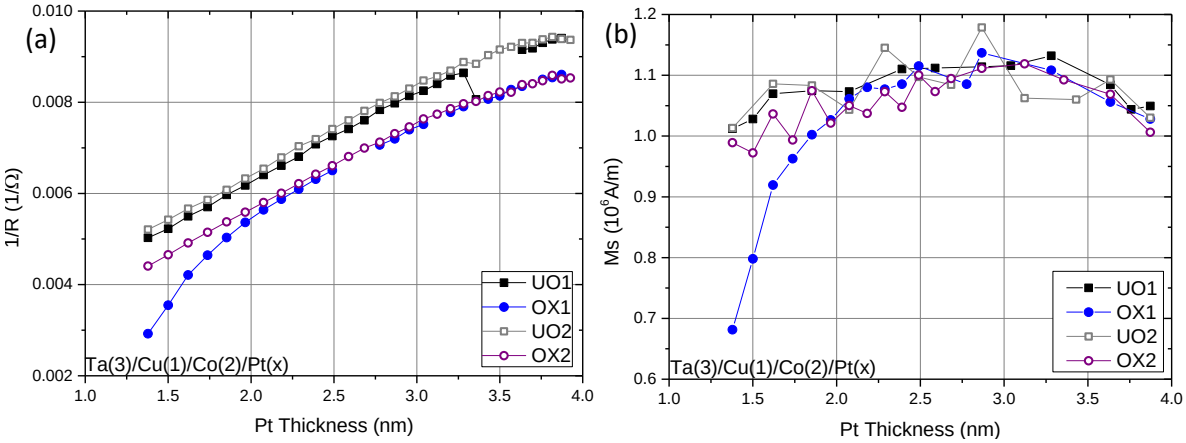

Figure 4.10: Effect of oxidation on (a) conductance and (b) saturation magnetization of two sets of samples. UO2 and OX2 refer to the second sample set.

One point to note is that the curves corresponding to UO1 and UO2 samples do not superimpose. This is due to the small differences in the deposition runs even when the parameters are kept constant. This highlights the need for performing all the measurements on the same wafer with a variation in thickness, keeping the growth conditions exactly the same. Also, the magnetization curve for this second set of samples is noisier due to a technical change in the VSM setup used for the measurements.

4.3.5 Sample characterization: Angle-Resolved X-ray Photoelectron Spectroscopy (AR-XPS)

In order to confirm this oxidation model, we performed Angle-Resolved X-ray Photoelectron Spectroscopy (AR-XPS) on our samples. These analyses were performed by Aymen Mahjoub, Sebastien Labau, and Bernard Pelissier at LTM, Grenoble. XPS analysis consists of irradiating the sample with soft X-rays and analyzing the spectrum of the emitted electrons. The spectrum indicates the number of electrons detected versus their kinetic energy. When a photon of a certain energy hits the sample surface, an electron is emitted with a kinetic energy equal to the difference between the energy of the photon and the binding energy of the atomic orbital plus the spectrometer work function. This binding energy is unique to the element and enables a material characterization of the sample. Energetic shifts in this elemental spectrum can arise from changes in the chemical potential of the material being analyzed and can be used to determine the chemical state of the sample. As the mean free path of the electrons is small, by analyzing photoemission signals at different angles, a depth profile of the material can be established. For our measurements, a Thermo-Fisher Scientific Theta 300 pARXPS with a monochromatic aluminum anode source at 1486.6eV was used. The analysis was performed at ultra-high vacuum conditions of $3x10^{-9}$ mbars.

We also studied the effect of oxidation along the platinum wedge in the OX1 samples, corresponding to different oxidation levels, specifically OX1 (1.5, 1.62, 1.97). Here the number indicates the thickness of platinum in nm. These are plotted in Figure 4.11. Here only the bulk spectra, measured at a lower photoelectron emission angles, are plotted as the surface spectra of Co are too noisy to be able to extract any meaningful information. The OX1(1.97) Pt spectrum, plotted in Figure 4.11 (a), consist primarily of un-oxidized $Pt^{4f}{}_{5/2}$ and $Pt^{4f}{}_{7/2}$ peaks, with much smaller Pt^{2+} peaks. This denotes the light Pt oxidation of this sample, with majority of Pt remaining metallic. The corresponding Co spectra shown in Figure 4.11 (b) doesn't show any oxidation at all, with only the $Co^{2p}{}_{3/2}$ peak visible. This is consistent with the magnetization curves plotted in Figure 4.8 (b). As the thickness of the top platinum layer is

decreased, we see an increased contribution of the Pt^{2+} peaks as shown in Figure 4.11 (c) and (e). This is evident in Co as well, where we see progressively increasing oxidation as the top platinum layer thickness is reduced, allowing more oxygen to reach the Co layer. This is plotted in Figure 4.11 (d) and (f).

In order to confirm these further, we can perform these spectroscopy scans to determine the atomic % contribution of different chemical species at various emission angles. From this, we can further determine the ratio of different chemical species of each atom, giving us a qualitative picture of the depth profile. These emission angle dependences of Pt and Co ions are plotted in Figure 4.12.

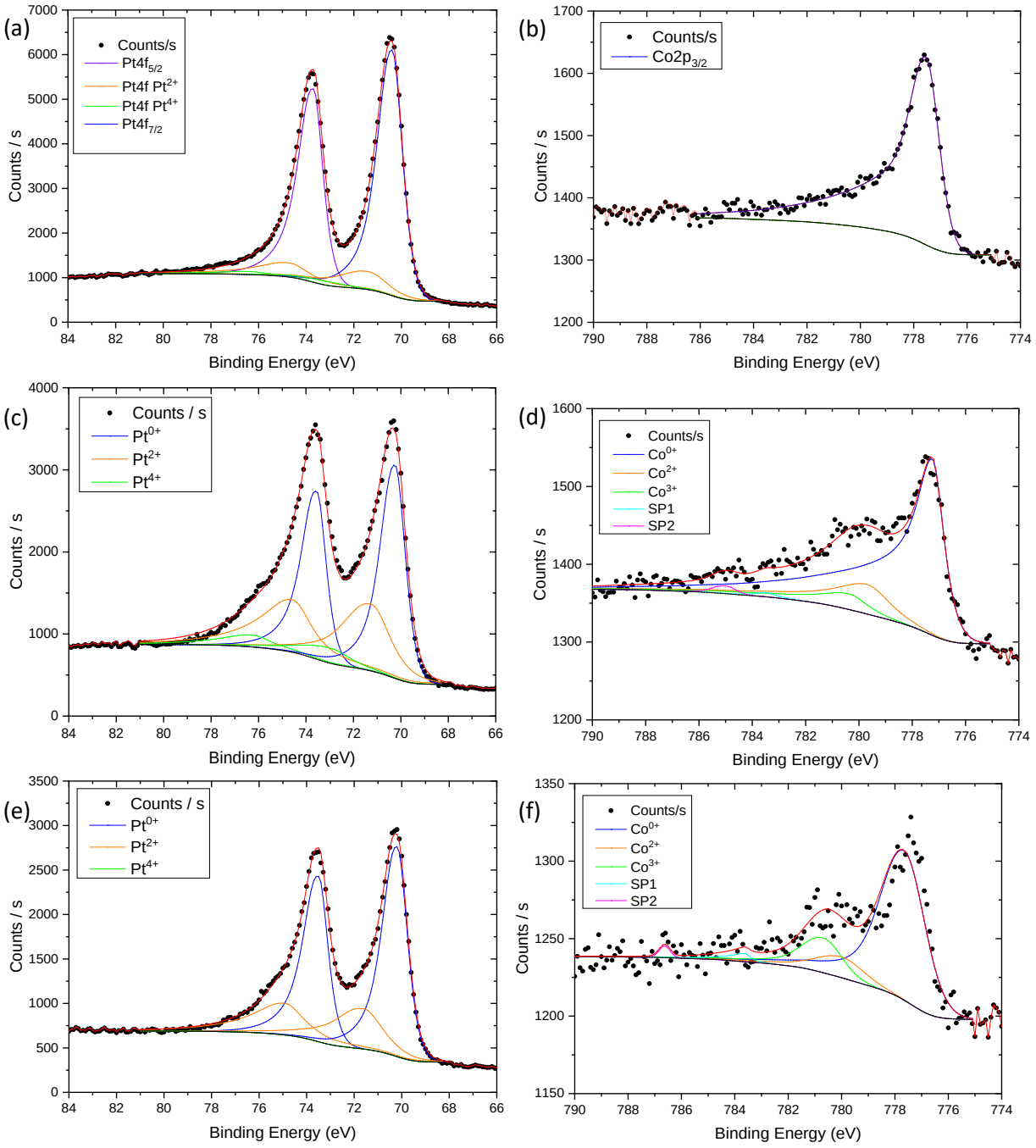

Figure 4.11: XPS spectra of bulk Pt (a, c, e) and bulk Co (b, d, f) of OX1(1.97, 1.62, 1.5) samples respectively.

Here, 76.25° refers to the surface-emission while 23.75° refers to the bulk emission. The Pt ion plot of OX1(1.97), plotted in Figure 4.12 (a), shows a dominant un-oxidized state with a smaller contribution of the Pt^{2+} species corresponding to the PtO state. This is consistent with our model of uniform Pt oxidation where the majority of Pt remains metallic and the thickness is too large for the oxygen to reach the Pt/Co interface. This is evident from the Co ion plot shown in Figure 4.12 (b), which shows that the Co is completely un-oxidized with no trace of any oxidation. This also corresponds well with our magnetization measurements.

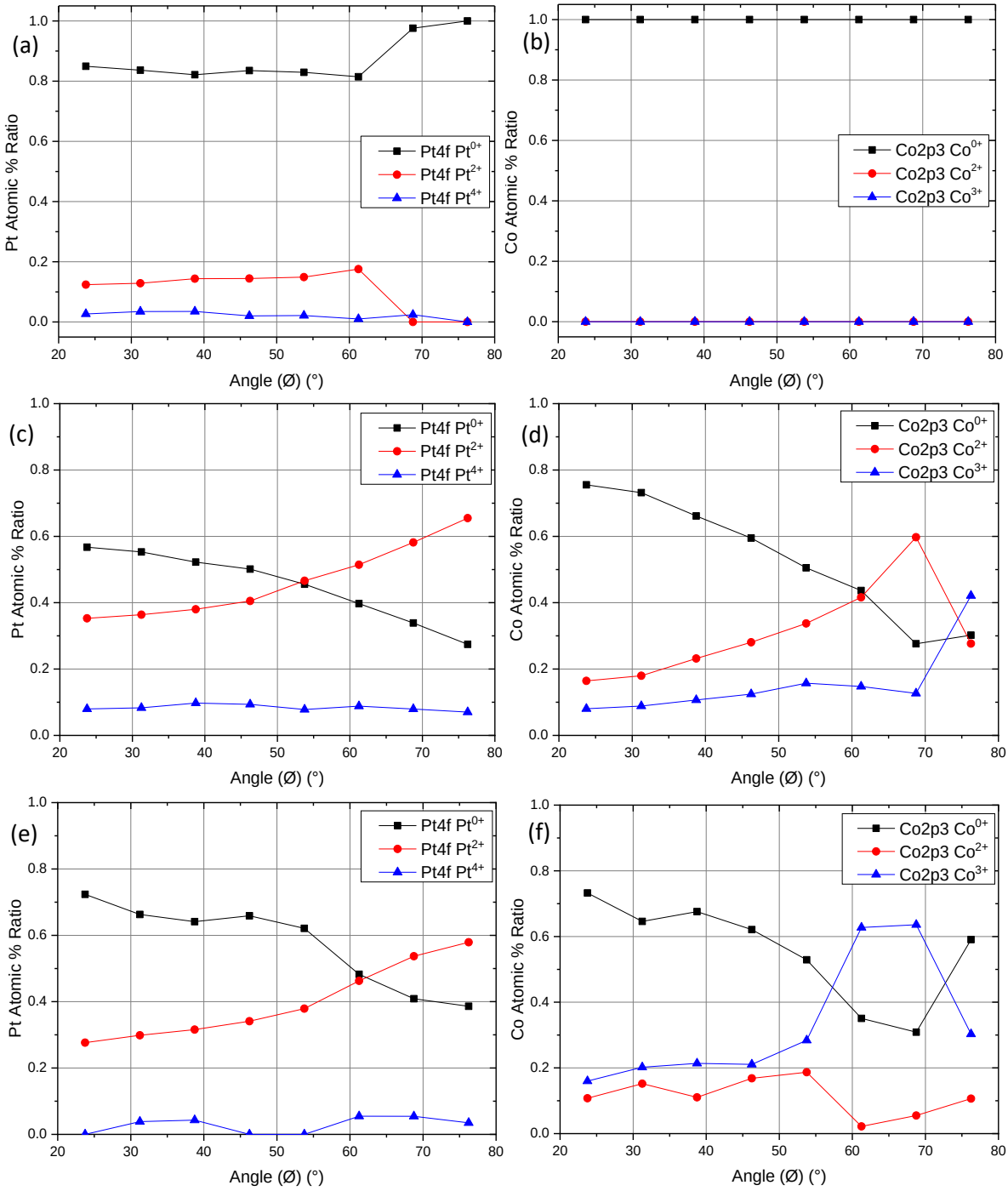

Figure 4.12: Emission angle dependence of Pt (a, c, e) and Co (b, d, f) ions of OX1(1.97, 1.62, 1.5) samples.

As we reduce the platinum thickness in OX1(1.62) sample, the effect of the same uniform oxidation is completely different. In Figure 4.12 (c), we notice substantial top-surface oxidation resulting in a dominant PtO state along with a smaller contribution of Pt^{4+} species corresponding to the PtO_2 state. The amount of oxidized species decreases with depth. The bulk shows a majority of un-oxidized platinum. However, this amount of oxidation was sufficient to reach the Pt/Co interface as evident in Figure 4.12 (d). Here, the Co is significantly oxidized at the top interface with dominant Co^{2+} contribution corresponding to CoO as well as significant amount of Co^{3+} species corresponding to Co_2O_3 and Co_3O_4. The sharpness of these curves could suggest significant interfacial oxidation.

The emission angle plot of Pt ions of OX1(1.5) sample also shows Pt oxidation corresponding to PtO. This is plotted in Figure 4.12 (e). As in the previous sample, the Pt is more oxidized on the top surface. The emission angle plot of Co ions of OX1(1.5) is plotted in Figure 4.12 (f). This sample has a dominant Co^{3+} state corresponding to Co_2O_3 and Co_3O_4 rather than a Co^{2+} state corresponding to CoO. This indicates an increased oxidation compared to the previous sample. This is also visible comparing the Co^{0+} state, indicating a slight decrease of metallic Co in OX1(1.5). This is consistent with saturation magnetization measurements. It should be noted here that the surface spectra of Co were noisy as a result of incomplete removal of the PMMA resist that we had spun on to prevent spurious oxidation. However, overall these AR-XPS data is consistent with our model that plasma oxidation results in non-uniform oxidation of platinum. At higher thickness, the oxidation strength is insufficient to reach the Pt/Co interface. However, at lower thicknesses, the platinum is significantly oxidized resulting in the oxidation of Co.

4.4 Effect of Oxidation on Spin-Orbit Torques

Now that we have thoroughly characterized our samples, we can quantify the effect of oxidation on SOTs. To do so, we perform 2^{nd} harmonic torque measurements and Ferro-Magnetic Resonance (FMR) on these sets of samples.

4.4.1 Second harmonic torque measurements

As discussed in the previous chapter, we perform second harmonic torque measurements on Hall crosses fabricated on “L-Dev” and “R-Dev” strips of the wafer. They correspond to oxidized and un-oxidized devices respectively. The fabrication process is performed using the microlithographic process described in the previous chapter. As these strips are elongated with a length of the wafer size, each strip is cut into three smaller ones to aid in the lithographic process. The samples are re-coated with a thick resist after the fabrication process. The sample is at no duration kept idle in ambient conditions without this resist covering to prevent unwanted oxidation. Once the fabrication process is complete, these strips are diced into smaller pieces corresponding to the chips of the lithographic mask. We now have the devices along the gradation of the platinum and hence the oxidation, ready for measurements.

These devices are wire-bonded to the contacts of the sample holder of this experimental setup and we perform the torque measurements as detailed extensively in the previous chapter. As these are in-plane samples, we perform in-plane angle scans and out-of-plane field scans. The resulting DL field as a function of platinum thickness is plotted in Figure 4.13. We will initially focus on Damping-Like

torques as these are the ones that act on the magnetization causing it to switch. The Field-Like torques will be detailed later. When performing these measurements, we obtain the effective fields generated by these torques in units of mT. These fields, however, needs to be normalized correctly to be able to compare different devices. An easy way to make such a comparison is by normalizing it either with the current applied in the device or with the voltage applied across it. These are plotted in Figure 4.13 (a) and (b) respectively. The platinum thickness was determined following the procedure described in the previous chapter. These plots are also normalized to the width of the devices used for measurements so as to account for any lithographic differences. The width was obtained by measuring the diagonal at the cross to account for any lithography induced curvature of the corners of the cross.

Let's consider the DL field normalized to the current of the first set of samples UO1 and OX1 plotted in Figure 4.13 (a). It is clear that the effective DL field generated by the current is similar between the oxidized and un-oxidized samples down to a platinum thickness of around 2 nm. Below this thickness, there is a significant increase with oxidation. It is however interesting to note the effective DL fields of the second set of samples UO2 and OX2. In this case, there is absolutely no increase in torques with oxidation.

Considering the DL field normalized to voltage for UO1 and OX1, plotted in Figure 4.13 (b), we notice that there is a reduction of torques with oxidation down to around 1.75 nm thickness of platinum. This is consistent with the net reduction of the effective thickness of platinum with oxidation. The last point at 1.5 nm of platinum, however, shows a tendency to increase. This increase might be more pronounced if the effective platinum thickness is considered, which would have shifted these OX1 curves to the left. Sample 2 of UO2, OX2 however, shows a decrease in torques consistent with an oxidative loss of platinum.

This increase depends on the amount of oxidation. If only the top surface of platinum is oxidized, we do not see an increase in torques. This is the case for OX2, where, from Figure 4.10 it is clear that the Pt/Co interface is not oxidized. However, when the oxygen oxidizes the Pt/Co interface, as in the case of OX1, we do see a net increase. Hence there is indeed an effective increase in DL-SOTs with the oxidation of platinum. These results are consistent with the works on HM oxidization where a net increase in SOTs was observed[109–111]. It is also similar to Demasius *et. al.*[108], although we do not see any saturation to this increase in DL fields with oxidation. In order to confirm the role of the Pt/Co interface in this enhancement of SOTs, we decided to perform FMR measurements.

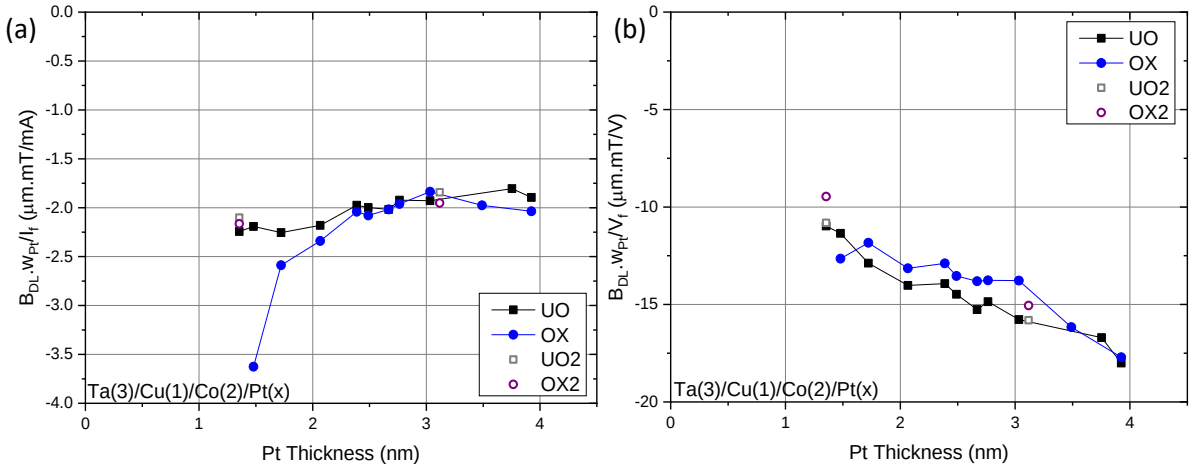

Figure 4.13: Damping Like effective field normalized to (a) the total current and (b) the voltage across the device. It is also normalized to the width of the device (w_{Pt}) to account for any variation from the lithographic process.

4.4.2 Ferro-Magnetic Resonance (FMR) measurements

The 2nd harmonic measurements detailed in the sub-section above studies the current-induced changes in magnetization due to transfer or accumulation of spins at the FM/NM. The counterpart of this technique is called spin-pumping and measures the spin current generation as a consequence of the magnetization dynamics. The theoretical work on this spin-pumping mechanism was pioneered by Tserkovnyak et. al.[117–119]. The magnetization dynamics of a ferromagnet is described by the Landau-Lifshitz-Gilbert (LLG) equation

$$\frac{d\boldsymbol{M}}{dt} = -\gamma\mu_0 \boldsymbol{M} \times \boldsymbol{H_{eff}} + \frac{\alpha}{M_s}\left(\boldsymbol{M} \times \frac{d\boldsymbol{M}}{dt}\right) \tag{4.1}$$

Here α denotes the dimensionless Gilbert damping constant which describes the damping of the magnetization in the presence of an external magnetic field. This causes the precession of the magnetization to decay and subsequently align with this external field. It is hence a technologically relevant parameter that plays a role in the switching of the FM in MRAMs etc. An enhancement of this damping constant has been observed when the FM is placed in contact with a NM[117–121]. This has been explained by the leakage of spin current into the adjacent NM layer. The action of the enhanced damping can be considered as the loss of the spin angular momentum of the precessing magnetization in the form of spin currents. The magnitude of this damping enhancement depends on the bulk effects in the NM as well as the NM/FM interfacial effects. If the spin diffusion length into the NM is short compared to the NM thickness, the spins pumped from the FM are effectively absorbed by the NM as is the case in heavy metals such as Pt, Pd. The high SOC in these metals also contributes to interfacial spin-flip scattering enhancing this effect. On the other hand, a light element such as Cu has a large spin diffusion length[121]. Hence, if the thickness of the Cu layer is not larger than its spin diffusion length, an enhanced spin accumulation at the FM/NM interface can lead to a backflow of spins into the FM. This can reduce the effective enhancement of damping.

The spin currents flowing out of the FM due to the precession is orthogonal to the magnetization. This implies that the accumulated spin and the spin backflow consists of spins which are perpendicular to the original magnetization of the FM layer. The transfer of angular momentum across the interface can be described by a parameter called the spin-mixing conductance, given by $g_{eff}^{\uparrow\downarrow}$, which is characteristic of the interface[119].

The enhancement of damping can be measured via FMR linewidth measurements[122] and manifests as a broadening of the FMR peak. The measurements for this study were performed by Mihai Gabor at TU Cluj-Napoca using a cavity FMR. A microwave TE 011 cavity operating in the X band (9.79 GHz) with a power of 1mW was utilized for these measurements. The FMR spectra are given by the derivative of the microwave absorption spectra, as an eternal field H modulated by an AC field is swept across the sample. An example[123] of this field dependence of the magnetic spectra, at different field angles θ_H is plotted Figure 4.144. Here θ_H denotes the polar angle, with respect to the sample normal. The resonance field H_R corresponds to the average of the peak and trough fields and the resonance line width ΔH corresponds to $\sqrt{3}$ times the width between the peak and trough fields.

The energy density of the FM per unit volume can be written as[120,123]

$$E = -M_S H\cos(\theta_H - \theta_M) - \frac{M_S H_{K1}^{eff}}{2}\cos^2\theta_M + \frac{M_S H_{K2}}{4}\cos^4\theta_M + K_1 + K_2 \tag{4.2}$$

Here M_S corresponds to the saturation magnetization, H the external field, θ_M and θ_H the angle of magnetization and the external field, H_{K1}^{eff} the effective first-order magnetic anisotropy including the

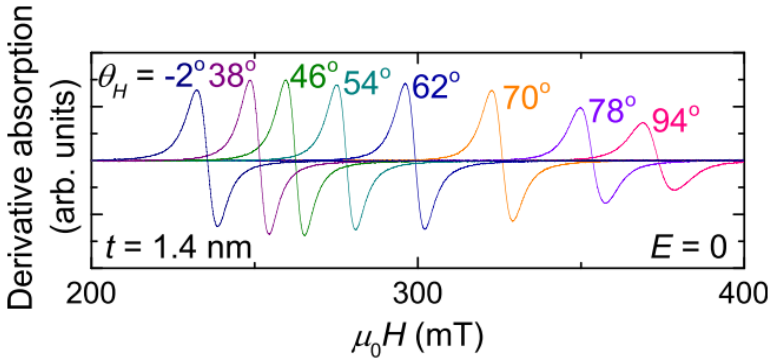

Figure 4.14: Magnetic field H dependence of the ferromagnetic resonance spectra for a CoFeB based stack at different field angles θ_H . Plot adapted from ref. [123].

demagnetization field, H_{K2} the second-order anisotropy and K_1 and K_2 the first and second-order anisotropy constants. Based on this equation and the LLG equation, the FMR condition can be derived as

$$f = \frac{g\mu_0\mu_B}{2\pi\hbar}\sqrt{H_1 H_2} \tag{4.3}$$

With

$$H_1 = H_R\cos(\theta_H - \theta_M) + H_{K1}^{eff}\cos^2\theta_M - H_{K2}\cos^4\theta_M \tag{4.4}$$

$$H_2 = H_R\cos(\theta_H - \theta_M) + H_{K1}^{eff}\cos 2\theta_M - \frac{H_{K2}}{2}(\cos 2\theta_M + \cos 4\theta_M) \tag{4.5}$$

By fitting the θ_H dependence of H_R with the above equations, we can determine the anisotropies, the demagnetization field, and the g- factor. We performed the FMR measurements for both sets of oxidized (OX1, OX2) and un-oxidized (UO1, UO2) samples. We also included a reference sample, REF, which does not have the top Pt layer, Ta(3)/Cu(1)/Co(2)/Al(2). The θ_H dependence of H_R of the first set of samples are plotted in Figure 4.15 (a). Here the number in the parenthesis indicates the thickness of the top platinum layer in nm. The larger resonant field at lower field angles denotes an in-plane anisotropy of our samples. The dependence of the linewidth ΔH on θ_H is plotted in Figure 4.15 (b).

The saturation magnetization and the effective magnetization are related via the anisotropies as

$$\mu_0 M_{eff} = -\left(2 * \frac{K_1}{M_s} + 4 * \frac{K_2}{M_s}\right) + \mu_0 M_s \tag{4.6}$$

M_{eff}, K_1, and K_2 are extracted directly from the FMR data. Hence, these values can be used to extract the M_s of the Co layer of our samples. The positive root of the quadratic equation, eq. (4.6), quantifies the M_s and is given by

$$M_s = \frac{M_{eff} + \sqrt{{M_{eff}}^2 + 4\left(\frac{2K_1}{\mu_0} + \frac{4K_2}{\mu_0}\right)}}{2} \tag{4.7}$$

The M_{eff} and the M_s of our samples are plotted in Figure 4.16 (a) and (c) respectively. The difference between these plots corresponds to the in-plane anisotropy, which is plotted in Figure 4.16 (b). Here K_1 and K_2 correspond to the first and second-order in-plane anisotropies. Both the first and second-order anisotropies were needed to obtain a good fit of the FMR data.

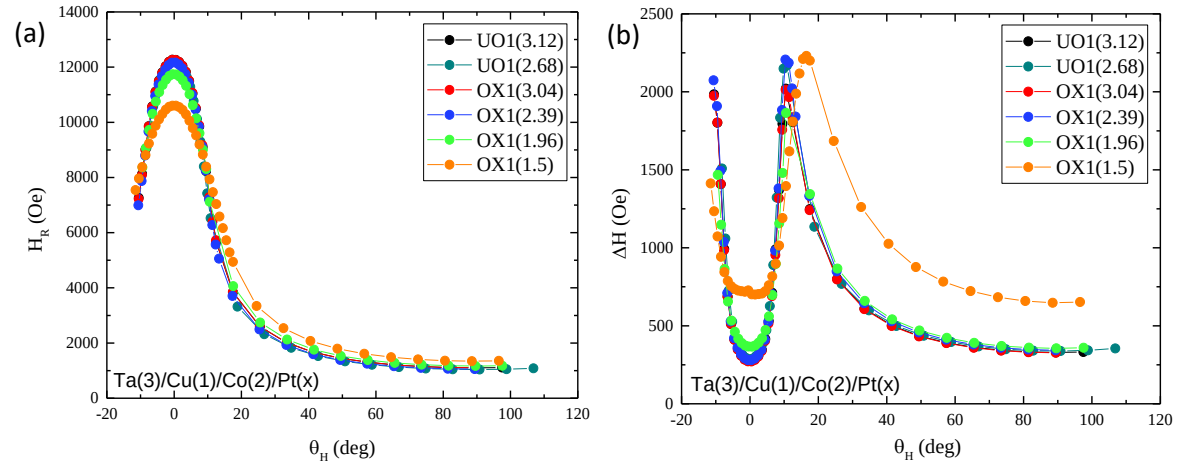

Figure 4.15: The external field angle θ_H dependence of (a) the resonant field H_R and (b) the linewidth ΔH of the first set of samples UO1 and OX1. The numbers in the parenthesis indicate the thickness of the top Pt layer in nm.

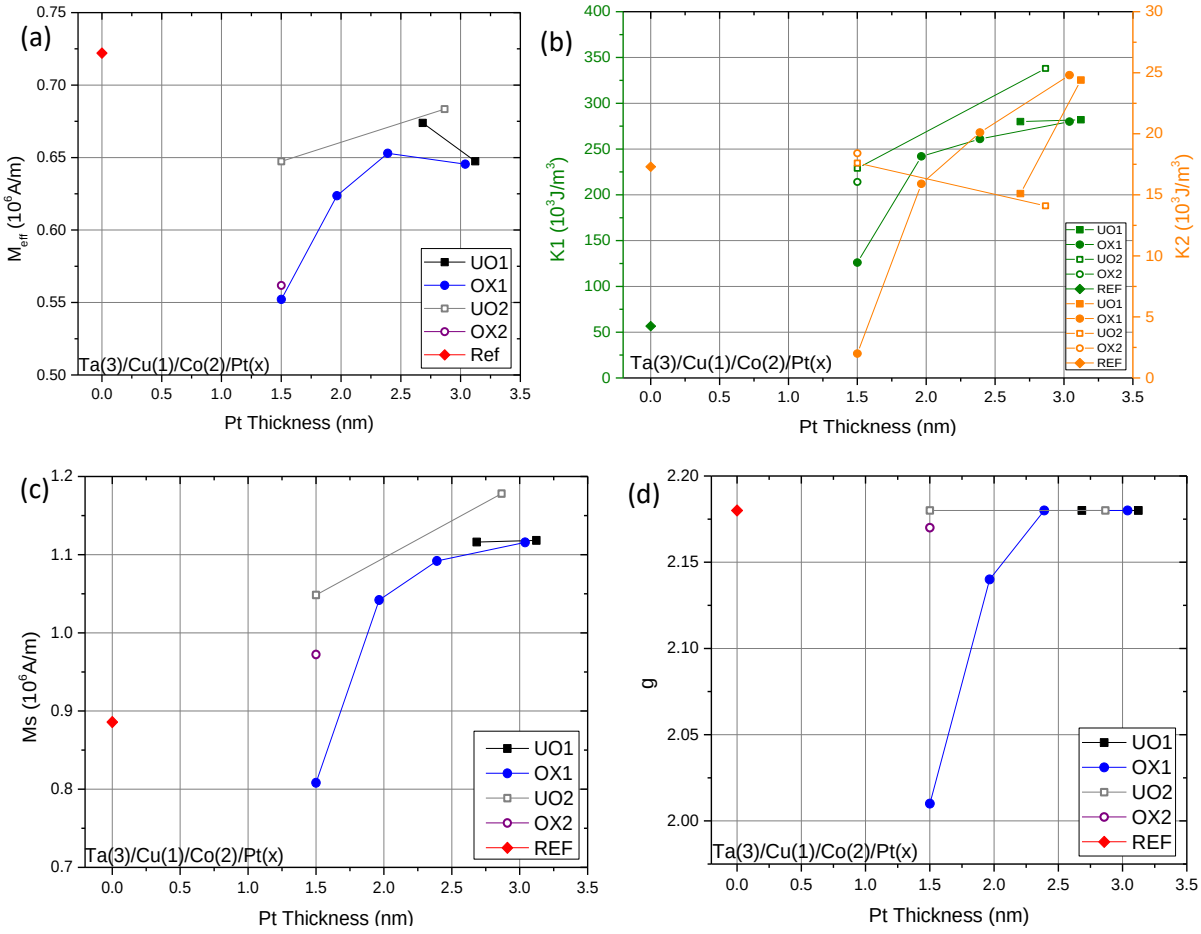

Figure 4.16: The dependence of (a) the demagnetization field, (b) the first K_1 and second K_2 order anisotropies, (c) the saturation magnetization and (d) the g-factor on the thickness of the top platinum layer. Here UO1, OX1, and UO2, OX2 refer to the first and second set of samples. REF refers to a reference sample without the top platinum layer, Ta(3)/Cu(1)/Co(2)/Al(2).

The calculated values of M_s correspond well with the VSM measured values confirming our FMR fits. The g-factor is plotted in Figure 4.16 (d) and relates the spin (μ_S) and orbital (μ_L) components of the net magnetic moment, $\frac{\mu_L}{\mu_S} = \frac{g-2}{2}$. The orbital component has a larger contribution at interfaces where the crystal symmetry is broken, especially with a HM with a large SOC. However, the presence of oxygen can enhance the crystal field, leading to a quenching of the orbital angular momentum. This can lead to a decrease in the g-factor shown in Figure 4.16 (d). Also, ideally we would expect REF sample to have lower g-factor than UO1, UO2. However, this is not the case as shown in the plot and we are presently unable to explain it. It could perhaps arise due to a decrease in the spin component due to alloying, which is larger in the REF sample with the Al capping, that also reduces the effective thickness of cobalt.

In order to measure the damping constant α, we need to consider the θ_H dependence of the linewidth plotted in Figure 4.15 (b). In an ideal system, the primary contributor to the linewidth is the intrinsic damping of the material α. However, there are other mechanisms that can contribute to the FMR linewidth. In this study we consider the effect of the inhomogeneous distribution of the effective magnetization and the anisotropy axis as well as the broadening effect of two-magnon scattering. The inhomogeneous distribution of the effective magnetization and anisotropy gives rise to local variations in the resonance field which results in the broadening of the FMR peak. The two-magnon scattering describes the phenomena where defects can scatter the FMR modes (zero wave vector) into finite wave-vector spin-wave modes[124]. This occurs at certain angles of the applied external field when the dispersion spectra of the system are degenerate causing the magnon to scatter to higher modes. A schematic of this scattering process is plotted in Figure 4.17. The inhomogeneous broadening of the FMR linewidth caused by these effects is considered the extrinsic contribution. The linewidth can hence be written in terms of these contributions as follows[123]

$$\Delta H = \Delta H_{in} + \Delta H_{ex} \tag{4.8}$$

$$\Delta H_{in} = \alpha \left| \frac{dH_R}{d(\sqrt{H_1 H_2})} \right| (H_1 + H_2) \tag{4.9}$$

$$\Delta H_{ex} = \left| \frac{dH_R}{dH_{K1}^{eff}} \right| \Delta H_{K1}^{eff} + \left| \frac{dH_R}{dH_{K2}} \right| \Delta H_{K2} + \Delta H_{TMS} \tag{4.10}$$

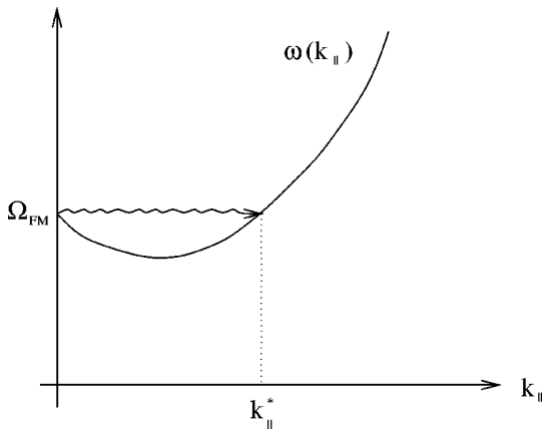

Figure 4.17: Schematic of an FMR dispersion spectra depicting the scattering process from the FMR mode to another mode of finite wave vector. Figure adapted from ref.[124].

Here ΔH_{in} and ΔH_{ex} correspond to the intrinsic and the extrinsic contributions to the FMR linewidth. ΔH_{K1}^{eff} and ΔH_{K2} are the distributions of the effective first order and the second-order anisotropy fields. Here the distribution of the effective first-order anisotropy can be further broken down into the inhomogeneous distribution of the effective magnetization, $\Delta(\mu_0 M_{eff})$, and the anisotropy axis, $\Delta\theta_H$, as detailed in Mizukami et. al.[120,121].

$$\left|\frac{dH_R}{dH_{K1}^{eff}}\right| \Delta H_{K1}^{eff} = \left|\frac{dH_R}{d(\mu_0 M_{eff})}\right| \Delta(\mu_0 M_{eff}) + \left|\frac{dH_R}{d\theta_H}\right| \Delta\theta_H \tag{4.11}$$

Further, by restricting to field angles < 45°, we can avoid the two-magnon scattering induced broadening[125]. Finally, by fitting these equations with the measured external field angle dependence of the linewidth, we can determine the damping constant, α. These values for our samples are plotted in Figure 4.18.

We observed that compared to the reference sample without the platinum layer, all the samples have a higher damping constant attributed to the higher SOC of the platinum layer. Comparing oxidized and un-oxidized samples, it is evident that there is a large increase of the damping constant with oxidation. This result is consistent with the work of Asami et. al.[111] who observe an increase of the damping constant of Py with the oxidation of the platinum layer. In this work, they assumed a completely insulating platinum oxide layer in contact with the permalloy layer. They then attributed this increase in damping constant to an interfacial Rashba effect based spin to charge conversion. In such a case of an ideal spin sink, the interfacial spin mixing conductance can be written in terms of the enhancement of the damping constant Δα as[126]

$$g_{eff}^{\uparrow\downarrow} = \frac{4\pi M_s d}{g\mu_B}\Delta\alpha \tag{4.12}$$

They measure a spin-absorption parameter defined as $\Gamma_0\eta = \frac{g_{eff}^{\uparrow\downarrow}}{6} = 2.3 \times 10^{18}$ (1/m²). If we make similar assumptions, we can plot the spin-mixing conductance of our samples as well using eq. (4.4). This is plotted in Figure 4.19. We extract a spin-mixing conductance of up to 4.9 x 10^{19}m^{-2} in our oxidized sample, consistent with their work. However, it needs to be noted that such a treatment ignores the Spin Memory Loss (SML) at the interface, which is the partial spin depolarization caused by interfacial spin-flip scattering. This needs to be considered for a more accurate picture of the spin pumping process in an FM/NM structure[127].

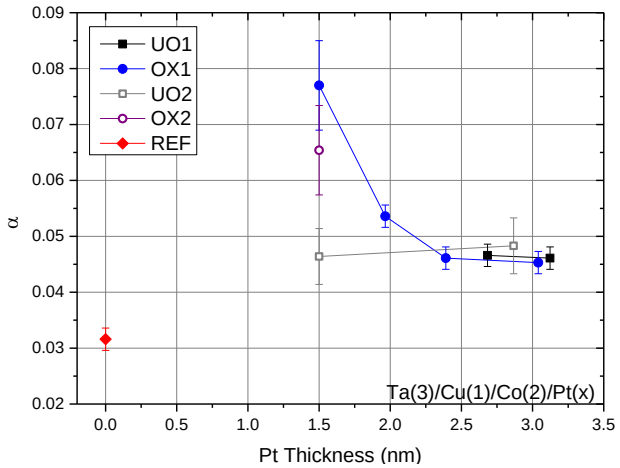

Figure 4.18: Dependence of the damping constant α on the top platinum thickness. Here UO1, OX1 and UO2, OX2 refer to the first and second set of samples. REF refers to a reference sample without the top platinum layer, Ta(3)/Cu(1)/Co(2)/Al(2).

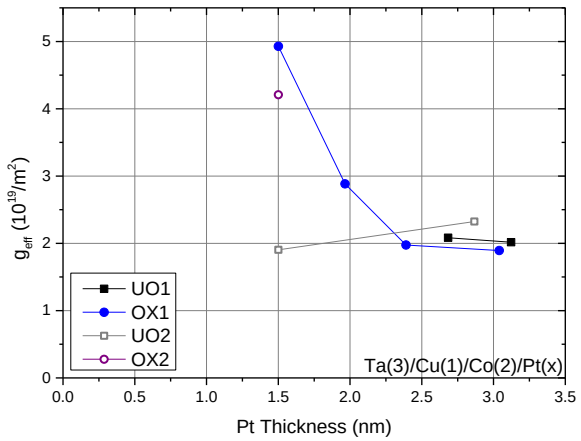

Figure 4.19: Spin-mixing conductance $g_{eff}^{\uparrow\downarrow}$ of the samples.

There could be two mechanisms behind such an increase of damping and the spin-mixing conductance. The first is the transparency of the interface. The interface transparency between the Co/Pt layers can have an effect on spin-pumping[74]. We have observed the loss of magnetization of the Co layer indicating its oxidation. Such an oxide of Co at the interface between the spin source and sink has been shown to enhance the interfacial spin-transparency which has been attributed to magnons or spin fluctuation in the thin AntiFerromagnetic (AF) layer[102]. This effect is expected to reach its maximum at the Néel temperature[128,129]. Although our experiments are performed at room temperature which is above the Néel temperature, there have been reports of spin-pumping in paramagnetic insulators as well[130,131]. Essentially, although this effect peaks at the Néel temperature, there might still be an increase in the interfacial spin-transparency between the Co/Pt layers above this magnetic transition temperature. The other mechanism leading to this increase in torques could be the Rashba interfacial effect between Co and oxidized Pt. The gradient of potential between the two layers can give rise to a large SOC at the interface resulting in spin-split electronic states[132]. Such an effect can give rise to spin-to-charge conversion via the Inverse Rashba Edelstein Effect (IREE) at the interface and can enhance the damping constant via spin-pumping[133–138].

4.4.3 Ab-initio DFT calculations: Damping constant α

In order to verify the increase in the damping constant, we calculated this constant for our structures from the first principles. All the Density Functional Theory (DFT) calculations in this study were performed by Ali Hallal and Mairbek Chshiev at SPINTEC. In order to account for spin-related phenomena such as spin-orbit coupling, spin polarization, magnetic ordering as a result of the oxygen at the interface, Korringa-Kohn-Rostoker (KKR) multiple scattering calculations can be performed to determine the Green's function (GF) directly[139]. GF determines the impulse response of an operator on a system. And in this case, it describes the electron scattering from the crystal potential. Hence, in this formalism the electronic structure of the system is not expressed in terms of the Bloch wave functions but instead using the GFs. KKR-GF enables the investigation of 3D periodic systems with chemical disorder such as ours. This was implemented using the spin-polarized relativistic KKR band structure package, SPRKKR[140]. In practice, a structure of 3 Mono-Layers (ML) of Co and 3ML of Pt were considered. A single site of oxygen was considered at the Co/Pt interface in the unit cell. The oxygen concentration at this site can be varied between 0% and 100%, corresponding to a vacuum and a single oxygen atom at this site. An intermediate value corresponds to a mixture of vacuum and oxygen, which can be considered as a partial monolayer of oxygen at the interface. This unit cell was repeated in all

three directions to obtain a supercell. One thing to note is that the oxygen site is present only on one interface of the cobalt with platinum. Thus, the repetition results in a Co/Pt layer with an interfacial oxygen layer with a coverage corresponding to the input oxygen concentration of the unit cell. Coherent Potential Approximation (CPA) enables us to model the oxygen at the interface by placing an effective potential at every site of the lattice and thereby simulating the electronic properties of the system. In this manner, we can avoid running multiple simulations with different placements of oxygen in order to determine the average electronic properties.

The results of this calculation are shown in Figure 4.20. Figure 4.20 (a) plots the dependence of the total magnetic moment on the oxygen concentration at the interface. The red and black curves correspond to hcp and fcc crystal orientations. In both cases, with an increase in oxygen concentration, there is a net reduction in the magnetic moment. This is consistent with our measurements using VSM. Figure 4.20 (b) plots the dependence of the damping constant on the oxygen concentration at the interface. There is an increase in damping corresponding to an increase in the oxygen concentration. This has the same trend as the damping measured using FMR plotted in Figure 4.18.

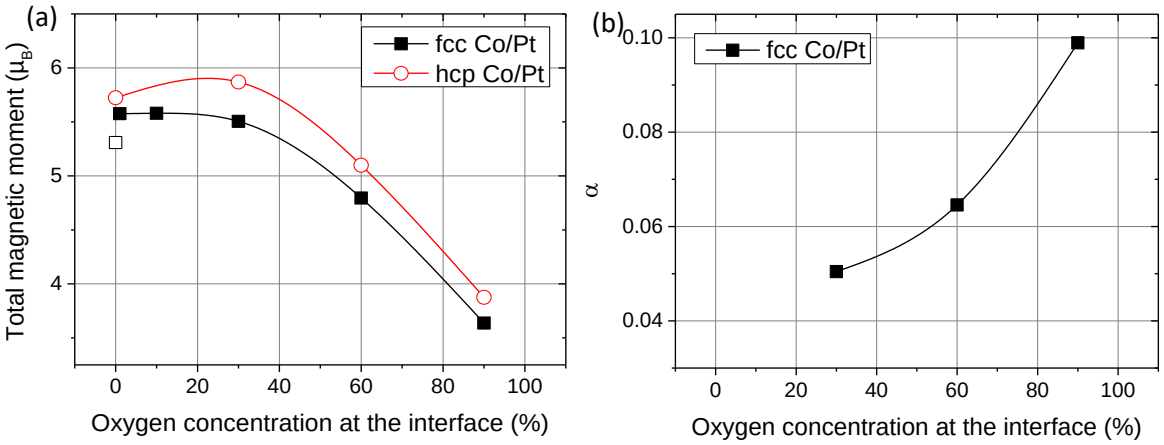

Figure 4.20: (a) The magnetic moment and (b) the damping constant α as a function of the oxygen concentration at the Co/Pt interface. Calculated using KKR-GF multiple scattering theory.

4.4.4 Technological application of the platinum oxide system

From the 2nd harmonic torque measurements and the FMR spin-pumping experiments, it is evident that there is an increase in SOTs and spin-pumping with oxidation. This is likely an interfacial effect as it manifests only at lower thicknesses of platinum when the Co/Pt interface is oxidized. These results are consistent with the works on HM oxidation[108–112]. We also measured the in-plane anisotropy field of these samples from the torque measurements. This is plotted in Figure 4.21. It shows that with the smaller thickness of platinum and hence a higher oxygen concentration at the interface, the in-plane anisotropy is reduced and subsequently there is an enhancement of the out-of-plane anisotropy. Such an enhancement of SOTs and the interfacial perpendicular anisotropy has advantages in the implementation of the SOT-MRAM.

In STT-MRAM, in order to obtain perpendicular anisotropy of the FM layer, Co is sandwiched between two layers of MgO. The oxygen at the interface can give rise to interfacial perpendicular anisotropy[82], as detailed previously. This structure is plotted in Figure 4.22 (a). However, such a structure is not conducive to SOT operation as shown in Figure 4.22 (b). The MgO layer could significantly decrease the Rashba induced spin accumulation at the interface, which contributes to SOTs. Hence, we could

envisage a structure shown in Figure 4.22 (c), with an oxidized Co/Pt interface. Such a structure would enhance the SOTs and thereby reduce the switching current as well as contribute to an interfacial perpendicular anisotropy allowing us to avoid the MgO based structure shown in Figure 4.22 (b).

Considering the technological potential of this interfacial oxidized system, as well as to gain an understanding of the actual cause of the enhancement of SOTs, we need to study the system further.

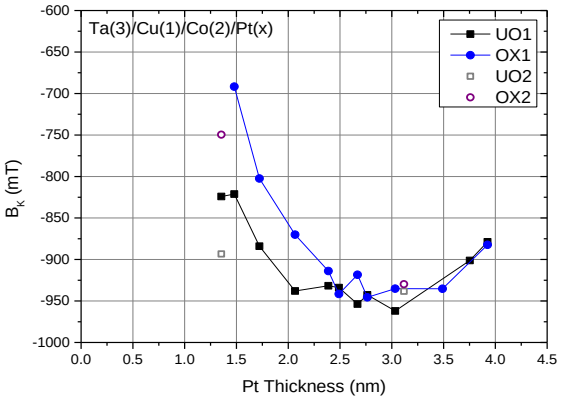

Figure 4.21: In-plane effective anisotropy field of the oxidized and un-oxidized samples.

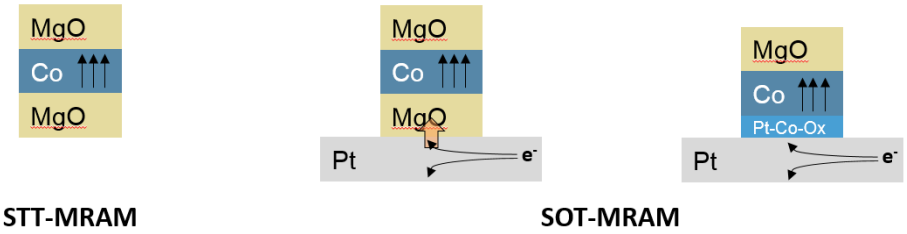

Figure 4.22: Schematic of the free layer of (a) STT-MRAM, (b) SOT-MRAM with MgO and (c) SOT-MRAM with Co/Pt interfacial oxidation.

4.5 Oxidation Model of the Platinum Oxide System

In determining the SOTs in the previous section, we ignored the loss of magnetization of the cobalt layer as well as the actual current flow in the platinum layer. These parameters need to be included in the analysis to determine the accurate value of torques generated by the applied current. Only then can we obtain a fair comparison between the oxidized and un-oxidized systems as well as determine the cause of these effects. In order to accurately evaluate the current density in platinum, we need to determine the resistivity of our platinum layer.

4.5.1 Corrections to the conductance measurements

One of the advantages of having all the devices made on the same wafer is that the growth conditions of all the devices are exactly the same, enabling us to determine material parameters accurately. Unlike bulk materials, the resistivity of thin films is not constant and instead varies with thickness.

Hence, having a wedge of platinum allows us to determine this dependence. Let us consider the thickness dependent conductance of our samples which was plotted previously and plotted here again in Figure 4.23 (a) for convenience. It shows that the conductance of our samples decreases with decreasing platinum thickness. This curve, however, hides the fact that there is an inherent curvature to our films arising from the growth technique. This was discussed in the previous chapter and is common to all sputtered films with planetary rotation. This effect is seen in the slight curvature of the conductance at thicker platinum thicknesses, where the resistivity being constant, should have had a linear dependence. This curvature can also be determined by considering the conductance perpendicular to the wedge of platinum and thereby keeping all the layer thicknesses constant in principle. These can be measured from the transverse strips on the wafer labeled L-TStrips and R-TStrips. The conductance of these strips is plotted in Figure 4.23 (b) and clearly shows the curvature of the deposited films. A renormalized fit of this plot, as it also includes the platinum film curvature, can be utilized to correct for this thickness variation in Figure 4.23 (a). The corrected plots for the UO and OX samples are plotted in Figure 4.24 (a) and (b) respectively. It shows that the conductance has a linear variation on the platinum thickness at higher thicknesses while it deviates from this linear behavior at smaller thicknesses. This is a signature of the variation of resistivity of the platinum films at the thinner side. This is a consequence of the fact that at such smaller thicknesses, the mean free path of the films is of the same order or larger than that of the platinum film thickness. This results in the surface scattering playing a much larger role in the resistivity of the films. In an ideal single-layer film, we can expect this deviation of conductance to continue on to much lower thicknesses until it drops sharply to zero at the percolation limit of the film. In a multilayer film such as ours, we wouldn't see the sharp conductance drop as below the percolation limit of platinum, the current would just flow in the lower layers beneath it. We, however, are above such a threshold and are not concerned by it.

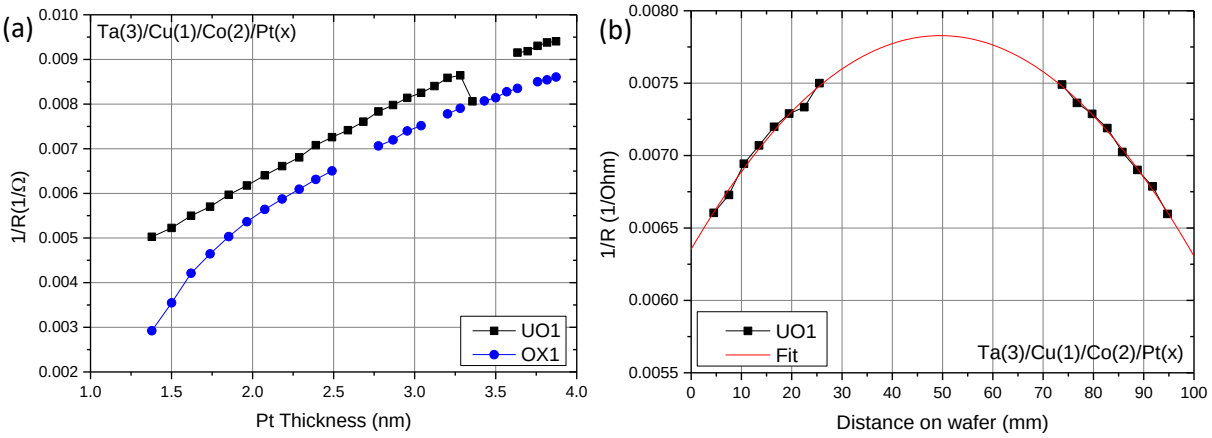

Figure 4.23: (a) Dependence of the conductance of the UO1 and OX1 samples on the Pt thickness. (b) The conductance of the strips perpendicular to the platinum gradient, of UO1. Plotted with respect to the transverse position on the wafer.

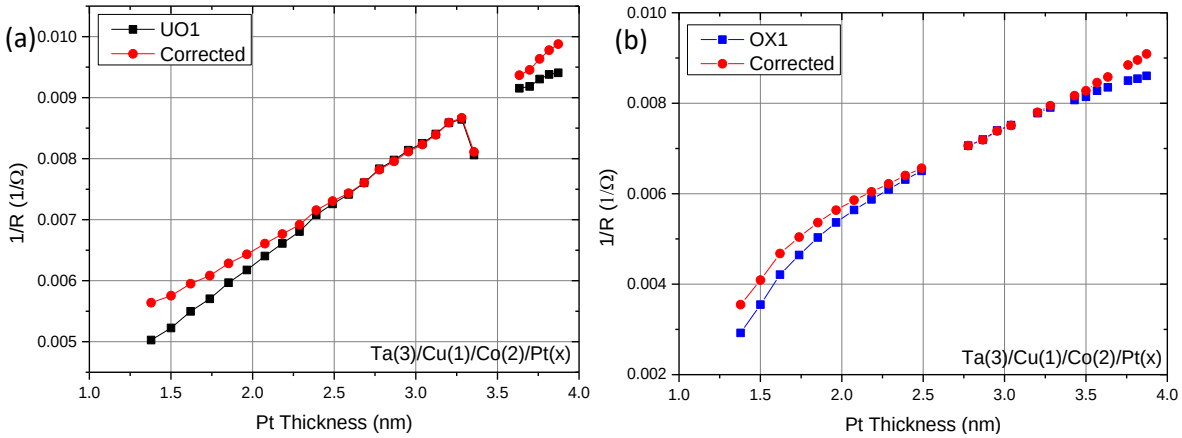

Figure 4.24: Conductance of (a) UO1 and (b) OX1 corrected for the curvature induced by the deposition of all the layers.

4.5.2 Evaluating the platinum resistivity

We can now determine the resistivity of our Pt layer utilizing the corrected conductance curves. There are multiple models that can be used to determine the resistivity of thin films depending on their thickness. Two of the commonly used ones are the Fuchs-Sondheimer (FS) model[141,142] and the Mayadas-Shatzkes (MS) model[143]. The FS model includes the isotropic scattering from phonons and point defects. In addition, it also considers the effect of non-specular reflection of the electrons from the film surfaces at reduced thickness causing the increased resistivity of the films. The MS model on the other hand also includes the scattering from the grain boundaries, modeled as planar potentials. In this work, we use a general FS model as the surface scattering effects should be more predominant. The conductance of the film considering these effects are given by

$$\frac{1}{R} = \frac{1}{R_0} + \frac{w*t}{\rho_0\left(1+\frac{3\lambda}{8t}\right)l} \times (1-p) \tag{4.13}$$

Here R is the total conductance, R_0 the conductance of the uniform layers of the film beneath the Pt layer, w the width of the strip, t the thickness of the platinum layer, ρ_0 the bulk resistivity of the platinum layer, λ the mean free path of the electrons in the film, l the distance between the voltage probes in our 4-point resistance measurement and p the specularity parameter. In this study, we assume a completely diffuse scattering of electrons from the surface of the metal leading to $p = 0$. This is a reasonable assumption in metals with surface roughness larger than the de Broglie wavelength of the free electrons. We can use this model to fit the corrected plot of the UO1 conductance. This fit is plotted in Figure 4.25 (a). The material-specific values we extracted for the UO1 sample are R_0 = 216.46 Ω, ρ_0 = 19.42 μΩcm and λ = 9.34 nm. These values are consistent with the values reported in the literature. Although the extracted mean free path is larger than the film thickness, the model fits our data quite well and the extracted values consistent with literature. This has been the case in multiple other samples as well, increasing our confidence in the model. Once we have determined these parameters, we can plot the resistance, the conductance and the resistivity of the platinum layer, shown in Figure 4.25 (b), (c) and (d) respectively. The resistance of the platinum layer is given by

$$R_{Pt}(t) = \frac{\rho_0\left(1+\frac{3\lambda}{8t}\right)l}{w*t} \tag{4.14}$$

And the resistivity is given by

$$\rho_{Pt}(t) = \rho_0\left(1+\frac{3\lambda}{8t}\right) \tag{4.15}$$

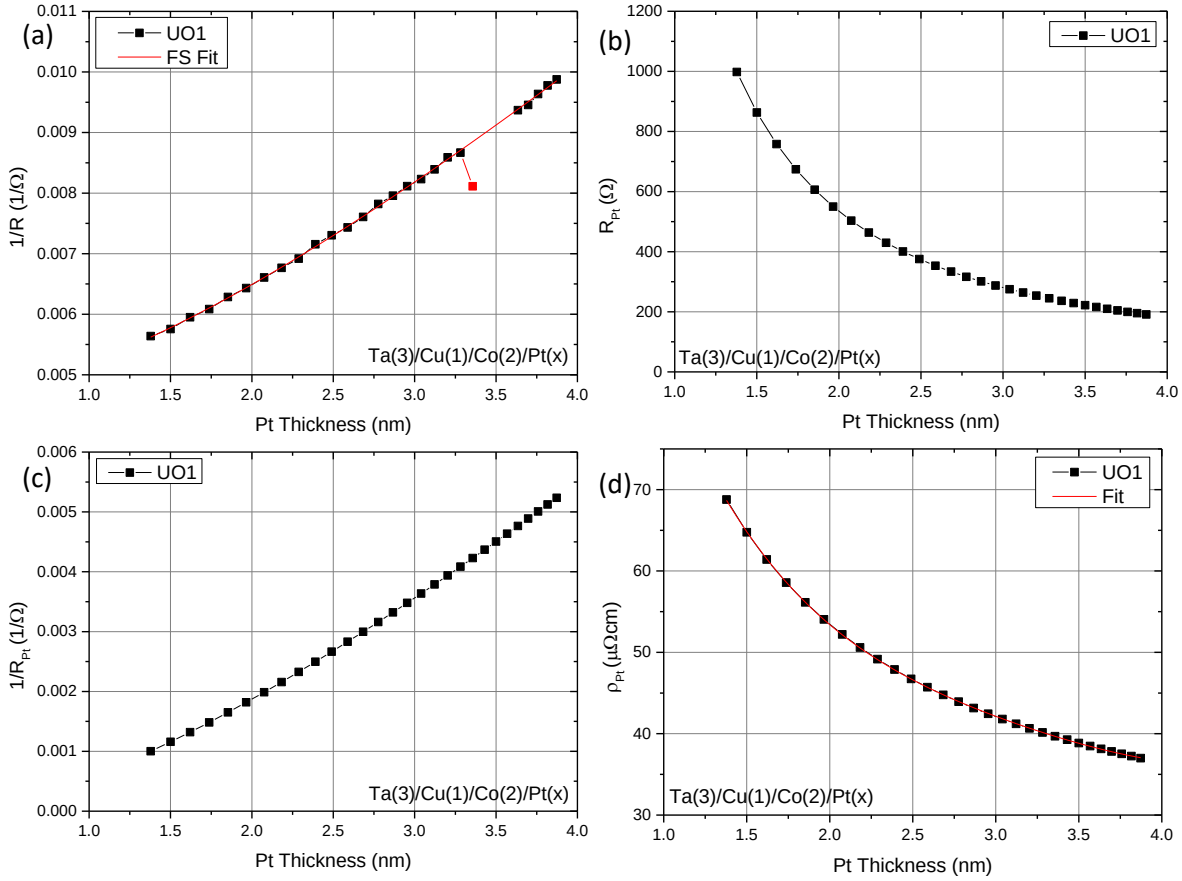

Figure 4.25: (a) Dependence of the total conductance on the Pt thickness of the UO1. The red curve shows the FS fit to this data. Dependence of (b) resistance (c) conductance and (d) resistivity on the platinum thickness. The red curve in the last plot is a polynomial fit to the data.

It is evident that the resistivity increases with decreasing thickness of platinum, as described by the model. This variation in current density is also significant in the context of normalizing SOTs. As the resistivity is no longer constant, current density might be an appropriate normalization factor rather than the current in the platinum layer.

Now that we have characterized the electrical properties of the un-oxidized sample, we can now turn our attention to the oxidized one. As plotted in Figure 4.23 (a), at larger thicknesses of platinum, there is a constant offset between the oxidized and the un-oxidized curves. As the plasma oxidation of platinum is expected to oxidize a uniform layer of platinum into platinum oxide, this constant offset can be considered as the reduction of the effective thickness of the electrically conducting platinum. This model can be visualized as shown in the schematic of Figure 4.26, where the light blue region shows the uniformly oxidized layer of platinum at larger thicknesses. The constant offset in conductance hence corresponds to this uniform platinum oxide layer. We can thus determine the thickness of this oxide layer from the conductance plot corresponding to the lateral offset. This is plotted in Figure 4.27 (a). The lateral offset is calculated from the conductance plots where the variation in conductance from the curvature of the underneath layers is corrected for, as discussed previously.

As the uniformly oxidized layers do not contribute to the conduction of current and hence to the SOTs, we can subtract out this thickness from the total platinum thickness, obtaining the effective thickness of platinum which contributes to the SOTs, plotted in Figure 4.27 (b). This plot indicates that if we consider the effective platinum thickness, both the UO1 and OX1 conductance plots line up perfectly

for larger platinum thicknesses. This is however not true for smaller thicknesses of platinum, where we see a large deviation from the expected curvature of conductance.

The same procedure can be repeated for the second set of samples UO2, OX2 and the conductance values are plotted in Figure 4.28 (a). The thickness of the uniform oxidized layer is similar to that of the first sample at around 0.4 nm. This oxide thickness is considered while shifting the oxidized curve laterally to produce the conductance plots as a function of the effective platinum thickness. The curves once again line up on top of each other, as plotted in Figure 4.28 (b).

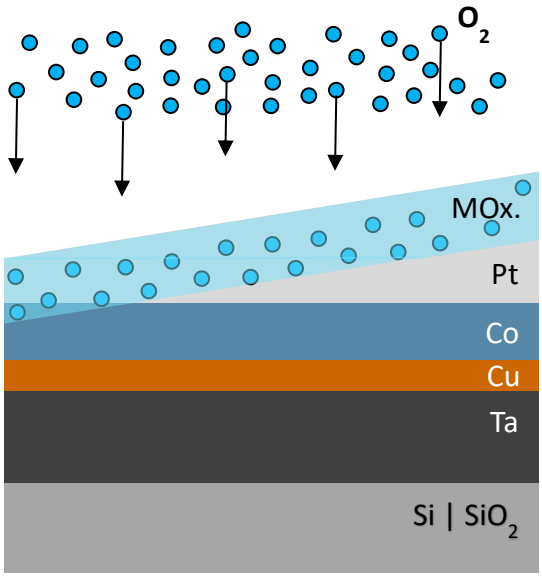

Figure 4.26: Schematic of the sample stack depicting the uniform plasma oxidation of the platinum layer in light blue color. This layer is denoted as MOx in the figure.

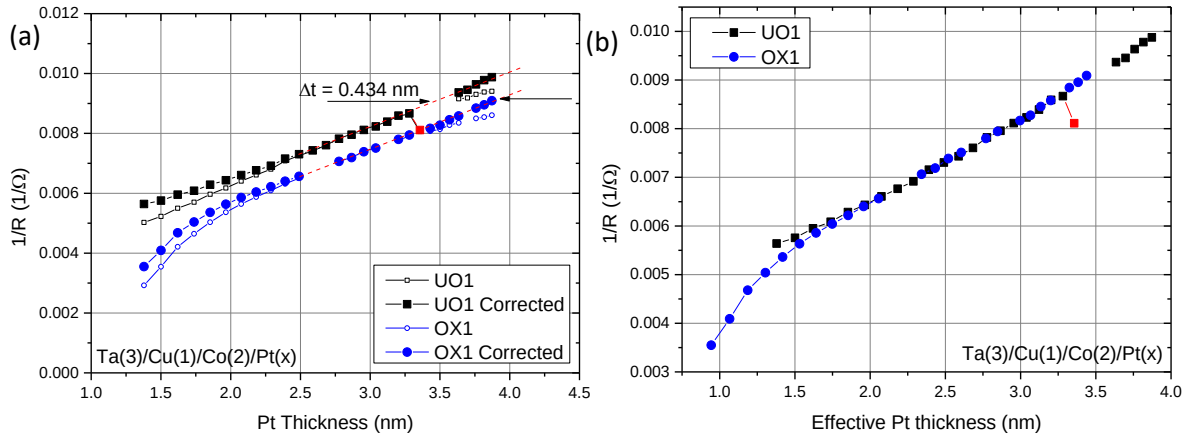

Figure 4.27: Conductance of UO1 and OX1 plotted against (a) the platinum thickness and (b) the effective platinum thickness. The platinum oxide thickness is determined from the constant offset between the two curves of (a) at higher thicknesses of platinum. The corrected curves refer to the layer curvature correction.

These curves then can be fit with the FS model to extract the material-specific parameters. These values for UO2 are R_0 = 206.98 Ω, ρ_0 = 20.55 μΩcm and λ = 8.74 nm. The corresponding resistance and resistivity plots are shown in Figure 4.29 (a) and (b) respectively. This set of samples, however, is different from the first set of samples at lower thickness. In this case, the uniform oxidation continues up to the thinnest sample, indicating that the interface is likely metallic Co/Pt with very light oxidation. As the conductance and magnetization values of both the UO1 and UO2 samples are similar, any significant structural differences can be ruled out. Hence, the deviation is most likely caused by a difference in the actual oxidation conditions.

Regardless, we need to determine the origin of this deviation in the conductance plot of OX1 and more importantly, what is happening at the interface. There are two main probable causes. The first is that the platinum thickness at the lower end is reduced to such an extent so as to significantly change the resistivity and hence the conductance. The other is that the oxygen enters the cobalt layer and the oxidation of the cobalt layer contributes to this deviation. We thus performed ab-initio DFT calculations on a Co/Pt structure in the presence of oxygen to guide us in our analysis.

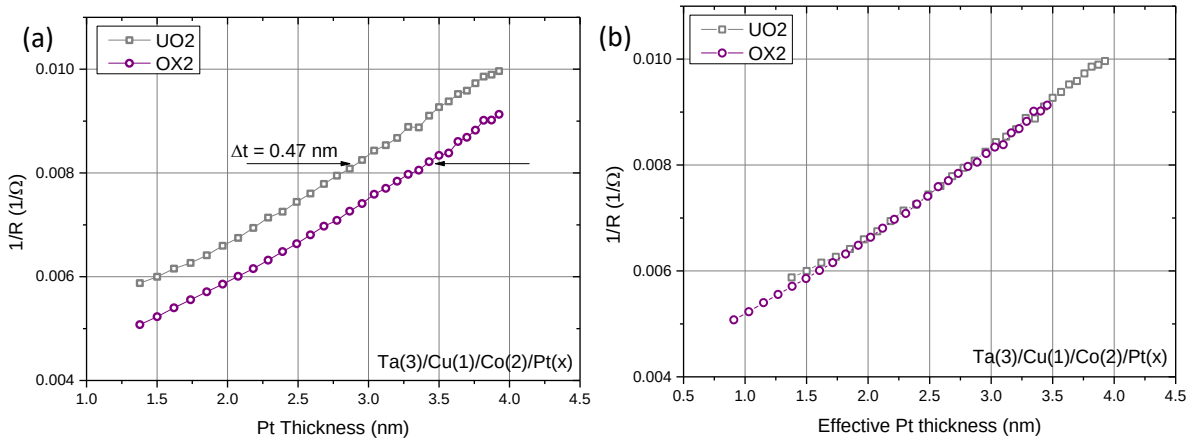

Figure 4.28: Conductance of UO2 and OX2 plotted against (a) the platinum thickness and (b) the effective platinum thickness.

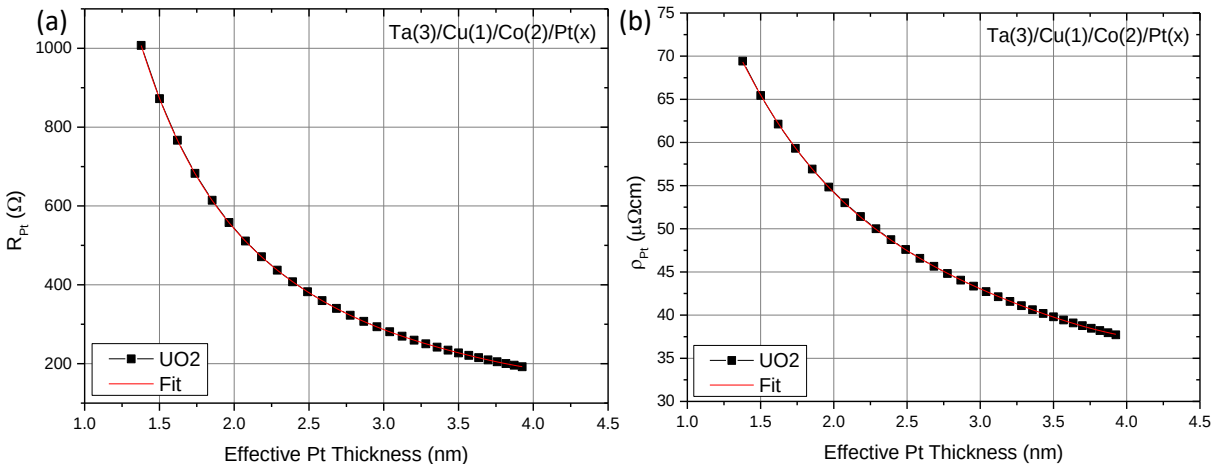

Figure 4.29: (a) Resistance and (b) resistivity as a function of Pt thickness of sample UO2.

4.5.3 Ab-initio DFT calculations: energetics

In order to understand the oxygen ion dynamics in the system, we performed ab-initio DFT calculations. These first-principle calculations are based on the Projector-Augmented Wave (PAW) method[144]. The valence electron wave function, modeled as a plane wave, tends to have rapid oscillations near the core of the ions, modeled as pseudo-potentials. This method transforms these wave functions into smooth wave functions and allows for an efficient calculation of the ground state of the electrons. This is implemented in the Vienna Ab initio Simulation Package (VASP)[145–147]. In order to determine the energetics and the electrical properties of a solid, it is necessary to solve the quantum mechanical equations governing all the electrons in the system, i.e. it is a many-body problem. Hohenberg P. and Kohn W., in 1964, showed that one can compute the energy and thereby the properties of a system from the knowledge of the average density of electrons in all points in space[148]. A density functional exists for all systems that connects its energy to the density of electrons. Kohn W. and Sham L. J. further proposed that this many-body problem can be treated as a system of one-electron Schrödinger equation of non-interacting electrons that generate the same density as the original system of interacting particles[149]. This forms the basis of Density Functional Theory and is known as ab-initio or first-principles calculation since the only inputs to this model are the physical constants. In order to determine the effective potential of this system, it is necessary to determine the exchange-correlation potential as a function of electron spin densities. Here exchange potential refers to the potential arising out of the exchange Hamiltonian whereas the correlation potential refers to the potential arising out of the interactions between the electron and the other electrons in the system such as the Coulomb potential. These potentials can be determined from the electron density at each point in space, i.e. Local Spin Density Approximation (LSDA). LSDA can be improved by including the first derivatives of the electron density, giving rise to Generalized Gradient Approximation (GGA)[150]. We use GGA in our DFT calculations.

Our system consists of a Pt(3 ML)/Co(3 ML)/Pt(5 ML) tri-layer structure, plotted in Figure 4.31 (a). This structure is periodic in the X-Y plane (orthogonal to the plane plotted in Figure 4.31). A kinetic energy cut off of 520eV has been used for the plane-wave basis set and an 11 x 11 x 1 k-point mesh to sample the first Brillouin zone. In order to determine the energy of the system with oxidation, a plane of oxygen atoms is placed into the lattice along the X-Y plane, as plotted in Figure 4.31 (b). This structure is then relaxed in the X-Y directions and the system energy is calculated. This enables us to move this plane of oxygen atoms within the structure along the Z-axis and determine its effect on the energetics. The oxygen displacement is described by moving the O atoms from the first Pt-Pt plane at the interface towards the Co-Pt plane. The in-plane lattice constant was fixed to that of Pt (a=2.115 Å), while the structure was relaxed until the forces became smaller than 1 me/Å. The resulting energetics plot is shown in Figure 4.30, which plots the dependence of the total energy of the system on the position of the oxygen atom. It clearly shows that it is energetically costly for oxygen to penetrate into the platinum layer, with the energy of the system increasing with each successive layer that the oxygen atoms penetrate into the platinum layer. However, once near the interface, it is far more favorable for the oxygen to jump to the Co/Pt interface as it is energetically more favorable. Also, the oxygen prefers to remain in sites between the planes of platinum rather than in the same plane, which is costly energetically. In other words, it costs energy to pump oxygen into platinum. This is understandable as platinum oxides have low (less negative) enthalpies of formation (PtO_2: -80 kJ/mol; Pt_3O_4: -163kJ/mol)[151]. However, once the oxygen reaches near the Co/Pt interface, it is very likely that the oxygen diffuses to the interface as it is far more favorable energetically. This is again consistent comparing the enthalpies of formation of Pt and Co. Co has a more negative enthalpy of formation (CoO: -237.9 kJ/mol; Co_3O_4: -891 kJ/mol)[152] compared to Pt. Hence, the oxygen prefers to bond with

Co and stay at the Co/Pt interface rather than in the bulk Pt. Further, once within the Co, the oxygen prefers to migrate further into the bulk of the Co rather than stay at the Co/Pt interface.

This model is drastically different from the oxidized HM models considered so far[108–111]. In all these cases, the HM is considered completely oxidized whereas the FM is completely un-oxidized. In such a scenario, the HM is completely insulating while all the current that generates the SOTs flows in the FM and the other un-oxidized layers. This has led the authors to attribute the increase in torques to a purely interfacial effect. Comparing this model with the tungsten oxide used in Demasius et. al.[108], it is to be noted that the enthalpy of formation of WO_3 (-842.91 kJ/mol)[153] is large compared to CoO (-237.9 kJ/mol). Though the interface could still support Co III and IV oxidized states as the enthalpy of formation of these states are still larger (891 kJ/mol).

We also calculated the magnetic moment on each atom with and without the presence of oxygen in the system, plotted in Figure 4.32. It shows that when the oxygen is present at the Co/Pt interface, there is a loss in the magnetic moment of the Co atoms at the interface. This is consistent with our saturation magnetization data obtained from VSM measurements, which shows a drop in Ms at thinner platinum thicknesses, allowing the oxygen to reach the interface and the Co bulk. We can thus use this model of oxidization to determine the platinum resistivity of our oxidized sample.

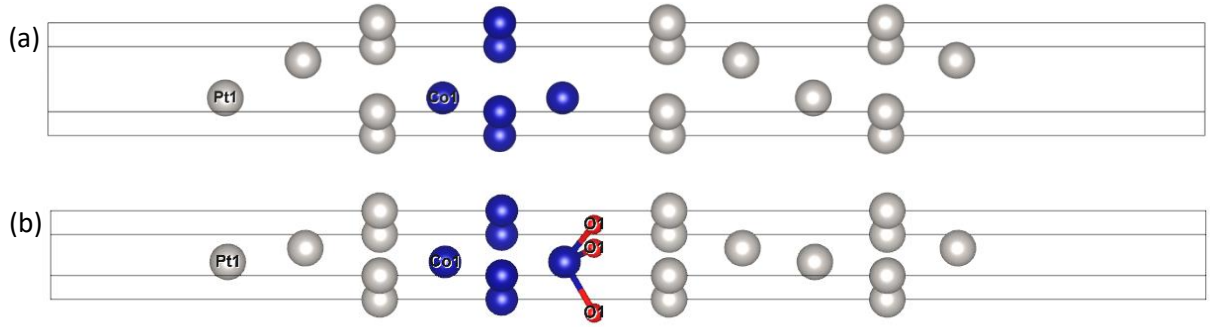

Figure 4.31: (a) Pt(3 ML)/Co(3 ML)/Pt(5 ML) structure used for the ab-initio DFT calculations. The grey circles denote Pt atoms and the blue Co atoms. (b) The structure with the oxygen atoms present at the Co/Pt interface denoted by the red circles.

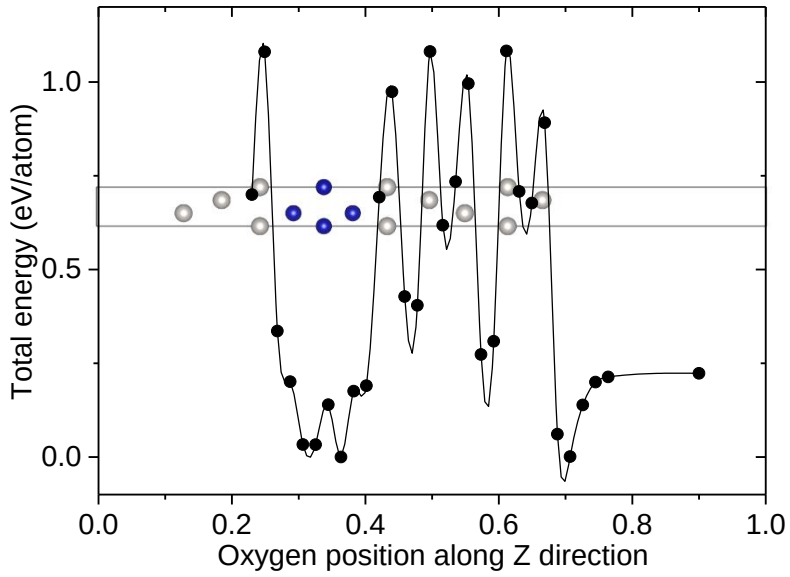

Figure 4.30: Energy of the system as the oxygen atom is moved from the surface (right) of the Pt/Co/Pt towards the Co/Pt interface.

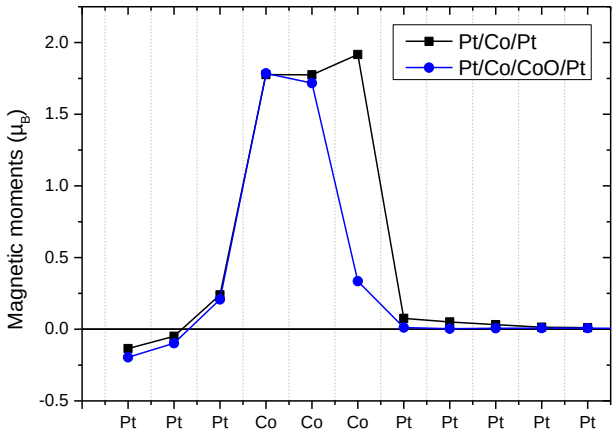

Figure 4.32: Atomic magnetic moment of each plane of the system with and without the presence of the oxygen atom at the interface.

4.5.4 Evaluating platinum resistivity of the oxidized sample

Now that we understand that the oxygen in platinum near the interface of Co/Pt prefers to stay on the cobalt side, we can model this into our resistivity calculations. Figure 4.33 (a) shows the schematic of the original model we had proposed with constant oxidation of the platinum layer. Only at the lower end when the platinum layer thickness was smaller than the constant oxidation thickness, would we expect the oxidation of cobalt. This, however, needs to be corrected for the affinity of oxygen for cobalt near the interface. This new model is plotted in Figure 4.33 (b), which shows that at thicker platinum thicknesses, there is indeed uniform oxidation of platinum. However, at lower thicknesses, when the oxygen reaches near the interface, it is able to overcome the energy barrier of platinum and reach the cobalt layer. Here it bonds with Co forming an oxide of cobalt and lowering the saturation magnetization. This also implies that at the interface, the platinum is no longer completely oxidized and insulating, but instead metallic and conducting. In reality, we do not expect completely oxygen-depleted platinum near the interface. We, however, expect the density of oxygen to be lower near the interface as it is pumped into the cobalt layer. We can now use this model to determine the resistivity of the platinum layer.

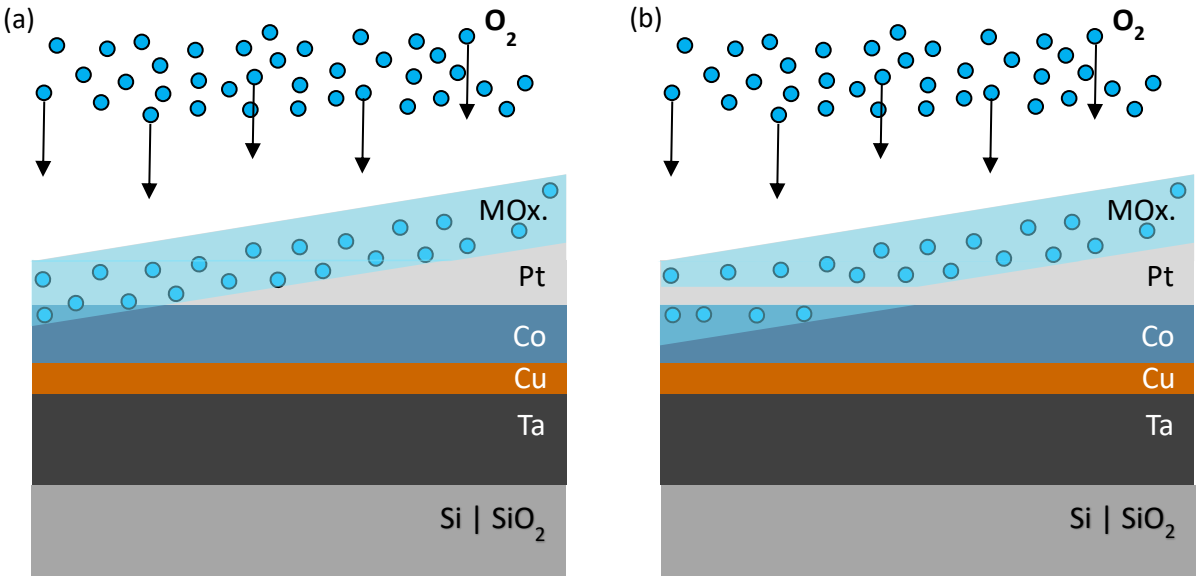

Figure 4.33: (a) Oxidation model with a uniform oxidation of Pt. (b) Oxidation model with pumping of oxygen into Co near the Co/Pt interface.

The conductance of the platinum layer of the OX1 sample is plotted in Figure 4.34. The portion of the curve on the white background corresponds to the thicker platinum where a layer of uniform thickness is oxidized by the oxygen plasma. The yellow background corresponds to the region where we do not see any significant deviation in the conductance plot compared to the UO1 sample. There is however superficial oxidation of Co visible in the magnetization curves. The red background corresponds to the thickness of platinum where the conductance plot deviates significantly from that of the UO1 sample and there is a significant drop in magnetization as well indicating the presence of oxygen in the Co layer. The red horizontal line corresponds to the conductance R0 of the layers underneath the Pt of the UO1 layer. The red dotted line that follows the curve is the Fuchs-Sondheimer fit to the conductance plot. Here the deviation of the conductance curve is considered to be originating from the oxidized cobalt rather than the platinum. Hence, above 1.8 nm of Pt, we observe uniform oxidation of Pt of a constant thickness. However, below this limit, the oxygen at the Co/Pt interface gets pumped into the Co layer and results in the deviation seen in the conductance curve. The extracted parameters are R_0 = 217.52 Ω, ρ_0 = 18.6 μΩcm and λ = 9.89 nm. These values are consistent with the values extracted for the UO1 samples as they are indicative of the metallic platinum, which is common in both samples, rather than the oxidized part. These values are then used to determine the resistance and the resistivity of platinum at all thicknesses, as plotted in Figure 4.35 (a) and (b) respectively.

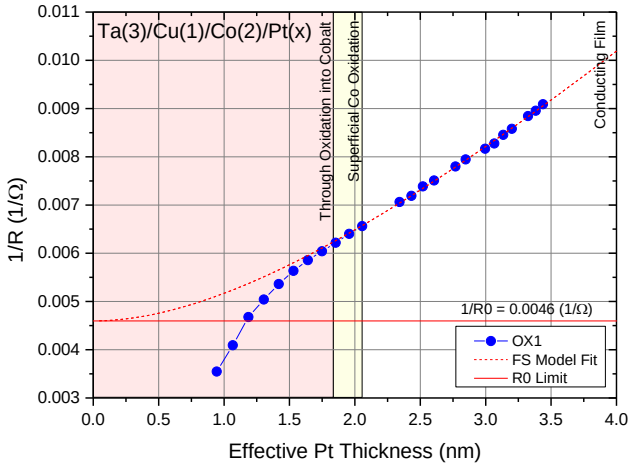

Figure 4.34: Conductance of the OX1 sample showing the Fuchs-Sondheimer fit.

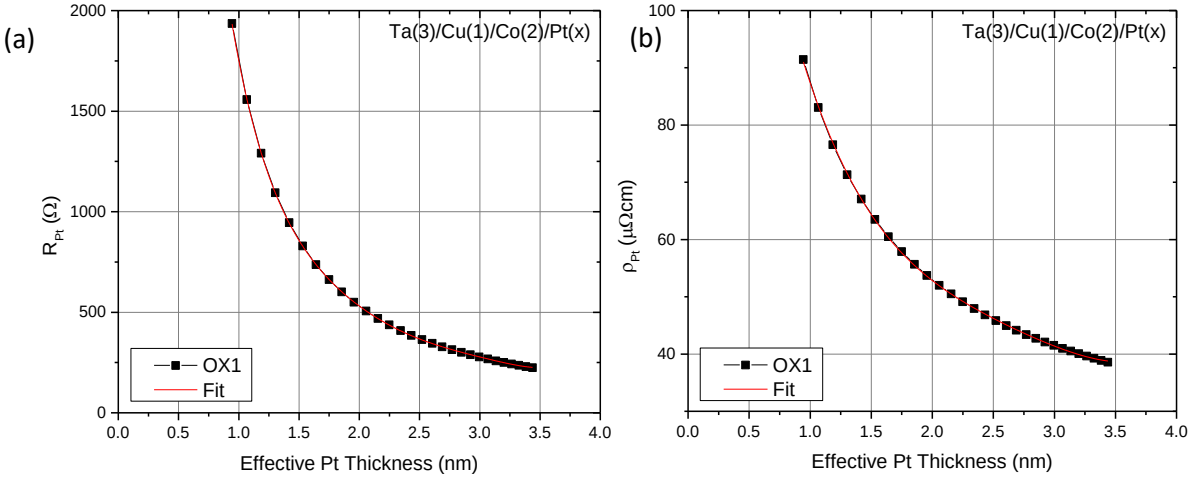

Figure 4.35: (a) Resistance and (b) resistivity of the OX1 sample as a function of Pt thickness.

We also fit the conductance plot of the OX2 sample using the FS model. Although in this case, it is more straightforward than in the case of OX1 as there is no significant deviation as a result of oxidation. The material parameters extracted are R_0 = 210.85 Ω, ρ_0 = 20.5 μΩcm and λ = 8.47 nm. The resistance and resistivity of the platinum are then calculated and plotted in Figure 4.36 (a) and (b) respectively.

It is to be noted here that this model that we have considered for the oxidized sample is a boundary condition. The actual sample would most likely have a gradual depletion of oxygen near the interface. One way to verify if this model is valid is to study the effect of oxygen on the Co layer. The presence of oxygen in the Co layer can affect the fundamental magnetic properties of the material leading to a loss of saturation magnetization. We study DMI and the Heisenberg exchange using the Brillouin Light Scattering (BLS) measurements.

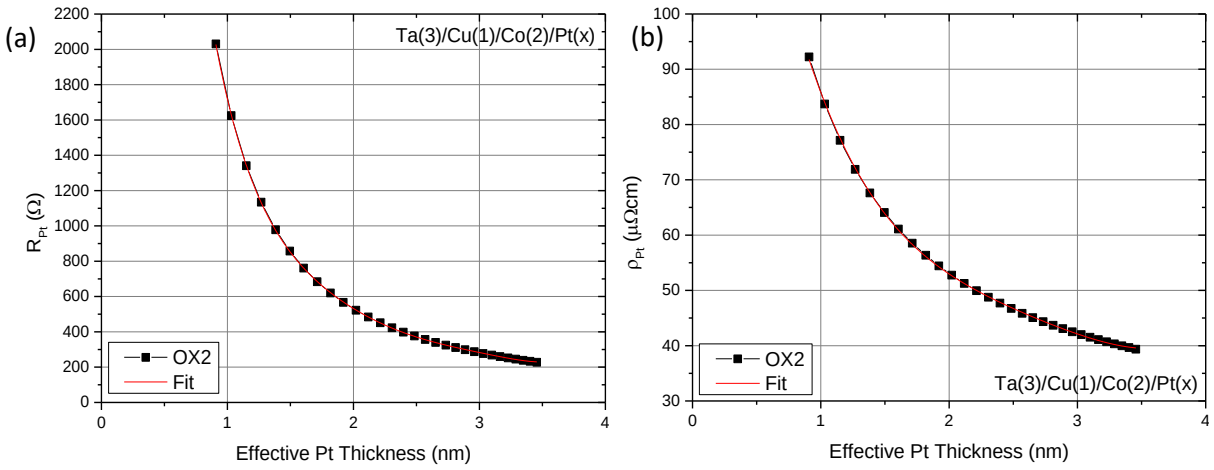

Figure 4.36: (a) Resistance and (b) resistivity of the OX2 sample as a function of Pt thickness.

4.5.5 Brillouin Light Scattering (BLS) measurements: symmetric and anti-symmetric exchange

The interaction between magnetic moments of 3d transition metals can be described by their electron-electron interactions. The wavefunction of a system of two electrons, at positions r_1 and r_2 with individual wave functions $\psi(r_1)$ and $\psi(r_2)$, can be described by the wavefunction $\mathbf{\Psi}(r_1,r_2)$. This wavefunction is antisymmetric so as to distinguish between the two electrons. The energy of such a system can be described by terms that correspond to the two different electrons as well as an interaction term. This interaction term denotes the energy that arises from exchanging the electrons between the two atomic sites and is called the exchange energy. If we also consider the spins of these electrons, the total wave function of the system can be written as[154]

$$\mathbf{\Psi}_{Tot}(\mathrm{r}_1,\mathrm{r}_2) = \mathbf{\Psi}(\mathrm{r}_1,\mathrm{r}_2)\varphi(s_1,s_2) \tag{4.16}$$

Here $\varphi(s_1,s_2)$ denotes the spin wave function of the system. Once again, for the electrons to be distinguishable, the total wave function must be antisymmetric. This implies that depending on the symmetry of $\mathbf{\Psi}(\mathrm{r}_1,\mathrm{r}_2)$, $\varphi(s_1,s_2)$ must be either symmetric or antisymmetric, corresponding to parallel or antiparallel spins. The exchange energy Hamiltonian can thus be written in terms of the spins as

$$H_{ex} = -J_{ij}\boldsymbol{S}_i \cdot \boldsymbol{S}_j \tag{4.17}$$

Here the sign of J_{ij} denotes the parallel or antiparallel alignment corresponding to the ferromagnetic or antiferromagnetic ordering.

The antisymmetric component of the magnetic exchange is known as the Dzyaloshinskii-Moriya Interaction (DMI). This type of exchange interaction arising from SOC was first worked out by Dzyaloshinskii I. E.[155] and Moriya T.[156] for non-centrosymmetric systems, i.e. systems which lack inversion symmetry. Fert A. and Levy P. M. further showed that spin-orbit scattering of the conduction electrons by non-magnetic HMs can result in the same phenomena[157]. Hence the typical FM/HM structure used for SOT-MRAM, which has broken inversion symmetry as well as the high SOC from the HM, is a suitable candidate for studying DMI. Here, the DMI between two spins of the FM is mediated by an adjacent atom of the HM. It is hence an interfacial phenomenon. DMI can lead to chiral magnetic textures such as Néel domain walls[158] and Skyrmions[159]. The corresponding Hamiltonian takes the form[160]

$$H_{DMI} = -\boldsymbol{D}_{ij} \cdot \left(\boldsymbol{S}_i \times \boldsymbol{S}_j\right) \tag{4.18}$$

Where $\boldsymbol{D}_{ij}$ is the DMI vector that is perpendicular to the unit vector connecting the two spins, $\hat{\boldsymbol{e}}_{ij}$, and lies in the symmetry breaking plane. It is given by

$$\boldsymbol{D}_{ij} = D_{ij}\hat{\boldsymbol{n}} \times \hat{\boldsymbol{e}}_{ij} \tag{4.19}$$

Here $\hat{\boldsymbol{n}}$ is the interface normal.

The Heisenberg exchange and the DMI depend on neighboring interactions. Hence any disruption to it via oxidation should lead to a net reduction of the exchange and the DMI. This would thus form a test to check the validity of our model.

DMI can also affect spin waves in thin-film multilayers. It can lead to asymmetric dispersion[161] as well as change its frequency and amplitude[162]. Moon J-H computed the analytical expressions for the spin-wave dispersion in the presence of DMI as[163]

$$\omega_k = \omega_k^0 + \omega_k^{DMI} = \mu_0\gamma\sqrt{\left(H + \frac{M_s}{4} + Jk^2\right)\left(H + \frac{3M_s}{4} + Jk^2\right) - \frac{e^{-4|k|d}M_s^2}{16}(1 + 2e^{2|k|d})} + \frac{2p\gamma Dk}{M_s} \tag{4.20}$$

Here ω_k is the spin-wave angular frequency, $\omega_k^{DMI}$is the DMI contribution to this dispersion, γ is the gyromagnetic ratio, *H* is the external field, M_s is the saturation magnetization, $J = 2A/\mu_0 M_s$, *A* is the exchange stiffness constant, *k* the wavenumber, *d* the film thickness and *p* = ±1 denotes the direction of the external field. The DMI contribution to the spin-wave dispersion is given by the last term of eq. (4.20). This term shows that the DMI leads to a linear, and hence asymmetric dispersion in *k*.

Light scattering is a versatile method for studying various systems where a beam of light is scattered off the system. The reflected beam contains information regarding the system. These techniques can be classified as elastic and inelastic. In the case of elastic scattering, there is no change in energy or frequency of the light after reflection. This is known as Rayleigh scattering[164]. Inelastic scattering, on the other hand, results in a change of both and is known as Raman scattering[165]. Specifically, a decrease in energy of the reflected photon is known as Stokes scattering and an increase in energy of the reflected photon leads to anti-Stokes scattering. Brillouin scattering is an inelastic scattering of light from low-frequency waves in the medium[166]. It is ideal to study phonons, polarons, and magnons in a system. We can thus use BLS to study the effect of DMI on spin waves in our system. These measurements were performed by Amrit Kumar Mondal, Avinash Kumar Chaurasiya and Anjan Barman at the S. N. Bose National Centre for Basic Sciences, India.

The BLS measurements were performed in the Damon-Eshbach (DE) mode[167] with an external field of up to $\pm$0.22 T applied in the plane of the film, orthogonal to the direction of propagation of the spin waves. The angle of incidence of the laser, θ, is varied to obtain the wave-vector selectivity, $k = (4\pi/\lambda)\sin\theta$, where λ is the wavelength of the laser, 532 nm. The details of the setup can be found in ref[168]. The material parameters are determined using the uniform precessional mode at the normal incidence of the laser (*k*=0). The external field dependence of the spin-wave frequency for sample UO1(2.68) is plotted in Figure 4.37 (a). This plot is fit with the Kittel equation to determine the Landé g-factor and the effective magnetization. The Kittel equation is given as

$$f = \frac{\mu_0\gamma}{2\pi}\left[H\left(H + M_{eff}\right)\right]^{1/2} \tag{4.21}$$

These were determined to be 2 and 8.9x10^5 A/m respectively. The effective magnetization for UO1 and OX1 samples are plotted in Figure 4.37 (b). It is to be noted that these values are higher than the values obtained from the FMR measurements which were plotted previously, that we attribute to difference in the experimental technique.

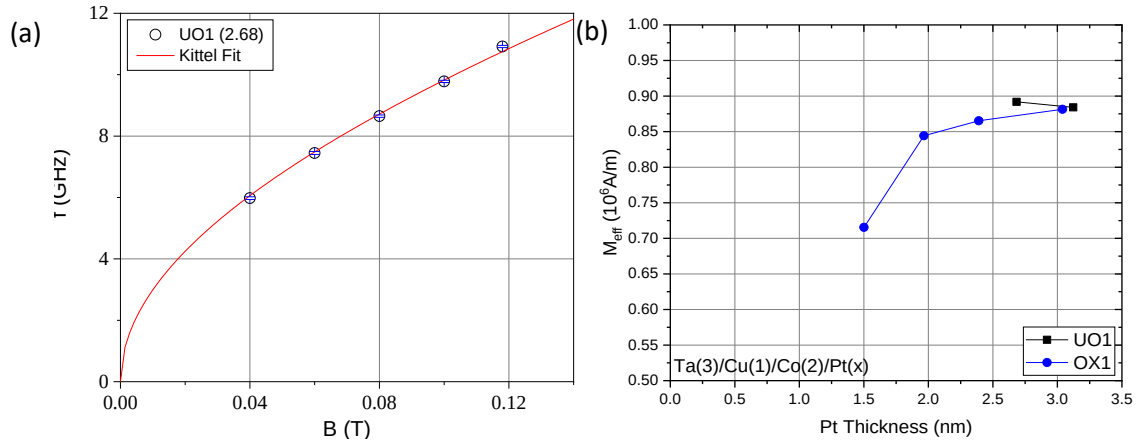

Figure 4.37: (a) External field dependence of the spin-wave frequency of UO1(2.68). (b) The effective magnetization of UO1 and OX1 samples determined from BLS measurements.

In order to determine the DMI, the dispersion spectra need to be determined. The BLS spectra for two different samples are plotted in Figure 4.38. These were measured with an external field of 0.1 T and a wave vector of 18.09 rad/µm. The DE spin waves are confined to the surface of the FM film with the spin-wave with positive wave vector propagating on the top surface and the negative wave vector propagating on the bottom surface. As the thickness of these films is smaller than the optical skin depth, we can detect both the spin waves in the film that correspond to the two peaks shown in the spectra. The solid blue curve is the Lorentzian fit of the spectra while the dotted blue curve is its mirror image. The difference between the peak positions of these two curves shows the asymmetry in the frequency of the counter-propagating spin waves. This difference in frequency can be written in terms of the DMI as

$$\Delta f = \frac{[\omega(-k)-\omega(k)]}{2\pi} = \frac{2\gamma}{\pi M_s} Dk \tag{4.22}$$

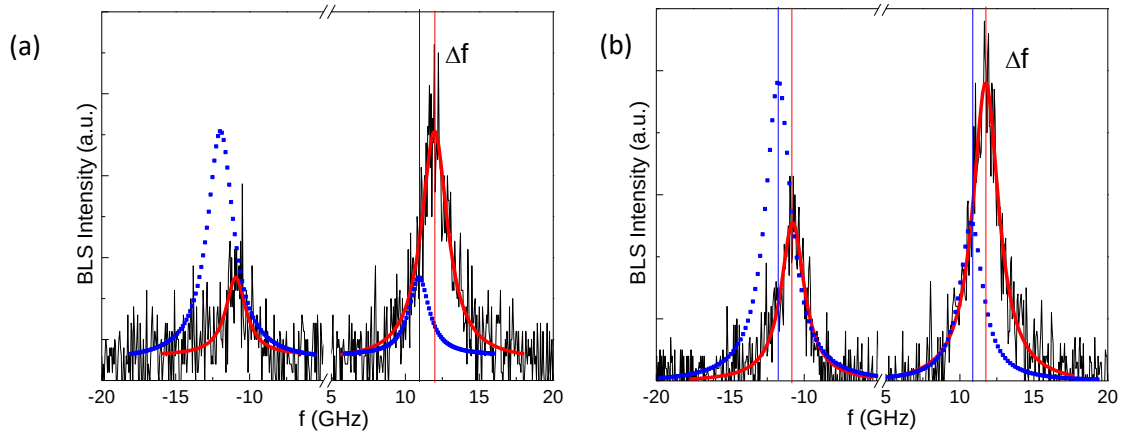

Figure 4.38: BLS spectra of (a) UO1(2.68) and (b) OX1(2.39) measured at wave vector k = 18.09 rad/µm with an external field of 0.1T. The lorentzian fit is shown by the red line. The frequency difference between the counter-propagating waves are marked as Δf.

The plot of the *k* dependence of Δ*f* is shown in Figure 4.39 (a). As per the above equation, the DMI is given by the slope of this curve and numerically equal to -0.53 mJ/m^2. The DMI can also be determined by fitting the dispersion spectra plotted in Figure 4.39 (b). To fit the spectra, we use a modified form of the eq. (4.20) given by[169]

$$\omega_k = \omega_k^0 + \omega_k^{DMI} = \mu_0\gamma\sqrt{(H + Jk^2 + \xi(kL)M_s)(H - H_K + Jk^2 + M_s - \xi(kL)M_s)} - \frac{2\gamma Dk}{M_s} \quad (4.23)$$

Here $\xi(x) = 1 - \left(1 - e^{-|x|}\right)/|x|$, *L* is the magnetic film thickness and $H_K = 2K/(\mu_0 M_s)$ is the uniaxial anisotropy. This fit is plotted as the red line in Figure 4.39 (b). As expected, this is asymmetric with respect to the wave vector. The yellow line in this figure is the plot of the dispersion relation without including the DMI and hence is symmetric.

The DMI values for UO1 and OX1 are plotted in Figure 4.40 (a). It shows that with decreasing thickness, there is a drop in the DMI. In other words, with increasing oxidation of the FM layer, the asymmetric exchange decreases. We can determine the interfacial DMI, by normalizing the DMI values to the thickness of the FM assuming the film has an fcc structure with a lattice parameter of 0.37 nm. It is given by[170,171]

$$D_{int} = D\frac{\sqrt{3}}{a}t \quad (4.24)$$

Here D_{int} is the interfacial DMI, D is the volume-averaged DMI, a is the lattice constant and t is the FM film thickness. The Pt thickness dependence of the interfacial DMI is plotted in Figure 4.40 (b). It too shows a decrease in the interfacial DMI indicating the oxidation of the FM. It should, however, be noted that the DMI is also expected to decrease with decreasing thickness of Pt as studied by Tacchi et. al[171]. They studied the DMI variation with Pt thickness in a CoFeB/Pt system. However, the drop in DMI with Pt thickness in our OX1 samples is almost twice as large as that observed by Tacchi et. al. Hence, the oxidation of the FM has a significant contribution to the decrease in DMI, consistent with our model.

Although the exchange constant *A* is weakly depended upon *k* in the low-*k* limit, it could be possible to remove the DMI contribution from the dispersion curve shown in Figure 4.40 (b) by symmetrizing this curve and thereby extract the value of *A*. The symmetric exchange extracted in this manner are shown in Figure 4.41 (a). This too shows a trend of decreasing exchange constant with decreasing thickness of Pt and increasing oxidation of the FM layer. As the magnetic exchange is a nearest-neighbor interaction, the presence of oxygen in the lattice can weaken this effect, leading to our observations. In other words, the drop in symmetric and antisymmetric exchanges are indicative of the oxidation of the FM.

We also plotted the dependence of the symmetric exchange A on the antisymmetric interfacial DMI in Figure 4.41 (b). This shows a linear dependence of the symmetric and antisymmetric exchange, consistent with the work of Nembach et. al[170]. In their work, by varying the thickness of NiFe, the saturation magnetization and the Curie temperature was changed. This in turn led to their observation of linear relationship between the exchange and the DMI. We observe the same relationship by keeping the Co thickness constant, but instead affecting its magnetic properties via oxidation. This would imply that both the symmetric and antisymmetric exchanges share the same underlying physics and are affected the same way upon oxidation of the FM layer. In order to verify this method of extraction of the exchange constant, we performed temperature dependence measurements of the magnetization.

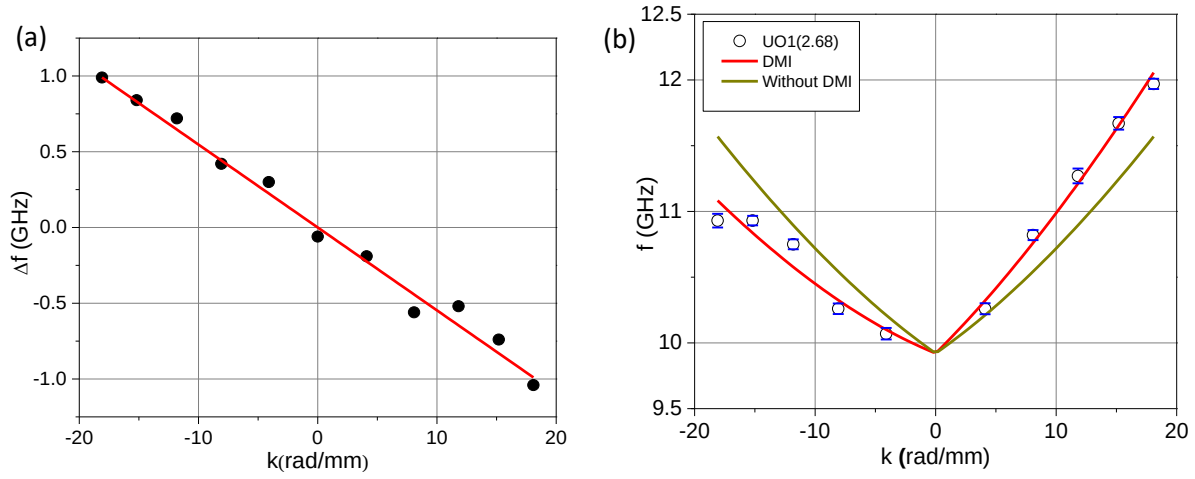

Figure 4.39: The wave vector dependence of (a) the frequency difference of the counter-propagating spin waves and (b) the frequency of the spin waves of the UO1(2.68) sample. The red line is the fit with the dispersion equation including the DMI and the yellow without.

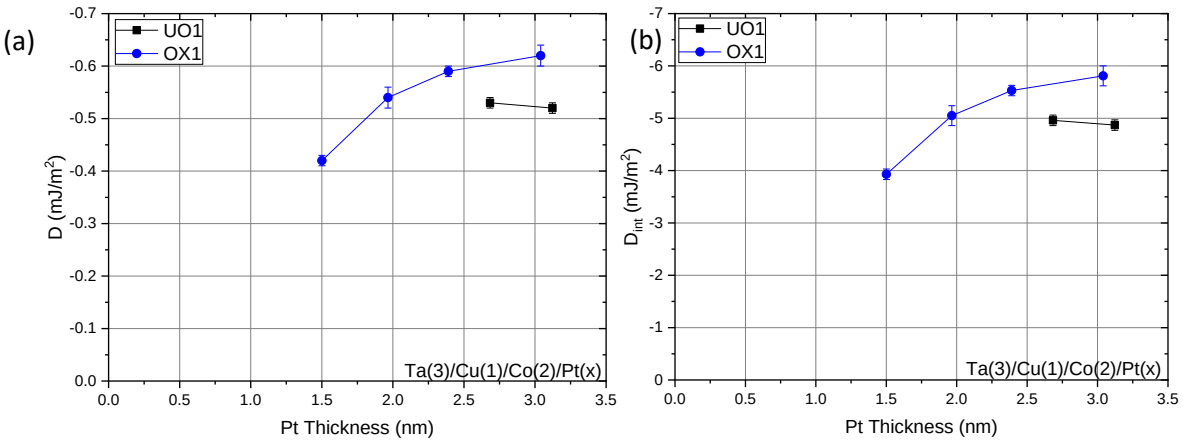

Figure 4.40: (a) The volume-averaged DMI and (b) the interfacial DMI as a function of Pt thickness of UO1 and OX1 samples. The error bars include the errors in M_S and Δf.

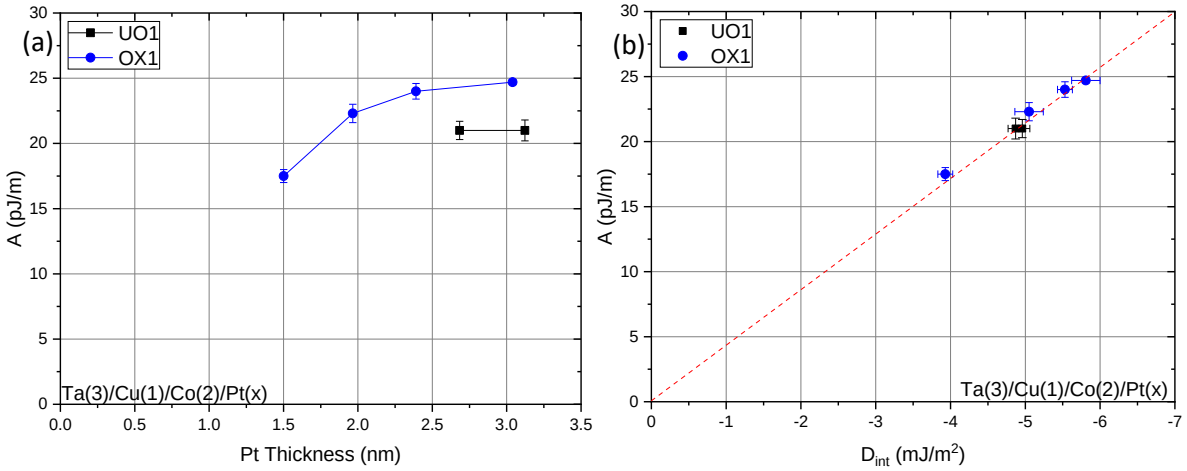

Figure 4.41: Exchange constant A as a function of (a) the Pt thickness and (b) the interfacial DMI.

4.5.6 Extraction of the Heisenberg exchange from temperature dependence measurements

In order to verify the exchange constant *A* extracted from the BLS measurements, we performed temperature dependence measurements of the saturation magnetization. The saturation magnetic moment m_S^T depends on the temperature according to the Bloch $T^{3/2}$ law given by[170,172]

$$m_S^{0K} - m_S^T \propto \left(\frac{k_B T}{D_{spin}^{0K}}\right)^{3/2} \tag{4.25}$$

Where m_S^{0K} is the saturation magnetic moment at 0K, k_B is the Boltzmann constant, T is the temperature, D_{spin}^{0K} is the spin-wave stiffness at 0 K. This can be re-written as

$$m_S^T = m_S^{0K} \times \left(1 - \frac{g\mu_B \eta}{M_S^{0K}} \left(\frac{k_B T}{D_{spin}^{0K}}\right)^{3/2}\right) \tag{4.26}$$

Here g is the Landé g-factor, M_S^{0K} the saturation magnetization at 0 K and η a dimensionless constant that depends on the sample geometry. For bulk films[172] η = 0.0587. However, for smaller thicknesses, it increases and can be determined from the magnon density at temperature *T,* n_m^T, in thermal equilibrium as

$$\eta = \frac{n_m^T}{\left(\frac{k_B T}{D_{spin}^{0K}}\right)^{3/2}} \tag{4.27}$$

The magnon density can the determined numerically and is detailed in ref[170]. The spin-wave density at room temperature can be determined as

$$D_{spin}^{300K} = D_{spin}^{0K} \left[\frac{M_S^{300K}}{M_S^{0K}}\right]^{\gamma} \tag{4.28}$$

Here γ = 1 as per the mean-field theory though it can vary considering magnon-electron interaction[170] etc. Finally, the exchange constant at room temperature can be determined as

$$A^{300K} = M_S^{300K} D_{spin}^{300K} / (2g\mu_B) \tag{4.29}$$

In practice, we use a Physical Property Measurement System (PPMS) VSM to perform these measurements. We sweep the temperature from 350 K to 10 K with an applied external field of 100 mT and measure the magnetic moment. This is plotted in Figure 4.42 (a) for the UO1(2.68) sample. It is observed that below around 150 K, the moment does not follow the Bloch $T^{3/2}$ law, with a peak at around 100 K. This is a known consequence of oxygen contamination in the chamber due to outgassing from the Teflon tape used to attach the sample to the holder[173]. There is a known oxygen liquid to solid phase transition at around 50 K and a paramagnetic to antiferromagnetic transition at 43 K. These transitions can result in peaks in the measurement and can distort the readings at lower temperatures.

Further, our oxidized samples are also sensitive to higher temperature with a likely oxygen migration out of the FM at higher temperatures. This implied that we were restricted to a very narrow range between 150 K and 300 K to fit our data with the Bloch $T^{3/2}$ law. However, as the Curie temperature of our samples is much higher at a few hundred Kelvins, we were unable to satisfactorily fit the measured data.

Hence, in order to gain a qualitative understanding of the exchange constant, we normalized the magnetic moment at 150 K and replotted the data for all the samples in Figure 4.42 (b). The slope of these lines is inversely proportional to its Curie temperature, which is, in turn, proportional to the

exchange constant. We can thus determine that at a lower thickness of Pt, there is a reduction in the exchange constant signifying the oxidation of the FM. This is consistent with our model and the BLS measurements.

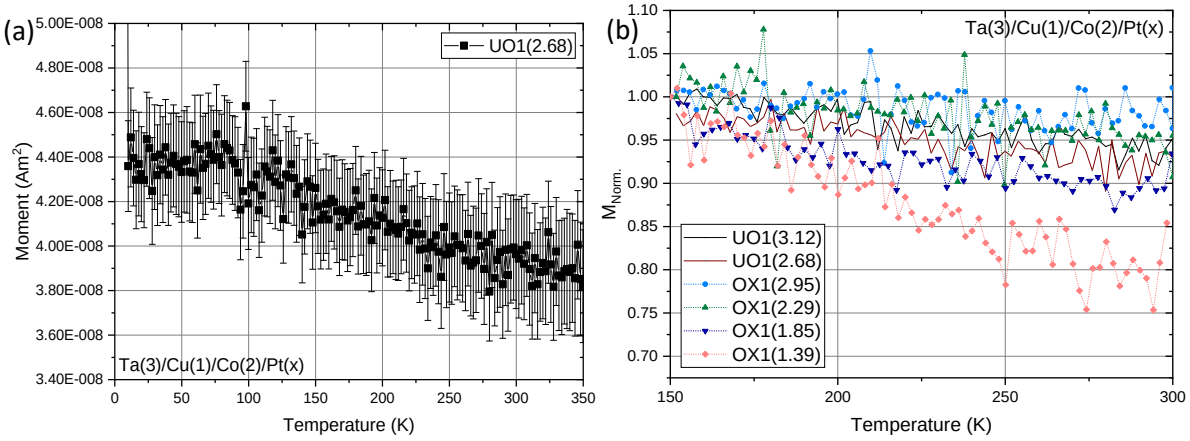

Figure 4.42: Temperature dependence of (a) the magnetic moment and (b) the moment normalized at 150 K.

4.6 Mechanism of DL SOTs in Platinum Oxide Systems

Now that we have confirmed the validity of our oxidation model, we can utilize it to determine the SOTs generated intrinsically by the oxidized platinum.

4.6.1 Intrinsic contribution of platinum oxide to SOTs

Previously, in Figure 4.13 we plotted the DL field normalized to the total current and voltage across the system, showing an increase in SOTs. In order to determine the intrinsic contribution of the oxidation to these SOTs, we need to consider all the effects the oxidation has on the system as well as contributions other than from Pt to the SOTs.

One of the first effects that we discussed was the loss of magnetization of Co upon oxidation. As the magnetization is proportional to energy, smaller energy is needed to drive smaller magnetization. In other words, a smaller magnetization can artificially inflate the SOTs. This is visualized in Figure 4.43 (a) and (b) corresponding to normalization by current and voltage across the system respectively. Both the plots are further normalized by the width of the Hall cross to account for any variation in device fabrication as well as the areal magnetization, M_S*t_{Co}. Compared to the previous case without normalizing the magnetization, there is only a smaller increase in the DL field when normalized by the current. In case of voltage normalization, however, there is in fact a decrease in the DL field. Hence, as expected, there is a significant decrease in torques after considering the magnetization of the samples. It has to be noted, however, that these plots are considering the original Pt thickness. After oxidation, a uniform thickness of Pt gets oxidized and shouldn't contribute to any torques as the current doesn't flow through it. Thus, according to our model, we need to consider the effective Pt thickness that contributes to the SOTs. These are plotted in Figure 4.44 (a) and (b) normalized to current and voltage respectively. These, however, do not include the areal magnetization correction in order to highlight the effect of the correction of Pt thickness alone. In these plots, the OX1 sample is moved to the left by 0.434nm as shown in Figure 4.27. In case of OX2, it is moved by 0.47nm.

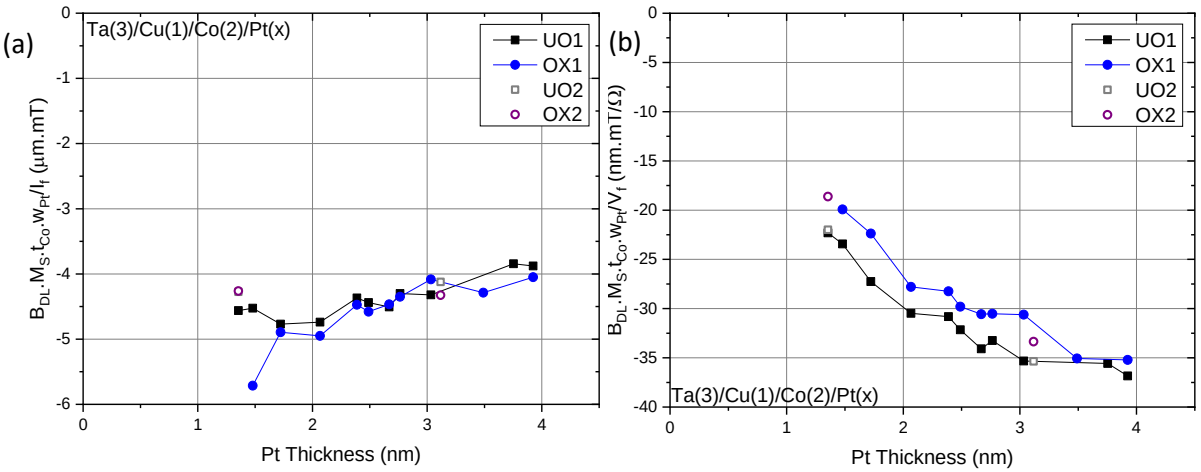

Figure 4.43: DL field normalized by areal magnetization and (a) current and (b) voltage across the sample.

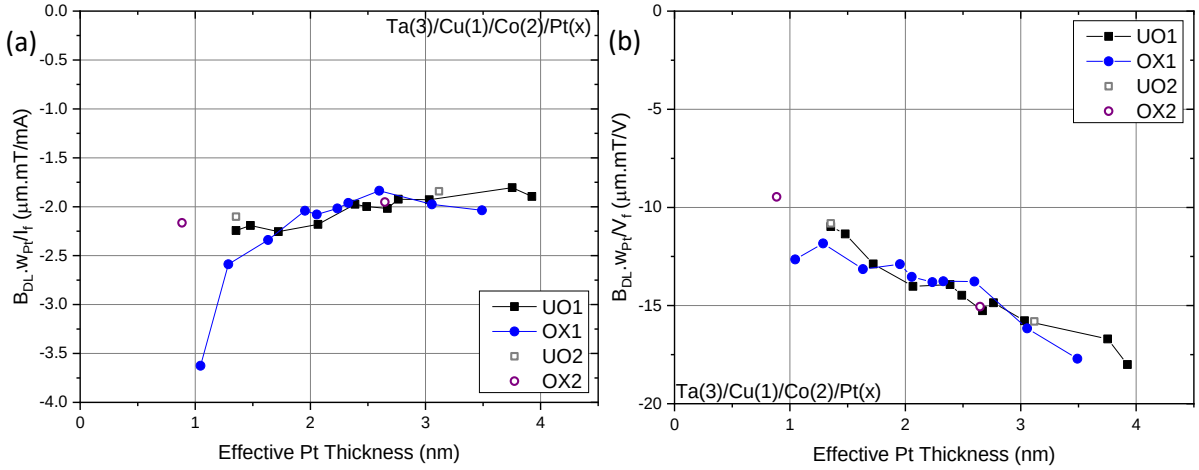

Figure 4.44: DL fields normalized by (a) current and (b) voltage across the sample. The x-axis denotes the effective thickness of metallic Pt that contributes to the generation of the SOTs.

By considering the effective Pt thickness, we notice that there is an increase of the DL field when normalized by current and by voltage. However, importantly, the oxidized and the un-oxidized curves line up perfectly on top of each other up above around 1.8 nm, consistent with our model of uniform oxidation of Pt. This physically implies that only the metallic Pt contribute to the SOTs. In order to determine the correct torques below this thickness, we need to normalize these with the areal magnetization as before. These are plotted in Figure 4.45 (a) and (b) corresponding to normalization by current and voltage respectively. As expected, there is a reduction in the increase of torques when normalized by current. However, the noteworthy point is that in the case of normalization by voltage, there is no increase in SOTs at all. There are two important aspects to this. The first is that it validates our model of oxygen pumping into the cobalt layer. Like the previous plot which did not consider normalization by areal magnetization, the oxidized and un-oxidized lines line up above 1.8 nm. However below this, when the loss in magnetization is accounted for, there is no longer any increase in torques. This implies that the metallic Pt follows the same gradient across the entire wafer. The sharp drop in resistivity is indeed due to the excess oxygen being pumped into the cobalt layer which then reduces the magnetization.

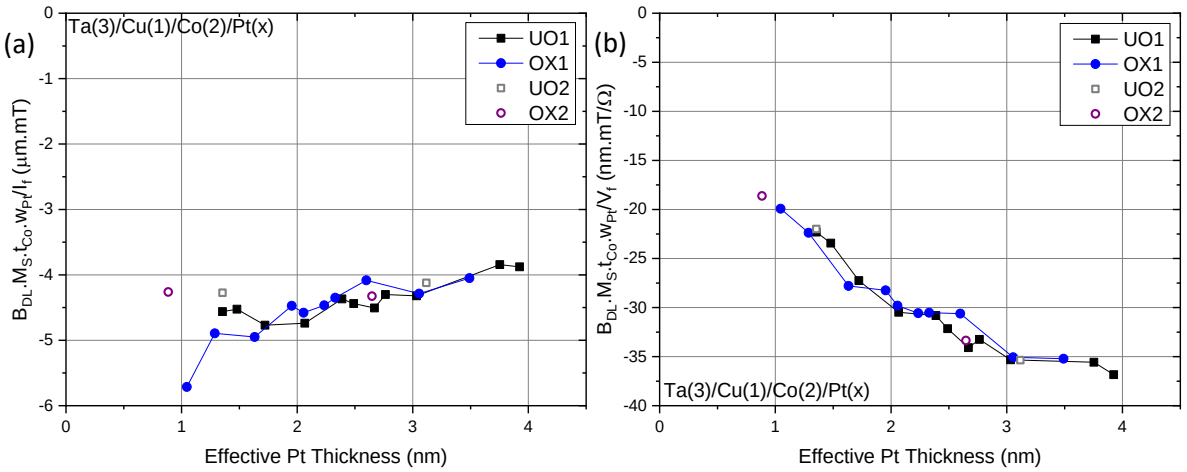

Figure 4.45: DL fields normalized by the areal magnetization and (a) the current and (b) the voltage across the sample. The x-axis denotes the effective metallic Pt contributing the generation of SOTs.

The second aspect of these plots is the difference between the current and voltage normalized plots. Although the voltage normalized plots do not show an increase in SOTs, the current normalized plot still has a significant increase in SOTs. This can be understood from the fact that the applied voltage is constant across all the samples, once normalized. However, a unit current flowing in the sample needn't generate the same torques. Instead, the generation of SOTs are determined by the effective current that flows within the Pt layer. Hence, we need to normalize these torques based on the current flowing through the Pt layer instead of through the whole sample.

The current through the Pt layer is determined by multiplying the Pt resistance plotted in Figure 4.25 and Figure 4.35 with the voltage across the active region of the Hall cross. This can further be used to calculate the current density in Pt. Doing so would intrinsically include the slight variations in the width of the Hall crosses and we would no longer have to explicitly normalize the SOTs to it. By using symmetric Hall crosses, the same argument would apply when using the electric field across the active region of the Hall cross rather than the voltage across the device.

Another contribution to these SOTs is from the tantalum under-layer. Although Ta is used for better growth of the layers above, having a high SOC, it too can contribute to the SOTs via the SHE. Copper being only 1 nm thick, easily transmits the spin current across to the Co layer, since the spin diffusion length in Cu is much larger. This results in a contribution of the Ta layer to the SOTs, which needs to be corrected. To do so, we fabricated a reference sample of Ta(3)/Cu(1)/Co(2)/AlOx(2) and measured the DL field to be 1.13695×10^{-8} mTm/Ω. This number is normalized to the areal magnetization and the voltage. Charge current through the sample is not a good normalization factor as it could vary between the reference and experimental samples.

Finally, we can write the SOT fields in terms of the SOT efficiency normalized to the current density through the Pt layer as well as to the electric field across the sample as

$$\xi_{DL(FL)}^{j_{Pt}} = \frac{2e}{\hbar}\mu_0 M_S t_{Co} H_{DL(FL)}/j_{Pt} \tag{4.30}$$

$$\xi_{DL(FL)}^{E} = \frac{2e}{\hbar}\mu_0 M_S t_{Co} H_{DL(FL)}/E \tag{4.31}$$

Here $\hbar$ is the reduced Planck's constant, j_{Pt} is the current density through the platinum layer and E is the electric field across the sample. These SOT efficiencies are plotted in Figure 4.46 (a) and (b) respectively.

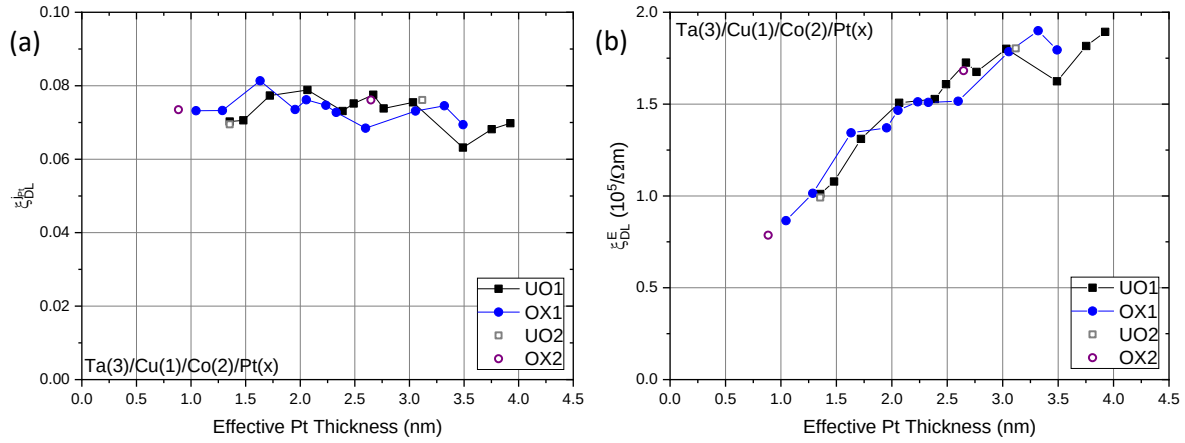

Figure 4.46: Damping like SOT efficiency per unit applied (a) current density in Pt and (b) the electric field across the device, as a function of effective Pt thickness.

These plots show that regardless of the normalization, either by the charge current density in Pt or the electric field across the device, the SOT generated by the oxidized and the un-oxidized samples are exactly the same. This implies that even though we see an increase in torques upon oxidation when we consider the whole system, it is not an intrinsic effect. The torques are still generated by the metallic Pt in the system and the platinum oxide plays no role in the enhancement of toques as claimed in the literature.

Regarding the shapes of these curves, they correspond well with other metallic systems that we have studied, plotted in Figure 4.47 (a)[174]. The DL torques scale with the current density in the HM. Hence in Figure 4.46 (a), when normalized by the current density in platinum, we observe a constant SOT efficiency as a function of Pt thickness. The slight upturn towards the lower thicknesses is consistent with the increased resistivity of Pt at these lower thicknesses. The SOT efficiency plot shown in Figure 4.46 (b) is also consistent with other metallic systems and scales with the conductivity of Pt as shown in Figure 4.47 (b). Here, the red curve corresponds to the conductivity of the Pt layer. This dependence on the conductivity of the Pt layer points to a significant contribution of the interface to the SOT generation, along with the SHE.

These data prove that there is no net intrinsic increase in SOTs generated by the current. Only the metallic Pt layer is responsible for the SOTs and the platinum oxide layer does not enhance or contribute to the SOTs.

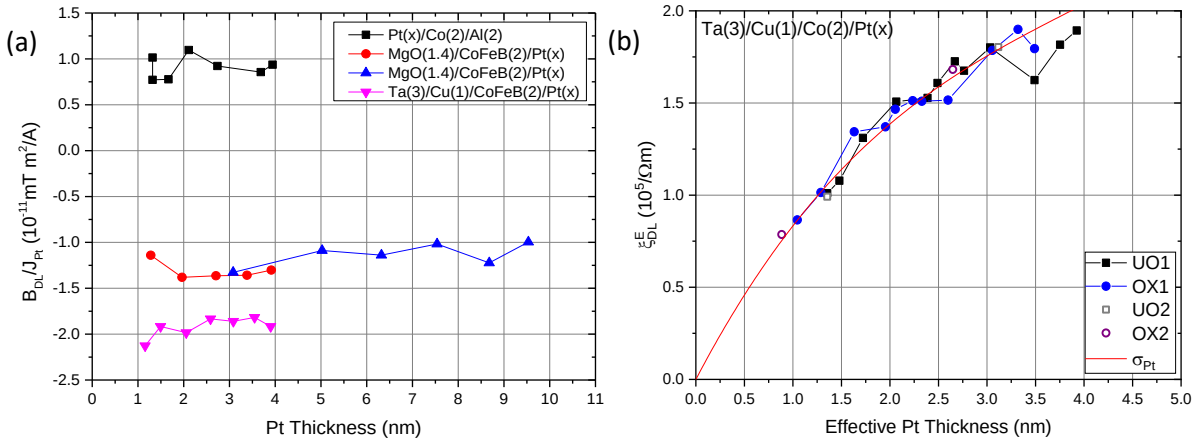

Figure 4.47: (a) DL field normalized by the current density in the HM for various systems. Plot adapted from data already published in a previous thesis[174]. (b) DL SOT efficiency normalized by the current density, fit with the Pt conductivity denoted by the red curve.

4.7 FL SOTs in Platinum Oxide Systems

Like the DL torques, the oxidation can also affect the FL torques. The FL torques affect the motion of the magnetization in the plane of the film. This section describes the normalization of the FL torques and the consequence of oxidation on these torques.

The FL fields are extracted as detailed in appendix A. Following the data corrections we made to the DL fields, we can plot the FL fields which accounts for the difference in areal magnetization as well as the effective Pt thickness. These are plotted in Figure 4.48 (a) and (b) corresponding to current and voltage normalizations. We can infer from these plots that oxidation has no effect on the FL fields as both the curves line up on top of each other, without showing any increase in torques. However, there are two other major factors that needs to be accounted for in these plots.

The first is the effect of the Ta seed layer. We can estimate the effect of Ta on FL fields by measuring the torques of our reference sample, Ta(3)/Cu(1)/Co(2)/AlOx(2). We determined FL field of 3.6938×10^{-9} mTm/Ω. The other factor affecting the FL field is the Oersted fields from the non-magnetic layers that act on the magnetization. These include the current induced fields from the Ta, Cu and Pt layers. However, as we have not corrected for the Oersted fields in our reference sample, the numbers mentioned above are inclusive of this effect. Hence, we only need to correct for the Oersted field arising from Pt.

The Oersted fields generated by the Pt layer can be calculated from the current that flows in the Pt layer based on the Oersted's law as

$$B_{Oe} = \frac{\mu_0 I_{Pt}}{w_{Pt}} \tag{4.32}$$

Based on our sign convention introduced in the previous chapter in section 3.1.1, this field acts along the same direction as the measured field, as the Pt is above the Co in this system. It is hence subtracted from the measured field.

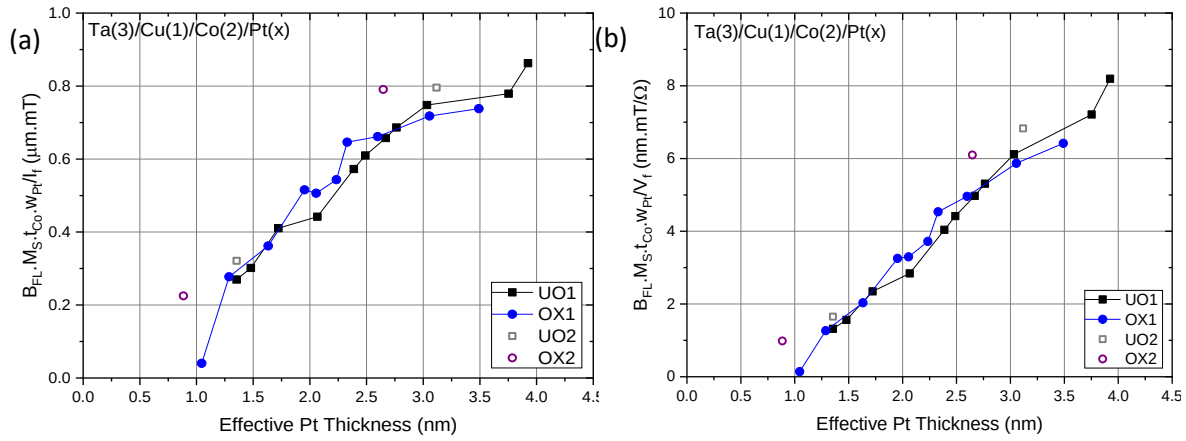

Figure 4.48: Effective Pt thickness dependence of the FL field normalized by the magnetization and (a) the current and (b) the voltage across the device.

Accounting for these factors, we can plot the FL contribution to the SOTs as plotted in Figure 4.49 (a) and (b) corresponding to the normalization by the current density in Pt and the electric field across the Hall cross. It is clearly visible in these plots that regardless of the normalization, there is no intrinsic increase to the FL SOTs with oxidation. This is consistent with our observations of the DL fields. Here, UO1 and OX1 lie on top of each other indicating no effect of oxidation. There could be some effect on OX2 samples. However, we do not have sufficient data points on this sample to draw any conclusions. In the first sample, when normalized with current density, FL fields remain constant with a small upturn at smaller thicknesses. While there is a decrease in FL SOT efficiency normalized by electric field with decreasing Pt thickness. However, the most interesting aspect of the measured DL and FL fields arises when comparing them, as plotted in Figure 4.50. Here grey corresponds to DL fields and red corresponds to FL fields. The ratio between the two orthogonal fields remains constant with Pt thickness. This could point to a singular origin of these two types of torques and warrants further study.

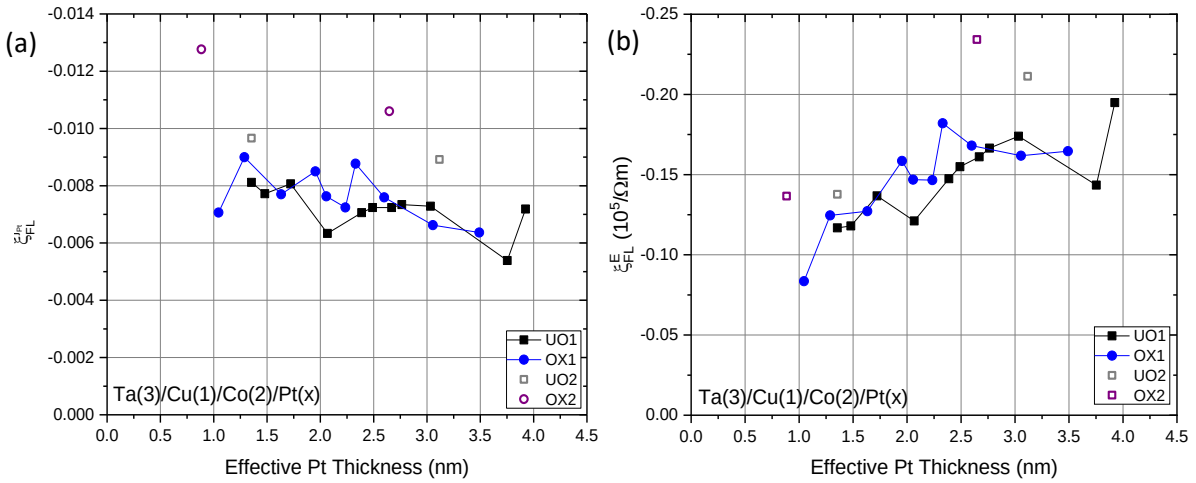

Figure 4.49: Dependence of FL SOT efficiencies on effective Pt thickness, normalized by (a) current density through Pt and (b) electric field across the Hall cross. Values determined using the linear fit method.

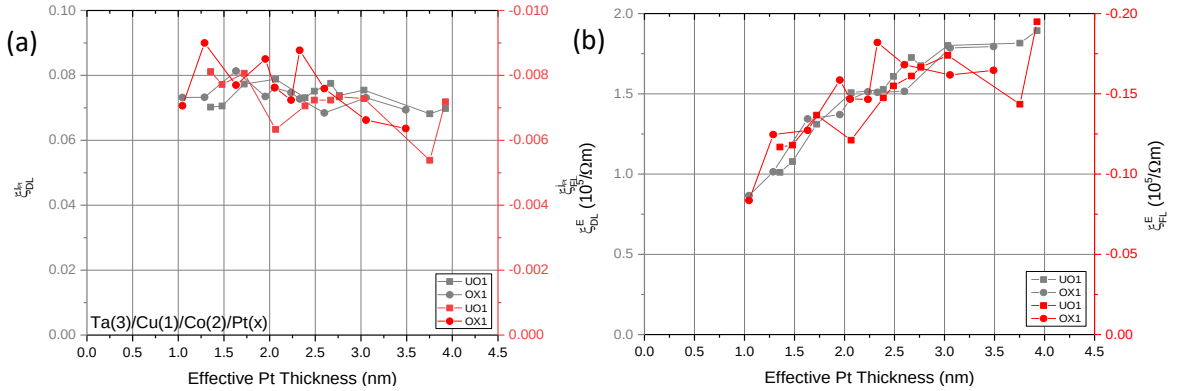

Figure 4.50: Comparison of the DL and FL fields, normalized by (a) the current density in Pt and (b) the electric field across the Hall cross.

4.8 Conclusion and Outlook

As the MRAMs are being developed to compete with and replace traditional CMOS technologies, there is a push to better its favorable metrics, namely the speed and power consumption. While the use of SOT-MRAM tackles the issue of speed, various approaches have been adopted to reduce its power consumption. From the earliest approaches of using transition metals with a high SOC[1,2,65,66,57–64] and resistivity[2,62,68–70] and using metallic alloys[71–73], to interfacial engineering using ultra-thin insertion layers[64,74,75,175] and spin-sink capping materials[80,81]. Another route to enhance the SOTs and thereby reduce the power consumption is via oxidation. Oxidation has been widely studied in the development of pMTJs[83–87]. Here, interfacial oxidation results in PMA of the FM layer due to the hybridization of the energy bands of the oxygen and the FM[82,86,88]. Oxidation induced interfacial electric field between an FM and a MOx lies at the heart of the Rashba effect, giving rise to SOTs[17,93] and has been used to break lateral inversion symmetry resulting in field-free SOT switching[94]. Specific studies on the enhancement of SOTs using oxidation focused on FM oxidation[95,96,99–101], Cu capping oxidation[103–105] and HM oxidation[108–112]. Most of these works attribute the increase in SOTs to either an interfacial Rashba effect[97,133–138] or to an enhanced spin mixing conductance[102,128–131] due to the paramagnetic nature of CoOx. However, till date, there has been no conclusive evidence pointing to the exact underlying mechanism.

In this work we studied the effect of oxidized platinum HM layer on SOTs in Ta(3)/Cu(1)/Co(2)/Pt(x) structures. In order to have a consistent comparison between samples, we performed the measurements on devices fabricated out of a single 4” wafer allowing us to keep the growth conditions between samples. This also enabled us to have a gradation of oxidation, allowing us to study the oxygen dependence of the SOTs. The samples were oxidized in an oxygen argon plasma resulting in soft oxidation conditions. Torque measurements were performed on the oxidized and un-oxidized samples using second harmonic torque measurements. It showed a clear increase in torques with interfacial oxidation. These measurements were supported by spin-pumping measurements using FMR. Furthermore, electrical conductance measurements were performed using a 4-point resistance method, saturation magnetization using VSM and material characterizations using TEM, X-EDS, and AR-XPS. These measurements allowed us to determine that at larger platinum thicknesses, oxidation results in a uniform platinum oxide layer of around 0.4 nm. However, below 1.8 nm of Pt thickness, there was a clear drop of conductance and saturation magnetization with oxidation. These

corresponded well with the increasing SOTs as well, steering our research direction towards determining the oxidation mechanism in this region. Based on the electrical and magnetic data as well as significant ab-initio DFT modeling, we proposed an oxidation model where at lower thicknesses once the oxygen is able to reach the Co/Pt interface, it gets pumped into Co layer due to the larger enthalpy of formation of cobalt oxides than platinum oxides. This led us to the conclusion that unlike the previous works on HM oxidation[108–111], which assumed a completely oxidized HM in contact with a metallic FM, in reality, depending on the enthalpies of formation, the HM is metallic at the interface. This raises doubts regarding the enhanced Rashba-interface based mechanism that was proposed to account for the increase in torques as the HM is in effect metallic rather than an oxide reducing its contribution to torques. In order to further validate this model, we performed BLS measurements and temperature dependence measurements of magnetization to determine that both the symmetric and asymmetric exchanges decrease, which is symptomatic of FM oxidation, consistent with our model. This model allowed us to accurately determine the effective metallic Pt thickness and electrical properties along with the magnetic properties of the FM. This, in turn, enabled us to accurately normalize the SOTs we measured. Upon doing so we observed that regardless of the normalization of the SOTs, either with the current density in Pt or the electric field across the device, the DL and FL SOTs remain exactly the same for both oxidized and un-oxidized samples. Moreover, the DL and FL fields share the same trend with Pt thickness, indicating a singular origin of both torques.

Based on these observations we can conclude that although there seems to be an increase in SOTs on a device level which is clearly visible in the experiments, this increase is not intrinsic to the platinum oxide system. Instead, they are artificially generated due to a confluence of different factors. Although such SOT-MRAM devices, if manufactured, would unquestionably have good power metrics, they would also undoubtedly suffer from short retention times due to the oxidized FM, when compared to un-oxidized ones. The effect of oxidized Co on TMR is also unclear at the moment. This highlights the importance of accurate normalization of SOTs and having a significant understanding of the system under study. This is of utmost importance as MRAMs are pushed further into the mainstream.

Appendix

A. Extraction of FL fields

The FL torques in Pt-based systems are generally an order of magnitude smaller than the DL torques. Hence an accurate measurement and extraction of these torques require careful measurements at higher external fields, slightly higher currents and longer average times. However, at very large fields the magnetization stiffens and the effect of FL torques are neglibigible. Depending on the material system, these effects constraint the usable experimental parameters. Although, this can be overcome. One of the issues with the extraction of FL torques, however, is the curvature and the resulting non-zero y-intercept of the dependence of the FL component of the second harmonic resistance on the inverse of the external field. This was detailed previously in section 3.1.2. We have observed progressively increasing the curvature of this plot with decreasing Pt thickness. These are plotted in Figure A.1 for oxidized and un-oxidized samples.

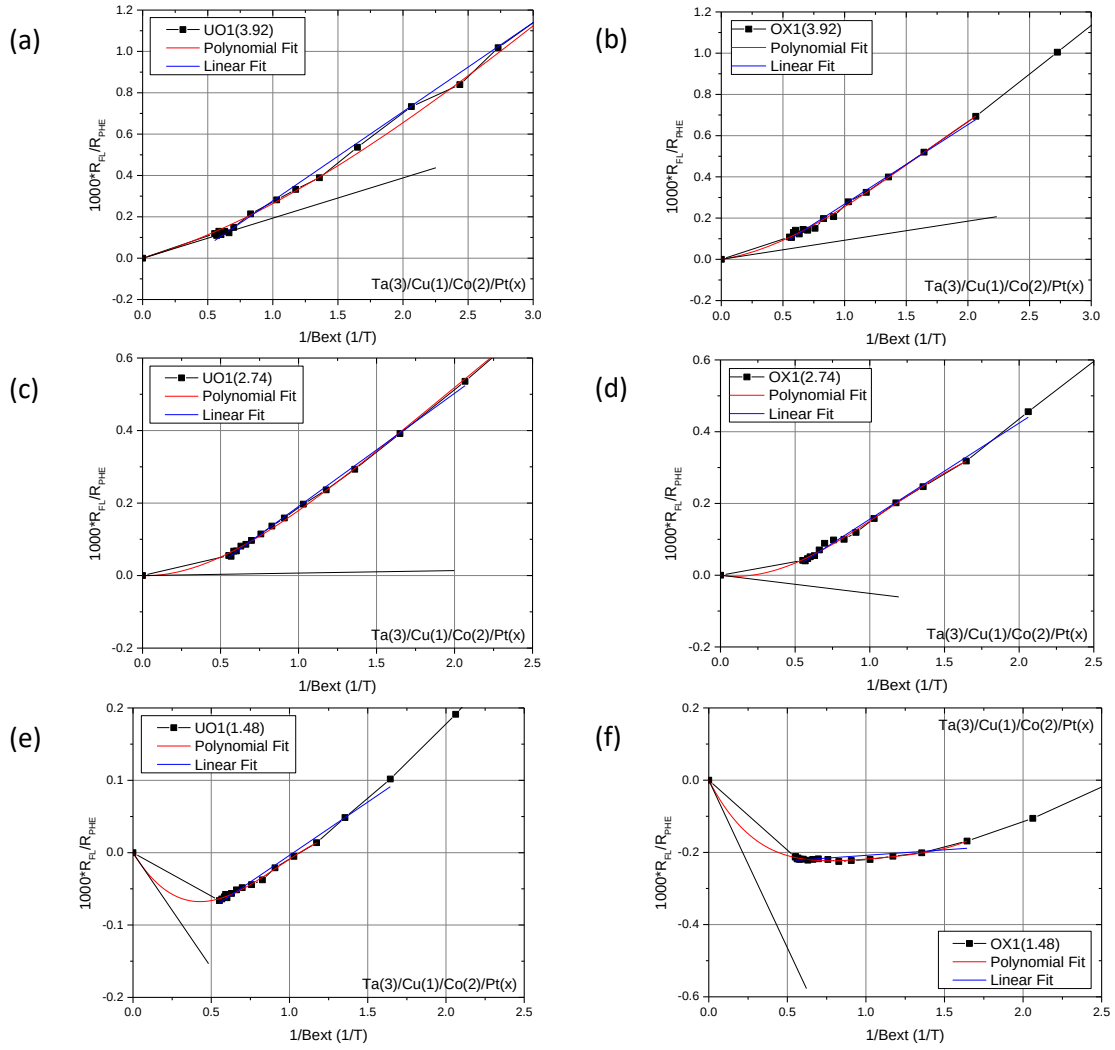

Figure A.1: Dependence of the amplitude of the FL component of the 2nd harmonic resistance normalized by the PHE coefficient on the inverse of the external field for (a),(c),(e) un-oxidized and (b),(d),(f) oxidized samples.

Here, (a),(c),(e) and (b),(d),(f) corresponds to UO1 and OX1 samples respectively. The number in the parenthesis correspond to the original Pt thickness. In order to extract the FL field from these plots, we divided it into two regimes. In the first part, we fit the points with a linear curve, whose slope is indicative of the FL field. This is indicated by the blue line in the plots. However, as is noticeable in the plots, these lines have a non-zero intercept. However, unlike the DL plot where the thermal contribution can result in non-zero y-intercept, there are no such contributing factors in case of the FL plot. At very high fields, or at zero on the x-axis, the magnetic field is expected to be strong enough to freeze out any component of the FL SOT, resulting in a zero amplitude on the y-axis.

We have noticed, in this and other material systems, that the curvature of the FL plot can be extended to zero using a polynomial fit. This is indicated by the red line on the plots. By drawing a tangent to this curve at zero, we can obtain another number for the FL field. However, very often, the fields extracted by this method tends to be opposite in sign to the one extracted using the linear fit. Hence, we need to understand the origin of this curvature.

This curvature cannot be caused by a thermal effect as such an effect wouldn't have a dependence on the external field, leading to the curvature in the data. It neither could be AHE or PHE induced torques as they do not correspond to the FL signal symmetry. To understand this effect better, we plotted the FL fields as a function of Pt thickness as shown in Figure A.2 (a) and (b) corresponding to the normalization by current and voltage respectively. Here, the data-points with the crosses indicate the FL values extracted from the polynomial fit and the other data-points the values extracted from the linear fit. In each of the plots, it is evident that the two curves corresponding to different means of FL field extraction are parallel to each other and are just offset by a constant amount. This presents a problem when comparing samples as in the case of the linear fit, there is a reduction in FL fields with oxidation while in the case of the polynomial fit there is an increase of FL fields with oxidation at a lower thickness of Pt. However, the constant offset is representative of a uniform difference in FL field between the methods of extraction. In other words, there is a constant field acting on the samples at higher fields that leads to the curvature of the plot of the external field dependence of the FL component. A hint regarding its origin can be found in the fact that the curvature of the FL plots progressively increases as the Pt thickness is reduced. Hence, we suspect that this effect arises from the non-uniformity of the FM layer.

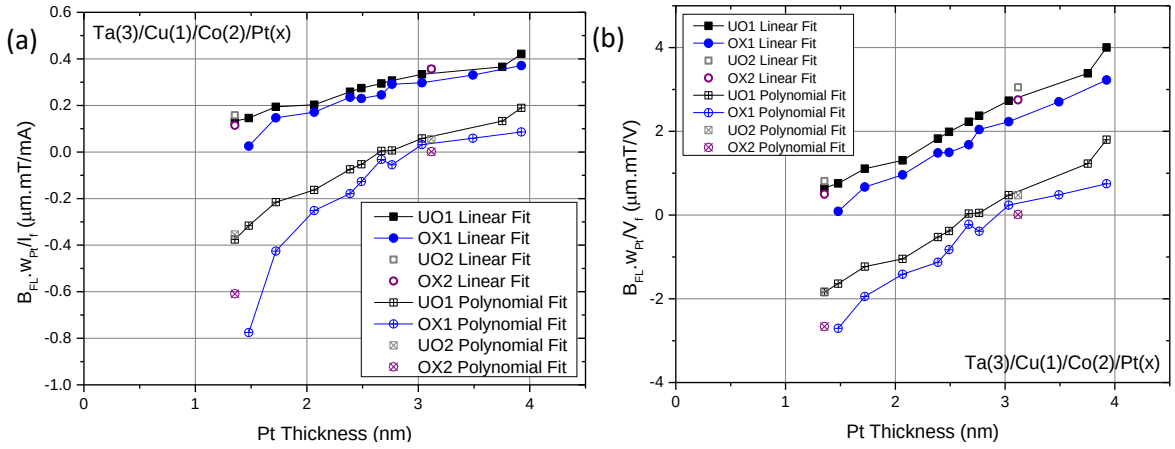

Figure A.2: Dependence of the FL field normalized by (a) the current and (b) the voltage across the device, on the Pt thickness. The data-points with the crosses denote the values extracted from the polynomial fit.

As shown in Figure A.3, at moderate fields the magnetization follows the geometry of the FM film, consistently staying in the plane of the film. However, at larger fields, the magnetization strictly follows the external field and can tilt out of the non-uniform FM layer. The combined actions of these two effects can lead to the curvature of the FL plot. This can be easily verified by studying the angular dependence of the FL torques[27], though is beyond the scope of this work. We, however, believe the number corresponding to the linear fit is more relevant to this study as they are more representative of the system with the magnetization restricted to the FM layer. We thus use the linear fit to study the dependence of FL fields on Pt oxidation.

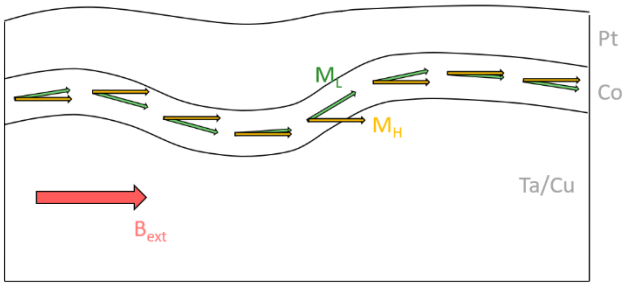

Figure A.3: Effect of the strength of the external field on the magnetization of the Co film. At moderate fields, the magnetization denoted by M_L lies in the plane of the film while at higher fields, the magnetization denoted by M_H lies along the external field direction.

B. Oxidized Systems with Non-Uniform Magnetization

To re-confirm our hypothesis as well as to verify if Co oxidation can indeed give rise to artificial increases in SOTs, we performed similar measurements on two other samples, Ta(3)/Pt(3)/Co(x)/Co(2)/Al(2) and Ta(3)/Pt(3)/CoOx.(x)/Co(2)/Al(2). Here, the wedge of Co denoted by Co(x) has a nominal thickness of 0.65 nm. Hence it is a very thin wedge that is deposited before depositing the primary Co layer. This allows us to oxidize this thin wedge in an oxygen atmosphere without the use of plasma, after the deposition of this layer. This represents the second sample. These samples will now be denoted as CoUO and CoOX respectively. The conductance and the magnetic moment of these samples along the Co wedge are plotted in Figure B.1 (a) and (b) respectively. There is a reduction in conductance with the oxidation of the wedge, visible as a vertical displacement of the conductance curve. Further, the magnetic moment of the CoOX sample remains fairly constant while it increases with increasing Co thickness in CoUO sample.

We performed 2nd harmonic torques measurements of these samples. However, oxidation has a significant effect on the magnetization of the CoOX sample, visible in the field-scan of a sample from the thicker part of the Co wedge, plotted in Figure B.2 (a). The shape of this curve indicates the presence of clusters of Co and Co-oxide, giving rise to higher-order anisotropies. Hence, we had to use the out-of-plane angular-scan method detailed in section 3.1.3 to determine the effective anisotropy and demagnetization fields. Using this value, we could calculate the SOTs, plotted in Figure B.2 (b). We observe an increase in the DL field, upon oxidation. This is consistent with our initial observations with OX1 sample. However, in order to accurately quantify the torques and determine if this is an intrinsic effect, we would need to determine the exact thickness of Co, the oxidation mechanism/migration, current distribution, etc.

(a)

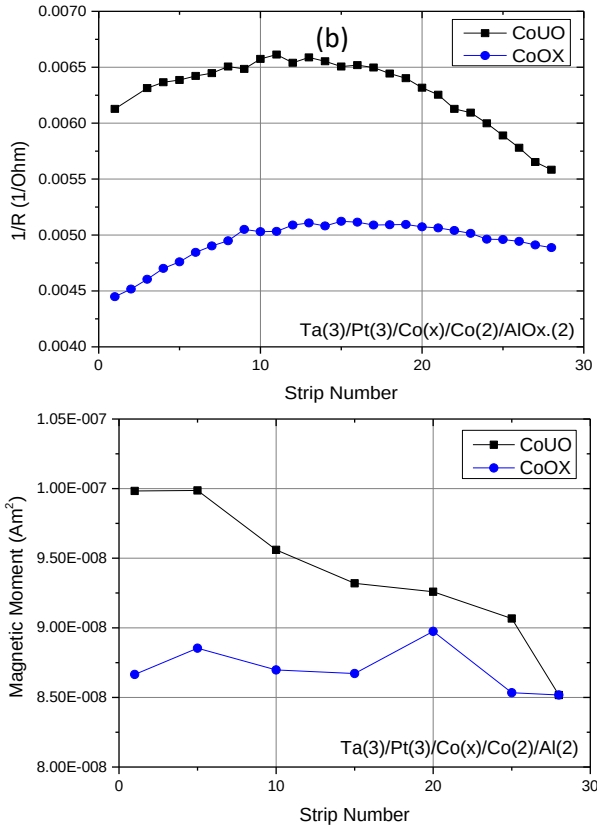

Figure B.1: Variation of (a) the Conductance and (b) the magnetic moment of the oxidized and unoxidized Co sample along the Co wedge. Here the strip number refers to the number of the strip along the wedge with 1 being the thickest part and 28 being the thinnest.

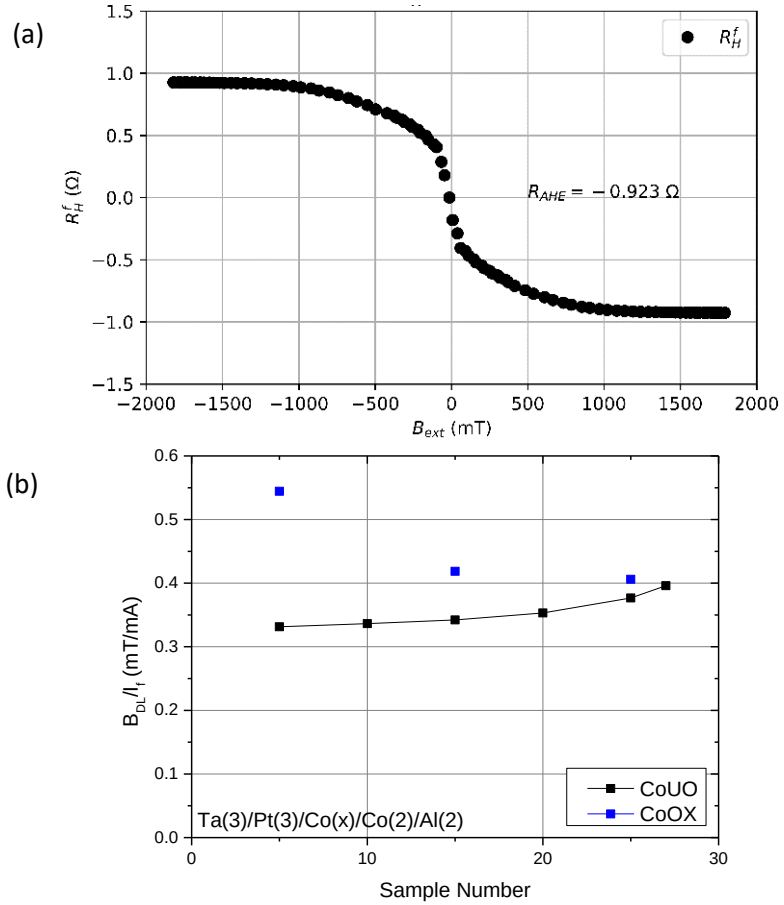

Figure B.2: (a) Field-scan of CoOX sample indicating the presence of higher-order anisotropies. (b) Variation of the DL field along the Co wedge, normalized by the applied current.

We also deposited similar samples with a thicker wedge of Co with a nominal thickness of 1.2 nm to determine if this effect increase with thickness. However, the oxidation affected the magnetization of the Co layer to such an extent leading to clusters, etc. that the magnetic layer was no longer single domain. Since our measurement is based on a single-domain model, we could no longer apply our data analysis methods to these samples to determine the torques. This needs to be considered in 2nd harmonic studies of similar material systems.

Bibliography

1. Miron, I. M. *et al.* Perpendicular switching of a single ferromagnetic layer induced by in-plane current injection. *Nature* **476**, 189–193 (2011).
2. Liu, L. *et al.* Spin-Torque Switching with the Giant Spin Hall Effect of Tantalum. *Science* **336**, 555 (2012).
3. Berry, M. V. Quantal Phase Factors Accompanying Adiabatic Changes. *Proc. R. Soc. Lond. A. Math. Phys. Sci.* **392**, 45–57 (1984).
4. Bruno, P. Geometric phase in magnetism. in *2D School @ Grenoble* (2018).
5. Xiao, D., Chang, M.-C. & Niu, Q. Berry phase effects on electronic properties. *Rev. Mod. Phys.* **82**, 1959–2007 (2010).
6. Pancharatnam, S. Generalized theory of interference, and its applications. *Proc. Indian Acad. Sci. - Sect. A* **44**, 247–262 (1956).
7. Casey, J. *Exploring Curvature*. (Vieweg+Teubner Verlag, 1996).
8. Karplus, R. & Luttinger, J. M. Hall Effect in Ferromagnetics. *Phys. Rev.* **95**, 1154–1160 (1954).
9. Onoda, S., Sugimoto, N. & Nagaosa, N. Intrinsic Versus Extrinsic Anomalous Hall Effect in Ferromagnets. *Phys. Rev. Lett.* **97**, 126602 (2006).
10. Nagaosa, N., Sinova, J., Onoda, S., MacDonald, A. H. & Ong, N. P. Anomalous Hall effect. *Rev. Mod. Phys.* **82**, 1539–1592 (2010).
11. Yao, Y. *et al.* First Principles Calculation of Anomalous Hall Conductivity in Ferromagnetic bcc Fe. *Phys. Rev. Lett.* **92**, 037204 (2004).
12. Dresselhaus, G. Spin-Orbit Coupling Effects in Zinc Blende Structures. *Phys. Rev.* **100**, 580–586 (1955).
13. Vas'ko, F. T. Spin splitting in the spectrum of two-dimensional electrons due to the surface potential. *JETP Lett.* **30**, 541 (1979).
14. Bychkov, Y. A. & Rashba, E. I. Oscillatory effects and the magnetic susceptibility of carriers in inversion layers. *J. Phys. C Solid State Phys.* **17**, 6039–6045 (1984).
15. Manchon, A., Koo, H. C., Nitta, J., Frolov, S. M. & Duine, R. A. New perspectives for Rashba spin–orbit coupling. *Nat. Mater.* **14**, 871–882 (2015).
16. Edelstein, V. M. Spin polarization of conduction electrons induced by electric current in two-dimensional asymmetric electron systems. *Solid State Commun.* **73**, 233–235 (1990).
17. Miron, I. M. *et al.* Current-driven spin torque induced by the Rashba effect in a ferromagnetic metal layer. *Nat. Mater.* **9**, 230–234 (2010).
18. Kato, Y. K., Myers, R. C., Gossard, A. C. & Awschalom, D. D. Observation of the Spin Hall Effect in Semiconductors. *Science* **306**, 1910 (2004).
19. Wunderlich, J., Kaestner, B., Sinova, J. & Jungwirth, T. Experimental Observation of the Spin-Hall Effect in a Two-Dimensional Spin-Orbit Coupled Semiconductor System. *Phys. Rev. Lett.*

94, 047204 (2005).

20. Murakami, S., Naoto, N. & Zhang, S.-C. Dissipationless Quantum Spin Current at Room Temperature. *Science* **301**, 1348–1351 (2003).

21. Sinova, J. *et al.* Universal Intrinsic Spin Hall Effect. *Phys. Rev. Lett.* **92**, 126603 (2004).

22. Sinova, J., Valenzuela, S. O., Wunderlich, J., Back, C. H. & Jungwirth, T. Spin Hall effects. *Rev. Mod. Phys.* **87**, 1213–1260 (2015).

23. Guo, G. Y., Murakami, S., Chen, T.-W. & Nagaosa, N. Intrinsic spin Hall effect in platinum: first-principles calculations. *Phys. Rev. Lett.* **100**, 096401 (2008).

24. Tanaka, T. *et al.* Intrinsic spin Hall effect and orbital Hall effect in 4 d and 5 d transition metals. *Phys. Rev. B* **77**, 165117 (2008).

25. Manchon, A. Spin–orbitronics: A new moment for Berry. *Nat. Phys.* **10**, 340–341 (2014).

26. Gambardella, P. Introduction to spin torques and spin-orbit torques in metal layers. in *Spinmechanics III* (2015).

27. Garello, K. *et al.* Symmetry and magnitude of spin–orbit torques in ferromagnetic heterostructures. *Nat. Nanotechnol.* **8**, 587–593 (2013).

28. Kim, K.-W., Lee, K.-J., Sinova, J., Lee, H.-W. & Stiles, M. D. Spin-orbit torques from interfacial spin-orbit coupling for various interfaces. *Phys. Rev. B* **96**, 104438 (2017).

29. Amin, V. P., Zemen, J. & Stiles, M. D. Interface-Generated Spin Currents. *Phys. Rev. Lett.* **121**, 136805 (2018).

30. Gibbons, J. D., MacNeill, D., Buhrman, R. A. & Ralph, D. C. Reorientable Spin Direction for Spin Current Produced by the Anomalous Hall Effect. *Phys. Rev. Appl.* **9**, 064033 (2018).

31. Safranski, C., Montoya, E. A. & Krivorotov, I. N. Spin–orbit torque driven by a planar Hall current. *Nat. Nanotechnol.* **14**, 27–30 (2019).

32. Amin, V. P., Li, J., Stiles, M. D. & Haney, P. M. Intrinsic spin currents in ferromagnets. *Phys. Rev. B* **99**, 220405 (2019).

33. Wang, W. *et al.* Anomalous spin–orbit torques in magnetic single-layer films. *Nat. Nanotechnol. 2019* 1 (2019) doi:10.1038/s41565-019-0504-0.

34. Mansueto, M. *et al.* Realizing an isotropically coercive magnetic layer by dry friction for memristive applications. *Phys. Rev. Appl.* **12**, 044029 (2019).

35. Avci, C. O. *et al.* Interplay of spin-orbit torque and thermoelectric effects in ferromagnet/normal-metal bilayers. *Phys. Rev. B* **90**, 224427 (2014).

36. Hayashi, M., Kim, J., Yamanouchi, M. & Ohno, H. Quantitative characterization of the spin-orbit torque using harmonic Hall voltage measurements. *Phys. Rev. B* **89**, 144425 (2014).

37. Huang, S. Y., Wang, W. G., Lee, S. F., Kwo, J. & Chien, C. L. Intrinsic Spin-Dependent Thermal Transport. *Phys. Rev. Lett.* **107**, 216604 (2011).

38. Wegrowe, J.-E., Drouhin, H.-J. & Lacour, D. Anisotropic magnetothermal transport and spin Seebeck effect. *Phys. Rev. B* **89**, 094409 (2014).

39. Avci, C. O. *et al.* Unidirectional spin Hall magnetoresistance in ferromagnet/normal metal bilayers. *Nat. Phys.* **11**, 570–575 (2015).

40. Ye, J. *et al.* Determination of magnetic anisotropy constants in Fe ultrathin film on vicinal Si(111) by anisotropic magnetoresistance. *Sci. Rep.* **3**, 2148 (2013).

41. Cao, W. N. *et al.* Temperature-dependent magnetic anisotropies in epitaxial Fe/CoO/MgO(001) system studied by the planar Hall effect. *Appl. Phys. Lett.* **98**, 262506 (2011).

42. Juge, R. *et al.* Current-driven dynamics of magnetic skyrmions in an ultrathin film: experiments and modelling. (2019).

43. McCord, J. & Hubert, A. Normalized Differential Kerr Microscopy An Advanced Method for Magnetic Imaging. *Phys. status solidi* **171**, 555–562 (1999).

44. Schäfer, R. Investigation of Domains and Dynamics of Domain Walls by the Magneto-optical Kerr-effect. in *Handbook of Magnetism and Advanced Magnetic Materials* (John Wiley & Sons, Ltd, 2007). doi:10.1002/9780470022184.hmm310.

45. McCord, J. Progress in magnetic domain observation by advanced magneto-optical microscopy. *J. Phys. D. Appl. Phys.* **48**, 333001 (2015).

46. Jiang, W. *et al.* Blowing magnetic skyrmion bubbles. *Science* **349**, 283–6 (2015).

47. Emori, S., Bauer, U., Ahn, S.-M., Martinez, E. & Beach, G. S. D. Current-driven dynamics of chiral ferromagnetic domain walls. *Nat. Mater.* **12**, 611–616 (2013).

48. Miron, I. M. *et al.* Fast current-induced domain-wall motion controlled by the Rashba effect. *Nat. Mater.* **10**, 419–423 (2011).

49. Jué, E. *et al.* Chiral damping of magnetic domain walls. *Nat. Mater.* **15**, 272–277 (2015).

50. Baumgartner, M. *et al.* Spatially and time-resolved magnetization dynamics driven by spin–orbit torques. *Nat. Nanotechnol.* **12**, 980–986 (2017).

51. Safeer, C. K. *et al.* Spin-orbit torque magnetization switching controlled by geometry. *Nat. Nanotechnol.* **11**, 143–146 (2015).

52. Weinberger, P. John Kerr and his effects found in 1877 and 1878. *Philos. Mag. Lett.* **88**, 897–907 (2008).

53. Faraday, M. I. Experimental researches in electricity.—Nineteenth series. *Philos. Trans. R. Soc. London* **136**, 1–20 (1846).

54. Saidl, V. *et al.* Optical determination of the Néel vector in a CuMnAs thin-film antiferromagnet. *Nat. Photonics* **11**, 91–96 (2017).

55. Xu, J. *et al.* Imaging antiferromagnetic domains in nickel oxide thin films by optical birefringence effect. *Phys. Rev. B* **100**, 134413 (2019).

56. EVICO Magnetics GmbH. (2019).

57. Liu, L., Lee, O. J., Gudmundsen, T. J., Ralph, D. C. & Buhrman, R. A. Current-Induced Switching of Perpendicularly Magnetized Magnetic Layers Using Spin Torque from the Spin Hall Effect. *Phys. Rev. Lett.* **109**, 096602 (2012).

58. Ghosh, A., Garello, K., Avci, C. O., Gabureac, M. & Gambardella, P. Interface-Enhanced Spin-Orbit Torques and Current-Induced Magnetization Switching of Pd/Co/AlOx Layers. *Phys. Rev. Appl.* **7**, 014004 (2017).

59. Gabor, M. S. *et al.* Spin-orbit torques and magnetization switching in perpendicularly

magnetized epitaxial Pd/Co2FeAl/MgO structures. (2019).

60. Kim, J. *et al.* Layer thickness dependence of the current-induced effective field vector in Ta|CoFeB|MgO. *Nat. Mater.* **12**, 240–245 (2013).

61. Kondou, K. *et al.* Influence of inverse spin Hall effect in spin-torque ferromagnetic resonance measurements. *Appl. Phys. Express* **9**, 023002 (2016).

62. Pai, C.-F. *et al.* Spin transfer torque devices utilizing the giant spin Hall effect of tungsten. *Appl. Phys. Lett.* **101**, 122404 (2012).

63. He, C. *et al.* Spin-torque ferromagnetic resonance measurements utilizing spin Hall magnetoresistance in W/Co40Fe40B20/MgO structures. *Appl. Phys. Lett.* **109**, 202404 (2016).

64. Pai, C.-F. *et al.* Enhancement of perpendicular magnetic anisotropy and transmission of spin-Hall-effect-induced spin currents by a Hf spacer layer in W/Hf/CoFeB/MgO layer structures. *Appl. Phys. Lett.* **104**, 082407 (2014).

65. Ramaswamy, R., Qiu, X., Dutta, T., Pollard, S. D. & Yang, H. Hf thickness dependence of spin-orbit torques in Hf/CoFeB/MgO heterostructures. *Appl. Phys. Lett.* **108**, 202406 (2016).

66. Akyol, M. *et al.* Effect of the oxide layer on current-induced spin-orbit torques in Hf|CoFeB|MgO and Hf|CoFeB|TaO $_x$ structures. *Appl. Phys. Lett.* **106**, 032406 (2015).

67. Ueda, K., Pai, C.-F., Tan, A. J., Mann, M. & Beach, G. S. D. Effect of rare earth metal on the spin-orbit torque in magnetic heterostructures. *Appl. Phys. Lett.* **108**, 232405 (2016).

68. Lee, J. W. *et al.* Enhanced spin-orbit torque by engineering Pt resistivity in Pt/Co/AlOx structures. *Phys. Rev. B* **96**, 064405 (2017).

69. Sagasta, E. *et al.* Tuning the spin Hall effect of Pt from the moderately dirty to the superclean regime. *Phys. Rev. B* **94**, 060412 (2016).

70. Wang, L. *et al.* Giant Room Temperature Interface Spin Hall and Inverse Spin Hall Effects. *Phys. Rev. Lett.* **116**, 196602 (2016).

71. Obstbaum, M. *et al.* Tuning Spin Hall Angles by Alloying. *Phys. Rev. Lett.* **117**, 167204 (2016).

72. Gu, B. *et al.* Surface-Assisted Spin Hall Effect in Au Films with Pt Impurities. *Phys. Rev. Lett.* **105**, 216401 (2010).

73. Niimi, Y. *et al.* Giant Spin Hall Effect Induced by Skew Scattering from Bismuth Impurities inside Thin Film CuBi Alloys. *Phys. Rev. Lett.* **109**, 156602 (2012).

74. Zhang, W., Han, W., Jiang, X., Yang, S.-H. & S. P. Parkin, S. Role of transparency of platinum–ferromagnet interfaces in determining the intrinsic magnitude of the spin Hall effect. *Nat. Phys.* **11**, 496–502 (2015).

75. Zhu, L. *et al.* Enhancing spin-orbit torque by strong interfacial scattering from ultra-thin insertion layers. (2019).

76. Nguyen, M.-H., Nguyen, K. X., Muller, D. A., Ralph, D. C. & Buhrman, R. A. Enhancement of the anti-damping spin torque efficacy of platinum by interface modification. *Appl. Phys. Lett.* **106**, 222402 (2015).

77. Pai, C.-F., Ou, Y., Vilela-Leão, L. H., Ralph, D. C. & Buhrman, R. A. Dependence of the efficiency of spin Hall torque on the transparency of Pt/ferromagnetic layer interfaces. *Phys. Rev. B* **92**, 064426 (2015).

78. Woo, S., Mann, M., Tan, A. J., Caretta, L. & Beach, G. S. D. Enhanced spin-orbit torques in Pt/Co/Ta heterostructures. *Appl. Phys. Lett.* **105**, 212404 (2014).

79. Yu, J. *et al.* Spin orbit torques and Dzyaloshinskii-Moriya interaction in dual-interfaced Co-Ni multilayers. *Sci. Rep.* **6**, 32629 (2016).

80. Ishikuro, Y., Kawaguchi, M., Kato, N., Lau, Y.-C. & Hayashi, M. Dzyaloshinskii-Moriya interaction and spin-orbit torque at the Ir/Co interface. *Phys. Rev. B* **99**, 134421 (2019).

81. Qiu, X. *et al.* Enhanced Spin-Orbit Torque via Modulation of Spin Current Absorption. *Phys. Rev. Lett.* **117**, 217206 (2016).

82. Dieny, B. & Chshiev, M. Perpendicular magnetic anisotropy at transition metal/oxide interfaces and applications. *Rev. Mod. Phys.* **89**, 025008 (2017).

83. Monso, S. *et al.* Crossover from in-plane to perpendicular anisotropy in Pt/CoFe/AlOx sandwiches as a function of Al oxidation: A very accurate control of the oxidation of tunnel barriers. *Appl. Phys. Lett.* **80**, 4157–4159 (2002).

84. Nistor, L. E. *et al.* Correlation Between Perpendicular Anisotropy and Magnetoresistance in Magnetic Tunnel Junctions. *IEEE Trans. Magn.* **46**, 1412–1415 (2010).

85. Rodmacq, B., Auffret, S., Dieny, B., Monso, S. & Boyer, P. Crossovers from in-plane to perpendicular anisotropy in magnetic tunnel junctions as a function of the barrier degree of oxidation. *J. Appl. Phys.* **93**, 7513–7515 (2003).

86. Manchon, A. *et al.* Analysis of oxygen induced anisotropy crossover in Pt/Co/MOx trilayers. *J. Appl. Phys.* **104**, 043914 (2008).

87. Nistor, L. E., Rodmacq, B., Auffret, S. & Dieny, B. Pt/Co/oxide and oxide/Co/Pt electrodes for perpendicular magnetic tunnel junctions. *Appl. Phys. Lett.* **94**, 012512 (2009).

88. Yang, H. X. *et al.* First-principles investigation of the very large perpendicular magnetic anisotropy at Fe|MgO and Co|MgO interfaces. *Phys. Rev. B* **84**, 054401 (2011).

89. Ikeda, S. *et al.* A perpendicular-anisotropy CoFeB–MgO magnetic tunnel junction. *Nat. Mater.* **9**, 721 (2010).

90. Alzate, J. G. *et al.* Voltage-induced switching of nanoscale magnetic tunnel junctions. in *2012 International Electron Devices Meeting* 29.5.1-29.5.4 (IEEE, 2012). doi:10.1109/IEDM.2012.6479130.

91. Shiota, Y. *et al.* Induction of coherent magnetization switching in a few atomic layers of FeCo using voltage pulses. *Nat. Mater.* **11**, 39–43 (2012).

92. Wang, W.-G., Li, M., Hageman, S. & Chien, C. L. Electric-field-assisted switching in magnetic tunnel junctions. *Nat. Mater.* **11**, 64–68 (2012).

93. Pi, U. H. *et al.* Tilting of the spin orientation induced by Rashba effect in ferromagnetic metal layer. *Appl. Phys. Lett.* **97**, 162507 (2010).

94. Yu, G. *et al.* Switching of perpendicular magnetization by spin–orbit torques in the absence of external magnetic fields. *Nat. Nanotechnol.* **9**, 548–554 (2014).

95. Emori, S., Bauer, U., Woo, S. & Beach, G. S. D. Large voltage-induced modification of spin-orbit torques in Pt/Co/GdOx. *Appl. Phys. Lett.* **105**, 222401 (2014).

96. Qiu, X. *et al.* Spin-orbit-torque engineering via oxygen manipulation. *Nat. Nanotechnol.* **10**, 333–338 (2015).

97. Krupin, O. *et al.* Rashba effect at magnetic metal surfaces. *Phys. Rev. B* **71**, 201403 (2005).

98. Park, S. R., Kim, C. H., Yu, J., Han, J. H. & Kim, C. Orbital-Angular-Momentum Based Origin of Rashba-Type Surface Band Splitting. *Phys. Rev. Lett.* **107**, 156803 (2011).

99. Mishra, R. *et al.* Electric-field control of spin accumulation direction for spin-orbit torques. *Nat. Commun.* **10**, 248 (2019).

100. Hibino, Y., Hirai, T., Hasegawa, K., Koyama, T. & Chiba, D. Enhancement of the spin-orbit torque in a Pt/Co system with a naturally oxidized Co layer. *Appl. Phys. Lett.* **111**, 132404 (2017).

101. Hasegawa, K., Hibino, Y., Suzuki, M., Koyama, T. & Chiba, D. Enhancement of spin-orbit torque by inserting CoO x layer into Co/Pt interface. *Phys. Rev. B* **98**, 020405 (2018).

102. Lin, W., Chen, K., Zhang, S. & Chien, C. L. Enhancement of Thermally Injected Spin Current through an Antiferromagnetic Insulator. *Phys. Rev. Lett.* **116**, 186601 (2016).

103. An, H., Kageyama, Y., Kanno, Y., Enishi, N. & Ando, K. Spin–torque generator engineered by natural oxidation of Cu. *Nat. Commun.* **7**, 13069 (2016).

104. Gao, T. *et al.* Intrinsic Spin-Orbit Torque Arising from the Berry Curvature in a Metallic-Magnet/Cu-Oxide Interface. *Phys. Rev. Lett.* **121**, 017202 (2018).

105. Enoki, R., Gamou, H., Kohda, M. & Nitta, J. Enhancement of spin–orbit interaction of Cu thin films by oxidation treatment. *Appl. Phys. Express* **11**, 033001 (2018).

106. Elliott, R. J. Spin-Orbit Coupling in Band Theory—Character Tables for Some Space Groups. *Phys. Rev.* **96**, 280–287 (1954).

107. Yafet, Y. g Factors and Spin-Lattice Relaxation of Conduction Electrons. *Solid State Phys.* **14**, 1–98 (1963).

108. Demasius, K.-U. *et al.* Enhanced spin–orbit torques by oxygen incorporation in tungsten films. *Nat. Commun.* **7**, 10644 (2016).

109. An, H. *et al.* Current-induced magnetization switching using an electrically insulating spin-torque generator. *Sci. Adv.* **4**, eaar2250 (2018).

110. An, H., Kanno, Y., Asami, A. & Ando, K. Giant spin-torque generation by heavily oxidized Pt. *Phys. Rev. B* **98**, 014401 (2018).

111. Asami, A. *et al.* Spin absorption at a ferromagnetic-metal/platinum-oxide interface. *Phys. Rev. B* **99**, 024432 (2019).

112. Hajzadeh, I., Rahmati, B., Jafari, G. R. & Mohseni, S. M. Theory of the spin Hall effect in metal oxide structures. *Phys. Rev. B* **99**, 094414 (2019).

113. Blackstock, J. J., Stewart, D. R. & Li, Z. Plasma-produced ultra-thin platinum-oxide films for nanoelectronics: physical characterization. *Appl. Phys. A* **80**, 1343–1353 (2005).

114. Li, Z., Beck, P., Ohlberg, D. A. A., Stewart, D. R. & Williams, S. R. Surface properties of platinum thin films as a function of plasma treatment conditions. *Surf. Sci.* **529**, 410–418 (2003).

115. Seriani, N., Pompe, W. & Ciacchi, L. C. Catalytic Oxidation Activity of Pt3O4 Surfaces and Thin Films. *J. Phys. Chem. B* **110**, 14860 (2006).

116. Li, W. X. *et al.* Oxidation of Pt(110). *Phys. Rev. Lett.* **93**, 146104 (2004).

117. Tserkovnyak, Y., Brataas, A. & Bauer, G. E. W. Enhanced Gilbert Damping in Thin

Ferromagnetic Films. *Phys. Rev. Lett.* **88**, 117601 (2002).

118. Tserkovnyak, Y., Brataas, A., Bauer, G. E. W. & Halperin, B. I. Nonlocal magnetization dynamics in ferromagnetic heterostructures. *Rev. Mod. Phys.* **77**, 1375–1421 (2005).

119. Tserkovnyak, Y., Brataas, A. & Bauer, G. E. W. Spin pumping and magnetization dynamics in metallic multilayers. *Phys. Rev. B* **66**, 224403 (2002).

120. Mizukami, S., Ando, Y. & Miyazaki, T. The Study on Ferromagnetic Resonance Linewidth for NM/80NiFe/NM (NM=Cu, Ta, Pd and Pt) Films. *Jpn. J. Appl. Phys.* **40**, 580–585 (2001).

121. Mizukami, S., Ando, Y. & Miyazaki, T. Effect of spin diffusion on Gilbert damping for a very thin permalloy layer in Cu/permalloy/Cu/Pt films. *Phys. Rev. B* **66**, 104413 (2002).

122. Platow, W., Anisimov, A. N., Dunifer, G. L., Farle, M. & Baberschke, K. Correlations between ferromagnetic-resonance linewidths and sample quality in the study of metallic ultrathin films. *Phys. Rev. B* **58**, 5611–5621 (1998).

123. Okada, A. *et al.* Electric-field effects on magnetic anisotropy and damping constant in Ta/CoFeB/MgO investigated by ferromagnetic resonance. *Appl. Phys. Lett.* **105**, 052415 (2014).

124. Arias, R. & Mills, D. L. Extrinsic contributions to the ferromagnetic resonance response of ultrathin films. *Phys. Rev. B* **60**, 7395–7409 (1999).

125. Lindner, J. *et al.* Two-magnon damping in thin films in case of canted magnetization: Theory versus experiment. *Phys. Rev. B* **80**, 224421 (2009).

126. Mosendz, O. *et al.* Quantifying Spin Hall Angles from Spin Pumping: Experiments and Theory. *Phys. Rev. Lett.* **104**, 046601 (2010).

127. Rojas-Sánchez, J.-C. *et al.* Spin Pumping and Inverse Spin Hall Effect in Platinum: The Essential Role of Spin-Memory Loss at Metallic Interfaces. *Phys. Rev. Lett.* **112**, 106602 (2014).

128. Qiu, Z. *et al.* Spin-current probe for phase transition in an insulator. *Nat. Commun.* **7**, 12670 (2015).

129. Frangou, L. *et al.* Enhanced Spin Pumping Efficiency in Antiferromagnetic IrMn Thin Films around the Magnetic Phase Transition. *Phys. Rev. Lett.* **116**, 077203 (2016).

130. Shiomi, Y. & Saitoh, E. Paramagnetic Spin Pumping. *Phys. Rev. Lett.* **113**, 266602 (2014).

131. Okamoto, S. Spin injection and spin transport in paramagnetic insulators. *Phys. Rev. B* **93**, 064421 (2016).

132. Ast, C. R. *et al.* Giant Spin Splitting through Surface Alloying. *Phys. Rev. Lett.* **98**, 186807 (2007).

133. Lesne, E. *et al.* Highly efficient and tunable spin-to-charge conversion through Rashba coupling at oxide interfaces. *Nat. Mater.* **15**, 1261 (2016).

134. Sánchez, J. C. R. *et al.* Spin-to-charge conversion using Rashba coupling at the interface between non-magnetic materials. *Nat. Commun.* **4**, 2944 (2013).

135. Zhang, W., Jungfleisch, M. B., Jiang, W., Pearson, J. E. & Hoffmann, A. Spin pumping and inverse Rashba-Edelstein effect in NiFe/Ag/Bi and NiFe/Ag/Sb. *J. Appl. Phys.* **117**, 17C727 (2015).

136. Sangiao, S. *et al.* Control of the spin to charge conversion using the inverse Rashba-Edelstein

effect. *Appl. Phys. Lett.* **106**, 172403 (2015).

137. Isasa, M. *et al.* Origin of inverse Rashba-Edelstein effect detected at the Cu/Bi interface using lateral spin valves. *Phys. Rev. B* **93**, 014420 (2016).

138. Jungfleisch, M. B. *et al.* Interface-driven spin-torque ferromagnetic resonance by Rashba coupling at the interface between nonmagnetic materials. *Phys. Rev. B* **93**, 224419 (2016).

139. Ebert, H., Ködderitzsch, D. & Minár, J. Calculating condensed matter properties using the KKR-Green's function method—recent developments and applications. *Reports Prog. Phys.* **74**, 096501 (2011).

140. Ebert, H. SPRKKR. (2017).

141. Fuchs, K. & Mott, N. F. The conductivity of thin metallic films according to the electron theory of metals. *Math. Proc. Cambridge Philos. Soc.* **34**, 100 (1938).

142. Sondheimer, E. H. The mean free path of electrons in metals. *Adv. Phys.* **50**, 499–537 (2001).

143. Mayadas, A. F. & Shatzkes, M. Electrical-Resistivity Model for Polycrystalline Films: the Case of Arbitrary Reflection at External Surfaces. *Phys. Rev. B* **1**, 1382–1389 (1970).

144. Blöchl, P. E. Projector augmented-wave method. *Phys. Rev. B* **50**, 17953–17979 (1994).

145. Kresse, G. & Hafner, J. *Ab initio* molecular dynamics for liquid metals. *Phys. Rev. B* **47**, 558–561 (1993).

146. Kresse, G. & Furthmüller, J. Efficient iterative schemes for *ab initio* total-energy calculations using a plane-wave basis set. *Phys. Rev. B* **54**, 11169–11186 (1996).

147. Kresse, G. & Furthmüller, J. Efficiency of ab-initio total energy calculations for metals and semiconductors using a plane-wave basis set. *Comput. Mater. Sci.* **6**, 15–50 (1996).

148. Hohenberg, P. & Kohn, W. Inhomogeneous Electron Gas. *Phys. Rev.* **136**, B864–B871 (1964).

149. Kohn, W. & Sham, L. J. Self-Consistent Equations Including Exchange and Correlation Effects. *Phys. Rev.* **140**, A1133–A1138 (1965).

150. Perdew, J. P., Burke, K. & Ernzerhof, M. Generalized Gradient Approximation Made Simple. *Phys. Rev. Lett.* **77**, 3865–3868 (1996).

151. Nagano, Y. Standard enthalpy of formation of platinum hydrous oxide. *J. Therm. Anal. Calorim.* **69**, 831–839 (2002).

152. Rumble, J. R. *CRC handbook of chemistry and physics : a ready-reference book of chemical and physical data*. (CRC Press, 2019).

153. Chase, M. W. . J. NIST-JANAF Themochemical Tables, Fourth Edition. *J. Phys. Chem. Ref. Data, Monogr. 9* 1–1951 (1998).

154. Jiles, D. *Introduction to magnetism and magnetic materials*. (CRC Press, 2015).

155. Dzialoshinskii, I. E. Thermodynamical Theory of 'Weak" Ferromagnetism in Antiferromagnetic Substances. *J. Exp. Theor. Phys.* **5**, 1259 (1957).

156. Moriya, T. Anisotropic Superexchange Interaction and Weak Ferromagnetism. *Phys. Rev.* **120**, 91–98 (1960).

157. Fert, A. & Levy, P. M. Role of Anisotropic Exchange Interactions in Determining the Properties of Spin-Glasses. *Phys. Rev. Lett.* **44**, 1538–1541 (1980).

158. Thiaville, A., Rohart, S., Jué, É., Cros, V. & Fert, A. Dynamics of Dzyaloshinskii domain walls in ultrathin magnetic films. *EPL (Europhysics Lett.* **100**, 57002 (2012).

159. Bogdanov, A. N. & Rößler, U. K. Chiral Symmetry Breaking in Magnetic Thin Films and Multilayers. *Phys. Rev. Lett.* **87**, 037203 (2001).

160. Moriya, T. New Mechanism of Anisotropic Superexchange Interaction. *Phys. Rev. Lett.* **4**, 228–230 (1960).

161. Udvardi, L. & Szunyogh, L. Chiral Asymmetry of the Spin-Wave Spectra in Ultrathin Magnetic Films. *Phys. Rev. Lett.* **102**, 207204 (2009).

162. Costa, A. T., Muniz, R. B., Lounis, S., Klautau, A. B. & Mills, D. L. Spin-orbit coupling and spin waves in ultrathin ferromagnets: The spin-wave Rashba effect. *Phys. Rev. B* **82**, 014428 (2010).

163. Moon, J.-H. *et al.* Spin-wave propagation in the presence of interfacial Dzyaloshinskii-Moriya interaction. *Phys. Rev. B* **88**, 184404 (2013).

164. Rayleigh, Lord. XXXIV. On the transmission of light through an atmosphere containing small particles in suspension, and on the origin of the blue of the sky. *London, Edinburgh, Dublin Philos. Mag. J. Sci.* **47**, 375–384 (1899).

165. RAMAN, C. V. A Change of Wave-length in Light Scattering. *Nature* **121**, 619–619 (1928).

166. Brillouin, L. Diffusion de la lumière et des rayons X par un corps transparent homogène. *Ann. Phys. (Paris).* **9**, 88–122 (1922).

167. Eshbach, J. R. & Damon, R. W. Surface Magnetostatic Modes and Surface Spin Waves. *Phys. Rev.* **118**, 1208–1210 (1960).

168. Haldar, A., Banerjee, C., Laha, P. & Barman, A. Brillouin light scattering study of spin waves in NiFe/Co exchange spring bilayer films. *J. Appl. Phys.* **115**, 133901 (2014).

169. Di, K. *et al.* Direct Observation of the Dzyaloshinskii-Moriya Interaction in a Pt/Co/Ni Film. *Phys. Rev. Lett.* **114**, 047201 (2015).

170. Nembach, H. T., Shaw, J. M., Weiler, M., Jué, E. & Silva, T. J. Linear relation between Heisenberg exchange and interfacial Dzyaloshinskii–Moriya interaction in metal films. *Nat. Phys.* **11**, 825–829 (2015).

171. Tacchi, S. *et al.* Interfacial Dzyaloshinskii-Moriya Interaction in Pt / CoFeB Films: Effect of the Heavy-Metal Thickness. *Phys. Rev. Lett.* **118**, 147201 (2017).

172. Vaz, C. A. F., Bland, J. A. C. & Lauhoff, G. Magnetism in ultrathin film structures. *Reports Prog. Phys.* **71**, 056501 (2008).

173. *MPMS Application Note 1014-210: Oxygen Contamination*. https://www.qdusa.com/siteDocs/appNotes/1014-210.pdf (1997).

174. Trifu, A. V. Mesures de Couples de Spin Orbite dans des heterostructures métal lourde /ferromagnet a base de Pt, avec anisotropie magnétique planaire. (Université Grenoble Alpes, 2017).

175. Nguyen, M.-H., Nguyen, K. X., Muller, D. A., Ralph, D. C. & Buhrman, R. A. Enhancement of the anti-damping spin torque efficacy of platinum by interface modification. *Appl. Phys. Lett.* **106**, 222402 (2015).

176. Zhou, F. L., Erwin, J. K., Brucker, C. F. & Mansuripur, M. Wavelength dependencies of the Kerr rotation angle and ellipticity for the magneto-optical recording media. *J. Appl. Phys.* **70**, 6286

(1991).

177. Hilson, G. Embedded MRAM Can Take the Heat. *EETimes* https://www.eetimes.com/document.asp?doc_id=1331958 (2017).

178. Dorrance, R. W. Modeling and Design of STT-MRAMs. (University of California, Los Angeles, 2011).

179. Akashi, T. & Yoshimura, Y. Deep reactive ion etching of borosilicate glass using an anodically bonded silicon wafer as an etching mask. *J. Micromechanics Microengineering* **16**, 1051–1056 (2006).